

**SIMULATION OF LITHIUM-ION BATTERIES BASED ON PULSED CURRENT
CHARACTERIZATION**

by

Chi Wah Eddie Fok

M.A.Sc., The University of British Columbia, 2006

B.A.Sc., The University of British Columbia, 2003

A THESIS SUBMITTED IN PARTIAL FULFILLMENT OF
THE REQUIREMENTS FOR THE DEGREE OF

DOCTOR OF PHILOSOPHY

in

THE FACULTY OF GRADUATE AND POSTDOCTORAL STUDIES

(Electrical and Computer Engineering)

THE UNIVERSITY OF BRITISH COLUMBIA

(Vancouver)

August 2016

© Chi Wah Eddie Fok, 2016

Abstract

Simulation of lithium-ion and other cells is important for basic understanding, design of cells, application in devices including automotive, and as part of system simulations for control and safety purposes. This thesis proposes a new cell equivalent circuit model, called the distributed state of charge model, which consists of a series resistance, and a non-linear RC transmission line. The circuit model components are dependent on the SOC, with the circuit being unique in considering the local (depth dependent) charge state.

A pulsed discharge and charge technique is put forth for extracting the model parameters, and their dependence on cell state of charge. The extraction method is applied to commercial lithium-ion cells. It is shown that the extracted parameters are largely independent of magnitude of the pulsed currents. This distinguishes the model from other widely used equivalent circuits in which parameter extraction is generally performed as a function of current. Therefore, this approach is promising for reducing time required for this extraction phase.

Validation experiments are performed using both static discharge and a variable-current profile. Two versions of the model are developed based on the governing diffusion mechanism – planar or spherical. Simulations using the planar model matched experimental results well for large current pulses (up to 2.0 C discharge) with slow average discharge (0.20 C discharge) – root-mean-square error typically within 0.84%, and maximum error within 3.7%. On the other hand, the spherical model performs well for higher continuous discharge current (up to 0.50 C discharge), but for lower current pulses (up to 0.67 C discharge) – root-mean-square error

typically within 0.95%, and maximum error within 3.3%. This tradeoff may be attributed to the distribution of capacitances in the corresponding electrode models.

Parameters of the proposed equivalent-circuit are also extracted for a lithium-alloying tin electrode. Tin is an electrode of interest due to its high specific and volumetric capacity. The response is much different from those obtained from the commercial lithium ion cells, including apparent drops in effective diffusion coefficient by three orders of magnitude over narrow regions of SOC. These characteristics are explained qualitatively using the phase transformation effect.

Preface

This thesis is the original work of the author, Chi Wah Eddie Fok. It is previously unpublished, except Chapter 4. Chapter 1 provides an introduction, background and motivation. Chapters 2 and 3 describe a proposed new equivalent circuit model for describing lithium ion cells. The approach and methods were devised by the author, with guidance from supervisor Dr. John Madden and Dr. William Dunford. The experimental testing apparatus used in chapters 2 and 3 was based on a design suggested by William Dunford. The implementation, measurements, model validation and analysis were performed by the author in consultation with John Madden. The work in Chapter 4 is based on that in [Measurement of the Diffusion Coefficient of Lithium in Tin Thin Films Including Phase Transformation Effects](#) by ECW Fok, JD Madden, which appears in the ECS Transactions, volume 53 (30), pages 131-142. This follows up on an abstract and presentation of the same title presented at the 223rd Electrochemical Society (ECS) Meeting, and with myself as first author, Dr. Usgaocar as second author, Mr. Mahmoudzadeh as third author, and finally Dr. Madden. This publication was written and led by the author of this thesis. The project was devised by the author, who performed all aspects, with the exception of several experiments. The author trained Dr. Ashwin Usgaocar and Mr. Ali Mahmoudzadeh on the assembly and testing of tin electrode cells. They ran several of the tests. They, along with Dr. John Madden, provided technical and editorial feedback on the article manuscript. Chapter 5 is a summary and conclusions chapter. All work in this thesis – experimental and in simulation – is my own. Regular discussions with Dr. Madden have helped clarify the contributions and increase the degree of validation. Feedback from my committee members has also greatly

helped guide me towards putting the work in perspective and better explaining my results and contributions. In this sense Dr. Dunford, Dr. Cretu, Dr. Bizzotto and Dr. Walus – supervisory and examining committee members past and present – have contributed to improving the work. That said, I take full responsibility for this thesis. More detail on the evolution and progression of the thesis is provided in the remainder of the preface.

Chi Wah Eddie Fok, Hong Kong, January 17th 2016

Table of Contents

Abstract.....	ii
Preface.....	iv
Table of Contents	vi
List of Tables	ix
List of Figures.....	xii
Glossary	xxv
Acknowledgements	xxvi
Chapter 1: Introduction	1
1.1 Research Aims and Motivation.....	3
1.2 Lithium-Ion Cells.....	4
1.2.1 Lithium-Ion versus Other Rechargeable Battery Technologies.....	5
1.2.2 Lithium-Ion Cell Operation	7
1.3 Cell Modeling	14
1.3.1 Electrochemical Models.....	15
1.3.2 Equivalent Circuit Models	24
1.3.2.1 Thévenin Model	25
1.3.2.2 Impedance Model.....	29
1.3.2.3 Runtime Model	37
1.4 Key Contributions	48
Chapter 2: Polymer Cell Characterization and Modeling.....	51
2.1 Model Development.....	52

2.2	Experimental Setup	63
2.3	Extraction	65
2.3.1	Parameter Extraction Procedure	65
2.3.2	Experimental Method.....	77
2.3.3	Results and Analysis	81
2.4	Validation.....	88
2.4.1	Simulation Model.....	89
2.4.2	Validation Tests	91
2.5	Chapter Conclusions	101
Chapter 3: Cylindrical Cell Characterization and Modeling		103
3.1	Experimental Setup	104
3.2	Extraction	107
3.2.1	Initial Estimation of the OCV Dependence on SOC	108
3.2.1.1	Procedure	109
3.2.1.2	Results and Analysis	110
3.2.2	Pulsed Experiments.....	116
3.2.2.1	Procedure	116
3.2.2.2	Results and Analysis	119
3.2.2.3	Comparison to Relaxation Pulse Analysis	148
3.3	Validation.....	161
3.3.1	Validation Test #1	162
3.3.1.1	Test Procedure	162
3.3.1.2	Results and Analysis	167

3.3.1.3	The π -Model and Comparisons between Different Number of Segments.....	179
3.3.2	Validation Test #2.....	187
3.3.2.1	Test Procedure	188
3.3.2.2	Results and Analysis	189
3.3.2.3	Spherical Model	197
3.4	Chapter Conclusions	225
Chapter 4: Characterization of Tin Electrodes.....		235
4.1	Background	236
4.2	Experimental Method.....	245
4.3	Results and Analysis	248
4.4	Chapter Conclusions	267
Chapter 5: Conclusion.....		269
Bibliography		276

List of Tables

Table 1-1. Advantages and disadvantages of lithium ion rechargeable cells relative to other commercial cells..	7
Table 1-2. Tabulation of the simulation errors for runtime validation tests of some of the literature equivalent-circuit models. As there is no commonly accepted method to validate the model, or quantify the simulation errors, the test methods differ between the results, and the missing data in the table cannot be filled.	47
Table 2-1. List of cell model parameters of the distributed SOC equivalent-circuit model.	63
Table 2-2. List of model parameters of the distributed SOC equivalent-circuit model and their corresponding extraction equations.	77
Table 2-3. Test Procedure for estimating the open-circuit voltage V_{OC} dependence on SOC, $V_{OC}(SOC)$.	78
Table 2-4. Durations of pulses in the discharge pulse experiment used for model parameter extraction.	81
Table 2-5. Pulse phase durations for the four validation experiments.	92
Table 2-6. RMSE for different number of RC-segments for validation experiment #1.	95
Table 3-1. Experimental procedure for slow discharge experiment to estimate the open-circuit voltage V_{OC} dependence on SOC.	110
Table 3-2. Total pulse charge of each pulse in the pulsed discharging experiment. The corresponding cumulative discharged capacity, estimated SOC, and estimated OCV after the pulse are also listed.	114

Table 3-3. Total pulse charge for each pulse in the pulsed charging experiment. The corresponding cumulative discharged capacity, estimated SOC, and estimated OCV after the pulse are also listed.	115
Table 3-4. Pulsed discharge procedure for the parameter extraction experiments.	117
Table 3-5. Pulsed charge procedure for the parameter extraction experiments.....	118
Table 3-6. Table of tested pulsed current magnitudes and their corresponding C-rates.....	119
Table 3-7. Fitted parameters for the OCV dependence on SOC. The empirical relationship between the OCV and SOC has the form shown in equation [3-7].	143
Table 3-8. Fitted parameters for the diffusion resistance dependence on SOC. The empirical relationship between the diffusion resistance and SOC has the form shown in Equation [3-8].	145
Table 3-9. Fitted parameters for the series resistance dependence on SOC. The empirical relationship between the series resistance and SOC has the form shown in Equation [3-9].	148
Table 3-10. DDT procedure, and the associated step currents for the three chosen max test currents of a) 6.0 A, b) 2.0 A, and c) 600 mA.	166
Table 3-11. Characteristics of the three DDTs.	167
Table 3-12. Tabulated results of the MAPVE (in terms of both percentage and voltage), and RMSPVE (also in terms of percentage and voltage) for the beginning 95% duration of the three DDTs. The results shown are the average over the three tested cells.....	172
Table 3-13. The model configuration and number of equivalent circuit elements that are tested in order to compare simulation accuracy.	181
Table 3-14. Test procedure for constant current discharge tests for validation of the distributed SOC model.....	189

Table 3-15. Tabulated results of the MAPVE (in terms of both percentage and voltage), and RMSPVE (also in terms of percentage and voltage) for the beginning 95% duration of the four constant current discharge tests. The results shown are the average over the three tested cells.	191
Table 3-16. Tabulated results of the MAPVE (in terms of both percentage and voltage), and RMSPVE (also in terms of percentage and voltage) for the beginning 95% duration of the four constant current discharge tests. Results for both planar and spherical electrodes are shown. The results shown are the average over the three tested cells.....	213
Table 3-17. Tabulated results of the MAPVE (in terms of both percentage and voltage), and RMSPVE (also in terms of percentage and voltage) for the beginning 95% duration of the three DDTs. Results are shown for both planar and spherical models. The results shown are the average over the three tested cells.	217
Table 4-1. Values of Model Parameters Used in the Calculations	262

List of Figures

Figure 1-1. Comparison of energy density and specific energy between lithium ion and other rechargeable cell technologies..	5
Figure 1-2. Comparison of different rechargeable battery technologies in terms of specific energy and specific power.	6
Figure 1-3. Illustration of the principles of operation of a lithium ion battery during charge and discharge. In both illustrations, the positive electrode is depicted on the left, while the negative electrode is depicted on the right.	8
Figure 1-4. Illustration of the interior structure of a typical cylindrical lithium-ion cell.	11
Figure 1-5. Depiction of the one-dimensional simplification of the cell structure.	12
Figure 1-6. Capacity vs. potentials of various positive and negative electrode materials.	14
Figure 1-7. Illustration of cell structure and the physics involved during charging. The negative electrode occupies the domain between $x=0^-$ and $x=L^-$, as indicated at the top of the diagram. The separator is situated between $x=0^{sep}$ and $x=L^{sep}$. The positive electrode occupies the domain between $x=L^+$ and $x=0^+$. During charging, lithium ions are released from the positive electrode particles (green) and inserted into the negative electrode particles (red). Correspondingly, electrons travel externally from the positive electrode to the negative electrode via the current collectors at $x=0^+$ (positive) and $x=0^-$ (negative). This external circuit connection would require an electrical power source (not illustrated) to provide the required energy.	16
Figure 1-8. Depiction of the three different lithium ion cell models. A) The P2D model. B) The SPM. C) The distributed SOC model.	22

Figure 1-9. The distributed SOC equivalent-circuit model (linear version) proposed in this thesis work.	24
Figure 1-10. Circuit diagram for Thévenin equivalent circuit models.	26
Figure 1-11. Depiction of the discharging pulse used to characterize the cell under test.....	26
Figure 1-12. Typical current (Top) and voltage (Bottom) response of a cell to a discharging current pulse. The negative applied current corresponds to discharge of the cell.	28
Figure 1-13. Charging, and subsequent relaxation, response of a typical cell. The positive applied current charges the cell.....	28
Figure 1-14. The Randles circuit model.	30
Figure 1-15. Foster structure representation of the Warburg element.	32
Figure 1-16. Cauer structure representation of the Warburg element.	33
Figure 1-17. Time-domain equivalent of the Warburg element in [27].	33
Figure 1-18. Complete time-domain model from [27].	34
Figure 1-19. Impedance model used in [28].	34
Figure 1-20. Time-domain equivalent of Z_{ZARC} in [28].....	35
Figure 1-21. Time-domain equivalent of the Warburg element in [28].	35
Figure 1-22. Impedance model used in [53].	36
Figure 1-23. One segment of the RC transmission line used to model the electrode porosity impedance in [53].	36
Figure 1-24. Circuit diagram for run-time model proposed by Chen and Rincon-Mora.....	38
Figure 1-25. Depiction of the discharging pulses used to characterize the cell under test.	41
Figure 1-26. Voltage response of a cell during the pulse phase of a discharge pulse. The flat initial cell voltage is the open-circuit voltage of the initial cell SOC before the current step. Once	

the current step is applied (beginning of the pulse phase), the cell voltage falls rapidly. Then as time proceeds, the cell voltage falls according to $t^{1/2}$	42
Figure 1-27. Cell voltage response during the relaxation phase of a discharge pulse. The initial falling cell voltage that is shown coincides with the discharging current that is still being applied (latter portion of the pulse phase). At <i>ca.</i> 1.02×10^4 seconds, the relaxation phase begins (the applied current falls to zero), and the cell voltage rises jumps up instantaneously due to the absence of the <i>IR</i> drop. The cell voltage continues to rise as the cell relaxes. It can be seen that the cell voltage reaches an equilibrium value as time proceeds. This is the OCV at this cell SOC. Then, towards the far right, the next discharging current pulse is applied and the cell voltage falls again.....	43
Figure 1-28. Illustration of the charging pulses used to characterize the cell under test.	44
Figure 2-1. Randles circuit model, which is commonly used in impedance spectroscopy.	52
Figure 2-2. One-dimensional diffusion element used to model the lithium ion diffusion process in the lithium ion cell.	54
Figure 2-3. Transmission line model consisting of resistors and capacitors to model diffusion..	56
Figure 2-4. Equivalent circuit model consisting of the RC transmission line and a series resistance.....	59
Figure 2-5. Final distributed SOC equivalent circuit model, with dependent voltage sources replacing the capacitors of the RC transmission line.....	61
Figure 2-6. Charging setup for testing the Dow Kokam lithium-ion polymer cell.....	64
Figure 2-7. Discharging setup for testing the Dow Kokam lithium-ion polymer cell.....	65

Figure 2-8. Depiction of the discharging pulses used to characterize the cell under test (left). The corresponding illustration of charging pulses used to characterize the cell under test is shown on the right.	67
Figure 2-9. Illustration of the voltage response from a discharge current pulse.....	68
Figure 2-10. Typical voltage response (bottom) to an applied charging current pulse. The current profile is shown in the top plot.	69
Figure 2-11. Representative short time response of a commercial lithium ion cell to a current pulse. The data is from experiments discussed in Chapter 3.	74
Figure 2-12. Representative long time response of a commercial lithium ion cell to a current pulse. The data is from experiments discussed in Chapter 3.	75
Figure 2-13. Effects of changes in model parameter on the resulting predicted cell voltage response. The data is from experiments, discussed in Chapter 3, on a commercial lithium ion cell.....	76
Figure 2-14. Cell voltage measured during 3.0 A discharge from SOC of 1.0. During discharge, the cell SOC decreases. The slope of the measured cell voltage is highest at SOC of <i>ca.</i> 0.5, indicating that the effective capacitance at that SOC is highest.	80
Figure 2-15. Measured cell voltage during the pulsed current parameter extraction experiment using 15 A pulses.	82
Figure 2-16. Comparison of the extracted fit and the cell voltage response to the first current pulse of the pulsed current parameter extraction experiment.	83
Figure 2-17. Comparison of the extracted fit and the cell voltage response to the second current pulse of the pulsed current parameter extraction experiment.	83

Figure 2-18. Comparison of the extracted fit and the cell voltage response to the 36 th current pulse of the pulsed current parameter extraction experiment.	84
Figure 2-19. Extracted diffusion capacitance C_D as a function of SOC.	86
Figure 2-20. Extracted diffusion resistance R_D as a function of SOC.	87
Figure 2-21. Extracted series resistance R_S as a function of SOC.	88
Figure 2-22. Lumped equivalent-circuit model.	90
Figure 2-23. Final lumped equivalent-circuit model.	90
Figure 2-24. Measured and simulated voltage response of the Dow Kokam cell for validation test #1.....	94
Figure 2-25. Measured and simulated voltage response of the Dow Kokam cell for validation test #2.....	96
Figure 2-26. RMSE for different number of RC-segments for validation experiment #2.....	97
Figure 2-27. Measured and simulated voltage response for validation test #3.....	98
Figure 2-28. RMSE for different number of RC-segments for validation experiment #3.....	98
Figure 2-29. Measured and simulated voltage response for validation test #4.....	99
Figure 2-30. RMSE for different number of RC-segments for validation experiment 4.....	100
Figure 3-1. Cell holder for cell testing. The three metallic cylinders in the bottom half of the photo are the 30U cylindrical lithium ion cells.....	105
Figure 3-2. Two metallic contacts for contacting the cell cap, which is the cell's positive terminal.	106
Figure 3-3. Bottom portion of the cell holder, showing the spring-loaded center pin for current conduction, and outer metallic tube for voltage measurement.	106
Figure 3-4. Cell cabinet for the experiments.	107

Figure 3-5. Measured cell voltage of the 30U cell for slow (0.020 C) discharge.....	111
Figure 3-6. Pulse discharge interval for the subsequent tests. Greens open circles are points equally spaced in voltage drop that are selected as the states of charge at which discharge steps will be applied in order to extract model parameters open-circuit voltage V_{OC} , diffusion capacitance C_D , diffusion resistance R_D , and series resistance R_S	112
Figure 3-7. 6.0 A pulsed discharge experimental results for the 30U cell. The current pulse profiles are shown in the top plot, while the measured cell voltage is shown in the bottom.....	120
Figure 3-8. Cell response to the first 6.0 A discharge current pulse. The top plot shows the applied current, and the bottom plot shows the measured cell voltage response.	121
Figure 3-9. 60 mA pulsed discharge experimental results for the 30U cell. The top plot shows the long duration pulse phase of the current pulses, separated by relaxation phase of 60 minutes. The bottom plot shows the measured cell voltage.	122
Figure 3-10. Cell response to the first 60 mA discharge current pulse. The top plot shows the applied current, and the bottom plot shows the measured cell voltage response.	123
Figure 3-11. 6.0 A pulsed charging experimental results. The top plot shows the short pulse phase of the current pulses with high current, separated by the 60 minute relaxation phases. The bottom plot shows the measured cell voltage.	124
Figure 3-12. 60 mA pulsed charging experimental results. The top plot shows the mostly long duration pulse phases, separated by 60 minute relaxation phases. Initial pulses are short due to the small diffusion capacitance near full discharge. The bottom plot shows the measured cell voltage.....	125

Figure 3-13. Cell voltage as a function of cumulative discharged capacity for 6.0 A pulsed discharge. Here the vertical lines show relaxation of cell voltage (upwards) over the course of the one hour relaxation phase, and the following rapid discharge.....	126
Figure 3-14. Cell voltage as a function of cumulative discharged capacity for 60 mA pulsed discharge. The small upward spikes represent relaxation at open circuit following the pulse phase.	127
Figure 3-15. Cell voltage as a function of cumulative discharged capacity for all five tested pulsed discharge current magnitudes.	128
Figure 3-16. Experimental results for the 6.0 A charging pulse experiment.	129
Figure 3-17. Cell voltage as a function of cumulative discharged capacity for the charging pulse experiments at different current magnitudes.....	130
Figure 3-18. Extracted OCV from discharge and charge current pulses of different pulse magnitudes.	131
Figure 3-19. Magnified view of the extracted OCV as a function of SOC in the low SOC region.	132
Figure 3-20. Diffusion capacitance as a function of SOC, extracted from discharging pulses. .	134
Figure 3-21. Diffusion capacitance as a function of SOC, extracted from charging pulses.....	135
Figure 3-22. NRMSE for the discharging pulse experiments at different current magnitudes. The left plot shows the entire SOC range, while the right plot shows the magnified view of the low SOC region.....	138
Figure 3-23. NRMSE for the charging pulse experiments at different current magnitudes. The left plot shows the entire SOC range, while the right plot shows the magnified view of the low SOC region.....	138

Figure 3-24. Comparison of the experimental data and calculated fit of the pulse phase cell voltage for the 1 st pulse in the 6.0 A discharging pulse experiment. The NRMSE of the fit is 0.96.....	139
Figure 3-25. Comparison of the experimental data and calculated fit of the pulse phase cell voltage during the 2 nd pulse in the 129 mA pulsed discharge experiment. The NRMSE of the fit is 0.71.....	140
Figure 3-26. Comparison of the experimental data and calculated fit of the pulse phase cell voltage during the 13 th pulse in the 6.0 A discharging pulse experiment. The NRMSE of the fit is 0.81.....	141
Figure 3-27. Plot of the OCV as a function of SOC obtained from the different pulsed current experiments, and the empirical fit.....	143
Figure 3-28. Plot of the extracted diffusion resistance R_D from pulsed current experiments at different current magnitudes, and the obtained empirical fit.....	145
Figure 3-29. Plot of the extracted series resistance as a function of SOC, and the empirical fit of the dependence of the series resistance parameter R_S on the cell SOC.	147
Figure 3-30. 30U cell voltage during the relaxation phase of the first pulse of the pulsed discharge experiment at the five tested discharge current magnitudes.....	153
Figure 3-31. Plot of the term $(V_{Batt}-V_{OC}, i)/iBatt$ during the initial 9 seconds of the pulse phase at different current magnitudes.	158
Figure 3-32. The SOC distribution in the electrode model during the initial eight seconds of the first 6.0 A discharge pulse.	160
Figure 3-33. The SOC distribution in the electrode model during the relaxation phase of the first 6.0 A discharge pulse.....	161

Figure 3-34. (A) The DST profile. It is a variable-power profile defined using percentages of the peak discharge power of the test. (B) The DDT profile defined in this work. This profile has the same shape as the DST, but is defined using percentages of the peak discharge current of the test. The DDT profile is simpler to simulate than the DST.....	164
Figure 3-35. Plot of results from the 6.0 A DDT. The top plot shows the experimental and simulated results. The middle plot is the PVE of the simulated cell voltage compared to the experimental voltage. The bottom plot shows the measured current profile. As per the convention adopted in this work, negative and positive current corresponds to discharging and charging currents, respectively.	170
Figure 3-36. Plot of results from the 2.0 A DDT. The top plot shows the measured and simulated cell voltages. The bottom plot shows the PVE.....	173
Figure 3-37. Plot of results from the 600 mA DDT. The top plot shows the measured and simulated cell voltages. The bottom plot is the PVE.	176
Figure 3-38. Schematic diagram of the one segment transmission line model using π -form segments.....	180
Figure 3-39. Schematic diagram of the two segment model using π -form segments.....	180
Figure 3-40. Plot of the RMSPVE for the simulated response of 6.0 A DDT for different structure of the proposed model. The x-axis shows the number of segments in the transmission line for the original-form (outside parentheses) and π -form (inside parentheses).....	183
Figure 3-41. Plot of the RMSPVE for the simulated response of 2.0 A DDT for different structure of the proposed model. The x-axis shows the number of segments in the transmission line for the original-form (outside parentheses) and π -form (inside parentheses).....	185

Figure 3-42. Plot of the RMSPVE for the simulated response of 600 mA DDT for different structure of the proposed model. The x-axis shows the number of segments in the transmission line model for the original-form (outside parentheses) and π -form (inside parentheses).....	186
Figure 3-43. Experimental and simulated results for four constant current discharge tests.	190
Figure 3-44. Plot of PVE during cell discharge at different constant discharge currents.....	192
Figure 3-45. Depiction of A) the equivalent-circuit derived from the planar model and B) the spherical model geometry.	199
Figure 3-46. Plot of the differential capacitance C_r , and differential resistance R_r , according to equations [3-23] and [3-24]. The plotted differential capacitance C_r is normalized to material capacitance per unit volume β , while the plotted differential resistance R_r is normalized to material resistivity κ	201
Figure 3-47. RC-network representation of a shell of inner-radius r_i , and outer-radius r_o	203
Figure 3-48. Breakdown of spherical electrode into 4 sections, consisting of 3 shells and a spherical core.	204
Figure 3-49. Completed linear version of the distributed SOC equivalent-circuit model for a spherical electrode.	205
Figure 3-50. Final (non-linear) spherical distributed SOC equivalent-circuit model, based on the spherical electrode model.	209
Figure 3-51. Depiction of the geometries of the four lithium ion cell models. A) P2D model, B) SPM, C) planar distributed SOC model, and D) spherical distributed SOC model.	211
Figure 3-52. Simulated results from the spherical model is shown together with the experimental ones for the four constant current discharge tests.	212

Figure 3-53. The PVE for the simulated cell voltage using the spherical distributed SOC model.	214
Figure 3-54. Plot of results from the 6.0 A DDT. The top plot shows the measured and simulated cell voltages. The simulations were performed using the spherical electrode model. The bottom plot is the PVE.	216
Figure 3-55. Plot of results from the 2.0 A DDT. The top plot shows the measured and simulated cell voltages. The simulations were performed using the spherical electrode model. The bottom plot is the PVE.	219
Figure 3-56. Plot of results from the 600 mA DDT. The top plot shows the measured and simulated cell voltages. The simulations were performed using the spherical electrode model. The bottom plot is the PVE.	219
Figure 3-57. Equivalent-circuit model that adds solution-phase resistance effects to the spherical electrode to model the thickness of the porous electrode. This is an avenue for extending the range of applicability of the distributed SOC model.	223
Figure 4-1. Comparisons of capacities (gravimetric (green) and volumetric (purple)) between different elemental electrodes.	237
Figure 4-2. Planar diffusion element for modeling lithium ion diffusion into the tin thin film.	240
Figure 4-3. Depiction of the pulsed charging experiment profile is shown in the left diagram. As the tin electrode would be used as the negative electrode active material, charging of the electrode consists of a negative current, and leads to a decreasing electrode potential. The corresponding depiction of the pulsed discharging experiment profile is shown in the right diagram. Discharging of the electrode consists of a positive current, and leads to an increasing electrode potential.	248

Figure 4-4. Scanning electron microscope image of the tin surface.....	250
Figure 4-5. Potential of the tin electrode during constant current charge and discharge at 60 $\mu\text{A}/\text{cm}^2$	251
Figure 4-6. The top plot shows the applied current profile during the pulsed charging experiment for the tin thin film electrode. The bottom plot shows the corresponding measured electrode potential.....	252
Figure 4-7. The top plot shows the applied current profile during the pulsed discharging experiment for the tin thin film electrode. The bottom plot shows the corresponding measured electrode potential.....	255
Figure 4-8. Open-circuit potential of the tin thin film during charge and discharge.	256
Figure 4-9. Diffusion capacitance C_D of the tin thin film, extracted from the pulsed discharging data.....	257
Figure 4-10. Diffusion resistance R_D of the tin thin film, extracted from the pulsed discharging data.....	258
Figure 4-11. Lithium ion diffusion coefficient in the tin film, extracted from the pulsed discharging experiment.....	259
Figure 4-12. Potential transients during four consecutive discharging pulses of the experiment (1st: cross, 2nd: star, 3rd: circle, 4th: dot) near the 0.54 V open-circuit potential plateau.....	260
Figure 4-13. Calculated transient cell voltage during the pulse phase (when current is applied) of a pulsed experiment using the single phase model. The scale is much larger here than in the previous figure as the single phase model leads to a continued rise in overpotential, while the existence of a phase boundary acts as a charge sink which can be close to the surface.....	261

Figure 4-14. Illustration of the phase transformation model that consist of two regions of different phases. 263

Figure 4-15. Calculated concentration transient during the pulse phase of the pulsed discharging experiment using the phase transformation model. The four curves correspond to different starting phase boundary locations ξ_0 : 0.2 (dash dot), 0.4 (dash), 0.6 (dot), and 0.8 (solid). 264

Glossary

DDT	Dynamic Discharge Test
DOD	Depth of Discharge
DST	Dynamic Stress Test
EIS	Electrochemical Impedance Spectroscopy
FUDS	Federal Urban Driving Schedule
GITT	Galvanostatic Intermittent Titration Technique
MAPVE	Maximum-Absolute-Percent-Voltage-Error
NRMSE	Normalized-Root-Mean-Square-Error
OCV	Open-Circuit Voltage
P2D	Pseudo-Two-Dimensional
PVE	Percent-Voltage-Error
RMSE	Root-Mean-Square-Error
RMSPVE	Root-Mean-Square-Percent-Voltage-Error
SOC	State of Charge
SPM	Single Particle Model
USABC	United States Advanced Battery Consortium
USCAR	United States Council for Automotive Research

Acknowledgements

I owe a tremendous amount of gratitude to Dr. John Madden, who remained unyieldingly supportive throughout this degree. I would also like to thank the many labmates who provided help in designing experiments, and their moral support.

Special thanks are owed to my wife and parents, who provided tremendous support throughout my years in this program.

Chapter 1: Introduction

There is an increase in adoption of lithium-ion technology in industrial and motive applications where cell response understanding is critical. In the shipping industry for example, hybrid diesel electric tugboats and ferries are being implemented that use lithium ion cells to store energy and deliver power [1]. Models are useful for many aspects of this application, ranging from use by designers of the DC-to-DC converters to validate their approaches, to implementation as part of system models required for the purpose of marine insurance. Indeed, this project was motivated by a request for such model development expressed by Corvus Energy of Richmond, British Columbia.

There is a large number of models in the literature that can be applied to model lithium-ion cells, with the vast majority falling into two classes. They are: 1. equivalent-circuit models, and 2. electrochemical models. Equivalent-circuit models consist of electrical elements such as resistors and capacitors. These are easily understood by engineers and are relatively straightforward to use. Their accuracies typically lie within the 1-5% range [2]. Electrochemical models account for all the key physical mechanisms operating inside the cell. They model detailed phenomena of electron transport, ion transport, and ion insertion and extraction. They can offer higher accuracy over a larger range of operating conditions than equivalent-circuit models. They are most often employed in academia and by cell manufacturers for cell design optimization. However, due to their complexity and the need to obtain and understand the detailed physical parameters operating inside the cell, it is difficult for most engineers to employ

this type of model. Also, speed and computing resources are key decision factors for the choice of model. Therefore, equivalent-circuit models have remained very popular.

In order for an equivalent-circuit model to be useful for system engineers, there are a number of key requirements that need to be met. First, the battery model needs to be implemented in commonly used simulation environments, such as MATLAB® Simulink®. This allows the battery model to form part of a larger system model that enables the engineer to simulate the whole system behavior under different use cases. Second, the accuracy of the model needs to meet the requirements of the application. As mentioned above, the accuracy achieved for equivalent-circuit models is typically 1-5%. Third, the extraction effort required to employ a model should ideally be low, reducing the time- and engineering-resources needed to obtain the cell model. The aim of the present work is to describe and demonstrate a new equivalent-circuit model, called the distributed State of Charge (SOC) model, which satisfies these requirements.

The distributed SOC model builds upon literature models by including a nonlinear transmission line. This transmission line models the local SOC of the cell throughout the depth of the cell's electrodes. The transmission line parameters at each depth depend on the local SOC. This model is implemented in MATLAB® Simulink®, and demonstrates a root-mean-square accuracy within 1% (average value from three tested cells) over the full range of SOC, for dynamic currents provided the average discharge current is restricted below 0.20 C. For higher average discharge currents, an alternative model derived from spherical diffusion is proposed. These models consist of a series of resistive, capacitive, and dependent-voltage sources that are easily understood by system engineers. The advantage of these models is that the number of

experiments required to extract the model parameters can be much lower than competing models in the literature. While the literature models require parameter extraction experiments for each applied current, the models developed in this work are demonstrated to only require two sets of characterization experiments – at least for the tests performed herein. This greatly reduces the characterization effort to complete the model before simulation. So this model’s key advantage is its ease of parameter extraction. It is shown in this work that the model complexity is comparable to that of the most popular ones available in the literature.

The rest of this chapter presents background material for the remainder of this thesis. The development and use of the model for commercial lithium-ion cells are shown in Chapters 2 and 3. In Chapter 4, an investigation of a pulsed method to characterize a thin film tin electrode is presented. In this case the interest is in investigating the suitability of using the distributed SOC model in modeling the tin electrode. The interest in tin electrodes in lithium-ion batteries stems from tin’s potential to offer much better gravimetric and volumetric energy densities than currently used carbon electrodes.

1.1 Research Aims and Motivation

As mentioned above, a novel aspect of the proposed distributed SOC model is that it allows for local SOC dependence of the circuit elements, allowing for variation within an electrode and cell. A cell’s SOC is the ratio of a cell’s remaining charge to its full capacity. The cell’s full capacity is the maximum amount of charge, usually measured in Ampere-hours (Ah), that can be reversibly stored and then extracted from it. An ampere-hour is equivalent to 3,600 Coulombs.

A fully charged cell is defined to have an SOC of 1, whereas an empty cell has an SOC of 0. It is well known that the behavior of the cell is a function of the cell's SOC. Present equivalent-circuit models in the literature account for this by making the model parameters vary depending on the cell's SOC. However, it is shown in multiple recent works [3]–[7] that the model parameters for these models need to be extracted for the full range of charging and discharging currents. This means that the model construction process can be tedious, and operation of the cell outside the characterized current range would not be accurate.

The aim of this thesis is to introduce a new equivalent-circuit model that uses a nonlinear transmission line to model the variation of SOC through the depth of the cell's electrodes. In this work, this new model is called the distributed SOC model. The performance of this model is studied by applying it to two commercial lithium-ion cells. By including the effect of SOC variation in the cell's electrodes, it is hoped that the parameter extraction process can be simplified to two extraction experiment. This significantly reduces the model construction efforts. Additionally, the physical intuition that can be obtained from this model is enhanced compared to present equivalent-circuit models, as will be discussed further below.

1.2 Lithium-Ion Cells

Some background on lithium-ion cells is now provided to introduce the reader to their basic operation and properties. This background is intended to help the reader understand the assumptions used in deriving the model and cell characterization approach presented in the thesis, as well as put the present work in perspective.

1.2.1 Lithium-Ion versus Other Rechargeable Battery Technologies

A key reason for the widespread adoption of lithium-ion cells is that the stored energy per unit mass (Wh/kg), known as specific energy, and its stored energy per unit volume (Wh/L), known as energy density, are high compared to other rechargeable battery technologies. This is illustrated in Figure 1-1. These advantages mean that they are especially attractive in portable applications, where size and weight are key considerations, such as in mobile phones, laptop computers, and wearable electronics.

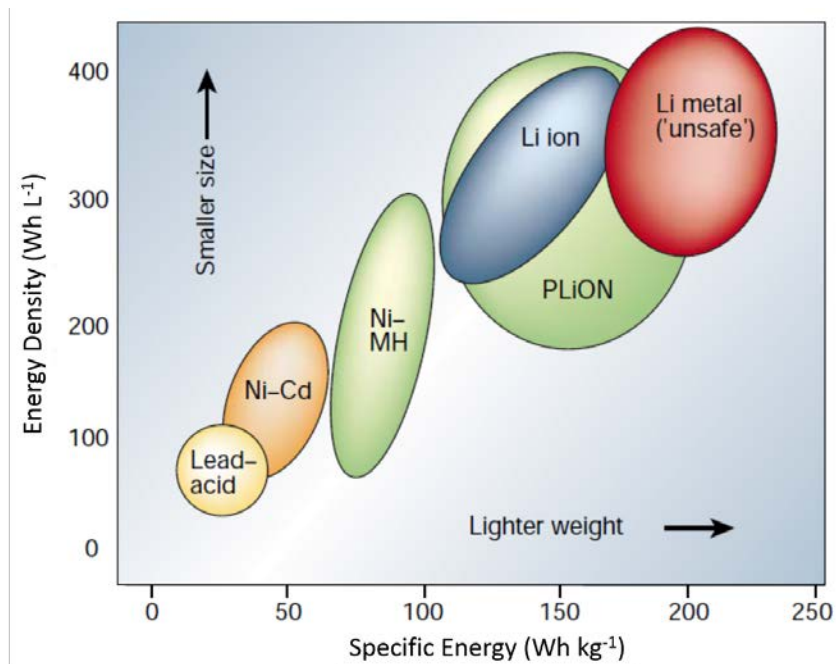


Figure 1-1. Comparison of energy density and specific energy between lithium ion and other rechargeable cell technologies. Reprinted by permission from Macmillan Publishers Ltd: Nature [8], copyright 2001.

Lithium-ion cells also have an advantage in their deliverable power per unit mass (W/kg), known as its specific power. A comparison of lithium-ion cells and other rechargeable cell technologies in terms of specific power (W/kg) and specific energy (Wh/kg) is shown in Figure 1-2. The combination of high specific power and specific energy has resulted in adoption of lithium-ion cells in an increasing number of motive applications, which involves the use of electrical power in the transportation of people and materials. In these applications, the total energy available as well as the rate of the delivery of this energy are major considerations. Motive applications that are seeing the increasing adoption of lithium-ion technologies include electric bicycles, electric vehicles, and as mentioned earlier, marine applications. For example, Ford has announced their intention to launch 13 additional electric vehicle models by 2020 [9].

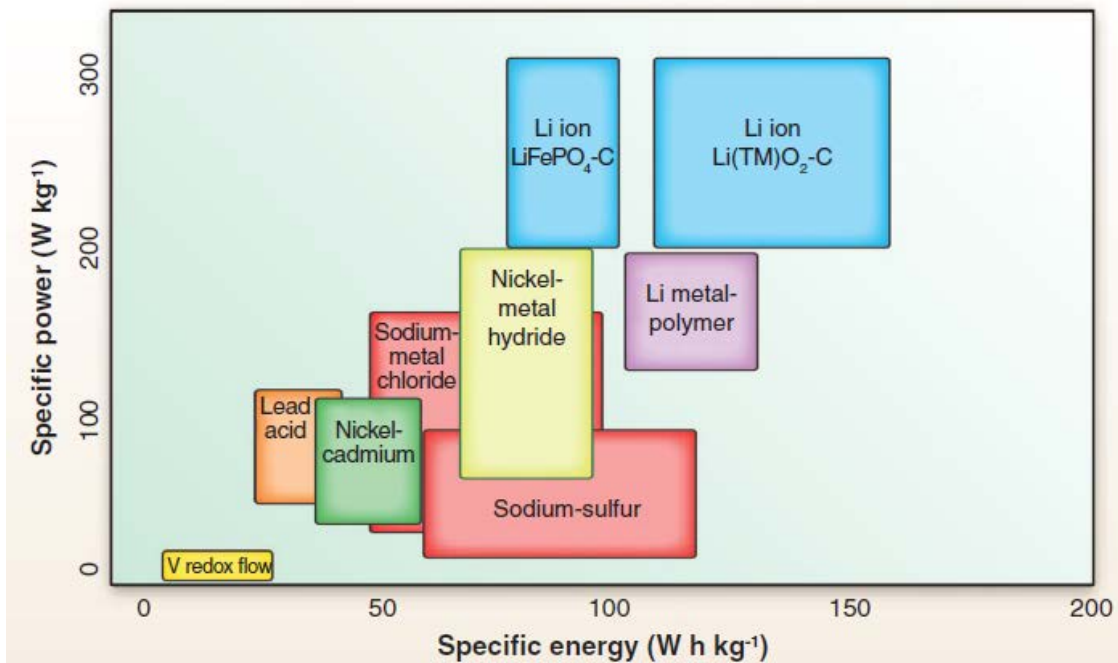


Figure 1-2. Comparison of different rechargeable battery technologies in terms of specific energy and specific power. From [10]. Reprinted with permission from AAAS.

Table 1-1 lists some of the advantages and disadvantages of lithium-ion cells. Besides the high energy density and good rate capability, lithium-ion cells also possess good cycle life, high energy efficiency and absence of memory effects. However, one widely cited concern regarding lithium-ion cells is their safety. Failure events such as fires and explosions [11] have caught worldwide attention, and have led some companies to shun lithium-ion technologies. Other lithium-ion disadvantages are that they are relatively expensive and can sustain damage when over-charged or over-discharged. The addition of battery protection circuitry to prevent damage to the cell is widely used to prevent cell over-charge and over-discharge. On the other hand, this incurs additional costs to the already expensive lithium-ion battery solution.

Advantages	Disadvantages
Chemistry with highest energy per unit weight (Wh/kg)	Relatively expensive
No memory effect	Not tolerant of over-charge and over-discharge
Good cycle life	Requires protection circuitry for safety and to prevent over-charge and over-discharge
High energy efficiency	Thermal runaway concern
Good high-rate capability	

Table 1-1. Advantages and disadvantages of lithium ion rechargeable cells relative to other commercial cells.

Adapted from [12].

1.2.2 Lithium-Ion Cell Operation

The lithium-ion cell operated based on the rocking-chair (also known as shuttle-cock) mechanism. The popular LiCoO_2 /Graphite cell is used as an example here in Figure 1-3. The situation during charge is shown in the left diagram, while the right diagram illustrates the

situation during discharge. In both diagrams, the left electrode is the positive electrode, and the right electrode is the negative electrode. Both electrodes are immersed in an electrolyte solution rich in lithium ions. Lithium ions in the cell can exist as free solution-phase ions in the electrolyte solution, or in the solid-phase when inserted in the bulk of either positive or negative electrodes.

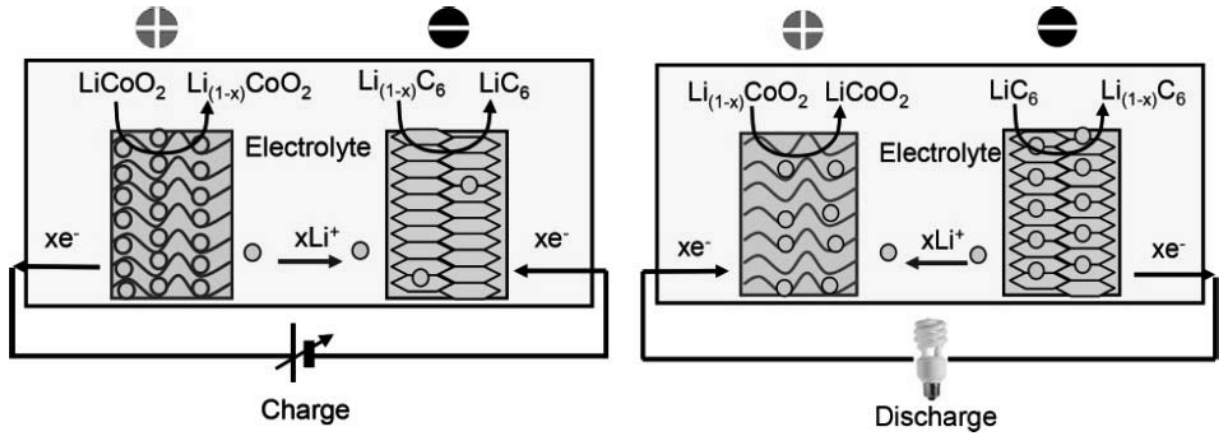
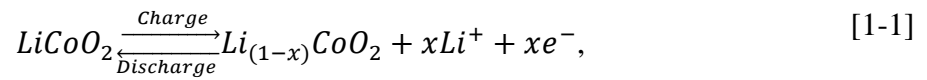
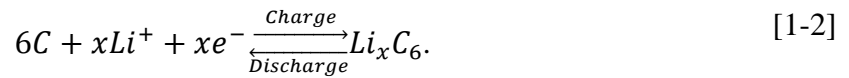


Figure 1-3. Illustration of the principles of operation of a lithium ion battery during charge and discharge. In both illustrations, the positive electrode is depicted on the left, while the negative electrode is depicted on the right. From [13]. © 2013 Wiley. Reprinted with permission from Wiley.

The positive electrode reaction during cell charge and discharge are



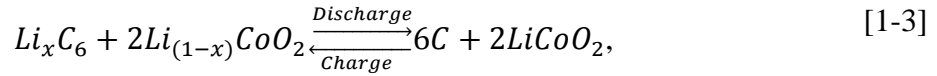
with the corresponding graphite negative electrode (indicated as elemental carbon here) reaction



Here x is between zero (fully discharged) and 1 (fully charged). When the cell is in the fully discharged state, the lithium ions exist in the solid-phase inside the CoO_2 crystal structure in the positive electrode. Correspondingly, the graphite is devoid of lithium ions. During cell charge,

indicated by the reaction proceeding to the right in reactions [1-1]-[1-2], the solid-state lithium ions are released from the positive LiCoO_2 electrode into the electrolyte solution, becoming solution-phase lithium ions. At the negative electrode, solution-phase lithium ions are converted to solid-phase lithium ions and inserted in between the layered structure of the graphite active material. This process is illustrated in the left diagram of Figure 1-3. The quantity of lithium ions that are extracted from the positive electrode is equal to that inserted into the negative electrode. This process is facilitated by the lithium-ion-rich (usually Lithium Hexafluorophosphate, in concentration ≥ 1 Molar) electrolyte solution. The lithium ions that are transferred from the positive electrode to the negative electrode possess a positive charge. During this charging reaction, balancing electrons of reactions [1-1]-[1-2] move from the positive to negative electrode through the external circuit. An energy source is required to drive this reaction, which is illustrated as a voltage source in the external circuit in the left diagram of Figure 1-3.

During discharge, the lithium ions and electrons travel in the reverse direction. This situation is illustrated in the right diagram of Figure 1-3. Lithium ions are extracted from the negative graphite electrode and inserted into the positive LiCoO_2 electrode by transporting through the electrolyte solution. The charge balancing electrons travel from the negative electrode to positive electrode via the external circuit. This flow of electrons forms the discharge current that provides energy to the desired load (illustrated as a light bulb in the right diagram of Figure 1-3). In this way, the lithium ions are “rocking” back-and-forth between the positive and negative electrodes during cell charge and discharge. The overall reaction is given by



with the right hand side representing the fully discharged state, and the left side a partial charge.

Lithium-ion cells come in three main forms, which are cylindrical, prismatic, and polymer.

Cylindrical cells, as their name suggests, are cylinder-shaped, while prismatic cells are rectangular-shaped. Both cylindrical and prismatic cells are housed inside metallic housing.

Lithium ion polymer cells are so-called because they use a laminated polymeric casing, and they can come in cylindrical, rectangular, and even curved shapes. They are also called pouch cells.

The cylindrical cell is by far the most common. The internal structure of a cylindrical lithium-ion cell is shown in Figure 1-4. The cylindrical volume inside the housing is mostly occupied by what is known as spiral-wound. This spiral-wound is made by stacking the positive electrode, the negative electrode, and two layers of separator together, and rolling it into the shape of a cylinder. In Figure 1-4, the positive electrode consists of a cathode composite (light orange) coated on both sides of the aluminum current collector (light blue). The aluminum current collector carries current between the cell cap (which is the cell positive terminal) and the cathode composite. The negative electrode consists of anode composite coatings (dark green) on the two sides of the copper current collector (red). The copper current collector carries current between the cell can (negative terminal) and the anode active material.

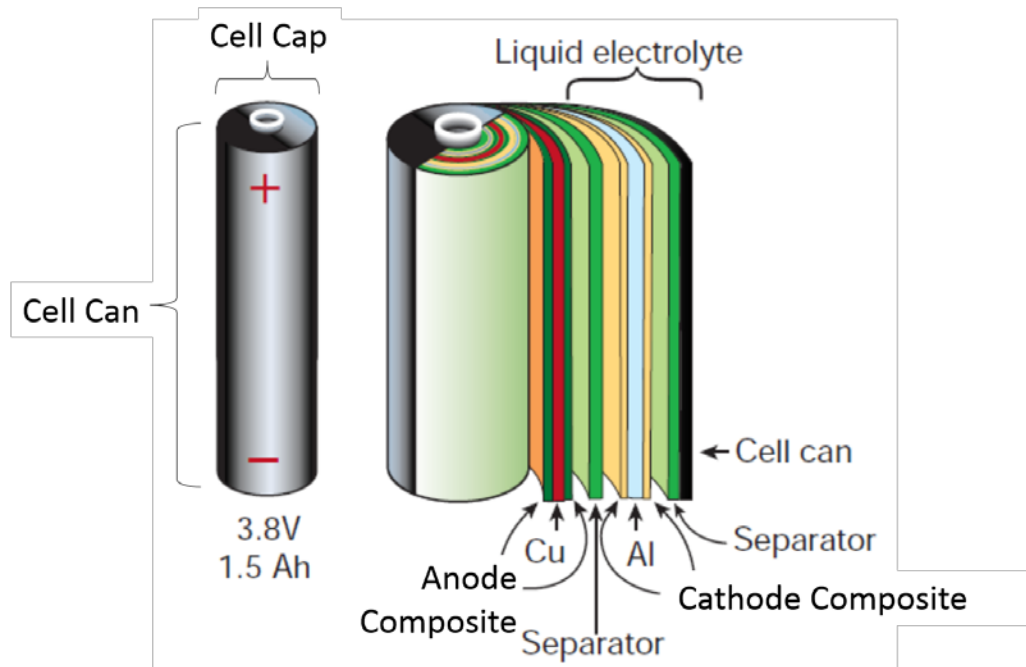


Figure 1-4. Illustration of the interior structure of a typical cylindrical lithium-ion cell. Adapted by permission from Macmillan Publishers Ltd: Nature [8], copyright 2001.

In a typical lithium ion cell, including the cylindrical, prismatic and polymer types, the distance between the positive and negative current collectors, defined by the thicknesses of the composite materials and the separator, is on the order of hundreds of microns. On the other hand, the other two dimensions of the sandwich structure extends tens of millimeters or more. Therefore, the edge effects from these other two dimensions are negligible, and the cell model is often simplified as a one dimensional structure shown in Figure 1-5. The left side is the negative electrode (anode) and the right side is the positive electrode (cathode), with a separator sandwiched in between. The electrode coatings mentioned above consists of a mixture of active material, conductive fillers, and binder. The active materials are where the energy is stored. In the example in Figure 1-3, the positive electrode active material is LiCoO_2 , while the negative electrode active material is graphite. The conductive filler is usually a carbon that is added to

improve the electrical conductivity of the composite material. This filler provides a conductive pathway for electrons to travel from the individual active material particles to the current collector at the back of the electrode. The polymeric binder serves to hold the composite material together, and bound to the current collector. The positive electrode, negative electrode, and separator are porous. A concentrated electrolyte solution containing lithium ions (usually lithium hexafluorophosphate, LiPF_6) fills the pores. This solution provides the medium for lithium ions to transport between the positive and negative electrodes as discussed earlier in this section.

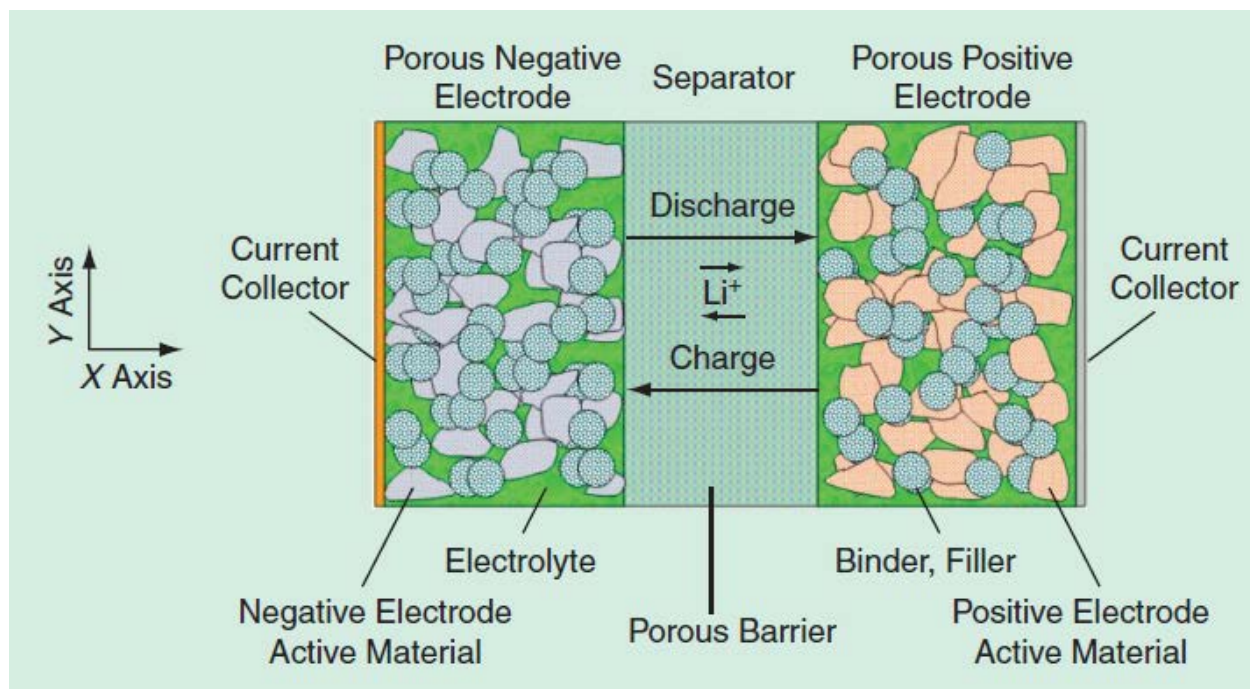


Figure 1-5. Depiction of the one-dimensional simplification of the cell structure. From [14]. © 2010 IEEE.

A key measure of a cell's energy storage capability is its capacity. The cell's full capacity is the maximum amount of charge, usually measured in Ampere-hours (Ah), that can be reversibly

stored and extracted from the cell. This is measured by fully charging the cell, and subsequently discharging the cell to its fully discharged state. One Ah is equivalent to 3,600 Coulombs. The charge state of a cell is commonly indicated in one of several ways. The most popular is the SOC. The SOC is the ratio between the remaining capacity and the full capacity of the cell. A SOC of 1 indicates a fully charged cell, while an SOC of 0 indicates a fully discharged cell. The Depth of Discharge (DOD) is the fraction of full capacity of the cell that has been discharged from the cell. Therefore,

$$DOD = 1 - SOC. \quad [1-4]$$

A DOD of 1 indicates a fully discharged cell, whereas a DOD of 0 indicates a fully charged cell. Another popular measure of the charge state of the cell is the cumulative discharged capacity. A cell's cumulative discharged capacity is the accumulated total capacity that has been discharged from a fully charged cell. For example, a 3 Ah cell at a SOC of 0.33 is at a state of 2 Ah cumulative discharged capacity, because 2 Ah would need to be removed from a fully charged 3 Ah cell for the SOC to be 0.33.

The capacity of a cell is determined by the masses of positive and negative electrode active materials, and the specific capacities (capacity per unit mass, usually expressed in Ah/g or Ah/kg) of these active materials. The specific capacities of a number of active materials are shown in Figure 1-6. By carefully matching the capacities of the positive and negative electrode active material masses, the cell's capacity can be optimized [15].

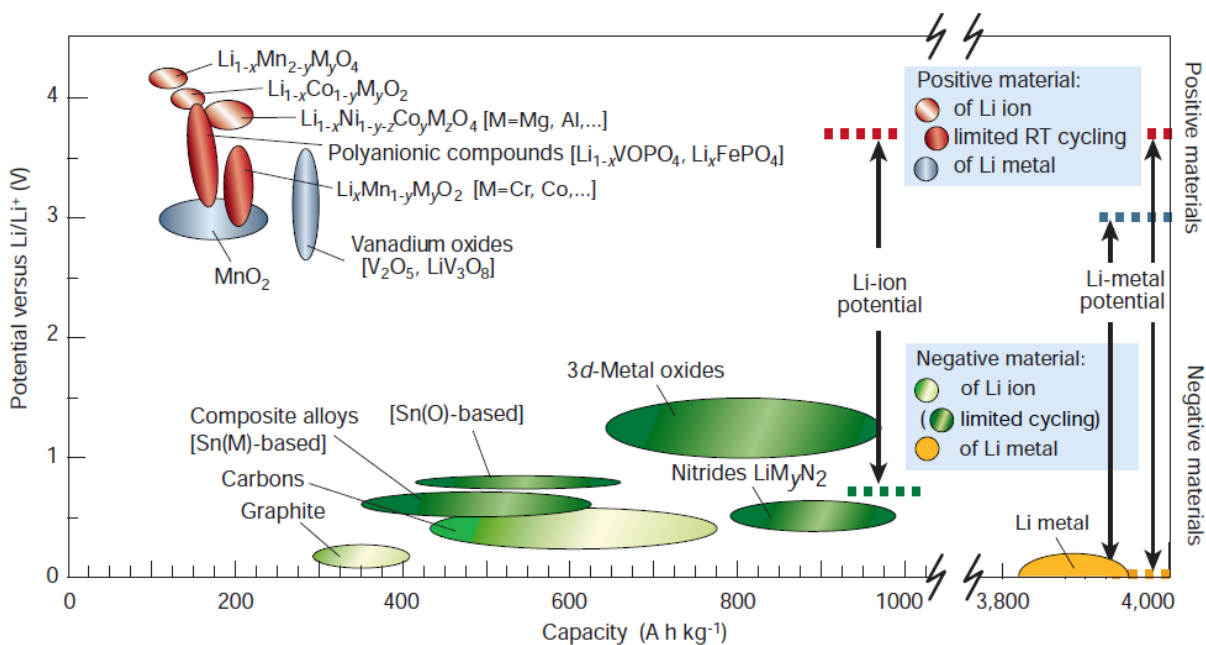


Figure 1-6. Capacity vs. potentials of various positive and negative electrode materials. Reprinted by permission from Macmillan Publishers Ltd: Nature [8], copyright 2001.

So far the description of the cell has been in the static condition, i.e. no current flows in the cell.

As cells' full capacities can vary over many orders of magnitude, quoted applied currents are typically normalized to the full capacity of the cell. This is referred to as the current's C-rate.

The C-rate is the ratio between the applied current, in Amperes, to the full capacity of the cell, in Ampere-hours. Therefore, for a 3.0 Ah cell, a 1 C current refers to 3.0 A, and a 0.5 C current refers to 1.5 A.

1.3 Cell Modeling

This section presents a review of the state-of-the-art in modeling for lithium-ion cells in order to put in perspective the runtime equivalent-circuit model developed in this work. Runtime

simulations enable the user to simulate the temporal behavior of the cell when subjected to a wide variety of loads. This type of model is useful for evaluating a cell in specific applications, such as in the full trip behaviour of the cells inside an electric bicycle. Cell models for lithium-ion cells can be classified in a number of different ways. For this work two classes will be considered [16]: 1. electrochemical models, and 2. equivalent-circuit models. Electrochemical models are generally suitable for runtime simulations, whereas some equivalent-circuit models are designed only for cell simulation over a narrow range of SOC. Electrochemical models are presented in Section 1.3.1. Then Section 1.3.2 discusses the background on equivalent-circuit models. The distributed SOC model proposed in this thesis (chapters 2 and 3) is an equivalent circuit model that is intended to be used for runtime simulations.

1.3.1 Electrochemical Models

The electrochemical model is the first class of lithium ion cell models. It was pioneered by J. Newman's group [17]–[21]. Two of the most popular electrochemical models – the pseudo-two-dimensional (P2D) model and the single particle model (SPM) – are discussed here. The P2D model [22]–[24] was first proposed by Fuller *et. al.* [21] to model a lithium ion cell that consists of two composite electrodes. It aims to include detailed mathematical descriptions of all important physical processes taking place inside the lithium-ion cell. To aid description of the processes included in the P2D model, an illustration of the cell during charging is shown in Figure 1-7. As described in Section 1.2.2, the cell's structure can be suitably simplified as a one-dimensional structure shown in the diagram that consists of the positive electrode, negative electrode, and separator. The positive and negative electrodes consist of the active material,

filler, and binder, but this diagram has been simplified by removing filler and binder materials, and only a few active material particles are depicted.

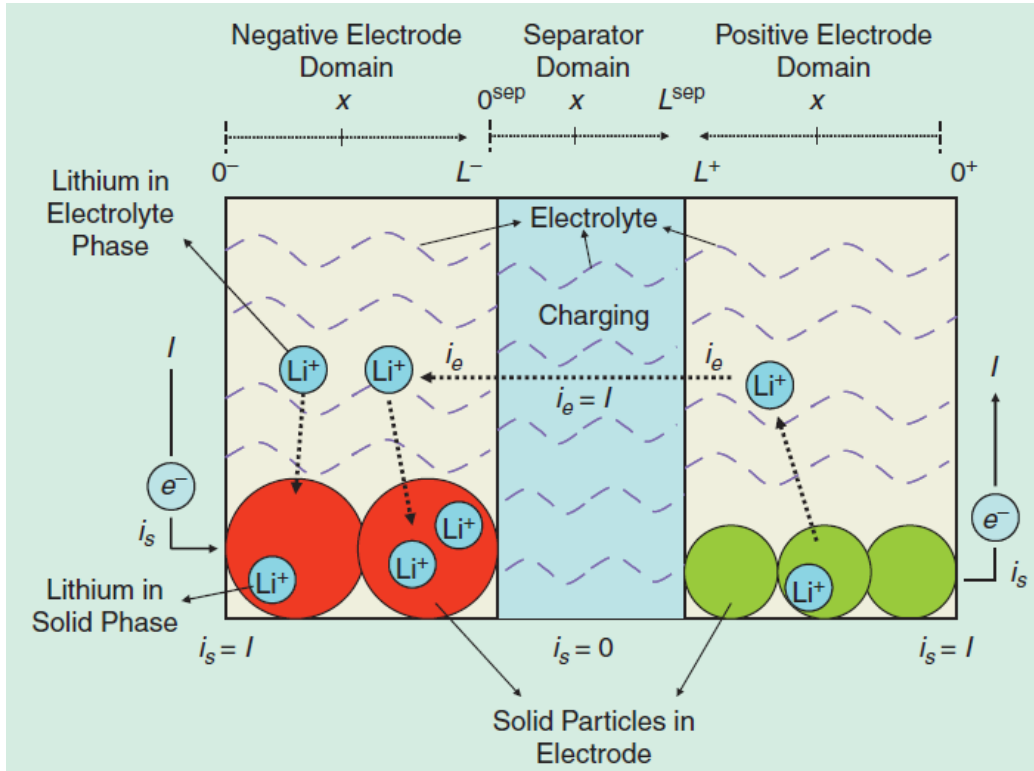


Figure 1-7. Illustration of cell structure and the physics involved during charging. The negative electrode occupies the domain between $x=0^-$ and $x=L^-$, as indicated at the top of the diagram. The separator is situated between $x=0^{sep}$ and $x=L^{sep}$. The positive electrode occupies the domain between $x=L^+$ and $x=0^+$. During charging, lithium ions are released from the positive electrode particles (green) and inserted into the negative electrode particles (red). Correspondingly, electrons travel externally from the positive electrode to the negative electrode via the current collectors at $x=0^+$ (positive) and $x=0^-$ (negative). This external circuit connection would require an electrical power source (not illustrated) to provide the required energy. From [14]. © 2010 IEEE.

During charging, lithium ions are transferred from the positive electrode to the negative electrode via the electrolyte. At the far right side is the positive electrode current collector, which conducts the charge balancing electrons from the positive electrode to the negative electrode through an external power source (not shown). At the far left side is the negative electrode current collector, which serves as a bridge for the electrons to reach the negative electrode active material particles.

The key physical effects modeled in the P2D model are described here.

1. Lithium ion transport in the electrolyte inside the electrode pores

As described in Section 1.2.2, the electrodes consist of composites that contain a porous mixture of active material, filler, and binder. The detailed configuration of the particle locations and the pores is complex and not known with perfect detail. In the P2D model, a simplification of the electrode structure is employed, which is called the porous electrode theory [17]–[19], [21]. According to this theory, the position variable (in this case, the x -direction) is volume averaged, and each variable in the model is a continuous function of this direction. Instead of accounting for the explicit details of the pores inside the electrode, the material is assumed to exist as a continuous material. The physical relationships between the parameters are modified by factors that account for the porosity [17].

As described in Section 1.2.2, the electrolyte is rich in mobile solution-phase ions, and facilitates the transfer of lithium ions between the positive and negative electrodes. At the high concentrations usually employed, it is found that Fick's law that accurately models

dilute solutions is no longer suitable. For these solutions, concentrated solution theory is required [25]. This theory considers that the driving force of the flux of ions is the electrochemical potential.

2. Lithium ion transport in the electrolyte inside the separator pores

The separator is a porous polymeric material, and the electrolyte contained herein allows lithium ions to travel between the positive and negative electrodes. Like in the pores of the electrodes, lithium ion transport in the porous separator is modeled using concentrated solution theory, and adjusted for the tortuosity of pores in the separator. The tortuosity of the pore characterizes its twists and turns that increases the distance traveled by the ion and impedes the ion flow. Higher tortuosity results in higher ionic resistance.

3. Lithium ion insertion and extraction at the active material particle surfaces in the electrodes

The conversion of solution-phase lithium-ions to solid-phase ones inside the active material particles in either positive or negative electrodes can only occur at the particle surface. To model this reaction, the Butler-Volmer equation [26] is most often used. This equation models the relationship between the flux density of ions at the particle surface and the electrode overpotential. Physically, this overpotential is the potential loss required to drive the reaction at the desired rate. Higher currents require a larger overpotential according to the Butler-Volmer equation.

4. Lithium ion transport inside the bulk of the electrode active material particles

While the insertion and extraction of lithium ions only occurs at the active material particle surface, the charge storage effect extends through the bulk of the particles. Inside the particles, the lithium ions are in solid-phase, and their transport is governed by the diffusion equation. In the solid-phase, the diffusion coefficient is several orders of magnitude lower than in the solution-phase [21]. Therefore, the bottleneck in the lithium ion processes in the cell is typically the solid-phase lithium ion diffusion in the active material particles. The P2D model usually assumes the active materials consist of spherical particles.

5. Potential of the electrodes

The potentials of both electrodes are non-linear functions of the surface concentration of lithium ion. At equilibrium, the cell voltage is given by the difference in potentials between the positive and negative electrodes because there is no voltage drop due to concentration gradients, overpotentials, or resistive losses in this model. This equilibrium cell voltage is known as the cell open-circuit voltage (OCV).

6. Electron transport in the electrodes

As described above, the extraction of lithium ions from an active material particle requires the corresponding movement of electrons from that particle. These electrons need to travel to the opposite electrode as charge-balancing electrons. As illustrated in Figure 1-7, active material particles are positioned throughout the depth of the electrode's thickness. The electrons located closer to the current collector travel a shorter distance to reach it. The transport of electrons in the solid phase is modeled using Ohm's law. This flow of electrons

leads to a voltage drop in the electrode. Compared to the solution phase conductivity, this solid phase conductivity is typically higher.

One notable exception to the included physics of the model is the omission of double-layer effects. This process models the surface capacitive charging of the particles. In lithium-ion cells, this effect's omission is justified by the low capacitance of the double-layer, and short timescales when it is observed. On timescales of typically below 1 second, the capacitance is observable [27]–[29]. In most lithium-ion runtime simulations, the timescale of interest is on the order of seconds and above [2], [4], [6], [30]–[37].

As seen in the descriptions of the major physical effects above, the P2D model includes a significant amount of detail of the cell. This model includes enough details that high fidelity simulations can be obtained [18], [19], [21], [38]–[40]. This type of model is used for example in academia to study the fundamental effects in cells.

However, this modeling effort requires a significant understanding of electrochemistry and an excellent command of numerical techniques, so it is not readily accessible to most engineers. Additionally, the model requires as inputs the fundamental properties of the materials, including lithium ion diffusion coefficients in the electrolyte, and in the positive and negative electrode active materials, as well as particle sizes, electrode thicknesses, conductivities etc. There are thirty-three material parameters in this model, which requires substantial expertise and effort to obtain.

Another model that can be classified as an electrochemical model is the SPM first introduced by R. White's group [23], [24], [41]–[43]. Through simplifying the P2D model, the SPM is obtained by making the following changes:

1. The effects of ion concentration and potential differences in the electrolyte solution are ignored in the SPM. This simplifies the physics of transport in the solution phase of the cell, including inside the pores of the separator, the positive electrode, and the negative electrode.
2. The thicknesses of the porous electrodes are neglected in the SPM. Then, the SPM consists effectively of one layer of active material particles in both the positive and negative electrodes. The P2D model and the SPM are depicted in diagrams A and B, respectively, of Figure 1-8. As all particles are at the same location (depth-wise in the porous electrode thickness direction) in the SPM, all the particles in each electrode behave identically. Each electrode in the cell can therefore be modeled as a single spherical particle with the surface area equivalent to that of all the active material particles in the electrode. This removes the need to use porous electrode theory to consider the differing states of the active material particles at different locations in the electrodes. Also, the electron transport in the thickness direction of the electrode is ignored.

One of the key physical mechanisms that is retained in the SPM is the solid-state lithium ion diffusion that occurs inside the active material particles. The two simplifications above reduce the complexity of the P2D model, but retain the diffusion physics that occurs inside the cell. Useful physical intuition can still be obtained from such a model, as has been shown in its ability to explain heat generation during internal short-circuits [43], and lifetime degradation of lithium

ion cells [42]. On the other hand, there are still 15 material and structural parameters that need to be extracted to use this model. Extraction of these parameters still requires strong understanding of the underlying physics of cell operation, and significant experimental effort. This means that this model remains out of reach of most system engineers that need models as part of larger system design and validation.

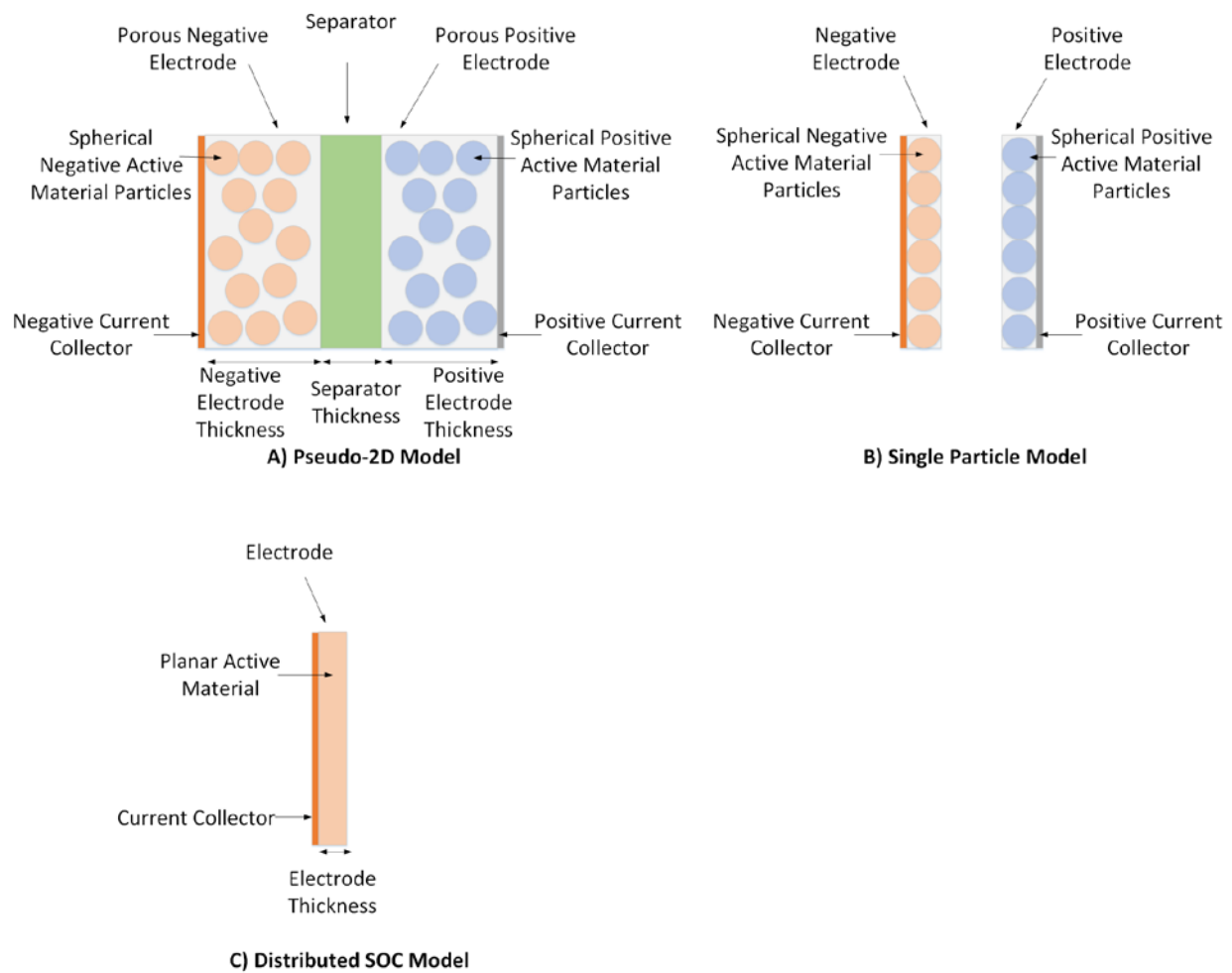


Figure 1-8. Depiction of the three different lithium ion cell models. A) The P2D model. B) The SPM. C) The distributed SOC model.

Relative to equivalent circuit models, these electrochemical models capture the physical processes more completely, and are able to provide high accuracies. However, these benefits come at the cost that a high degree of expertise in electrochemistry, and a significant amount of detail of the physical parameters of the cell are required. Therefore, the model construction takes a considerable amount of effort.

The distributed SOC model proposed in this thesis has some similarities to the SPM discussed in this section. The distributed SOC model is an equivalent-circuit model, and is shown in Figure 1-9. As will be discussed later in section 2.1, the RC transmission line in the model is derived based on diffusion in the thickness direction of a planar element. The planar element is depicted in diagram C of Figure 1-8. Like the SPM, this RC transmission line and its non-linearized counterpart capture one of the key physical effects inside the lithium ion cell, which is the diffusion of ions inside the active material particles. Unlike the SPM, however, the distributed SOC model does not require knowledge of the underlying material and structural parameters internal to the cell. The distributed SOC model abstracts away the physical details inside the cell by performing a non-dimensionalization procedure that results in a non-linear transmission line with a dimensionless length of 1. As will be shown in Section 2.1, there are only four parameters in the distributed SOC model, and three of them depend on the cell SOC. A simple parameter extraction procedure is put forth in Section 2.3 that only requires testing the lithium ion cell using standard cell charge and discharge instruments. Therefore, the proposed distributed SOC model retains some of the key physical effects of cell operation, and allows system engineers to construct the model using relatively less time and effort.

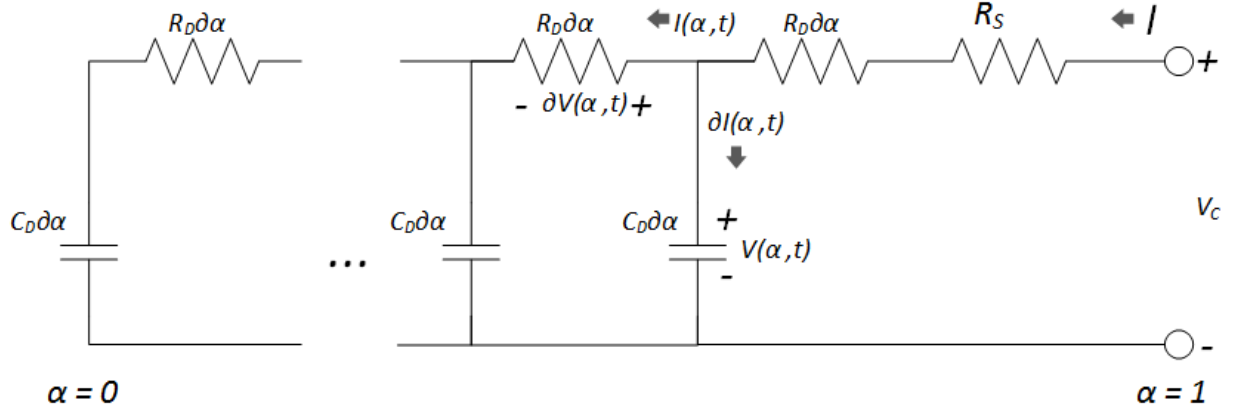


Figure 1-9. The distributed SOC equivalent-circuit model (linear version) proposed in this thesis work.

1.3.2 Equivalent Circuit Models

The second class of lithium-ion cell models is equivalent-circuit models. In this section, the background on equivalent-circuit models is presented, and contrasted to the electrochemical models described in the previous section. Equivalent-circuit models consist of electrical elements such as resistors, capacitors, inductors, and voltage sources as model elements. As such, they are popular because they are easy to understand for engineers.

As the major contribution of this thesis work involves the development of a new equivalent-circuit model for runtime simulations, this section will go into deeper detail to better illustrate this work's contributions. Runtime models aim to predict the cell's temporal terminal behavior under a wide variety of loads, over the full range of SOC that is expected during a cell's application. For example, in an e-bike, the runtime model could be used to predict the cell's voltage during a trip. Equivalent circuit models are widely classified into three types [16], [44]:

1. Thévenin models, 2. impedance models, and 3. runtime models. These three types of equivalent circuit models are discussed in Sections 1.3.2.1 to 1.3.2.3. While runtime models are specifically designed to be used for runtime simulations, Thévenin and impedance models are typically used at a specific cell SOC. Suitability of these models for runtime simulation are addressed in the respective sections.

1.3.2.1 Thévenin Model

Thévenin models are the simplest type of equivalent circuit models. They are made up of a voltage source in series with an equivalent series impedance. This impedance usually consists of one or more resistors and capacitors. In Thévenin equivalent-circuit models, these circuit elements are constant. A typical example is shown in Figure 1-10. The voltage source V_{OC} represents the cell voltage. In this example the series impedance consists of resistance R_0 in series with the parallel arrangement of R_l and C_l . The resistance R_0 in this model represents the internal resistance associated for example with ion transport through the electrolyte between the electrodes, and polarization losses of the cell, or overpotential, that is required to drive the required rate of reaction at the surface of the active material particles. The R_l and C_l elements provide an approximate description of the distributed charging that occurs throughout the electrodes. Extensions to this model include additions of multiple RC elements, which can improve the simulation accuracy [45].

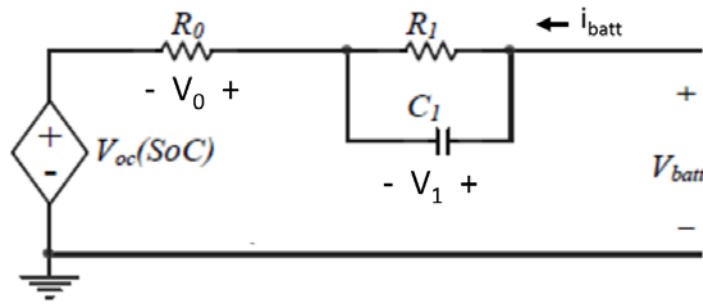


Figure 1-10. Circuit diagram for Thévenin equivalent circuit models. Adapted from [44]. © 2011 IEEE.

Construction of the Thévenin model requires the circuit parameters to be extracted. The discharge analysis method is most often used [2], [4], [6], [30]–[33]. This extraction method consists of subjecting the cell to a discharge current pulse. Depiction of a constant current pulse is shown in Figure 1-11. The pulse consists of the pulse phase, followed by the relaxation phase. The pulse is characterized by its amplitude, and duration as shown in the figure. In this work, the convention is adopted in which positive applied current charges the cell, while negative applied current discharges the cell.

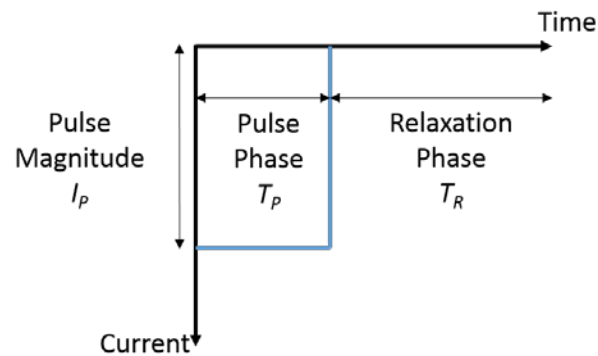


Figure 1-11. Depiction of the discharging pulse used to characterize the cell under test.

In the example in Figure 1-10, the circuit response to a constant current i_{batt} is given by:

$$V_0 = i_{batt}R_0 \quad [1-5]$$

$$V_1 = i_{batt}R_1(1 - \exp(-\frac{t}{R_1C_1})) \quad [1-6]$$

$$V_{batt} = V_{OC} + i_{batt}R_0 + i_{batt}R_1(1 - \exp(-\frac{t}{R_1C_1})) \quad [1-7]$$

The cell voltage response of a commercial lithium ion cell (data from experiments performed in Chapter 3) to a 0.60 A discharging pulse of *ca.* 1400 s duration is shown in Figure 1-12. The top portion of the plot shows the applied discharge current pulse. The voltage response of the cell to the discharge current pulse is shown in the bottom plot. Discharge analysis estimates the equivalent-circuit parameters by matching the measured voltage response during pulse phase of the applied current pulse to equation [1-7]. Before the pulse begins, the cell is assumed to have reached equilibrium. The cell voltage at this equilibrium state gives the cell open-circuit voltage V_{OC} . At the beginning of the pulse phase of the applied current pulse, the cell experiences an instantaneous voltage drop. The value of this drop corresponds to the term $i_{batt}R_0$ in equation [1-7]. As time proceeds, the cell voltage evolution is fitted to the equation's third term to obtain model parameters R_1 and C_1 . Considering the detailed physics models discussed in Section 1.3.1, the parameters R_1 and C_1 do not carry definitive physical meaning, and are understood to only serve as fitting parameters to the measured response. A typical charging response of the same cell is shown in Figure 1-13. The positive applied current indicates that the direction of current flow charges the cell.

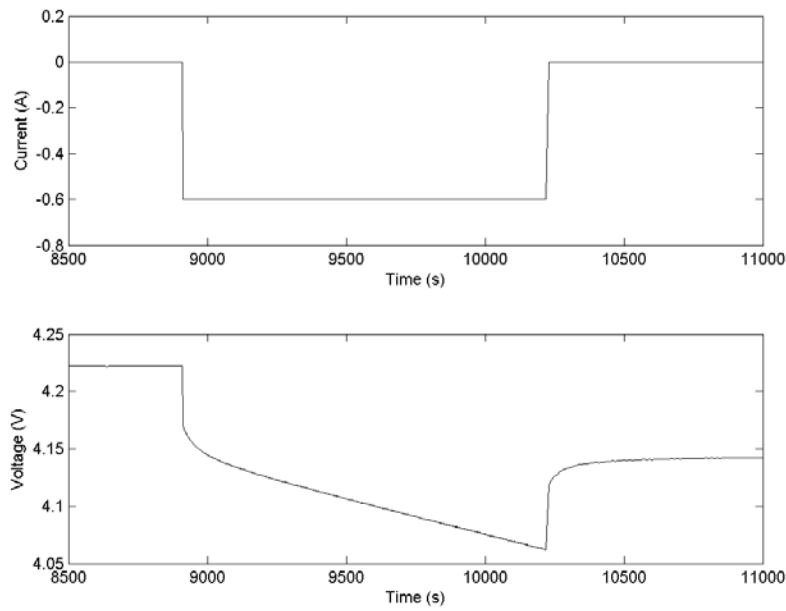


Figure 1-12. Typical current (Top) and voltage (Bottom) response of a cell to a discharging current pulse.

The negative applied current corresponds to discharge of the cell.

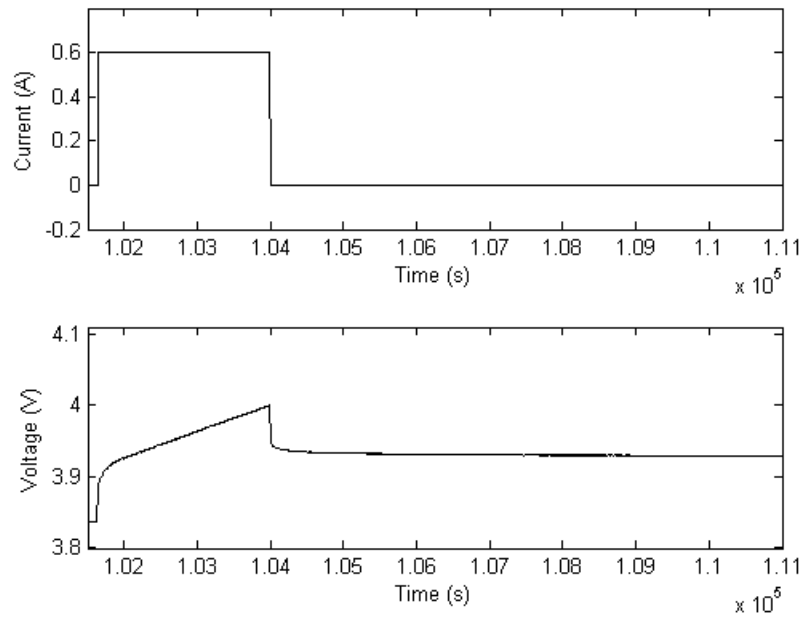


Figure 1-13. Charging, and subsequent relaxation, response of a typical cell. The positive applied current charges the cell.

However, cell response is well known to be functions of SOC. For example, the cell OCV depends on the lithium ion surface concentration of the active material particles, as discussed in Section 1.3.1. Therefore, Thévenin equivalent-circuit models are only accurate for a narrow range of SOC. However, in runtime simulations of real life applications, the cell is expected to undergo large variations in SOC. Therefore, Thévenin models do not accurately simulate the cell behavior at runtime. More recent modifications to use non-linear capacitance [46] to allow for simulating runtime behavior have improved accuracy, but these are still less accurate than runtime models described later in this section.

1.3.2.2 Impedance Model

The impedance model is a frequency domain model that is used for analyzing data obtained from Electrochemical Impedance Spectroscopy (EIS) on a cell. This technique involves applying small magnitude sinusoidal excitations (voltage or current) to a cell, and measuring the cell's corresponding response (current or voltage), which gives the impedance at the applied frequency. The frequency of the AC excitation is typically swept over a wide range (for example, from 10 kHz to 0.1 mHz) to obtain the impedance spectrum as a function of frequency.

A representative model that is often used for impedance spectroscopy is the Randles model [26], shown in Figure 1-14. R_s represents the resistive loss of the cell at high frequency, which serves the same role as R_0 in the model in Figure 1-10. C_{DL} represents the double-layer charging, which is the charging of the electrode-to-electrolyte interfaces within the cell, and R_{CT} models the

charge-transfer resistance across this interface. W is the Warburg element that models the diffusive effects in the electrode. In particular, a diffusion or diffusion-like process is involved when charge is transferred from the double layer interface into and through the solid electrode. The Warburg element W is a frequency-domain element [47] with impedance Z_W in the form of

$$Z_W = \frac{\sigma_w(1-j)}{\sqrt{w}}, \quad [1-8]$$

where σ_w is the Warburg coefficient, w is the angular frequency of the test signal, and j is the imaginary number.

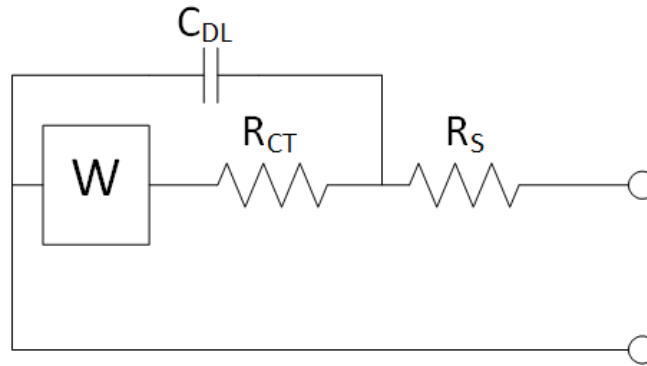


Figure 1-14. The Randles circuit model.

Compared to the electrochemical models described in Section 1.3.1, R_S is primarily attributed to the ionic conduction in the electrolyte. R_{CT} is a representation of the over-potential for driving the charge transfer reaction at the particle surfaces. The Warburg element W represents the diffusive behavior of the solid-phase lithium ions inside the active material particles. As mentioned in Section 1.3.1, C_{DL} is typically not included in the electrochemical models.

Physically, the Randles model shown in Figure 1-14 should be used for modeling a single electrode. As a lithium ion cell contains two electrodes in series, its impedance model should consist of two Randles models in series. However, it is typically found that using a single Randles or Randles-like model is sufficient for the entire lithium ion cell [28], [29], [48], [49]. This is because the impedance response of the two electrodes overlap significantly, and so the individual electrode responses cannot be clearly distinguished [48].

Contrasting to the Thévenin model (an example is in Figure 1-10), the impedance equivalent-circuit model has physical meaning, with physical effects assigned to each of its constituent components. The aim of impedance spectroscopy is to analyze the physical effects taking place in the electrode at the tested SOC. The process of obtaining the impedance data is relatively slow as the applied frequency needs to sweep to fairly low values (for example, often 0.1 mHz or lower) to be able to obtain information stemming from the solid-state diffusion process. In contrast, the step current responses used in discharge analysis for Thévenin models are performed much more quickly, where in effect multiple frequencies are probed simultaneously.

The equivalent-circuit models used with impedance spectroscopy are frequency-domain models. To employ these in time-domain simulations, these models would need to be converted to their time-domain equivalents. A number of works have used impedance spectroscopy to characterize the lithium-ion cell, followed by conversion of the frequency-domain model into a time-domain one [27], [28], [50]–[54].

The general approach is akin to the Thévenin approach in that at a specific SOC, the at-rest cell voltage, which gives the cell OCV, is measured together with the cell's impedance. A time-domain representation of the impedance is extracted at this SOC. The resulting model is the cell OCV in series with the model of the cell impedance.

In order to simulate the impedance model in the time-domain, the most complicated step is to convert the Warburg element, defined in equation [1-8], into its time-domain equivalent. Kuhn *et al.* showed in [52] that the Warburg impedance can be expressed as combinations of resistors and capacitors in two ways: 1. The Foster structure, shown in Figure 1-15, or 2. The Cauer structure, shown in Figure 1-16. The Cauer structure has the form of a traditional RC transmission line, but with the places of the resistors and capacitors switched.

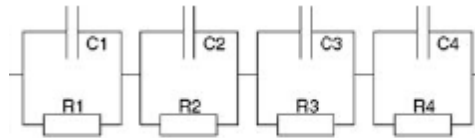


Figure 1-15. Foster structure representation of the Warburg element. Reprinted from Journal of Power Sources, Vol. 158, E. Kuhn, C. Forgez, P. Lagonotte, and G. Friedrich, “Modelling Ni-mH battery using Cauer and Foster structures,” pp. 1490–1497, Copyright 2006, with permission from Elsevier.

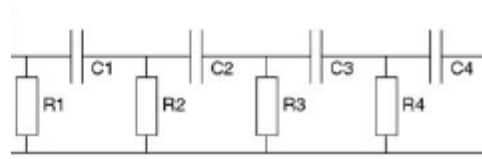


Figure 1-16. Cauer structure representation of the Warburg element. Reprinted from Journal of Power Sources, Vol. 158, E. Kuhn, C. Forgez, P. Lagonotte, and G. Friedrich, “Modelling Ni-mH battery using Cauer and Foster structures,” pp. 1490–1497, Copyright 2006, with permission from Elsevier.

An example of application of this approach is in the work of Moss *et al.* [27], where the Warburg impedance is replaced with the circuit shown in Figure 1-17. The complete runtime model is shown in Figure 1-18. In this model, the electrical components all depend on the cell SOC. These are determined as a function of SOC by performing repeated frequency sweeps over a range of cell voltages. The models are sometimes extended to higher frequencies by adding an inductor to account for cell inductance.

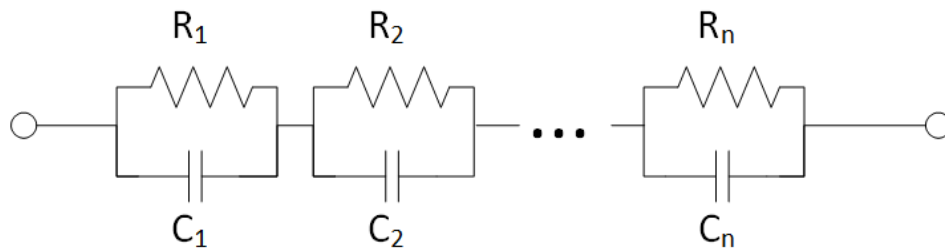


Figure 1-17. Time-domain equivalent of the Warburg element in [27]. Adapted from [27].

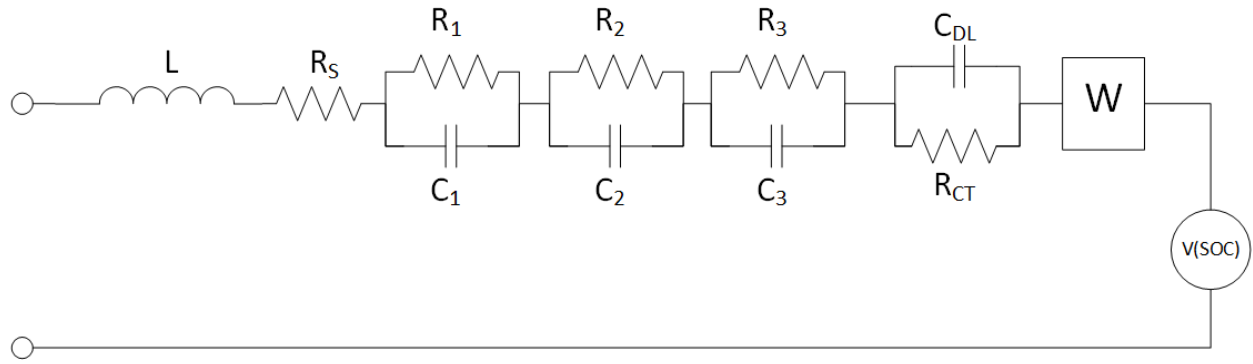


Figure 1-18. Complete time-domain model from [27]. Adapted from [27].

Another work that characterized the lithium-ion cell using impedance spectroscopy, and converted the results to a time-domain runtime model is that of Buller *et al.* [28]. Similar to the work of Moss *et al.* [27], the runtime model consists of the cell voltage in series with an impedance model. The impedance model that is used is shown in Figure 1-19. The frequency domain impedance is converted into the time-domain by replacing the \underline{Z}_{ZARC} element with the time-domain circuit shown in Figure 1-20, and the Warburg impedance \underline{Z}_W is replaced with the time-domain equivalent in Figure 1-21.

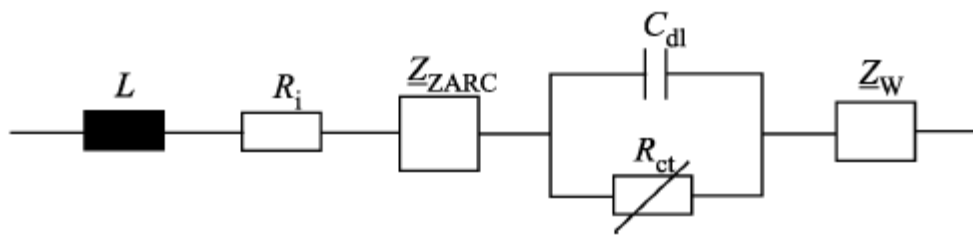


Figure 1-19. Impedance model used in [28]. From [28]. © 2005 IEEE.

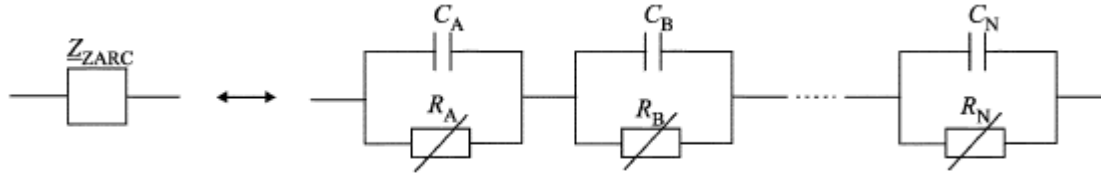


Figure 1-20. Time-domain equivalent of Z_{ZARC} in [28]. From [28]. © 2005 IEEE.

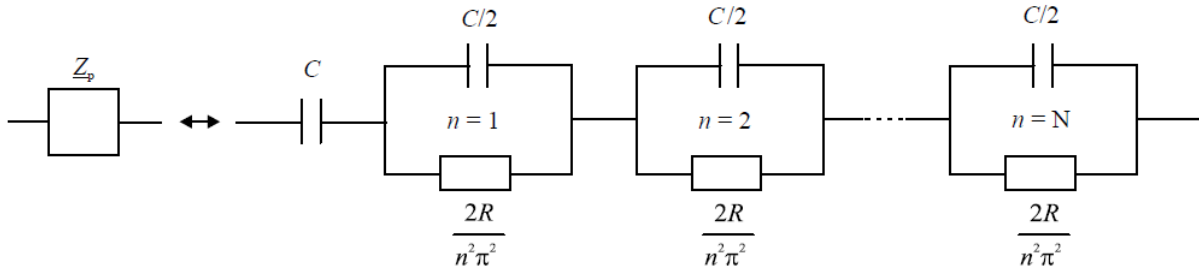


Figure 1-21. Time-domain equivalent of the Warburg element in [28]. From [28]. © 2005 IEEE.

The work of Urbain *et al.* [53], [54] employs the impedance model shown in Figure 1-22. The charge storage element is modeled as a capacitive element C_s . This capacitive element is a non-linear one that is analogous to the voltage source in the models in Buller *et al.* [27], [28]. The Z_p element models the impedance of the electrode porosity, which is physically analogous to the Warburg impedance. The electrode porosity impedance is implemented as a 50-segment RC transmission line of the form shown in Figure 1-23.

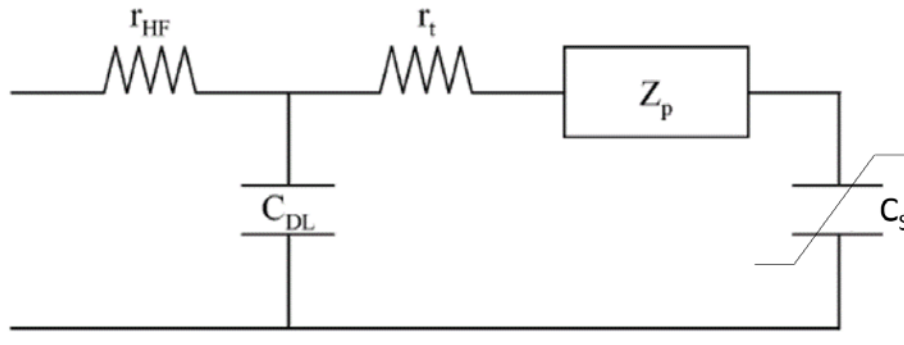


Figure 1-22. Impedance model used in [53]. Adapted from [53]. © 2007 IEEE.

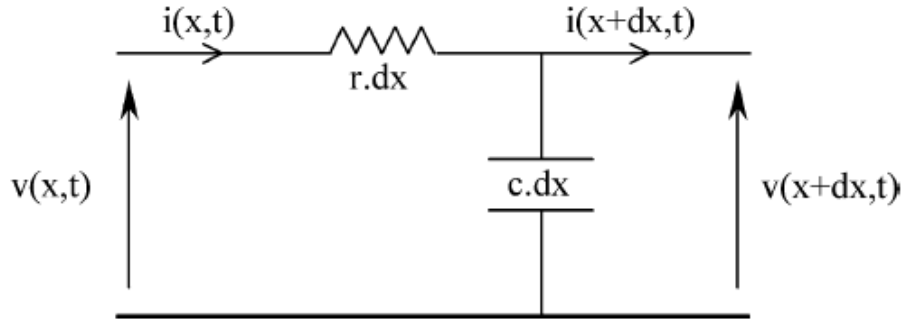


Figure 1-23. One segment of the RC transmission line used to model the electrode porosity impedance in [53]. From [53]. © 2007 IEEE.

The model construction and time-domain representation of the cell impedance discussed above requires impedance spectroscopy to be performed at a particular cell SOC, and the circuit parameters for this SOC are extracted by fitting to the measured impedance response. For runtime simulations of real life applications, which changes the cell SOC over the course of the cell's use, the model parameters over the full range of cell SOC is required. Therefore, for model construction for runtime simulations, impedance spectroscopy experiments need to be repeated over a wide SOC range. As mentioned above, since impedance spectroscopy is time-consuming due to the need for excitation of the cell at low frequencies (for example, 0.1 mHz),

and often frequencies are applied in sequence, the model construction process using impedance spectroscopy is time-consuming. This is one key advantage of model building using discharge analysis that is employed in this thesis work.

The linear version of the distributed SOC equivalent-circuit model proposed in this work is shown in Figure 1-9 (p. 24), which consists of a RC transmission line. The non-linearized version is derived from this model by making non-linear the resistive and capacitive components, and is shown later in Figure 2-5. There are two key differences between this model and the ones described above in this section. First, the transmission line capacitive elements in the distributed SOC model give the local SOC inside the transmission line, a key distinction from other equivalent circuit models where the entire cell is assumed to be at the same SOC. These other models disregard the variation in charging level through the cell. Second, the transmission line capacitive elements in the distributed SOC model represent energy storage in the cell, whereas the RC network in the other equivalent circuits physically represent an impedance at each characterized SOC.

1.3.2.3 Runtime Model

Runtime models allow the user to examine a cell's behavior over the course of usage of the cell. For example, in an electric bicycle application, the cell's voltage evolution during a trip can be accurately modeled. In the previous section, runtime models obtained by conversion of frequency-domain impedance models into the time-domain are discussed. In this section, runtime models obtained directly from time-domain characterization are discussed.

Chen and Rincon-Mora [2] proposed a model, shown in Figure 1-24, which is one of the most cited runtime equivalent-circuit models in the literature. This model has been employed in a large number of follow-on works including [3], [4], [7], [30]–[32], [45], [55]–[62]. In Chapters 2 and 3, the model proposed in this thesis, which is called the distributed SOC model, is compared to Chen and Rincon-Mora’s model to illustrate the key advantages of the proposed model.

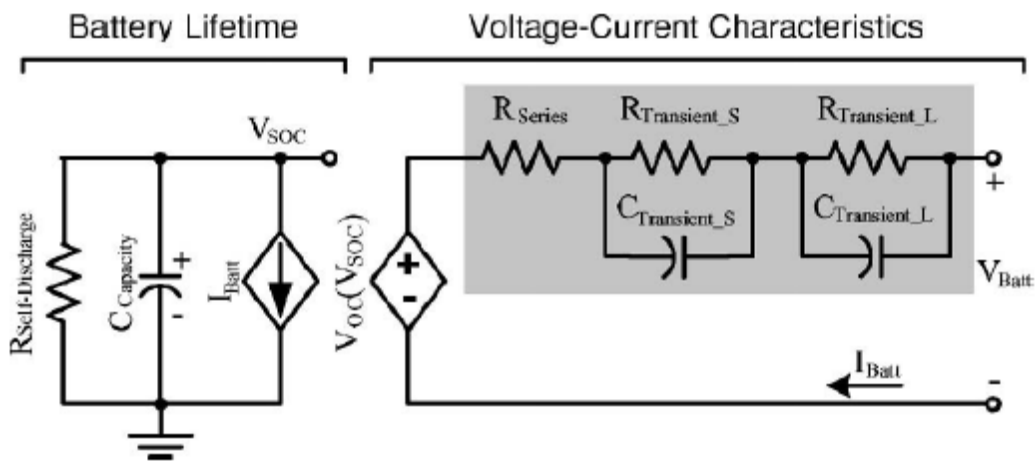


Figure 1-24. Circuit diagram for run-time model proposed by Chen and Rincon-Mora. From [2]. © 2006 IEEE.

The circuit proposed by Chen and Rincon-Mora [2] is made of two circuits. The circuit on the right is the main circuit, consisting of a voltage source V_{OC} , a series resistor R_{Series} , and two RC-pairs. The current to the cell is indicated by I_{Batt} in the main circuit. The terminal voltage of the cell is V_{Batt} , which can be broken into contributions from the components V_{OC} , R_{SERIES} , and the two RC pairs. In this model’s main circuit (right diagram in the figure), the voltage source V_{OC}

is dependent on the SOC, V_{SOC} , which provides the cell's SOC. This functional dependence is given by a nonlinear relationship between the cell SOC and its OCV.

Increasing the number of RC-pairs increases the fidelity of the model. The most commonly used configuration is two RC-pairs, which is observed to provide a good tradeoff between accuracy and computational effort [45]. The elements in the model are functions of SOC, and in some cases also current [3], [4], [6], temperature and/or cycle number. Comparing to the impedance-based runtime model of Section 1.3.2.2, the model in Figure 1-24 in effect models the Warburg impedance with two RC pairs. Therefore, the models in Section 1.3.2.2 are expected to have more accuracy as they include more elements.

Like the circuits of the last two sections, the circuit proposed by Chen and Rincon-Mora is also Thévenin-like in that it consists of a voltage source in series with a combination of resistive and capacitive elements. Instead of a constant voltage in the case of a Thévenin model, the voltage source changes as a function of SOC through the SOC-tracking circuit on the left of the figure.

The left circuit consists of three parallel-connected components: the dependent current source I_{Batt} , the capacitor $C_{Capacity}$, and the resistor $R_{Self-Discharge}$. The dependent current source I_{Batt} has the same value as the current in the main circuit. The voltage across the capacitor, V_{SOC} , is the SOC of the cell, and ranges between zero and one. The resistor $R_{Self-Discharge}$ represents the self-discharge effect of the cell. The capacitor $C_{Capacity}$ has capacitance value (expressed in Farads) equivalent to the full capacity of the cell (expressed in Coulombs). For example, a 1 Ampere-hour (Ah) cell, with a capacity of 3600 C, has a $C_{Capacity}$ of 3600 F in this model. When the cell

is charged to 0.5 SOC (or 0.5 Ah, which is equivalent to 1800 C), V_{SOC} would have a value of 0.5 V. Self-discharge is typically very small ($< 1\%$ per month) in lithium ion cells, so its effect on the cell response is minimal during runtime simulations. Therefore, $R_{Self-Discharge}$ is most often removed from equivalent-circuit models [2], [57], [63]. In comparison with the impedance-based runtime model discussed in Section 1.3.2.2, the method of tracking the cell's SOC and the dependence of the main circuit components on the cell SOC is formalized using the SOC-tracking circuit. In short, the left-hand circuit has measured cell current as its input, and keeps track of SOC. This SOC is then related to open circuit voltage, V_{OC} on the right hand side through measured values obtained at equilibrium at a range of states of charge.

The discharge analysis method demonstrated by Schweighofer *et. al.* [30], which was discussed in Section 1.3.2.1, and in which the shape of the constant current discharge voltage is fit with an exponential or series of exponentials, is often used in the extraction of parameters in runtime models [2], [4], [6], [30]–[36]. Due to the need for parameter extraction as a function of SOC, a series of current pulses over a range of SOC's are required. A depiction of a series of constant current discharging pulses is shown in Figure 1-25. Each pulse consists of the pulse phase, followed by a relaxation phase. The pulse is characterized by its amplitude, and duration, as shown in the figure. In this work, the convention is adopted in which positive applied current charges the cell, while negative applied current discharges the cell.

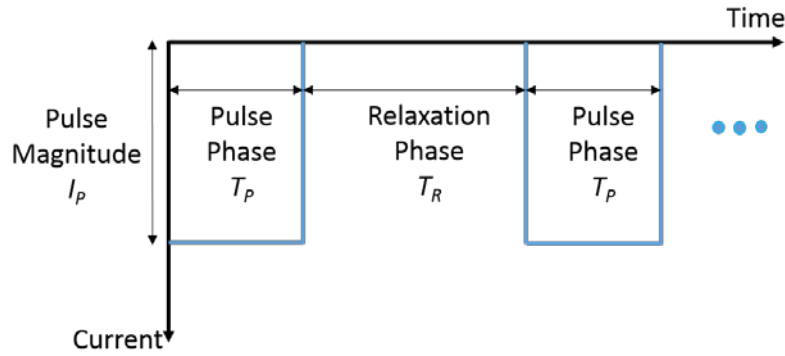


Figure 1-25. Depiction of the discharging pulses used to characterize the cell under test.

There are two common approaches to pulse discharge analysis – 1. pulse phase extraction [2], [30], [59], and 2. relaxation phase extraction [3], [4], [6], [7], [64]. In pulse phase extraction, the parameters are extracted while the discharge current is applied. An example is shown in Figure 1-26, where the initial *ca.* 38 s of the voltage response of a commercial lithium ion cell to a discharge current pulse (data from experiments discussed in Chapter 3) is shown. The disadvantage is that the current pulse is changing the cell SOC, so the extraction is restricted to the very initial times of the pulse phase (few seconds). Beyond this time period, the SOC is considered appreciably altered. Therefore, the time constants that can be extracted are typically very short ($< 10\text{s}$) [30], [59].

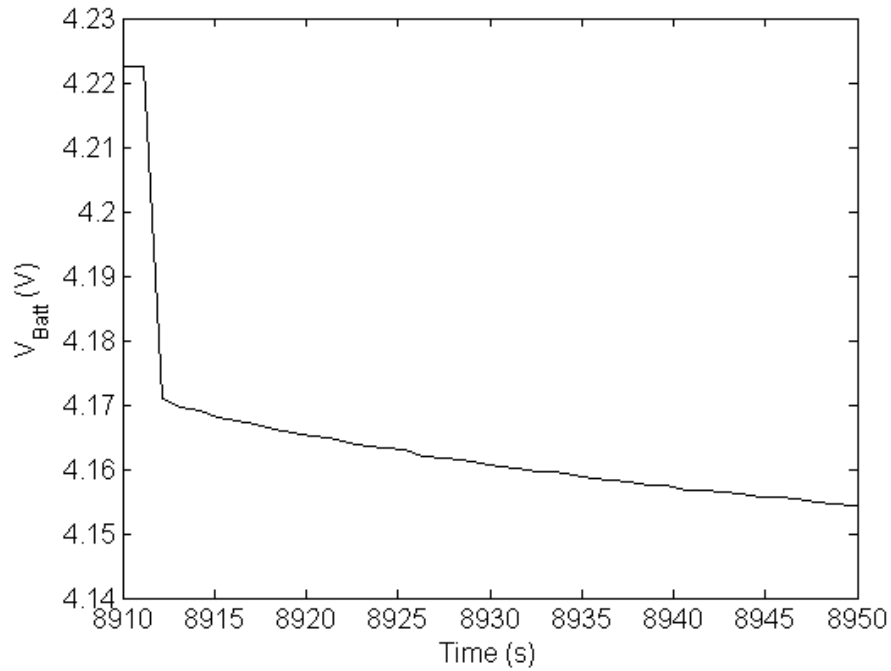


Figure 1-26. Voltage response of a cell during the pulse phase of a discharge pulse. The flat initial cell voltage is the open-circuit voltage of the initial cell SOC before the current step. Once the current step is applied (beginning of the pulse phase), the cell voltage falls rapidly. Then as time proceeds, the cell voltage falls according to $t^{1/2}$.

A number of recent works perform parameter extraction during the relaxation phase of the current pulse [3], [4], [6], [7], [64]. The relaxation response of the same cell above (data from experiments discussed in Chapter 3) during the relaxation phase is shown in Figure 1-27. As the cell has already reached the desired SOC during the current pulse phase, the SOC of the cell during the relaxation phase is considered constant throughout the relaxation phase. The relaxation phase can last tens of minutes to hours. Therefore, a wider range of time constants, including longer time constants, can be obtained [6], as opposed to the pulse phase parameter extraction.

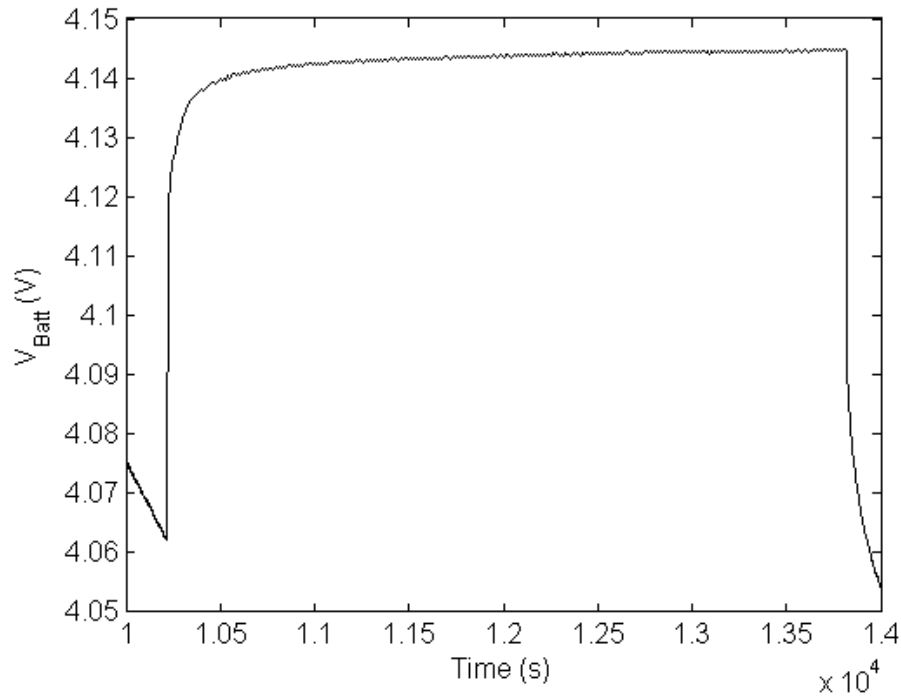


Figure 1-27. Cell voltage response during the relaxation phase of a discharge pulse. The initial falling cell voltage that is shown coincides with the discharging current that is still being applied (latter portion of the pulse phase). At *ca.* 1.02×10^4 seconds, the relaxation phase begins (the applied current falls to zero), and the cell voltage rises jumps up instantaneously due to the absence of the IR drop. The cell voltage continues to rise as the cell relaxes. It can be seen that the cell voltage reaches an equilibrium value as time proceeds. This is the OCV at this cell SOC. Then, towards the far right, the next discharging current pulse is applied and the cell voltage falls again.

Some works have shown that the direction of applied current (discharging vs. charging) affects the parameters obtained [3], [4], [6]. So in these cases, the model parameters are extracted as a function of magnitude of current, as well as current direction (discharging vs. charging). The corresponding series of charging current pulses is shown in Figure 1-28. The applied current is

positive because the convention adopted in this work is that charging current has positive polarity.

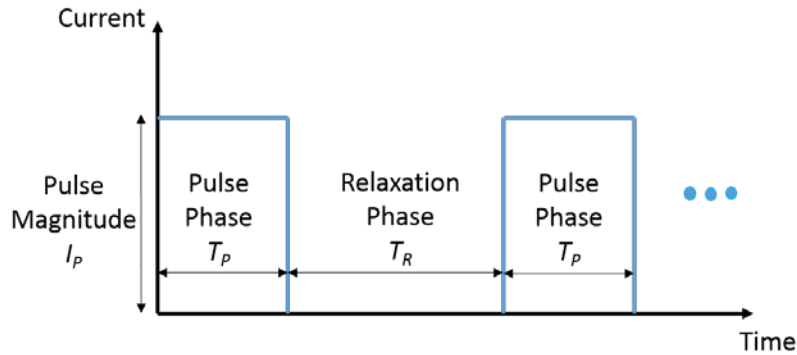


Figure 1-28. Illustration of the charging pulses used to characterize the cell under test.

In Chen and Rincon-Mora's model [2], the assumption is that the cell parameter is only dependent on the bulk SOC – that is the overall SOC of the cell. By fitting parameters of the RC segments to the relaxation voltage curve, the model parameters are obtained at the specific SOC. The OCV at the new SOC is given by the voltage that plateaus at the end of the relaxation period. Like in the case of Thévenin models in Section 1.3.2.1, the model parameters are fitting constants at each SOC that allow the best fit to the measured cell response during the current pulse – or in this case the relaxation phase.

Other approaches, including the electrochemical models in Section 1.3.1, impedance model in Section 1.3.2.2, and the distributed SOC model developed in this thesis work, have more readily apparent physical meaning attached to the model variables. The work in chapters 2 and 3 of this thesis seeks to provide a more physically relevant model. It also allows for a non-uniform level

of charging within the cell during and following charge or discharge, and which results primarily from the finite rate of mass transport within the cell.

The linear version of the distributed SOC model proposed in this work is shown in Figure 1-9 (p. 24). Even though the distributed SOC model and the ones described in this section are runtime models, there are major differences. The models described in this section assumes that the model parameters depend on the bulk SOC. The consequence of this assumption is discussed in more detail later in Section 3.2.2.3. In the distributed SOC model, the concept of local SOC is introduced, and represents the fractional charge state as a function of position within the cell's electrode. The cell's voltage in the electrochemical model depends on the lithium ion concentration at the surface while internally the lithium ion concentration is governed by diffusion.

As mentioned earlier in this section, equivalent-circuit models are typically less accurate than electrochemical models for runtime simulations, because they do not contain the detailed mathematical descriptions of the physical processes that occur inside the lithium ion cell. In uses such as initial design and verification of complex systems, models of each of the interconnecting components are needed. In these cases, models that can be constructed without significant time and engineering resources are important. Some relatively small inaccuracies of the model are acceptable and expected. To evaluate the simulation performance of a cell runtime model, the simulation error, which is the difference between the predicted and measured cell voltage, needs to be quantified. As mentioned in the introduction, Chen and Rincon-Mora [2] stated that the expected error of equivalent-circuit models is 1-5%, but whether that refers to the maximum

error or root-mean-square-error is not clarified. A closer survey of the literature equivalent-circuit models revealed that there is no commonly accepted method of model validation, as many different validation tests are used. Many works would use customized pulsed current tests for extracting the model parameters and validating the obtained model. This would appear to give more optimistic results, as the extraction and validation excitations are the same. For a more realistic evaluation of a model, the parameter extraction and validation tests should be different, as will be the case in this thesis work. Also, most works explored do not use a common approach to quantify the error. Therefore, it has been difficult to perform a direct comparison of different proposed equivalent-circuit models that are in the literature.

In this work, two useful ways of quantifying the simulation error over the course of the entire validation test are adopted, which are the maximum-absolute-percent-voltage-error (MAPVE) and root-mean-square-percent-voltage-error (RMSPVE). The percent-voltage-error (PVE) expresses the difference between the simulated and measured voltage at any time in the experiment as a percentage, which is given by

$$PVE (\%) = \frac{V_{sim} - V_{exp}}{V_{exp}} \times 100\%, \quad [1-9]$$

where V_{sim} and V_{exp} are the simulated and experimental cell voltages, respectively. The MAPVE is then defined as the maximum difference between the simulation and measured cell voltage, expressed as a percentage, for the entire test. It is

$$MAPVE(\%) = MAX|PVE|, \quad [1-10]$$

where PVE is the percent-voltage-error defined in equation [1-10]. The RMSPVE is a measure of the average deviation between the simulated and experiment results for the entire test, and is given by

$$RMSPVE = \sqrt{\frac{\sum_{i=1}^n (PVE)^2}{n}}, \quad [1-11]$$

where n is the number of data samples measured in the experiment. The few works that were found from the literature that had quantified the maximum-voltage-error or root-mean-square-error, and use validation tests that are not identical to the parameter extraction ones, are listed in Table 1-2. In this table, the validation methods of the respective proposed models, and their simulation performance are tabulated. As can be seen in the table, the root-mean-square error is on the low side of the 1-5% range, suggested by Chen and Rincon-Mora [2], while the max error is on the high side, and even exceeding it. These results provide a good basis for evaluating the simulation performance of the distributed SOC model proposed in this thesis.

Validation Method Description	MAPVE (%)	RMSPVE (%)	Reference
New European Driving Cycles [65]	-	1.6	[59]
FTP72 Urban Dynamometer Driving Schedule [66]	1.9	-	[60]
Pulsed current experiments with current magnitudes ranging from 0.75 to 1.75 C	6	-	[4]
Pulse current experiments with current magnitudes ranging from 1.0 to 2.5 C	7	-	[62]

Table 1-2. Tabulation of the simulation errors for runtime validation tests of some of the literature

equivalent-circuit models. As there is no commonly accepted method to validate the model, or quantify the simulation errors, the test methods differ between the results, and the missing data in the table cannot be filled.

1.4 Key Contributions

The key contributions of this work are:

a. A new equivalent-circuit model for runtime simulation, called the distributed SOC model, is developed, which is described in Section 2.1. This model consists of a transmission line to model the variation of SOC through the depth of the electrode of the lithium-ion cell. To the best of the author's knowledge, this is the first equivalent-circuit model that attempts to include the SOC through the depth of the electrode. In contrast, competing runtime equivalent-circuit models in the literature model the cell as a single dependent voltage source in series with various forms of RC networks. The voltage source represents the cell OCV, which is dependent only on the cell bulk SOC. The RC networks in these competing models do not represent charge storage in the cell, but act as impedances that give rise to the transient response of the cell model.

b. A pulsed current method to extract the parameters of the distributed SOC model is developed, which is described in Section 2.3.1. This method is applied to extract parameters from commercial cells in Chapters 2 and 3. The model parameters of the distributed SOC model is shown to be largely independent of the applied current magnitude and direction. This means that a fewer number of extraction experiments can be performed, when compared to conventional equivalent-circuit models. In these other equivalent-circuit models, the model parameters have been shown to be strongly dependent on current magnitude and direction [3], [4], [6]. Therefore, a large number of parameter-extraction experiments need to be performed to construct the model.

In contrast, due to the weak-dependence of the model parameters on current, the parameter-extraction experiments needed for the distributed SOC model is far fewer (two, at minimum), reducing the amount of effort required for model construction. The reason for this reduced dependence on current magnitude and direction may be attributed to the distributed SOC model's non-linear transmission line, which models the non-uniform SOC levels through the depth of the electrode. This is a more physically accurate model of the charge diffusion process inside the cell.

d. Circuit parameters for the developed model are extracted for commercially-obtained lithium-ion cells using the parameter extraction method. The model capabilities are shown by comparing the simulated to the experimental results of these cells from validation tests. In Chapter 2 this is performed at a single current value, while in Chapter 3 extractions and simulations are performed for widely varying currents.

e. Two versions of the distributed SOC model are developed. One is based on planar diffusion, while the other is based on spherical diffusion. The planar model is shown to work well for low average discharge currents, even with the presence of large current pulses. The spherical model is shown to perform well for higher average discharge currents, but performance is compromised for large pulsed currents. There is tradeoff seen here between the two models. This tradeoff behavior can be attributed to the difference in distribution of the charge storage capacitance in the corresponding electrodes as a function of depth.

f. The parameters for the proposed distributed SOC equivalent-circuit model are extracted for a lithium-alloying tin electrode. This is described in Chapter 4. Because the phase transformation effect dominates the charge and discharge process in this electrode, the extracted parameters show characteristics that can be attributed to the phase changes. This is explained using a phase change model. This type of electrode presents a challenge for the distributed SOC model, and particularly parameter extraction.

Chapter 2: Polymer Cell Characterization and Modeling

A key aim of this work is to develop a runtime equivalent-circuit model that includes the physical effects of diffusion, using a nonlinear transmission line. The construction of this model, called the distributed SOC model, for a commercial lithium ion cell is described in this chapter. As part of an initial study of this model, a lithium-ion polymer cell is characterized and validated at a single current. Lithium-ion polymer cells, also called pouch cells, are lithium ion cells that are encapsulated in a polymeric casing. They operate on the same principles as other lithium ion cells that are housed in metallic cans, such as cylindrical and prismatic cells. In the next chapter, the characterization and validation of a commercial cylindrical lithium ion cell at multiple charge and discharge currents will be examined.

The derivation of the distributed SOC model is discussed in Section 2.1. In order to validate the model, two sets of experiments are required. First, extraction experiments are performed on the cell, which enables the model parameters to be extracted. Second, validation experiments allow comparisons between the model simulation and experimental results. The experimental setup is described in Section 2.2. The parameter extraction from pulsed current experiments is presented in Section 2.3. The validation experiments, together with the analysis of the results and some of the limitations of the validation, are shown in Section 2.4.

2.1 Model Development

The circuit model developed in this work is derived from the Randles model that is presented in Section 1.3.2.2 and reproduced below in Figure 2-1. As mentioned in Section 1.3.2.2, although a lithium ion cell consist of the positive and negative electrodes placed in series, typical impedance models of the cell uses only a single Randles model [28], [29], [48], [49]. This is because the impedance response of the two electrodes overlap significantly, so the individual responses of the individual electrodes cannot be clearly distinguished [48]. In this work, only one Randles circuit is used as the starting point of the model derivation.

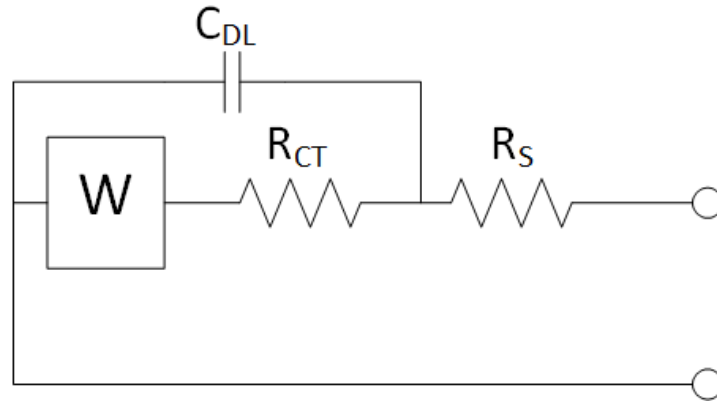


Figure 2-1. Randles circuit model, which is commonly used in impedance spectroscopy.

The Randles model includes four elements: 1) a series resistance R_S , 2) a charge-transfer resistance R_{CT} , 3) a Warburg element W , and 4) double-layer capacitance C_{DL} . The Randles model is described in detail in references such as that by Bard and Faulkner [26]. The series resistance models the effect of the resistive drop in the current path. This includes contributions from the current collectors, contact resistance, electrolyte, and particle-to-particle contacts within

the electrodes. The charge-transfer resistance R_{CT} is in series with the Warburg element W . The charge transfer resistance R_{CT} models the voltage drop that is associated with the insertion/extraction reactions at the electrode's surface. The Warburg element W , which is a frequency-domain impedance defined in equation [1-8], represents ion diffusion in the electrode active materials. The charge transfer resistance R_{CT} is in series with the Warburg element W because the lithium-ions need to be inserted into the active material particle in order for them to diffuse into the particle's bulk. C_{DL} models the effect of the double-layer capacitance. The double-layer capacitance is an effective capacitance that is observed in all electrode surface interfaces in contact with the electrolyte solution.

To simplify the model, the double-layer capacitance C_{DL} in Figure 2-1 is excluded in this work. This is a commonly used simplification [18], [19], [38], [67], because the timescale on which C_{DL} affects the voltage response of lithium-ion cells below 1 s [27]–[29], whereas runtime modeling typically operates on the timescale of seconds [2], [4], [6], [30]–[37]. Where higher frequency response predictions are required, the double layer capacitance can be added in relatively easily.

As described in Section 1.3.2.2, the Randles model is a frequency-domain model that only applies at a specific SOC. Not only is the Warburg element itself specified as a function of frequency, the effective value of capacitance of this element and the time constant associated with it are functions of SOC. As a result, this model only applies over a limited range of SOC. The charge transfer resistance is also linearized. The distributed SOC model proposed in this thesis is obtained by first converting the diffusive Warburg element into its time-domain

approximation, and then making the circuit components non-linear so the full range of cell SOC can be modeled. The conversion of the Warburg element into a time-domain circuit model is first described below, followed by treatment of the circuit components as non-linear ones.

The Warburg element is a frequency-domain element, defined in equation [1-8], that models the diffusion effect in the electrodes. As discussed in Section 1.3.1, the diffusion of solid-phase lithium ions in the electrodes is most often the slowest time constant process in the lithium ion cell [67]. In this work, the Warburg element is approximated by a one-dimensional finite diffusion element, shown in Figure 2-2. This element simulates a one-dimensional active material that occupies the space $0 \leq x \leq L$. The solid-to-electrolyte interface, and therefore the flux of lithium-ions into the active material, is placed at $x = L$. The current collector is at position $x = 0$.

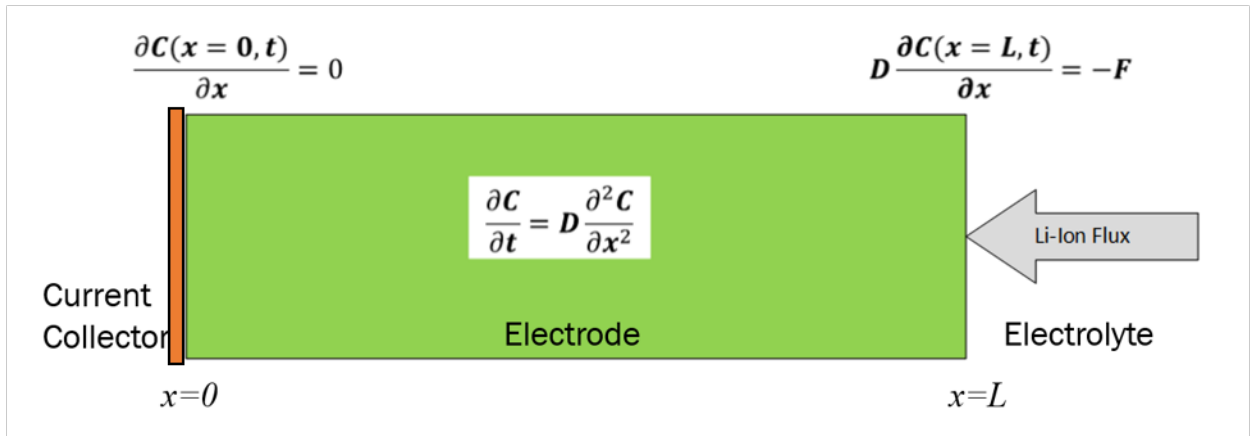


Figure 2-2. One-dimensional diffusion element used to model the lithium ion diffusion process in the lithium ion cell.

A one-dimensional diffusion equation is

$$\frac{\partial C}{\partial t} = D \frac{\partial^2 C}{\partial x^2}, \quad [2-1]$$

where x is the spatial direction, t is time, C is ion concentration, and D is the ionic diffusion coefficient. In this case of the lithium-ion cell, the mobile ion is the lithium ion. As discussed in Section 1.2.2, in the lithium-ion cell, the lithium ion is the ionic species that gets inserted and extracted in the two electrodes.

Following Fick's First Law, flux F_0 at boundary location $x = L$, where the surface of the electrode meets the electrolyte, and for the no flux condition at boundary location $x = 0$, (which corresponds to the metal contact at the edge of the electrode), the boundary conditions are expressed as:

$$-D \frac{\partial C}{\partial x} = -F_0, \quad \text{at } x = L, \quad [2-2]$$

and

$$\frac{\partial C}{\partial x} = 0, \quad \text{at } x = 0. \quad [2-3]$$

To obtain an electrical equivalent-circuit representation of the above diffusion element, a finite RC transmission line, shown in Figure 2-3, is used. R_d and C_d are respectively the resistance- and capacitance-per-unit-length of the transmission line. The differential resistive and capacitive elements of the transmission line are then $R_d \partial x$ and $C_d \partial x$, respectively. Here it is assumed that the electronic resistance is negligible compared to the ionic resistance, and so this is not shown (otherwise it would appear on the bottom of the transmission line, opposite the ionic resistances).

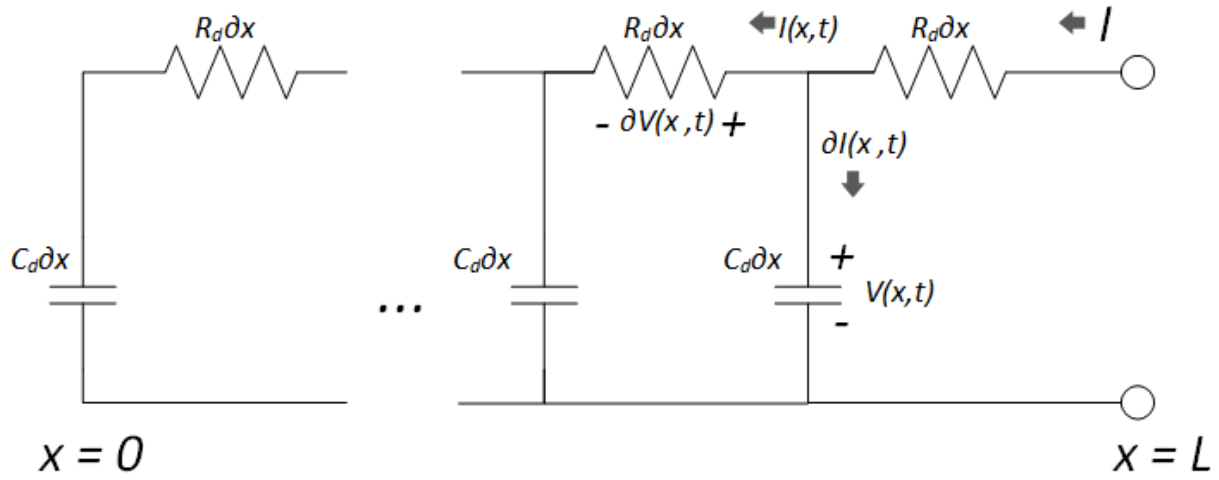


Figure 2-3. Transmission line model consisting of resistors and capacitors to model diffusion.

In the transmission line, the equations governing the relationship between current $I(x, t)$ and voltage in the transmission line $V(x, t)$ is given by

$$\partial V = IR_d \partial x, \quad [2-4]$$

and

$$\partial I = C_d \partial x \frac{\partial V}{\partial t}. \quad [2-5]$$

Equations [2-4] and [2-5] can be combined to give

$$\frac{\partial V}{\partial t} = \frac{1}{R_d C_d} \frac{\partial^2 V}{\partial x^2}, \quad [2-6]$$

with boundary conditions

$$\frac{\partial V}{\partial x} = 0, \quad \text{at } x = 0, \quad [2-7]$$

and

$$\frac{\partial V}{\partial x} = IR_d, \quad \text{at } x = L. \quad [2-8]$$

The analogous nature of the transmission line model to the diffusion system can be seen by the similarity between equation sets [2-6] to [2-8] and [2-1] to [2-3]. The transmission line voltage V and the term $(R_d C_d)^{-1}$ in equation [2-6] are analogous to ion concentration C and diffusion coefficient D in equation [2-1], respectively. This corroborates the observation by Urbain *et al.* [53], [54] that the diffusion impedance can be modeled in the time-domain by a RC transmission line. Urbain *et al.*'s model consists of this diffusion impedance in series with a single capacitor that models the charge storage inside the cell. The approach taken in the distributed SOC model is different in that the RC transmission line itself represents the energy storage effect of the material, with the capacitor charge representing the local charge state at a particular depth in the electrode.

This transmission line model of equations [2-6] to [2-8] depends on transmission line length L via equation [2-8]. In the construction of equivalent-circuit models for engineering applications, the cell internal parameters such as the electrode thickness should not be required to be obtained. This can be achieved by making the position variable x non-dimensionalized. Using dimensionless position variable α , where

$$\alpha = \frac{x}{L}, \quad [2-9]$$

the detailed electrode thickness is no longer required. Equation [2-6] becomes

$$\frac{\partial V}{\partial t} = \frac{1}{R_d C_d L^2} \left(\frac{\partial^2 V}{\partial \alpha^2} \right). \quad [2-10]$$

The boundary condition at the current collector boundary, equation [2-7], becomes

$$\frac{\partial V}{\partial \alpha} = 0, \quad \text{at } \alpha = 0, \quad [2-11]$$

and the boundary condition at the electrode-electrolyte interface, equation [2-8], becomes

$$\frac{\partial V}{\partial \alpha} = IR_d L, \quad \text{at } \alpha = 1. \quad [2-12]$$

Since R_d and C_d are per-unit-length resistance and capacitance of the transmission line, the resistance of the entire transmission line, hereby called the diffusion resistance R_D , is given by

$$R_D = \int_0^L R_d dx = R_d L, \quad [2-13]$$

and the capacitance of the entire transmission line, called diffusion capacitance C_D , is given by

$$C_D = \int_0^L C_d dx = C_d L. \quad [2-14]$$

Letting

$$\tau = R_d C_d L^2 = R_D C_D, \quad [2-15]$$

Equations [2-10] to [2-12] becomes

$$\frac{\partial V}{\partial \alpha} = \frac{1}{\tau} \frac{\partial^2 V}{\partial \alpha^2}, \quad [2-16]$$

$$\frac{\partial V}{\partial \alpha} = 0, \quad \text{at } \alpha = 0, \quad [2-17]$$

$$\frac{\partial V}{\partial \alpha} = IR_D, \quad \text{at } \alpha = 1. \quad [2-18]$$

Equations [2-16] to [2-18] are independent of electrode thickness L , as desired.

The above has demonstrated that the Warburg impedance of the Randles circuit model in Figure 2-1 can be approximated by the diffusion model of equations [2-16]-[2-18]. Then, by excluding the Randles model's double-layer capacitance C_{DL} (as mentioned earlier in this section), and

combining its charge-transfer resistance R_{CT} and series resistance R_S into a single resistance (also called R_S here), the equivalent-circuit model now becomes that shown in Figure 2-4.

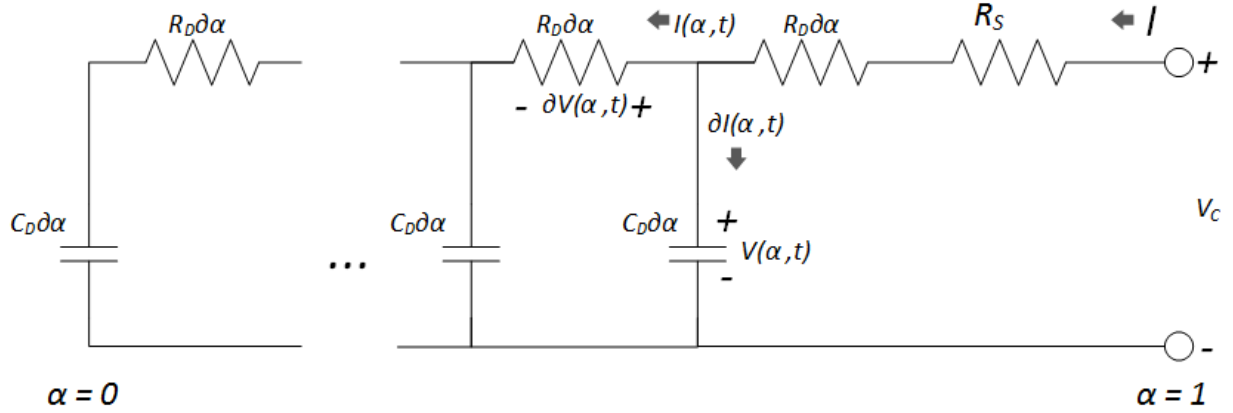


Figure 2-4. Equivalent circuit model consisting of the RC transmission line and a series resistance.

As discussed earlier, after obtaining a time-domain model, the circuit components need to be converted to their non-linear, SOC-dependent counterparts in order for the full range of SOC to be accurately modeled at runtime. Rather than directly expressing the circuit elements as non-linear capacitors and resistors, in this work an SOC-tracking circuit is employed, following the method introduced by Chen and Rincon-Mora [2]. This method is equivalent to having non-linear resistive and capacitive elements, and is simple to implement as is now explained.

In previous work by Chen and Rincon-Mora [2], the equivalent circuit, shown in Figure 1-24 (p. 38), consists of a main circuit and a SOC-tracking circuit. The SOC-tracking circuit contains a capacitor $C_{Capacity}$, the voltage of which, V_{SOC} , provides the cell SOC, as explained in Section 1.3.2.3. The cell OCV is modeled using the dependent voltage source $V_{OC}(V_{SOC})$, which is a

function of the cell SOC through a nonlinear mapping of the OCV dependence on cell SOC. In previous models such as this one, the total charge of the full cell is tracked. In the distributed SOC model proposed in this thesis, a key differentiating feature is the ability to locally determine the charge state. As is now described, the method employed by Chen and Rincon-Mora [2] is extended to keep track of SOC as a function of position along the transmission line in the distributed SOC model.

Each RC-segment in the model shown in Figure 2-4 represents the behavior of the electrode at a certain depth. By making the following changes to this circuit model, the final complete distributed SOC model in Figure 2-5 is obtained. First, as in the case of Chen and Rincon-Mora's model [2], a SOC-tracking circuit to keep track of the full cell SOC is added, which is shown in the bottom right of the figure. C_{FCE} is the full-capacity-equivalent capacitance of the cell, which plays the identical role to the $C_{Capacity}$ in Chen and Rincon-Mora's model [2]. For example, for a 3 Ah cell, which has a full capacity of 10,800 Coulombs, C_{FCE} would have a capacitance of 10,800 F. Current I flowing in the main circuit also flows in this SOC-tracking circuit, and the voltage across capacitor C_{FCE} indicates the full cell SOC. Second, the series resistance R_s is made to depend on the overall cell SOC. Third, in the distributed SOC model, the SOC of the electrode, and correspondingly the OCV, can vary as a function of depth. In other words, there is a depth-dependent local SOC. By extending the use of SOC-tracking circuits to each segment of the distributed SOC model, the SOC at each depth can be determined. This is shown in the rest of the SOC-tracking circuits in the bottom row of Figure 2-5. The full capacity of each segment of the model is given by $C_{FCE}\partial\alpha$, where $\partial\alpha$ is the fraction of the full electrode thickness that this segment represents. The voltages of the capacitors in these tracking

circuits give the SOC of the electrode at each depth. Fourth, a dependent voltage source V_{OC} maps the local SOC to the local OCV in the electrode. This dependent voltage source replaces the diffusion capacitance $C_D \partial \alpha$ of each RC-segment in Figure 2-4. This dependent voltage source element, together with the local SOC-tracking circuit, effectively acts as a non-linearized charge-dependent capacitor. Fifth, the diffusion resistance $R_D \partial \alpha$ of the transmission line model is made dependent on the voltage in the local SOC-tracking capacitor to reflect the dependence of the $R_D \partial \alpha$ element at each electrode depth on the corresponding local SOC. No leakage resistance is included as it is assumed that the time scales over which the runtime model is used will be much less than the leakage discharge time constant.

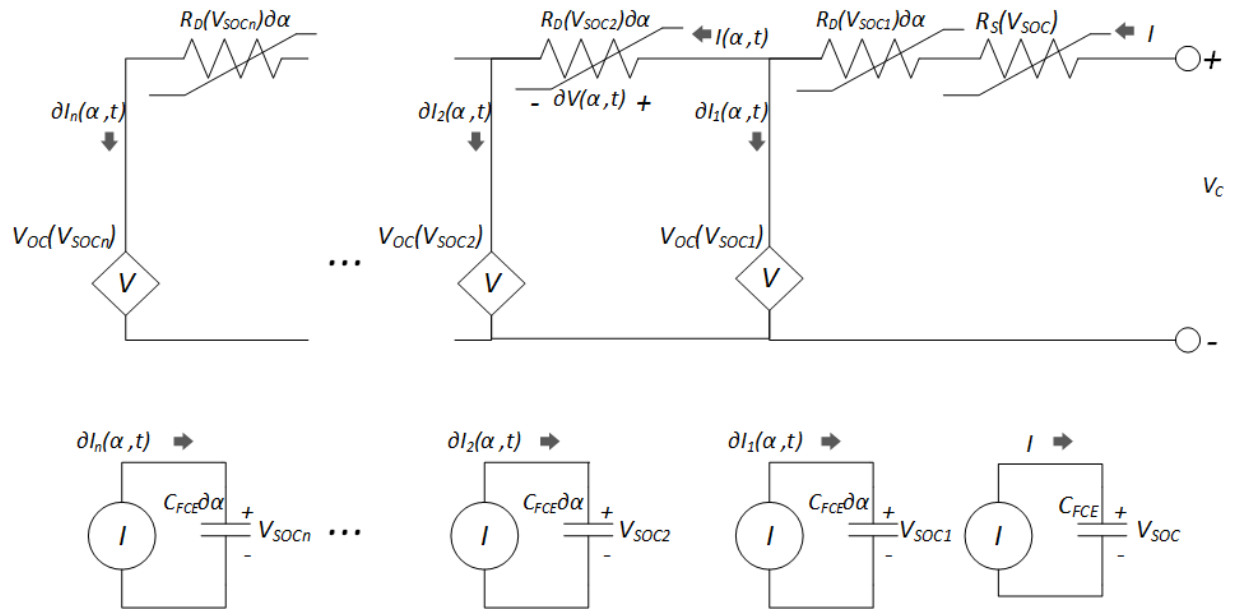


Figure 2-5. Final distributed SOC equivalent circuit model, with dependent voltage sources replacing the capacitors of the RC transmission line.

To summarize, by making the above changes, the linear equivalent-circuit model shown in Figure 2-4 is made non-linear with parameter values that depend on the cell SOC (overall bulk and local). The current I flowing into the cell also flows in the overall SOC-tracking circuit at the bottom right of the circuit. The voltage V_{SOC} across capacitor C_{FCE} indicates the cell's bulk SOC. The series resistance R_S is a function of the cell bulk SOC. Each pairing of diffusion resistance R_D and dependent voltage source V_{OC} elements in the circuit models the behaviour of a layer of thickness $\partial\alpha$ of the planar electrode. A local SOC-tracking circuit corresponds to each electrode layer, with a capacitance of $C_{FCE}\partial\alpha$. The current $\partial I(\alpha, t)$ flowing into the voltage source V_{OC} element also flows in the corresponding local SOC-tracking circuit. The voltage across the capacitor $C_{FCE}\partial\alpha$ indicates the layer's local SOC. The R_D and V_{OC} are functions of this local SOC. The V_{OC} element, together with the corresponding SOC-tracking circuit, behaves as a charge-dependent capacitor. Therefore, the network of R_D and V_{OC} elements behaves as a non-linear RC transmission line that depends on the local electrode SOC. As pointed out previously in Section 1.3.2, this is a key difference of the distributed SOC model when compared to competing equivalent-circuit models in the literature. In these equivalent-circuit models, the voltage source and RC circuit elements are dependent on the cell bulk SOC.

The cell model parameters that need to be obtained experimentally are summarized in Table 2-1. Four model parameters are functions of SOC. The method to obtain these parameters, and their dependence on SOC is discussed in Section 2.3.1.

Cell Model Parameter
Full Capacity Equivalent Capacitance C_{FCE}
Open-Circuit Voltage $V_{OC}(SOC)$
Diffusion Capacitance $C_D(SOC)$
Diffusion Resistance $R_D(SOC)$
Series Resistance $R_S(SOC)$

Table 2-1. List of cell model parameters of the distributed SOC equivalent-circuit model.

2.2 Experimental Setup

As mentioned in the introduction, this chapter is an initial study of the performance of the proposed distributed SOC model. For this study, the extraction and validation experiments are performed at a single current for simplicity of analysis. In the next chapter, the extension of the experiments and simulations to multiple charge and discharge currents on a commercial cylindrical lithium ion cell is discussed. The cell used for this initial study is a lithium-ion polymer cell produced by Dow Kokam Inc. The model number of this cell is SLPB125255255H. This cell has a nominal capacity of 75 Ah, and its dimensions are 12.5 mm x 255 mm x 255 mm (thickness x length x width). The maximum continuous discharge current for this cell is 450 A (or 6.0 C). This lithium-ion cell uses a Nickel-Manganese-Cobalt-Oxide active material as the positive electrode, and a carbon-based negative electrode.

For the experiments described in this chapter, two setups are used – one for charging and one for discharging. The charging setup is shown in Figure 2-6. The power supply connects across the lithium-ion cell and charges the cell. The discharging setup is shown in Figure 2-7. In this mode, the power supply is connected in series with the cell and is operated in constant current mode. The power supply current setting controls the discharge current of the lithium ion cell. Energy from both the power supply and cell is dissipated by the resistor bank. In both cases, the current into the cell is obtained by measuring the voltage across a shunt resistor. Voltages across the lithium ion cell and shunt resistor are monitored by a National Instruments Data Acquisition System NI PCI-6251 [68].

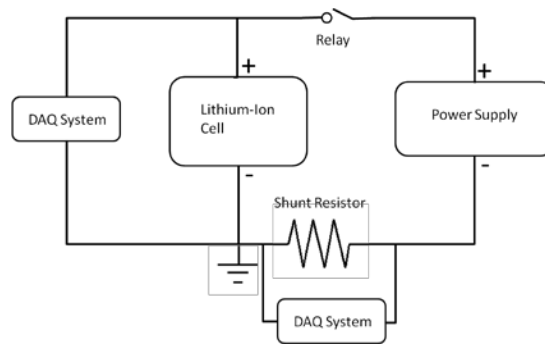


Figure 2-6. Charging setup for testing the Dow Kokam lithium-ion polymer cell.

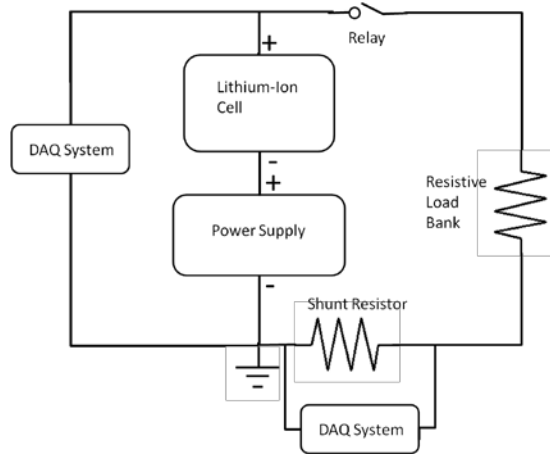


Figure 2-7. Discharging setup for testing the Dow Kokam lithium-ion polymer cell.

2.3 Extraction

To use the distributed SOC model discussed in Section 2.1 to simulate the behavior of a cell, extraction of the model parameters is required. In this section, the parameter extraction method is discussed. The method consists of a pulsed current experiment, and an algorithm to extract the circuit parameters. The results obtained from application of this parameter extraction method on the Dow Kokam cell at a single test current are discussed. In the next section (Section 2.4), these extracted circuit parameters are used to simulate the cell voltage response to validation experiments.

2.3.1 Parameter Extraction Procedure

The distributed SOC model developed in this work, shown in Figure 2-5, contains the following parameters: 1. full-capacity-equivalent capacitance C_{FCE} , 2. series resistance R_S , 3. diffusion resistance R_D , and 4. open-circuit voltage V_{OC} . A parameter extraction method that is used to

extract these model parameters, and their dependence on SOC, is discussed here. This method is based on that of the Galvanostatic Intermittent Titration Technique [69], which is also used in Chapter 4 to characterize a tin thin film as a lithium-ion cell electrode. GITT is well known for characterizing an electrode to extract the solid-phase diffusion coefficient of the solute in electrodes. Using the physical dimensions of the electrode, and the stoichiometries of the material, the GITT method consists of pulsed current experiments to obtain the diffusion coefficient of the solute. The method developed in this thesis to obtain the circuit parameters of the distributed SOC model works in a similar way. The physical dimensions and details of the electrodes of the lithium ion cell are abstracted away by using a non-dimensionalized equivalent-circuit model. Therefore, the use of the distributed SOC model does not require detailed knowledge of the internal structure of the cell or the occurring physical mechanisms. This is beneficial to engineers who only requires the equivalent-circuit model for application design and verification. This is one of the key advantages of equivalent-circuit models when compared to more sophisticated electrochemical models, in which the physical dimensions and properties of materials internal to the lithium ion cell are required for model construction.

As discussed in Section 2.1, the final distributed SOC model shown in Figure 2-5 effectively behaves as a non-linearized transmission line with parameter values that depend on local SOC along its length, in series with a resistance R_S that depends on the overall cell SOC. The method to obtain the model parameters described below consists of solution of response of the linear version of the distributed SOC model (shown in Figure 2-4) to a current pulse to extract the model parameter at each chosen SOC. Applying a series of these current pulses determines the dependence of the model parameters to SOC. By using these extracted model parameters, and

their dependence on SOC, the non-linear distributed SOC model would be completed and used to simulate the runtime cell behavior over the full range of SOC.

This parameter extraction method consists of constant current pulses, with periods of rest in between. A depiction of the series of constant current discharging pulses is shown in plot (a) of Figure 2-8. Each pulse consists of the pulse phase, followed by a relaxation phase. The pulse is characterized by its amplitude, and duration as shown in the figure. In this work, the convention is adopted in which negative applied current discharges the cell, while positive applied current charges the cell. The parameter extraction method that will be discussed here can be applied to discharging or charging current pulses. Charging current pulses are depicted in plot (b) of Figure 2-8.

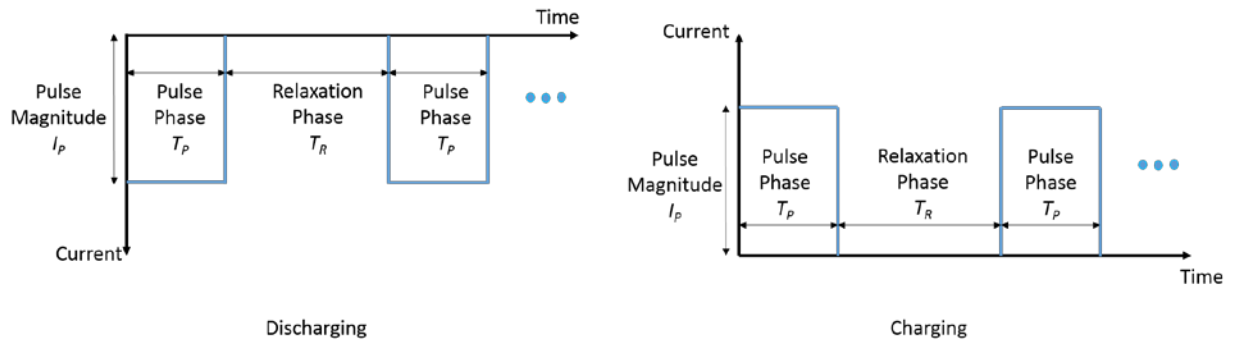


Figure 2-8. Depiction of the discharging pulses used to characterize the cell under test (left). The corresponding illustration of charging pulses used to characterize the cell under test is shown on the right.

Figure 1-12, which is reproduced in Figure 2-9 below, is a plot of the voltage response of a commercial lithium ion cell (data from experiments discussed in Chapter 3) to a discharging pulse. At the beginning of the pulse phase with pulse current magnitude I_P , the cell voltage first

drops by a value that is proportional to the internal resistance R_S , and is described in the model by $I_P R_S$. Then at short times, the cell voltage falls according to $t^{1/2}$, as will be shown in equation [2-25] later in this section. As time proceeds, the cell voltage decline slows down. Analytical expressions for the cell voltage evolution, discussed later in this section (equations [2-27]), are fit to the measured response to extract further model parameters. After the pulse phase concludes, the relaxation phase commences when the applied current falls to zero. The cell voltage rises instantaneously by a value of $I_P R_S$. As time proceeds, the cell voltage rises rapidly at first, and then relaxes to a steady state. Subsequently, the next pulse is applied and the above repeats.

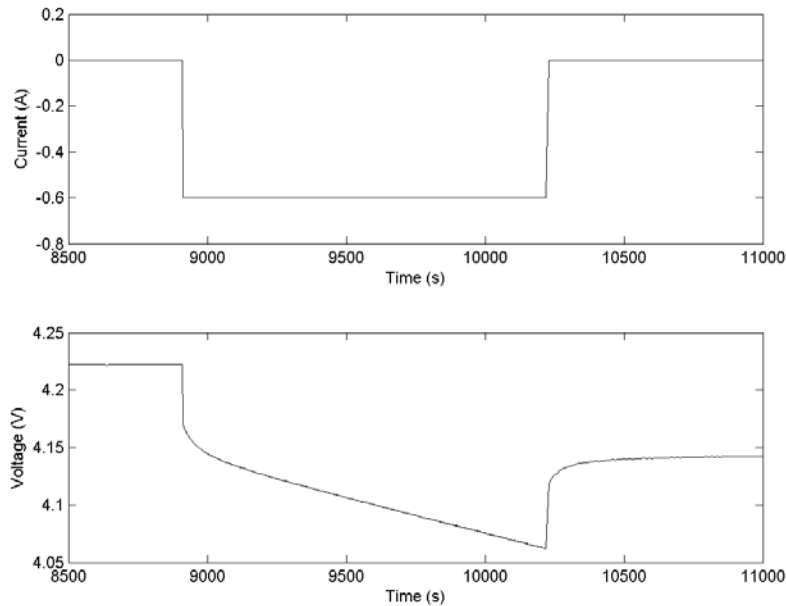


Figure 2-9. Illustration of the voltage response from a discharge current pulse.

If a charging current pulse is applied, the voltage response is inverted compared to that described above. An example is shown in Figure 2-10. This data is extracted from experiments and cells

described in Chapter 3. During the pulse phase, the cell voltage first rises by a value of $I_P R_S$. At short times, the cell voltage rises according to $t^{1/2}$, as will be shown in equation [2-25] later in this section. This is followed by a slowing voltage rise. When the applied charging current is removed during the relaxation phase, the cell voltage falls instantaneously by a value of $I_P R_S$. The cell voltage then falls rapidly at first, and then relaxes to a steady state.

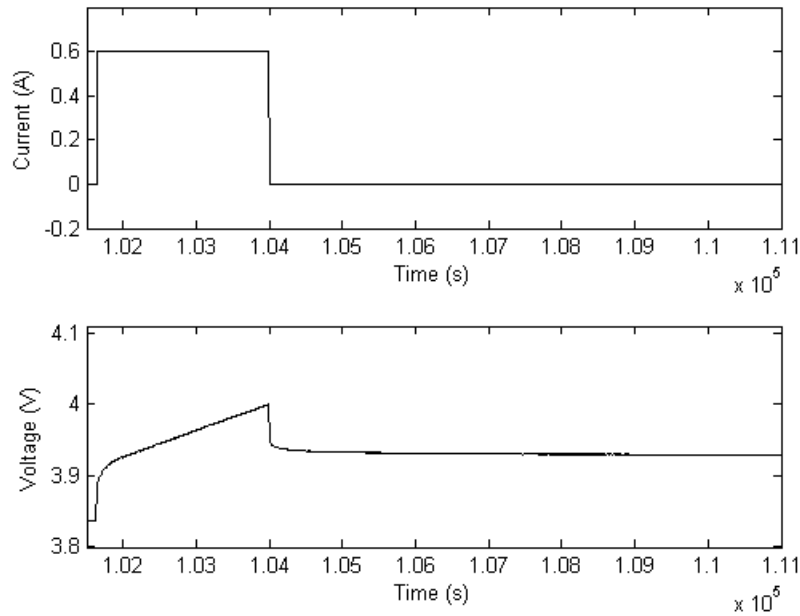


Figure 2-10. Typical voltage response (bottom) to an applied charging current pulse. The current profile is shown in the top plot.

Each pulse begins with a cell that is at a known SOC at equilibrium (for example 1.0, *i.e.* fully charged). The initial cell SOC is SOC_i and the corresponding OCV is $V_{OC,i}$. A current pulse of pre-determined magnitude I_P , and duration T_P , is applied, which changes the charge stored in the cell by ΔQ and shifts the cell to the final SOC, SOC_f . The current pulse is followed by a relaxation phase of period T_R , which allows the cell to relax to a new steady state with final

open-circuit voltage $V_{OC,f}$. In this way, the four variables SOC_i , SOC_f , $V_{OC,i}$, and $V_{OC,f}$, are all known for this applied current pulse. By performing a number of such current pulses that shift the cell SOC through its full range of intended operation, the dependence of the open-circuit voltage V_{OC} on SOC is obtained.

Further analyzing the measured cell voltage during the pulse described above, the model parameters R_S and R_D at cell SOC_i can be extracted. For the current pulse, the model parameters R_S , R_D and C_D in Figure 2-4 are assumed to be constant between SOC_i and SOC_f . The diffusion capacitance C_D of the entire cell in each small range of SOC is estimated as

$$C_D = \frac{\Delta Q}{(V_{OC,f} - V_{OC,i})}. \quad [2-19]$$

The estimation of R_S and R_D requires solution of the set of equations [2-16] to [2-18]. From Carslaw and Jaeger [70], $V(\alpha, t)$, which is the voltage at a dimensionless length, α , along the RC transmission line portion of the model (Figure 2-4) in response to a step in current I_P can be written as

$$V(\alpha, t) = V_{OC,i} + 2I_P R_T (t/\tau)^{1/2} \sum_{n=0}^{\infty} \left\{ ierfc \left(\frac{(2n+1) - \alpha}{2(t/\tau)^{1/2}} \right) + ierfc \left(\frac{(2n+1) + \alpha}{2(t/\tau)^{1/2}} \right) \right\} \quad [2-20]$$

where $ierfc(x)$ is related to the error function $erf(x)$ by

$$ierfc(x) = \frac{1}{\sqrt{\pi}} \exp(-x^2) - x[1 - \operatorname{erf}(x)]. \quad [2-21]$$

Here α is the dimensionless position ($0 \leq \alpha \leq 1$), t is time, and τ is the time-constant of the transmission line given by equation [2-15]. The summation applies to a finite transmission line,

but at short times the higher terms in n are small. This is taken advantage of in the parameter estimation procedure, as is now described. The cell terminal voltage V_C is given by

$$V_C = V(1, t) + I_P R_S. \quad [2-22]$$

The transmission line voltage $V(\alpha, t)$ at $\alpha = 1$ is of interest since this is the potential across the cell, not including any drop across R_S . $V(1, t)$ is given by

$$V(1, t) = V_{OC,i} + 2I_P R_D (t/\tau)^{1/2} \sum_{n=0}^{\infty} \left\{ ierfc\left(\frac{2n}{2(t/\tau)^{1/2}}\right) + ierfc\left(\frac{2n+2}{2(t/\tau)^{1/2}}\right) \right\} \quad [2-23]$$

This equation's short-time solution, i.e. $t \rightarrow 0$, can be simplified by making use of the rapid decay of $ierfc(x)$ as x increases. Therefore, the term in the summation in equation [2-23] can be approximated by

$$\sum_{n=0}^{\infty} \left\{ ierfc\left(\frac{2n}{2(t/\tau)^{1/2}}\right) + ierfc\left(\frac{2n+2}{2(t/\tau)^{1/2}}\right) \right\} \approx ierfc(0) = \frac{1}{\sqrt{\pi}} \quad [2-24]$$

Then the short-time solution of equation [2-23] becomes

$$V(1, t) = V_{OC,i} + 2I_P R_D \sqrt{\frac{t}{\pi\tau}}. \quad [2-25]$$

Substituting the transmission line time constant, $\tau = R_D C_D$, gives

$$V(1, t) = V_{OC,i} + 2I_P \sqrt{\frac{R_D t}{\pi C_D}}. \quad [2-26]$$

The measured cell terminal voltage V_C can be obtained by substituting Equation [2-26] into Equation [2-22], giving

$$V_C = V_{OC,i} + 2I_P \sqrt{\frac{R_D t}{\pi C_D}} + I_P R_S. \quad [2-27]$$

By measuring the cell voltage V_C , the only unknown left in equation [2-27] is the ratio R_D/C_D . C_D is already estimated in equation [2-19], so equation [2-27] gives a way to estimate R_D . At short-time, the recorded cell voltage can be fit to the function

$$V_C(t) = M_0\sqrt{t} + M_1, \quad [2-28]$$

to obtain fitting parameter M_0 and M_1 . From equation [2-27], R_D can then be estimated by

$$R_D = (M_0/2I)^2\pi C_D. \quad [2-29]$$

By recording the short time response of the cell voltage at the beginning of the current pulse, diffusion resistance R_D is obtained.

Further, series resistance R_S can be estimated as follows. By letting the instant the current pulse is applied be $t=0$, then the cell terminal voltage V_C at $t=0$ is given by

$$V_C(0) = M_1, \quad [2-30]$$

Since $M_1 = V_{OC,i} + I_P R_S$ from comparing equations [2-27] to [2-28], the series resistance R_S is given by

$$R_S = \frac{M_1 - V_{OC,i}}{I_P}. \quad [2-31]$$

In this model, the voltage drop from the current pulse is composed of two parts: 1. the voltage drop due to R_S , and 2. the voltage drop of the transmission line. $M_1 - V_{OC,i}$ is an estimate of the voltage drop at the instant the current pulse is applied, which is used to extract R_S . At this initial point the transmission line is shorted by its capacitors. Using the approach described in the above, V_{OC} , C_D , R_D , and R_S of the model can be extracted at each SOC point. This approach is expected to work providing the underlying physical model is correct – namely that a diffusion process and series resistance are dominating the impedance, that the current pulses used in the

extraction process are short compared to the diffusion time constant, and that the amount of charge transferred in the current pulse is sufficiently small to ensure that the cell remains in the linear region of response.

A typical cell voltage response during the pulse phase of a discharge current pulse is shown in Figure 2-11. The experimental data, shown as circles in this plot, is obtained from a commercial lithium-ion cell tested as described in Chapter 3. The applied current (top) and measured voltage (bottom) are shown as blue circles in the plots. The first data point is included to illustrate the cell voltage just prior to the application of the pulse. It shows the relaxed voltage from the previous pulse, so this is the open-circuit voltage V_{OC} at the initial SOC. The pulse phase begins at $t=0$, and the discharge current pulse is applied. There is a pronounced downwards shift in the cell voltage after this instant. This is due to the $I_p R_s$ drop, which occurs instantaneously as current is applied. The fit to equation [2-27], which predicts that the cell voltage evolves proportional to $t^{1/2}$, is shown as the solid line in the figure. This fit matches the experimental data well. This $t^{1/2}$ dependence is extrapolated backwards in time to $t=0$, to estimate the transmission line voltage $V(a=I, t=0)$, to obtain series resistance R_s from equation [2-31]. The use of just the initial nine seconds of the cell voltage response for the above parameter extraction enables the assumption that the cell model parameters are constant to be readily achieved. In other words, the parameters R_s , R_D , and C_D are assumed constant for this initial nine seconds over which the data is analyzed.

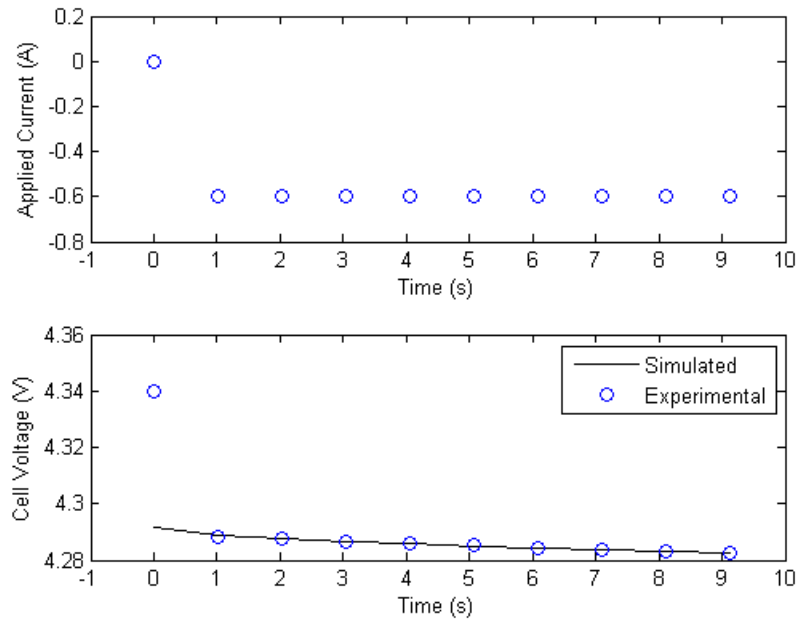


Figure 2-11. Representative short time response of a commercial lithium ion cell to a current pulse. The data is from experiments discussed in Chapter 3.

The cell voltage response beyond these initial seconds of the pulse can be predicted from the model using equation [2-23]. The applied discharge current (top) and measured cell voltage (bottom) are shown in Figure 2-12. Use of this equation assumes the model parameters are constant. The calculated response, shown as the solid line, is compared to the measured cell voltage response, shown as the dashed line, in the bottom plot of Figure 2-12. As this figure shows, the calculated and measured responses match well at the beginning, but deviate somewhat as time proceeds. This can be attributed to the appreciable change in cell SOC as the current continues to be applied during the pulse phase. This causes changes in the cell properties that are dependent on cell SOC. As discussed in Section 2.1, the distributed SOC model developed in this thesis work is made non-linear to account for such changes of the model parameters as a function of cell SOC.

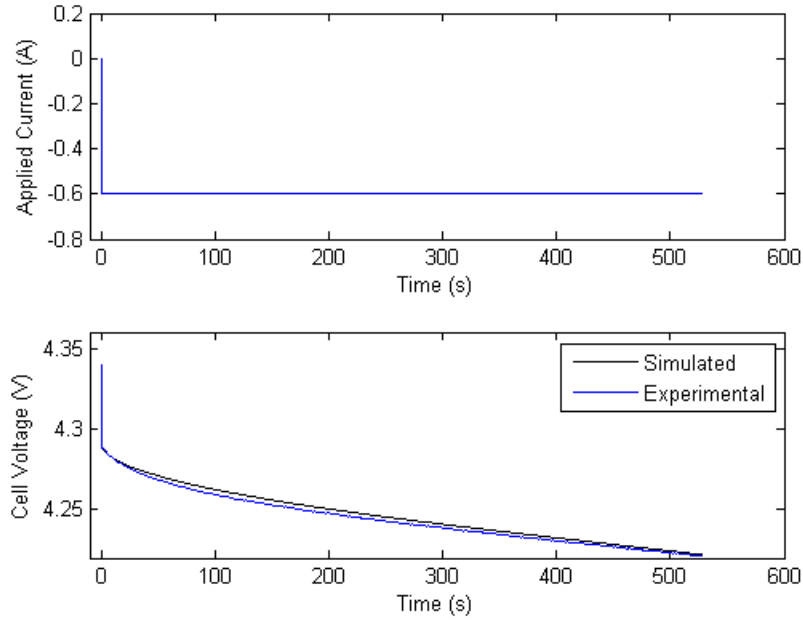


Figure 2-12. Representative long time response of a commercial lithium ion cell to a current pulse. The data is from experiments discussed in Chapter 3.

The uncertainty of the fit to the model parameters can be examined as follows. In Figure 2-13, the experimental (shown as circles) and simulated (shown as the black line) response from Figure 2-11 are compared to the simulated response for 10% changes in any of the three model parameters R_S , R_D , and C_D . As shown in the figure, changes in R_S affects the fit most significantly, as it shifts the response vertically by $R_S \cdot I_P$. Increasing C_D by 10% lowers the slope throughout the simulated response by a factor of $(1.1)^{0.5} \approx 1.05$, according to Equation [2-27]. From the same equation, increasing R_D by 10% increases the slope of the simulated response by a factor of $(1.1)^{0.5} \approx 1.05$. As the match between the experimental data and calculated response does not appear to be significantly affected by 10% changes in R_D and C_D , it can be concluded

that the uncertainties of the extracted model parameters R_D and C_D can be estimated to be on the order of $\pm 10\%$.

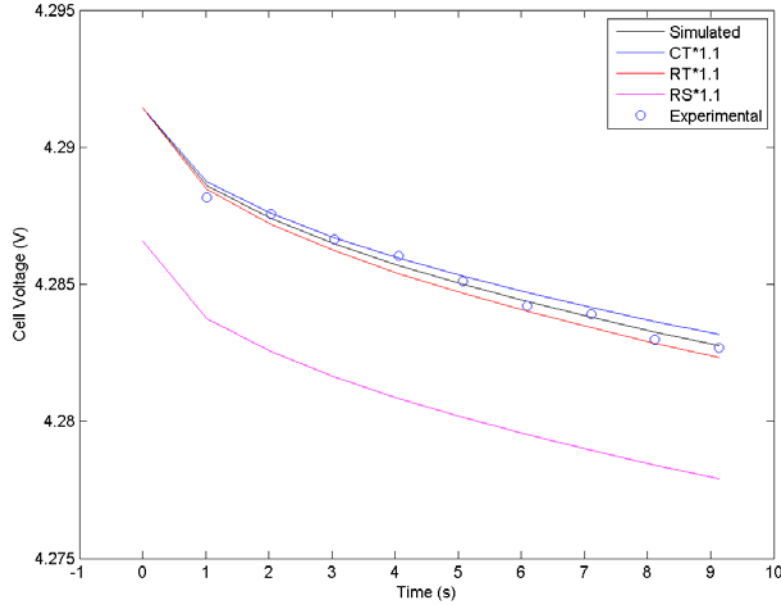


Figure 2-13. Effects of changes in model parameter on the resulting predicted cell voltage response. The data is from experiments, discussed in Chapter 3, on a commercial lithium ion cell.

Using the above extraction procedure, V_{OC} , C_D , R_D , and R_S are obtained by fitting the measured cell voltage response to each applied current pulse. Two examples of pulse responses and their fits to Equation [2-27] are shown later in Figure 2-16 and Figure 2-17. By performing a series of these current pulses, the dependence of these parameters on SOC can be estimated for the full SOC range. The cell model parameters of the distributed SOC model and their extraction functions are listed in Table 2-2. This same procedure is used again in Chapter 3 to perform a more thorough extraction.

Cell Model Parameter	Extraction Method	
Full Capacity Equivalent Capacitance C_{FCE}	Discharge fully charged cell at low C-rate until rated minimum cell voltage is reached	
Open-Circuit Voltage $V_{OC}(SOC)$	Measure relaxation voltage after each current pulse	
Diffusion Capacitance $C_D(SOC)$	$C_D = \frac{\Delta Q}{(OCV_f - OCV_i)}$	Equation [2-19]
Diffusion Resistance $R_D(SOC)$	$R_D = (M_0/2I)^2 \pi C_D$	Equation [2-29]
Series Resistance $R_S(SOC)$	$R_S = \frac{M_1 - OCV_i}{I}$	Equation [2-31]

Table 2-2. List of model parameters of the distributed SOC equivalent-circuit model and their corresponding extraction equations.

2.3.2 Experimental Method

As mentioned in the introduction to this chapter, this initial study of the distributed SOC model is applied at a single current of 15 A to the Dow Kokam lithium-ion polymer cell to simplify the experiments and subsequent analysis. 15 A is chosen as this is the standard discharge rate according to this cell's product specifications. At this current, the cell is expected to exhibit favorable characteristics such as minimal temperature rise, and long cycle life. In the next chapter, the treatment of parameter extraction and validation at multiple charge and discharge currents to a commercial cylindrical lithium ion cell is presented.

First, the full-capacity-equivalent capacitance C_{FCE} needs to be obtained. Also, for design of the parameter extracting experiments, an approximation of the dependence of the open circuit voltage on SOC (V_{OC} in the model in Figure 2-5) is needed. Using the setup described in Section 2.2, the Dow Kokam cell is tested according to the procedure shown below in Table 2-3. Steps 1 to 2 in the table forms the initialization phase of the test, which brings the cell to a repeatable starting SOC, and assigned an SOC value of 1.0. In the rest of this chapter, the cell undergoes this initialization phase to first obtain a fully charged cell for subsequent experiments. The discharge test data is obtained at step 3. The measured full capacity of the cell is 71.7 Ah, which gives a C_{FCE} of 2.6×10^5 F ($71.7 \text{ Ah} \times 3,600 \text{ C/Ah} = 2.6 \times 10^5 \text{ C}$) for use in the model. This value of C_{FCE} results in a value of 1.0 V across this capacitor when the cell is fully charged.

Phase	Step	Description
I. Initialization	1	Charge at 0.2 C (15 A) until the cell voltage reaches 4.20 V
	2	Rest for 1 hour
II. Constant Current Discharge	3	Discharge at 0.04 C (3.0 A) until cell voltage falls below 3.0 V

Table 2-3. Test Procedure for estimating the open-circuit voltage V_{OC} dependence on SOC, $V_{OC}(\text{SOC})$.

The initialization procedure used for the experiments in this chapter consists of steps 1 and 2 described in Table 2-3. It was found subsequent to the completion of the experiments described in this chapter that the recommended charging procedure for this cell according to its specifications contains an additional step (after step 1) that holds the cell at the maximum voltage of 4.20 V until the charging current falls below 3.75 A (or 0.050 C). This additional step charges the cell more fully by enabling the active material particles inside the cell to charge fully throughout their bulk. This explains why the measured full capacity (71.7 Ah) of the cell is

lower than its listed nominal capacity (75 Ah). Although the procedure described in Table 2-3 does not charge the cell to its maximum possible charge state, it is important to note that the initialization procedure described here still sets the cell to a reproducible starting SOC. This is assigned a SOC of 1.0, as this is the maximum SOC encountered in these experiments. The work described here remains useful as part of the initial study of the model performance at the single current tested. Also, there are some applications, such as in emergency lighting and satellites, that do not fully charge the cell [71], because this has been found to enhance cycle life of the cell [71]–[74]. The improved cycle life can be attributed to the reduced rate of side reactions [72]–[74] (due to the lower oxidative and higher reductive potentials of the positive and negative electrodes) and reduced lithium plating [75]. This is consistent with the understanding that one of the key capacity degradation mechanisms for lithium ion cells is the loss of lithium inventory (also called cyclable lithium) in the cell [76]–[81]. In the next chapter, the tests on the cylindrical lithium ion cell includes the described constant voltage step to ensure the maximum capacity of the cell is obtained and the full range of states of charge of the tested cells are characterized.

For this Dow Kokam lithium-ion polymer cell, the 3.0 A (0.040C) discharge current is considered a slow rate discharge that allows a good estimation of the open circuit voltage dependence on the cell SOC. This is because the low rate induces a low IR_s drop, and small disturbance of the cell from equilibrium. The 3.0 A discharge results are shown in Figure 2-14. The cell starts from the fully charged state (SOC = 1.0), which is represented at the most upper right end of the curve. As discharge proceeds, both the SOC and cell voltage decreases. From this figure, it can be seen that the voltage response is highly nonlinear, with the voltage

decreasing rapidly at high SOC. At the mid-range of SOC (close to 0.50), the slope of the voltage curve is the smallest. The cell voltage decreases most rapidly at low SOC. This change in slope during discharging is readily described by ascribing a non-linear capacitance to the battery. Based on the discharging curve, this capacitance is higher near 0.50 SOC (smallest slope), and drops near the ends of the potential range (as indicated by higher slopes at the ends).

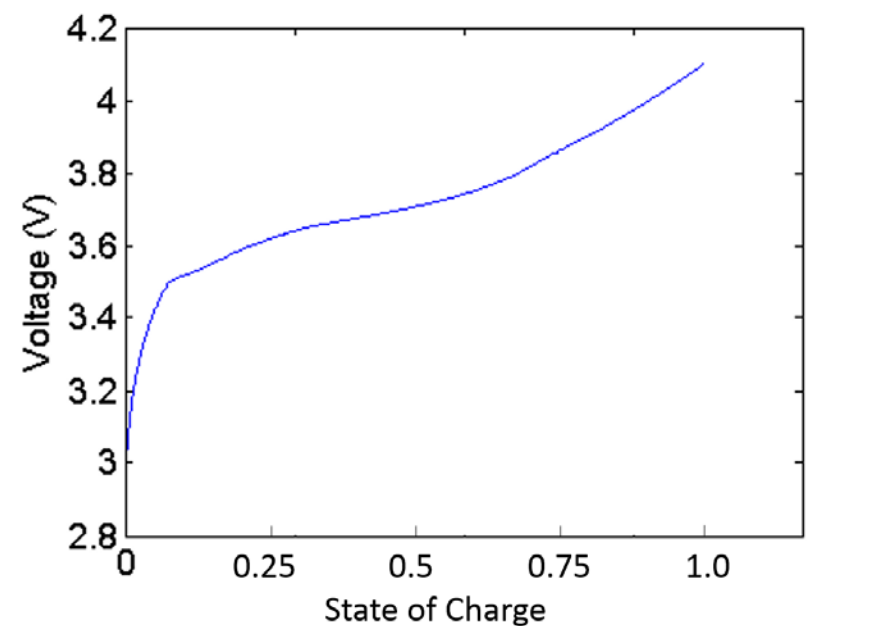


Figure 2-14. Cell voltage measured during 3.0 A discharge from SOC of 1.0. During discharge, the cell SOC decreases. The slope of the measured cell voltage is highest at SOC of *ca.* 0.5, indicating that the effective capacitance at that SOC is highest.

The characterization test used to obtain the model parameters in this chapter consists of a series of thirty-six discharge pulses, each of 15 A magnitude. Using the initialization phase procedure in Table 2-3, the cell was assumed to have reached its fully charged state (SOC = 1.0) before the current pulses. The pulse durations were set as tabulated in Table 2-4. The rest time between

pulses is one hour, as it is found to be sufficient for the cell voltage to approach equilibrium (< 0.6 mV change in cell voltage per 10 minutes afterwards). The SOC range from 0.0 to 1.0 was divided into 4 sections. The choice of pulse duration corresponded to the inverse of the dependence of cell voltage on SOC. If the voltage changed rapidly with change in SOC, the current pulse duration was chosen to be short, and vice versa. The cell's discharge cutoff voltage was set at 3.0 V, because there is negligible capacity below this cell voltage.

Pulse Number	Duration (minutes)
1 to 14	5
15 to 26	12
27 to 28	5
29 to 36	2.5

Table 2-4. Durations of pulses in the discharge pulse experiment used for model parameter extraction.

2.3.3 Results and Analysis

The cell voltage measured during the pulsed current parameter extraction experiment is shown in Figure 2-15. The cell voltage response to each pulse behaves according to that described earlier in Section 2.3.1. At the instant the current is applied (beginning of pulse phase), the cell voltage drops by a value of $I_P R_S$ ($I_P = 15$ A) due to the series resistance. Then, the cell voltage falls rapidly initially according to $t^{1/2}$ as expected from Equation [2-27]. As time proceeds, the cell voltage decline slows down. When the current is stopped (beginning of relaxation phase), the cell voltage rises instantaneously by a value of $I_P R_S$. Then, at short times, the cell voltage rises rapidly. This is followed by the relaxation of the cell to a steady state.

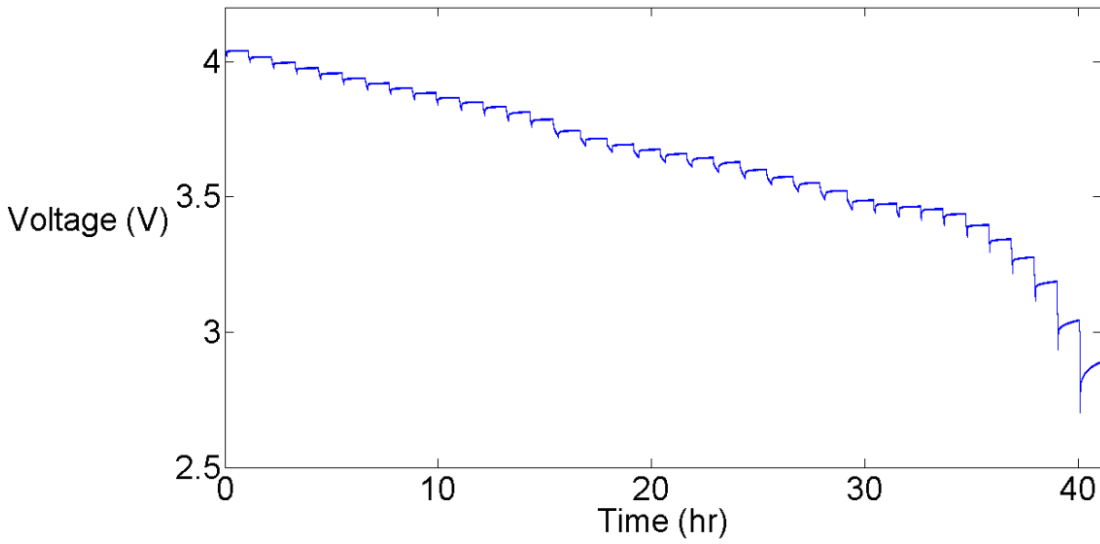


Figure 2-15. Measured cell voltage during the pulsed current parameter extraction experiment using 15 A pulses.

To extract the model parameters, the measured voltage response is fitted to the first-order equation in $t^{1/2}$ of equation [2-28]. In the majority of fits, there is a good match between the fit and the measured cell voltage response. For example, Figure 2-16 and Figure 2-17 shows the results for pulses 1 and 2, respectively. This shows the suitability of the transmission line model to approximate the Warburg element in the proposed model.

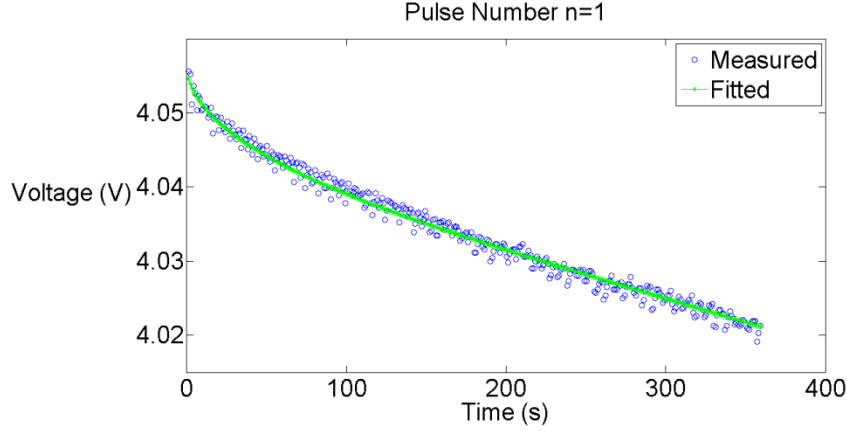


Figure 2-16. Comparison of the extracted fit and the cell voltage response to the first current pulse of the pulsed current parameter extraction experiment.

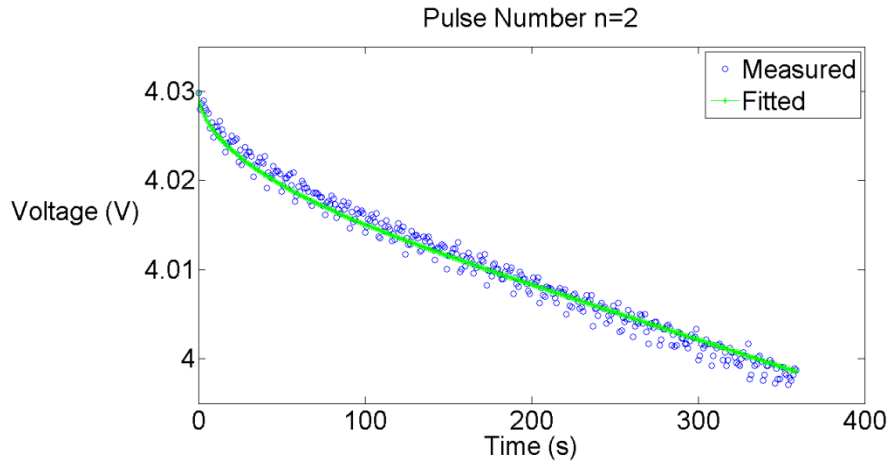


Figure 2-17. Comparison of the extracted fit and the cell voltage response to the second current pulse of the pulsed current parameter extraction experiment.

However, for the pulses 32 to 36 in the characterization experiment, the fit is not convincing.

This corresponds to a cell OCV below 3.3 V. An example is pulse 36, which is shown in Figure 2-18. This poor fit can be attributed to the rapid decrease in cell diffusion capacitance C_D at low SOC. At low SOC, the steep decline in voltage in Figure 2-14 means that the capacitance is low because, according to Equation [2-19], the diffusion capacitance C_D is inversely proportional

to the change in open circuit voltage ($V_{OC,f} - V_{OC,i}$) for each unit change in charge. The rapid change in diffusion capacitance C_D violates the assumption that the transmission line circuit parameters are constant, which is used to derive the extraction equations [2-19], [2-29], and [2-31]. During pulse discharge, a declining capacitance causes the cell voltage to fall more rapidly than the theoretical $t^{1/2}$ expectation of Equation [2-27]. As the fit between theoretical and experimental response is poor, the prediction accuracy of the model at this low SOC region is expected also to be poor. In the next chapter, where the case of multiple charge and discharge currents are treated, the pulses are designed so that more pulses are tested at low SOC, so that the model parameters there can be examined more closely.

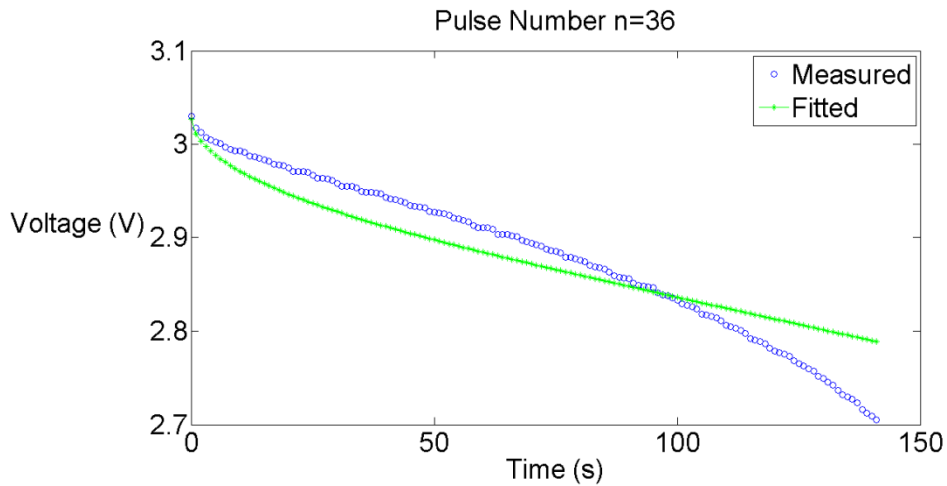


Figure 2-18. Comparison of the extracted fit and the cell voltage response to the 36th current pulse of the pulsed current parameter extraction experiment.

As described in Section 2.3.1, the model parameters C_D , R_D , and R_S are extracted for each pulse according to Equations [2-19], [2-29], and [2-31], respectively. By performing this extraction for the full series of pulses, the model parameters' dependence on SOC is measured. The

extracted diffusion capacitance C_D is shown in Figure 2-19. From this plot, there appears to be pronounced C_D peaks at states of charge of *ca.* 0.10, 0.25, and 0.45. Since diffusion capacitance C_D is given as the ratio of the charge of the applied pulse to the resulting change in the OCV according to Equation [2-19], peaks in C_D occurs when the induced OCV of the cell from the applied current pulse is small. A technique known as differential capacity analysis has been shown in works by Bloom *et. al.* [82], [83] and Smith *et. al.* [84] to measure a differential capacity of their cells. This technique uses a continuous discharge current to measure the differential capacity as a function of cell voltage. Therefore, the measured differential capacity has a similar physical meaning to the C_D in this work. It is shown that the differential capacity analysis technique measures the differential capacity continuously as a function of cell voltage, and that the individual peaks in the differential capacity can be traced to either the positive or negative electrode. It is pointed out by Bloom *et. al.* [82], [83] that the peaks in differential capacity is represented by quasi-phase equilibria in the positive or negative electrode. As mentioned in Section 2.2, the tested Dow Kokam cell in this work consists of a Nickel-Manganese-Cobalt-Oxide (NMC) positive electrode, and a carbon-based negative electrode. Therefore, the peaks in the diffusion capacitance C_D can also be related to the phase equilibria of the reactions in the positive electrode material (transition metal ions $\text{Ni}^{2+}/\text{Ni}^{3+}$, $\text{Mn}^{2+}/\text{Mn}^{3+}$, and $\text{Co}^{2+}/\text{Co}^{3+}$), and negative electrode material (intercalation of lithium-ions at different stages in the carbon negative electrode) [85]–[87]. Precise determination of the origin of the diffusion capacitance peaks will need to be determined using techniques such as differential capacity analysis [82]–[84].

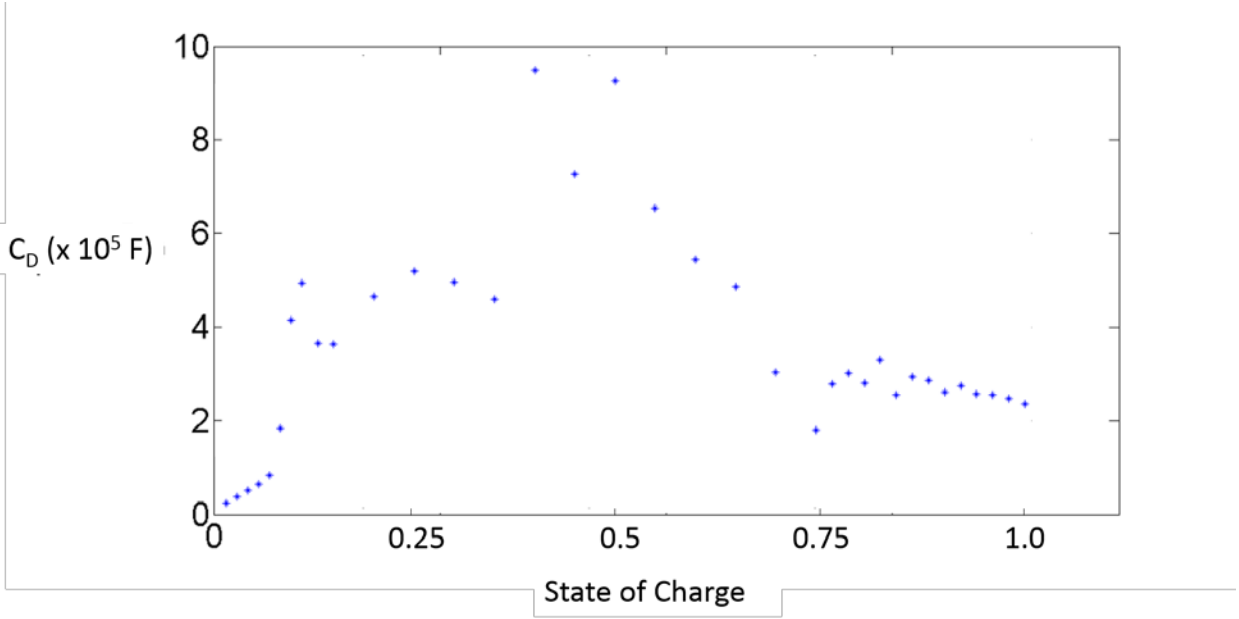


Figure 2-19. Extracted diffusion capacitance C_D as a function of SOC.

The extracted diffusion resistance R_D as a function of SOC is shown in Figure 2-20. There are small peaks in R_D at states of charge of *ca.* 0.1, 0.45 and 0.8. Additionally, the diffusion resistance appears to increase at very low SOC. Physically, this parameter is interpreted as a diffusion resistance that determines the rate of transport of ions inside the cell's electrodes. A lower diffusion resistance results in a faster equilibration along the depth of the transmission line. The variation in the diffusion resistance as a function of cell SOC can be attributed to the differences in diffusion coefficients in the electrodes as they evolve amongst various phases during the charge and discharge process [85]–[87].

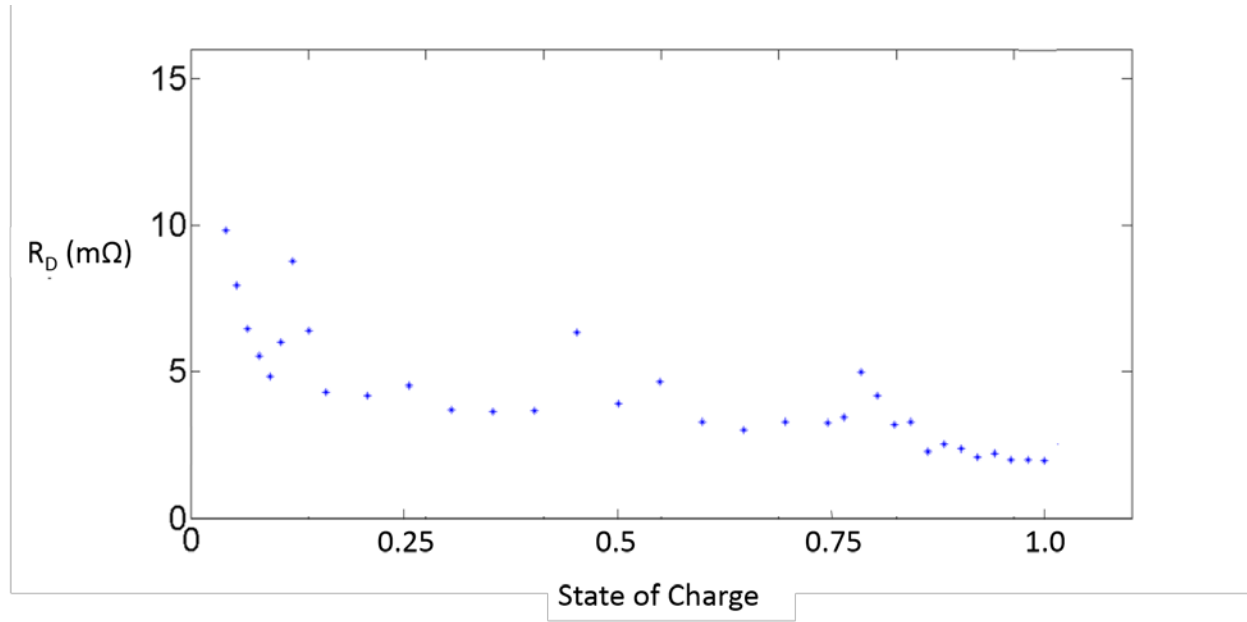


Figure 2-20. Extracted diffusion resistance R_D as a function of SOC.

The extracted series resistance R_S is plotted as a function of SOC in Figure 2-21. The R_S parameter shows a slight downward trend towards high SOC. This is consistent with the findings in a number of works in the literature [2], [27], [48], [57], [60], [88], [89]. A possible reason for this decreasing series resistance at increasing SOC is that the total volume of the positive and negative electrodes increase at increasing SOC. This is shown previously by Wang *et. al.* [90]. Since the volume of the Dow Kokam cell is confined by the cell encapsulation, the contact between the particles of the electrodes can be enhanced at increasing SOC, thereby decreasing the measured series resistance R_S .

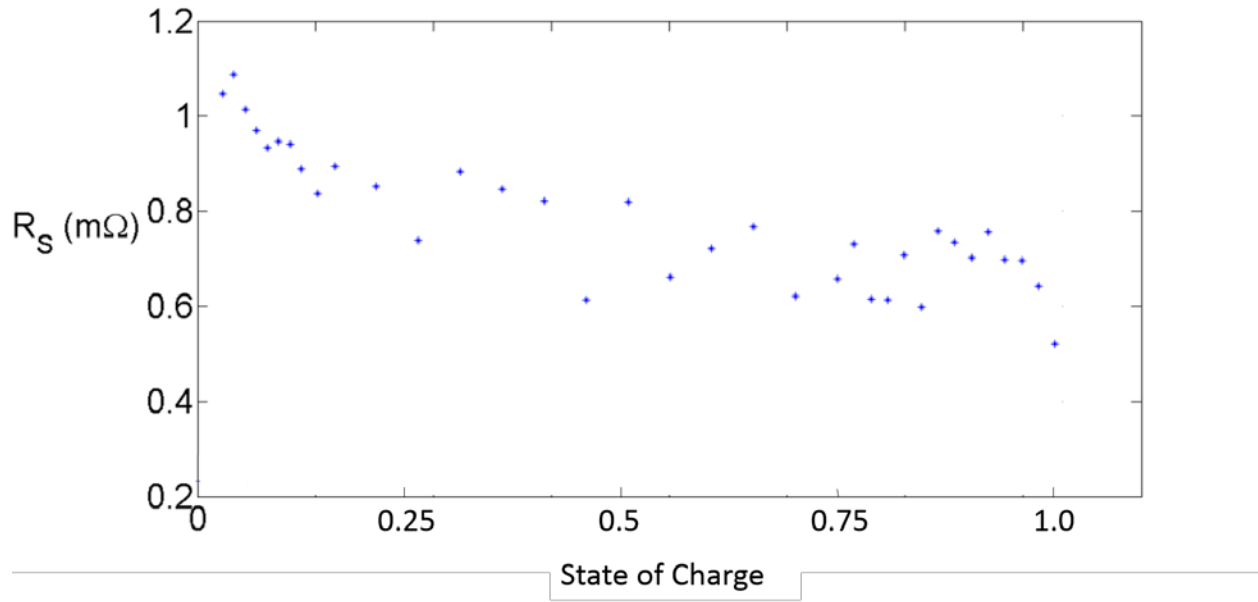


Figure 2-21. Extracted series resistance R_s as a function of SOC.

In this way, the use of pulsed discharging experiments can be used to extract the parameters of the distributed SOC model for use in simulation of the cell behavior. These extracted values are used in the equivalent circuit model to formulate a nonlinear equivalent circuit that can simulate the response of the cell. This is demonstrated in the next section. The work in this chapter is restricted to only charge and discharge currents of 15 A, as part of an initial study of this model. In the next chapter, the case of multiple charge and discharge currents is examined.

2.4 Validation

The model developed in Section 2.1 and the parameter extraction method presented in Section 2.3 can be validated by performing experiments and comparing results to simulation predictions.

In this chapter validation tests involve 15 A pulses. Chapter 3 extends the results to multiple charge and discharge currents.

In Section 2.4.1, the adaptation of the distributed SOC model to use in MATLAB® Simulink® is discussed. Section 2.4.2 presents validation testing of the Dow Kokam cell, and the results are compared to the simulated response.

2.4.1 Simulation Model

The circuit model shown in Figure 2-5 consists of an infinite number of RC-segments, each containing infinitesimal elements. To implement this circuit model in simulation packages such as MATLAB® Simulink®, the use of a finite number of RC-segments is required. In this chapter, the use of 1 to 32 RC-segments are investigated. In the literature, runtime models that contain RC networks typically employ 1 or 2 RC-segments.

To create a lumped equivalent-circuit model, the $R_D \partial \alpha$ and $C_{FCE} \partial \alpha$ values in the model of Figure 2-5 are replaced with $R_D \Delta \alpha$ and $C_{FCE} \Delta \alpha$, respectively. The resulting lumped equivalent-circuit model is shown in Figure 2-22. Since the dimensionless position variable α (discussed in Section 2.1) varies between 0 and 1, $\Delta \alpha$ has the value of $1/n$ for an n-segment lumped equivalent-circuit model. The final lumped-equivalent circuit is obtained as shown in Figure 2-23.

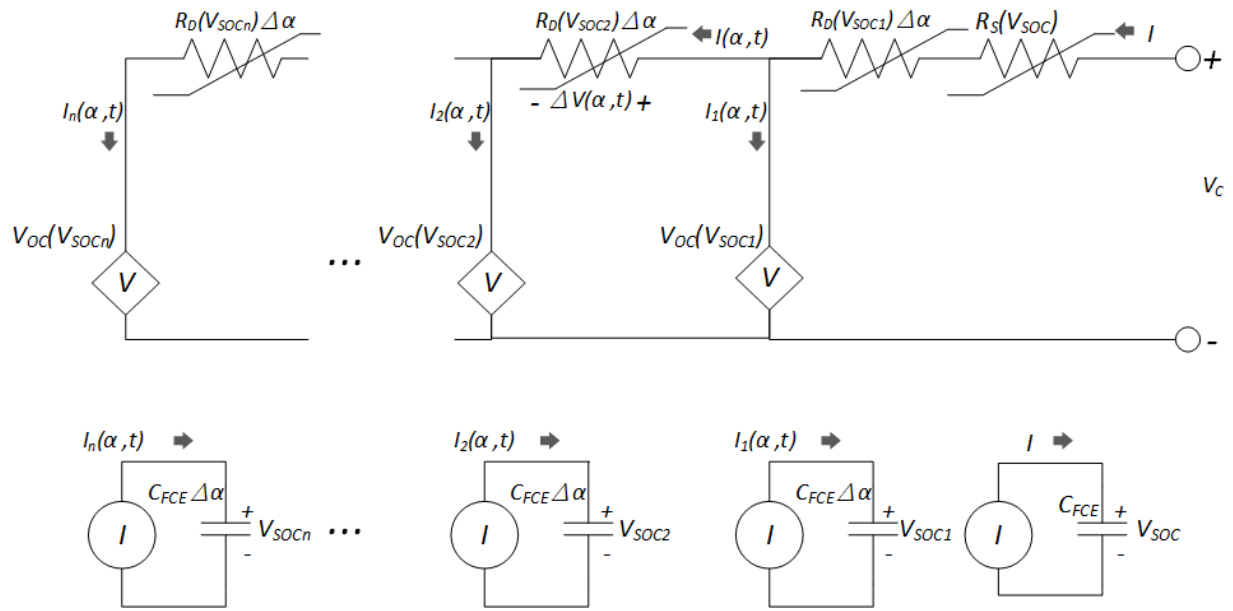


Figure 2-22. Lumped equivalent-circuit model.

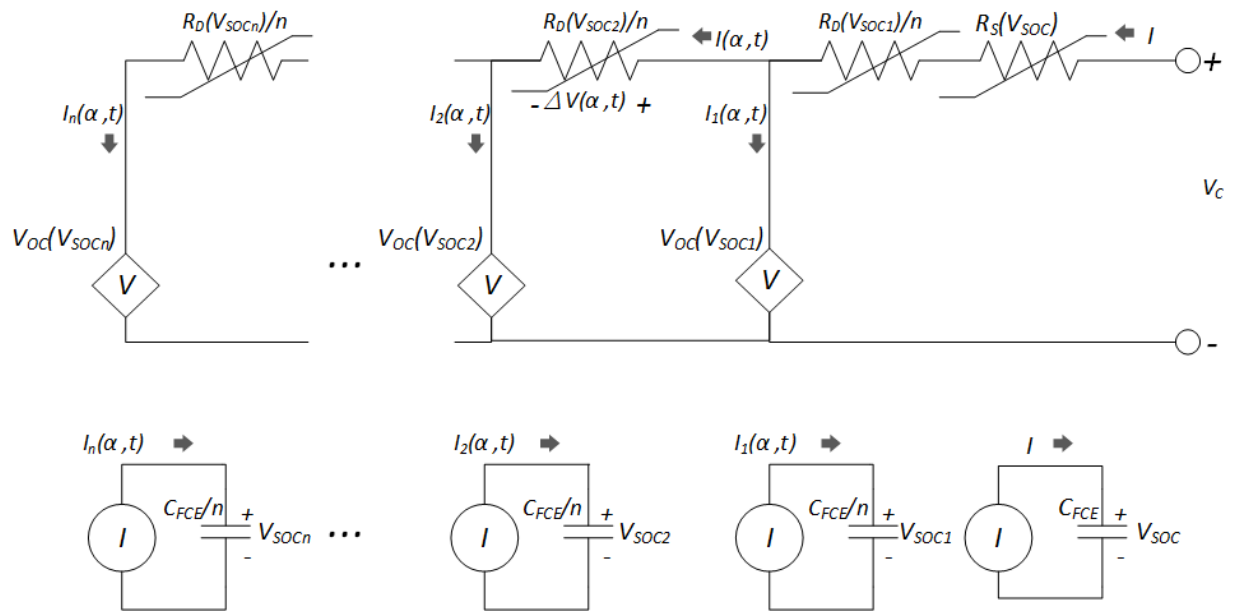


Figure 2-23. Final lumped equivalent-circuit model.

2.4.2 Validation Tests

Four validation tests were designed to test the performance of the cell model and parameter extraction method. As in the parameter extraction tests described in Section 2.3.2, the validation tests in this chapter consist of pulses of 15 A, with one hour of relaxation between pulses. One hour was found to be an appropriate plan as little further voltage relaxation (< 0.6 mV per 10 minutes) was observed in the cells at this time. Before each discharging validation test, the cell is first fully charged using the initialization procedure shown in Table 2-3. For the charging validation tests, the cell is first fully discharged at 3 A until the cell's rated minimum voltage before the validation test procedure is applied. The testing mode (charging or discharging), and pulse durations for the four validation tests are listed in Table 2-5. Validation test #1 is a constant current discharge test that discharges a fully charged cell to the lower voltage limit. Validation test #3 is a pulsed discharge test with pulse phase duration of 30 minutes. Validation tests #2 and #4 consist of pulsed charging tests with pulse phase durations of 100 minutes and 10 minutes, respectively. These four validation test profiles are chosen because they allow for quantifying the accuracy of the model in predicting the cell's runtime response to simple loads at different SOC. As mentioned earlier, this is part of an initial study to understand the performance of the model. In the next chapter, the extension of the model to a range of charging and discharging currents is investigated.

Validation Test Number	Mode	Pulse Duration (minutes)	Number of Pulses
1	Discharging	300	1
2	Charging	100	4
3	Discharging	30	14
4	Charging	10	40

Table 2-5. Pulse phase durations for the four validation experiments.

15A was chosen as the applied current because the effect from the charge transfer resistance R_{CT} , which contributes to the series resistance R_S , is expected to remain the same as that experienced for the parameter extraction tests. In order to check the model validity at other currents, extraction tests at different currents need to be performed. The effect of different applied currents is studied in Chapter 3.

The lumped distributed SOC model in Figure 2-23 is implemented in MATLAB® Simulink® using components in the SimPowerSystems package. By employing the extracted values of C_{FCE} , V_{OC} , R_D , and R_S from Section 2.3.3, the voltage response from the validation experiments are simulated and compared to the experimental results. To quantify the accuracy of the simulations, the root-mean-square-error (*RMSE*) of each applied pulse (which includes both pulse phase and relaxation phase) are calculated, defined as:

$$RMSE = \sqrt{\frac{\sum_{i=1}^n (V_{m,i} - V_{p,i})^2}{n}} \quad [2-32]$$

where n is the number of samples in each pulse, $V_{m,i}$ is the measured voltage of sample i , and $V_{p,i}$ is the predicted voltage of sample i . The summation is over all samples in each pulse.

In the following, the model predictions for each of the four validation tests is compared to the obtained experimental data.

Validation Test #1

Validation test #1 consists of a 15 A discharge from the fully charged state to the lower voltage limit of 3.0 V. The simulated results from a 4-segment version ($n=4$) of the distributed SOC model is compared to the experimental results in Figure 2-24. The RMSE for this validation experiment is 31 mV, or 0.86%. Examining the figure shows that the match between predicted and experimental response overlaps very well over the course of the discharge. The deviation between the predicted and experimental response appears in the relaxation phase after the discharge current has stopped. There are two parts to this deviation. First, in this relaxation phase, the predicted response relaxes to the equilibrium voltage much more quickly than the experimental results. This means that the diffusion resistance R_D and/or the diffusion capacitance, C_D , are mis-estimated, as the charges in the transmission line are re-distributing much quicker in the simulation than the measurements. One reason for this is that, as discussed in Section 2.3.3, the fit between the theoretical and measured response is poor for the last five pulses of the pulsed current parameter extraction experiment (*i.e.* at low SOC). As a result, the model can be expected to perform poorly in the low SOC region. Second, the predicted equilibrium voltage is offset from the measured one. This can be attributed to the cycle-to-cycle full capacity difference, and the slight changes in the initial cell SOC established by the initialization procedure. As the cell voltage drops drastically at low SOC, as shown in Figure

2-14, slight variation in full capacity and starting SOC can have an appreciable effect in the predicted cell voltage.

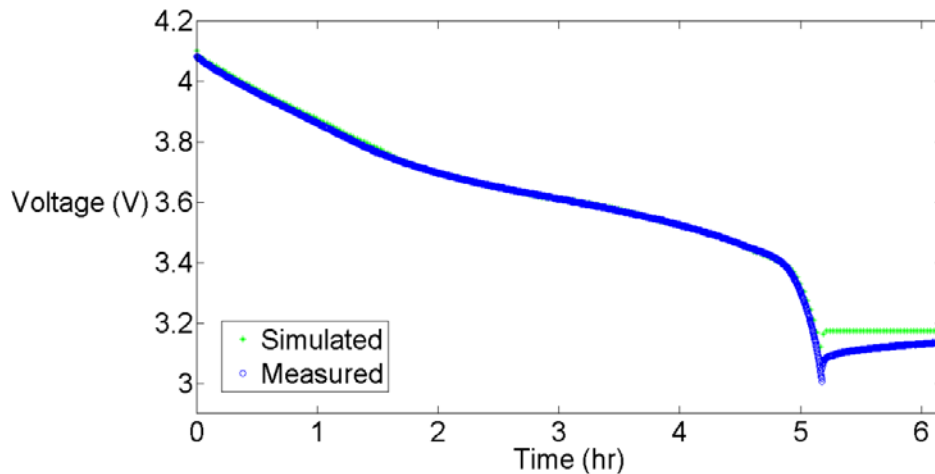


Figure 2-24. Measured and simulated voltage response of the Dow Kokam cell for validation test #1.

The simulation results presented in Figure 2-24 is calculated using a 4-RC segments transmission line to model the diffusive transport of lithium ions inside the electrode. The effect of using different number of RC elements is further investigated. As the number of RC segments is increased, the behavior of the lumped equivalent-circuit model becomes closer to the transmission line of the distributed SOC model. Therefore, increasing the number of RC segments is expected to improve the simulation results. However, as the distributed SOC model is an equivalent-circuit model that has simplified certain physics occurring inside the cell, there is expected to be a finite number of RC segments beyond which the simulation results will not improve. It is useful to identify this quantity of RC segments so that engineers can implement the fewest number of RC segments in the distributed SOC model which reduces the

implementation complexity of the model, while still obtaining near best-case simulation accuracy.

The RMSE for validation test #1 for up to 32-RC segments is shown in Table 2-6. It can be seen that, compared to the other number of segments, 1- and 2-RC segments perform significantly worse. As expected, increasing the number of RC segments reduces the RMSE. However, increasing the number of RC segments above 4 does not seem to perform appreciably better. A 4-RC segment model appears to achieve a good tradeoff.

# of RC-Segments	RMSE (mV)	RMSE (%)
1	54	1.5
2	35	0.97
4	31	0.86
8	30	0.83
16	30	0.83
32	30	0.83

Table 2-6. RMSE for different number of RC-segments for validation experiment #1.

Validation Test #2

Validation test #2 consist of four charging pulses of 15 A in magnitude. The duration of the pulse phase is 100 minutes. The simulated results from a 4-RC segment model is compared to the experimental results in Figure 2-25. The RMSE for simulation of this experiment using the 4-RC segment model is evaluated for each pulse, and the results are shown in Figure 2-26. The average RMSE for the overall test is 20 mV, or 0.54%. Even though the RMSE is lower for each pulse compared to validation test #1, the match between the experimental and predicted response

during the pulse phase in validation test #1 is better. In that test, the RMSE is influenced heavily by the large errors during the relaxation phase. From Figure 2-25, the measured response appears to be offset by a positive constant compared to the simulated response. This can be attributed to the hysteresis effect that is observed in lithium ion cells [5], [45], [91], [92]. This effect describes the dependence of the open circuit voltage on the history of the applied current to the cell. After a charging current is applied, the open circuit voltage is shifted positively when compared to the open circuit voltage after applying a discharging current. Figure 2-26 also shows the RMSE obtained between 1-RC- and 32-RC-segments in the transmission line model. As expected, increasing the number of segments increases the fidelity of the model, but there does not appear to be any significant improvement above 4-RC segments.

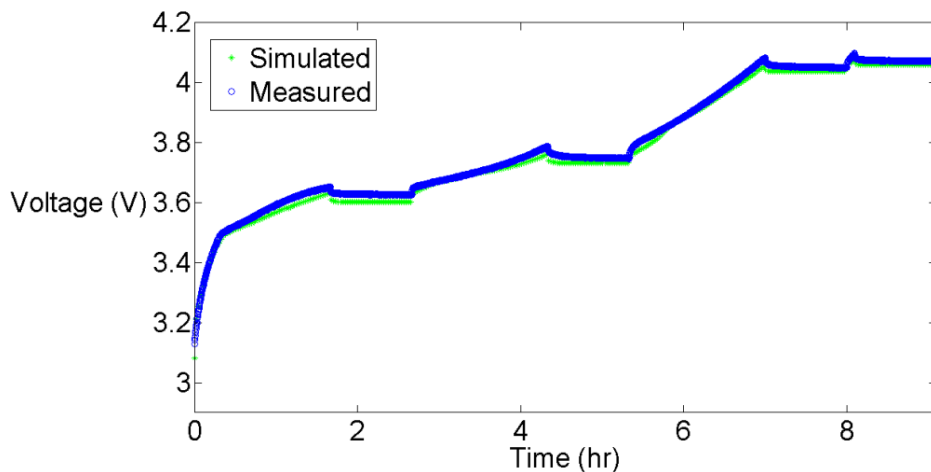


Figure 2-25. Measured and simulated voltage response of the Dow Kokam cell for validation test #2.

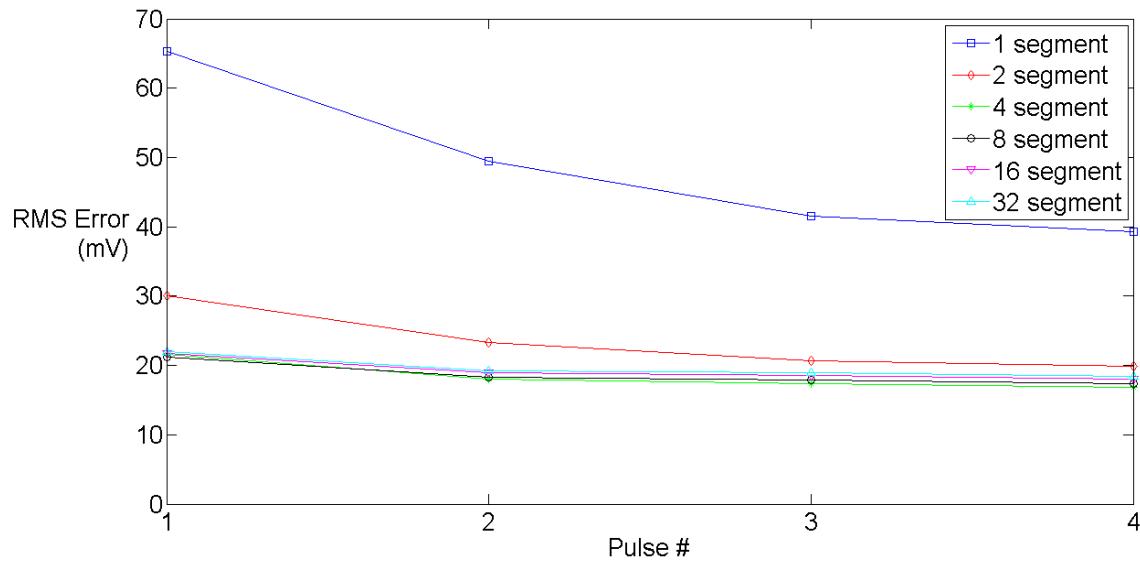


Figure 2-26. RMSE for different number of RC-segments for validation experiment #2.

Validation Test #3

Validation test #3 consists of fourteen discharge pulses, and the pulse phase duration is 30 minutes. The match between the simulated (using 4-RC segments model) and experimental results is very good, as shown in Figure 2-27. Figure 2-28 shows the RMSE of each pulse. The RMSE of all the pulses is below 13 mV, which is significantly better than the case for validation tests #1 and #2. The overall RMSE is 9.8 mV, or 0.27%. As the model parameters used in the simulation was obtained from discharge pulse characterization experiments, the hysteresis effect that affected the accuracy of predicting validation test #2 does not affect the results negatively here. Figure 2-28 shows the RMSE obtained for up to 32-RC segments. As in the cases of validation tests discussed above, the 1- and 2-RC segment models perform appreciably worse than the others. In this case, the plateau in performance appears to be obtained at 8-RC segments, above which there does not appear to be any improvements.

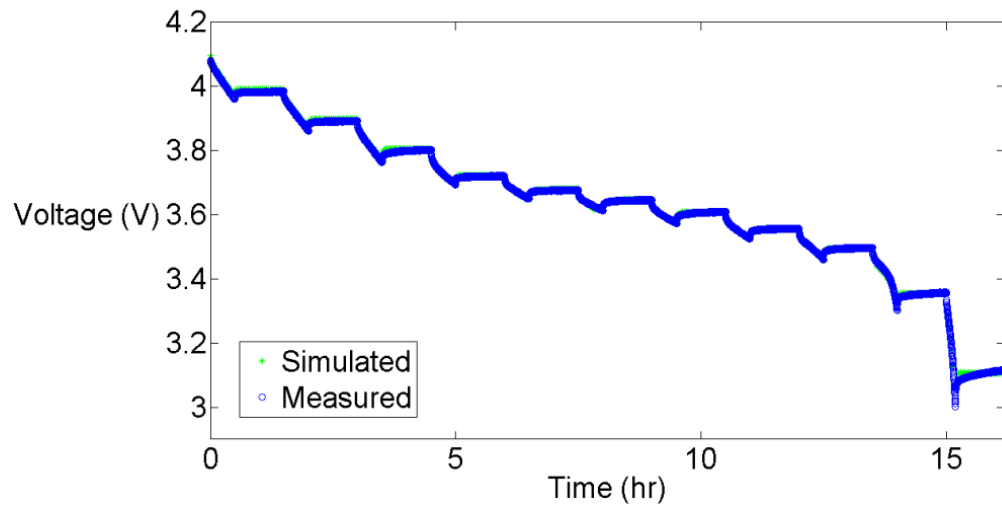


Figure 2-27. Measured and simulated voltage response for validation test #3.

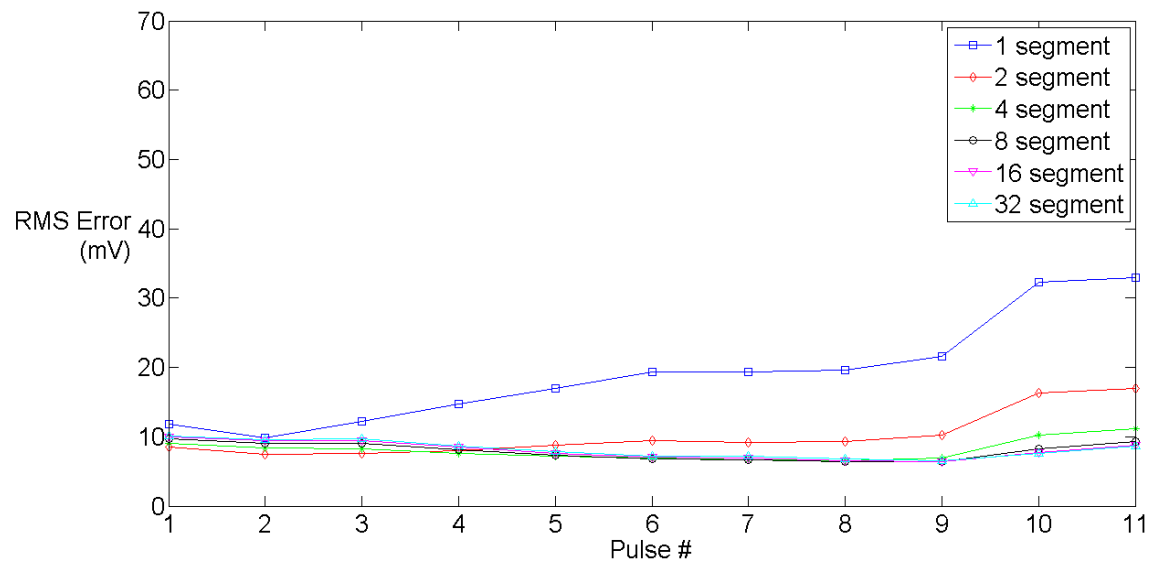


Figure 2-28. RMSE for different number of RC-segments for validation experiment #3.

Validation Test #4

Validation test #4 consist of forty charging pulses of 15 A current, with the pulse phase lasting 10 minutes. The simulated results from a 4-RC segment model is compared to the experimental data in Figure 2-29. As shown in this figure, there is a positive offset of the measured response compared to the simulated one, like that observed in the validation test #2 results. In both these cases, this positive offset can be attributed to the hysteresis effect described earlier. The RMSE for each pulse is shown in Figure 2-30. The average RMSE for the overall test is 19 mV, or 0.52%. The comparison of the RMSE of each pulse for different number of RC-segments is shown in Figure 2-30. As in the case of validation test #3, there does not appear to be any improvements above 8-RC segments.

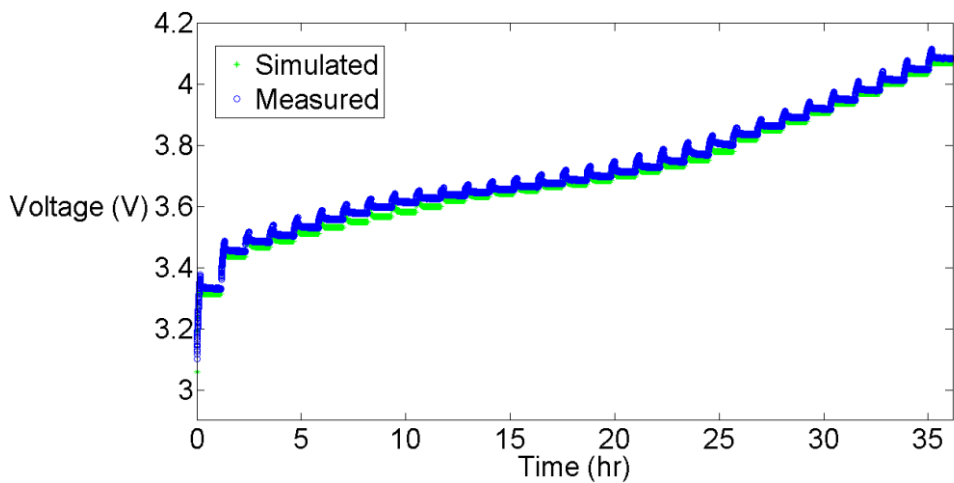


Figure 2-29. Measured and simulated voltage response for validation test #4.

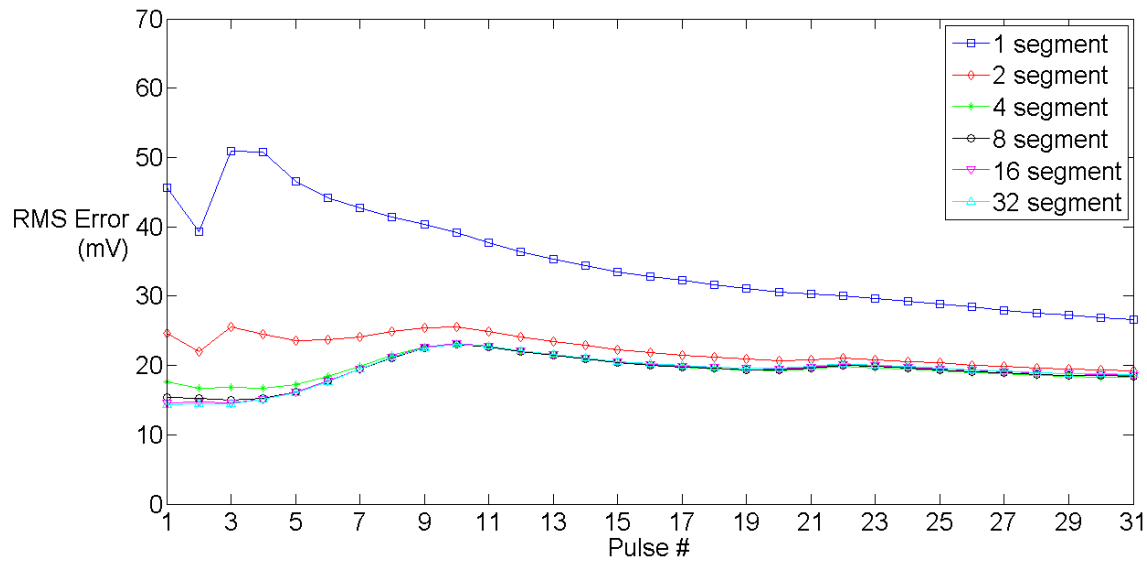


Figure 2-30. RMSE for different number of RC-segments for validation experiment 4.

The distributed SOC model worked well in predicting the results of these four validation tests. The range of RMSE for the 4 RC-segments implementation of the model ranged from 0.86% down to 0.27%. As discussed in Section 1.3.2.3, the expected root-mean-square accuracy of runtime simulations using equivalent-circuit models is on the low side of the 1-5% range suggested by Chen and Rincon-Mora [2], so these results are promising. It appears one factor that affected the accuracy of the charging pulse validation tests (#2 and #4) is the hysteresis effect. In Chapter 3, where the model is extended to consider multiple charge and discharge currents, the open circuit voltage during charging and discharging characterization experiments are used to reduce the contribution of the hysteresis effect.

2.5 Chapter Conclusions

In this chapter, the development of the distributed SOC equivalent circuit model for a lithium-ion cell is shown. A method to extract the model parameters as a function of cell SOC is presented, and used on data obtained from pulsed current parameter extraction experiments on a commercial lithium-ion polymer cell from Dow Kokam. An initial study is performed that used a single current for both parameter extraction, and the subsequent model validation experiments. This allows for evaluation of the model, and the parameter extraction method, for a cell subject to simple loads over a wide range of SOC. Four validation tests are performed at the chosen current (15 A, or 0.20 C). MATLAB® Simulink® is used to simulate the distributed SOC equivalent circuit and the results are compared to the experimental ones. In the four validation tests, the match between the experimental data and the proposed distributed SOC model is generally good. The RMSE of these experiments ranged from 0.86%, down to 0.27%. It is observed that the hysteresis effect has a significant contribution to the error for modeling of the charging pulse experiments. Increasing the number of RC-segments is shown to improve the performance of the proposed model because behavior of the lumped equivalent-circuit more closely approaches that of the model's transmission line. In these four cases, there does not appear to be any improvements beyond 8-RC segments.

It is important to keep in mind that this initial study has kept the applied current in both parameter extraction and validation experiments at 15 A (0.20 C). While this confirms that the model works well when the parameter extraction is performed at this current, the proposed

model's predictive abilities for different currents is uncertain. The extension of this model to a range of charge and discharge currents is discussed in Chapter 3.

Chapter 3: Cylindrical Cell Characterization and Modeling

The last chapter showed that the modeling and simulations of a lithium-ion polymer cell (from Dow Kokam) using the distributed SOC model performed well at a single current. In this chapter, the characterization and modeling of cylindrical lithium-ion cells is investigated. Like the lithium-ion polymer cell discussed in the last chapter, these cylindrical cells belong in the category of lithium ion cells. While lithium-ion polymer cells are encapsulated inside laminated polymer films, cylindrical lithium ion cells are housed inside a metallic can, as shown in Figure 1-4. As its name suggests, cylindrical cells are cylinder-shaped, which is the most commonly produced form on the market. This work builds on the previous chapter by performing experiments at different charge and discharge currents. Section 3.1 describes the experimental setup used for this work. The parameter extraction results are shown in Section 3.2, and the validation results are discussed in Section 3.3. It is shown that the distributed SOC model, which is independent of current, developed in the last chapter performed well, with a typical error below 1%, for dynamic currents provided the average discharge current is restricted below 0.60 A (or 0.20 C). For higher average discharge currents, an alternative model derived from spherical diffusion is proposed. A key aspect of the model that is not readily captured in other approaches is that the distributed SOC model allows for a variation in local SOC within the electrode. This allows the model parameters to be extracted at a single current, which is shown here to give simulation results that match well to certain validation experiments that excites the cell at a wide range of currents. This contrasts to the most popular literature equivalent-circuit models that require parameter extraction at multiple charge and discharge currents [3], [4], [6]. Based on comparisons with literature results, the model performance is excellent given its

relative simplicity. Two types of validation experiments are performed: 1. dynamic discharge tests, and 2. constant current discharge tests. It is shown that the planar electrode model simulates the dynamic discharge test accurately, while a spherical geometry model (intended to simulate the transport into spherical particles that make up the electrodes) is required to give accurate simulations for higher current constant discharge tests. In future the model could be made even more effective by providing temperature and state of health dependence. These aspects are not covered in this work.

3.1 Experimental Setup

The cell chosen for this work is the GP18650-30U cylindrical lithium ion cell [93] that was obtained commercially from GP Batteries International Limited. This cell will be simply referred to as 30U cells in the rest of this work. The cell has a nominal capacity of 3.0 Ah when discharged at 600 mA to 2.80 V at 23 °C, and a minimum capacity of 2.9 Ah. It has the 18650 form factor, meaning that it has a diameter of 18mm, and a height of 65mm.

This cell has a maximum charging voltage of 4.35 V, which is higher than the maximum charging voltage of 4.20 V that is most commonly seen in other cells on the market. This difference is clearly due to a different chemistry used in the 30U cell. This cell's fully discharged voltage is 2.80 V. This cell's maximum continuous discharge current is 6.0 A (referred to as 2.0 C, as it is double the current that discharges the rated full cell capacity in 1 hour. The definition of the C-rate is presented in Section 1.2.2). In this work, we test the cell up to this maximum discharge rate as this is the maximum rated discharge current for this cell. The

cell tests were conducted using a cell holder, which is shown in Figure 3-1. The metallic cylinders in the figure are the GP18650-30U cells.



Figure 3-1. Cell holder for cell testing. The three metallic cylinders in the bottom half of the photo are the 30U cylindrical lithium ion cells.

The top portion of the cell holder, shown in Figure 3-2, makes two contacts to the cell cap, which is the cell's positive terminal. The center pin of the holder is spring loaded, and is used to conduct current while the outer metallic hollow cylinder contacts the cell to measure the cell voltage. Likewise, the bottom portion of the cell holder, shown in Figure 3-3, makes two contacts to the bottom of the cell can, which is the cell's negative terminal. In this four point probe method, contact resistances of the probes are eliminated from the experimental data.

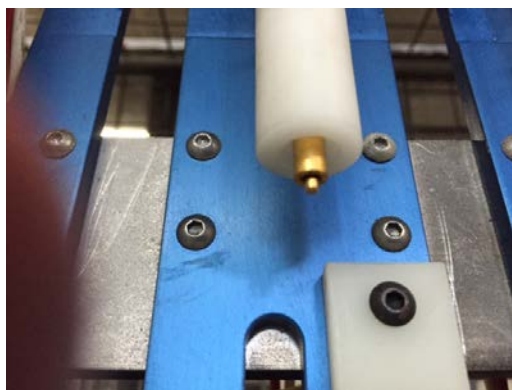


Figure 3-2. Two metallic contacts for contacting the cell cap, which is the cell's positive terminal.



Figure 3-3. Bottom portion of the cell holder, showing the spring-loaded center pin for current conduction, and outer metallic tube for voltage measurement.

During testing, the cell holders were mounted inside a cabinet, which is shown in Figure 3-4. The experiments were performed in a temperature-controlled room, with target temperature of 23 °C. The tests in this chapter were performed using an Arbin Instruments BT-2000 battery test system [94]. The experiments were controlled using MITS-Pro V.4, also from Arbin.



Figure 3-4. Cell cabinet for the experiments.

Three 30U cells are tested according to the procedures described in this chapter to confirm the model's applicability. To simplify the discussion, plotted results in this chapter were all obtained from the same cell. When quantifying the simulation performance of the proposed distributed SOC models, the results tabulated for the MAPVE and RMSPVE are averaged values obtained from the three cells. The obtained MAPVEs and RMSPVEs from the three cells are typically within 0.5% and 0.2%, respectively, of each other. This confirms the repeatability of the model predictions for these three tested cells.

3.2 Extraction

To employ the distributed SOC model to simulate the cell behavior, the model parameters need to first be extracted. In this chapter, the dependence of the parameters on different current magnitudes, SOC, as well as the effect of current direction (charge vs. discharge), are investigated.

This extraction process consists of two sets of experiments. The first is the estimation of the open-circuit voltage OCV dependence on cell SOC, which is described in Section 3.2.1. This is used to select appropriate states of charge at which to apply current pulses. The next parameter extraction experiments employ discharging and charging pulses as described in Section 3.2.2. In these experiments the model's open-circuit voltage V_{OC} , diffusion capacitance C_D , diffusion resistance R_D , and series resistance R_S are extracted, all as a function of SOC. This is achieved by using current pulses that induce relatively small changes in cell SOC, so that the effective model parameters are essentially constant. Following the current pulses, the cell voltage is allowed to equilibrate, and the ratio of the charge to voltage change is taken to estimate diffusion capacitance C_D . The current pulses are short in time compared to the diffusion time constant, allowing a resistor in series with an infinite diffusion element to be fit to the step current response, which, given the local diffusion capacitance C_D , allows the diffusion resistance R_D and the series resistance R_S to be estimated. SOC and current dependencies of the extracted parameters are then examined, as discussed, before using the parameters to predict cell response to different validation experiments in Section 3.3.

3.2.1 Initial Estimation of the OCV Dependence on SOC

To determine the length of the current pulses to use in the discharging and charging pulsed experiments, the dependence of cell OCV on SOC needs to be first estimated. In this work, a very slow discharge (60 mA, or 0.020 C) of the GP18650-30U cell was performed to estimate the OCV dependence on SOC. A slow discharge provides a good approximation because of two reasons: 1. the voltage drop due to internal resistance is small when current is small, and 2. the

cell is disturbed at a low rate, allowing the cell to maintain a near equilibrium state. The test procedure is described in Section 3.2.1.1. The results and their analysis are presented in Section 3.2.1.2.

3.2.1.1 Procedure

The experimental procedure of the slow discharge (0.020 C) experiment is shown in Table 3-1. As mentioned in Section 1.2.2, the cell SOC is not a directly measurable quantity. Therefore, a procedure is required that brings the cell to a reproducible starting point with an assigned reference SOC. In this work, that procedure is the initialization phase that contains steps 1 to 5 in Table 3-1. Step 4 of this initialization procedure, which consists of keeping the cell at its maximum voltage until the current falls below the pre-determined threshold (0.010 C in this case) is included in this procedure to ensure the cell's maximum full capacity is obtained and the cell's full range of SOC is characterized. After this process, the cell is assumed to be full, with a cell SOC of 1.0. All subsequent tests in this chapter will contain these first five steps as part of the initialization procedure.

Phase	Step	Description
I. Initialization	1	Discharge the cell at 0.50 C (1.5 A) until the cell voltage falls below 2.80 V
	2	Rest for 0.50 hour
	3	Charge at 0.20 C (0.60 A) until the cell voltage reaches 4.35 V
	4	Hold the cell at 4.35 V until the cell current falls below 0.010 C (0.030 A)
	5	Rest for 1 hour
II. Slow Discharge	6	Discharge at 0.020 C (60 mA) until the cell voltage falls below 2.80 V

Table 3-1. Experimental procedure for slow discharge experiment to estimate the open-circuit voltage V_{oc} dependence on SOC.

The second phase of the test consists of only one 0.020 C discharge step. The measured cell voltage during this phase gives an estimate of the open circuit voltage OCV dependence on cell SOC. This result is used only to provide a reference curve from which the pulse phase durations are decided for the pulsed experiments for model parameter extraction (discussed in Section 3.2.2).

3.2.1.2 Results and Analysis

The experiment results are shown in Figure 3-5. As in Chapter 2, the cell voltage declines slowly at the beginning, and slows even further at about half way through the discharge.

Towards the end of the experiment, the cell voltage drops rapidly. Viewing the cell as a voltage dependent capacitor, the slow drop in voltage corresponds to a high effective capacitance, and *vice-versa*. By scaling the recorded time with the applied current (60 mA), an approximation of the dependence of OCV on cumulative discharged capacity is obtained, which is shown as the solid line in Figure 3-6. As mentioned in Section 1.2.2, the cumulative discharged capacity is the

total quantity of charge that has been discharged from a fully charged cell. Similar to the cell SOC, the cumulative discharged capacity is an indication of the status of the cell. Small (large) cumulative discharged capacity corresponds to high (low) SOC. The full capacity of the cell is given by the cumulative discharged capacity when the cell lower limit voltage (*i.e.* 2.8 V) is reached. For the tested 30U cylindrical cells, the full capacity was measured to be 3.0 Ah, giving a full-capacity-equivalent capacitance C_{FCE} of 10,800 F (3.0 Ah x 3,600 C/Ah = 10,800 C). This value of full-capacity-equivalent capacitance gives a value of 1.0 V across C_{FCE} in the distributed SOC model when the cell SOC is 1.0.

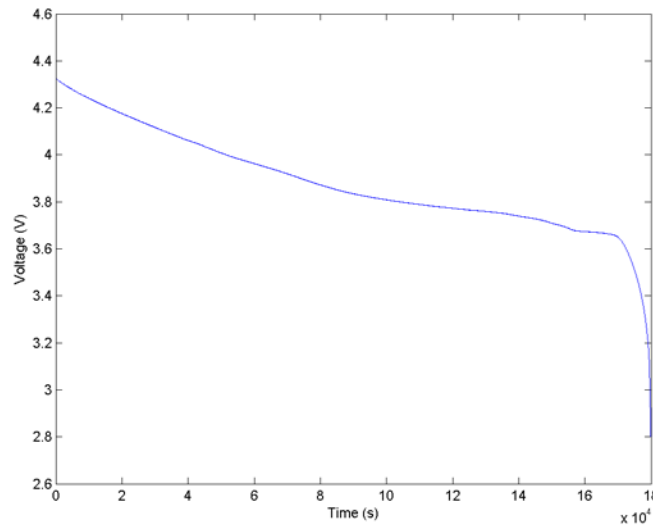


Figure 3-5. Measured cell voltage of the 30U cell for slow (0.020 C) discharge.

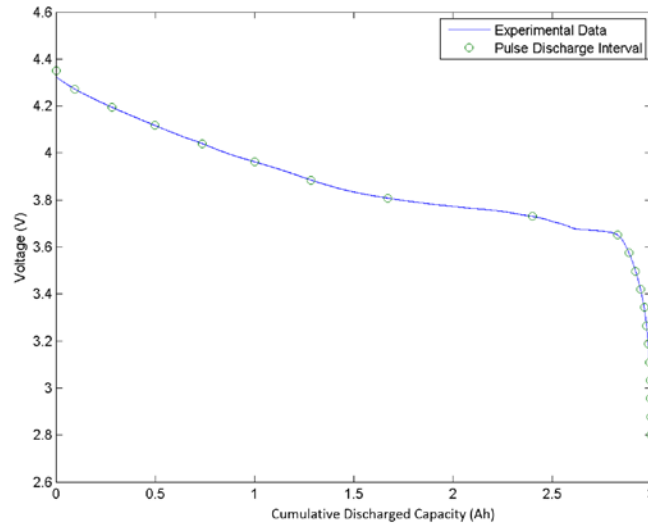


Figure 3-6. Pulse discharge interval for the subsequent tests. Greens open circles are points equally spaced in voltage drop that are selected as the states of charge at which discharge steps will be applied in order to extract model parameters open-circuit voltage V_{OC} , diffusion capacitance C_D , diffusion resistance R_D , and series resistance R_S .

Using the results shown in Figure 3-6, the duration of the pulses for pulsed discharge and charge experiments, which is described in Section 3.2.2, is determined. In this chapter, the approach taken is to divide the full OCV range (between 4.35 V and 2.80 V) into 20 equal sections. The total charge extracted (stored) in each discharge (charge) pulse is calculated such that the change in cell OCV is expected to be approximately one-twentieth of the total 1.55 V ($4.35 \text{ V} - 2.80 \text{ V} = 1.55 \text{ V}$) range in cell voltage. The aim is to make the diffusion capacitance be relatively constant in each interval. As can be seen in Figure 3-6, there can be some deviation in slope between points, particularly at a cumulative discharged capacity of around 2.5 Ah, so a slope-based method of determining sample point spacing could also be considered in the future, or extra points could be added to increase the precision of the estimates.

The total charge extracted for each of the 20 discharge pulses is described here. The required total charge of each discharging pulse and the cumulative discharged capacity after the pulse are shown in Table 3-2. The estimated OCV falls rapidly at large cumulative discharged capacity (at far right of Figure 3-6). Therefore, more pulses are needed there to more accurately capture the cell behavior.

Pulse	Total Pulse Charge (mAh)	Cumulative Discharged Capacity (mAh)	Estimated SOC	Estimated OCV Post-Pulse (V)
1	95.46	95.46	0.97	4.27
2	186.9	282.3	0.91	4.20
3	215.7	498.1	0.83	4.12
4	240.6	738.6	0.75	4.04
5	262.9	1002	0.67	3.96
6	284.1	1286	0.57	3.89
7	387.9	1674	0.44	3.81
8	729.4	2403	0.20	3.73
9	427.3	2830	0.056	3.65
10	57.95	2888	0.037	3.58
11	33.96	2922	0.026	3.50
12	24.41	2947	0.018	3.42
13	17.89	2965	0.012	3.34
14	12.87	2977	0.0074	3.27
15	8.860	2986	0.0045	3.19
16	5.014	2991	0.0028	3.11
17	2.842	2994	0.0019	3.03
18	2.006	2996	0.0012	2.96
19	1.838	2998	0.0006	2.88
20	1.758	3000	0	2.80

Table 3-2. Total pulse charge of each pulse in the pulsed discharging experiment. The corresponding cumulative discharged capacity, estimated SOC, and estimated OCV after the pulse are also listed.

For the charging pulse experiment, the cell starts at high cumulative discharged capacity (low SOC), and the sequence of charging pulses brings the cell to low cumulative discharged capacity (high SOC). The sequence of total charge of each charging pulse is therefore the reverse of the discharging pulses. The required total charge of each pulse and the cumulative discharged capacity after each pulse are shown in Table 3-3. At the beginning of the charging pulse experiment, the cell is first fully discharged. Therefore, the cumulative discharged capacity is 3.0 Ah. As the applied pulse are in the charging direction, the cumulative discharged capacity

decreases by the total charge of the pulse. The total charge of the first few charging pulses are very small, as the OCV changes rapidly in the large cumulative discharged capacity (low SOC) region.

Pulse	Total Pulse Charge (mAh)	Cumulative Discharged Capacity (mAh)	Estimated SOC	Estimated OCV Post-Pulse (V)
1	1.758	2998	0.0006	2.88
2	1.838	2996	0.0012	2.96
3	2.006	2994	0.0019	3.03
4	2.842	2992	0.0028	3.11
5	5.014	2987	0.0045	3.19
6	8.860	2978	0.0074	3.27
7	12.87	2965	0.012	3.34
8	17.89	2947	0.018	3.42
9	24.41	2923	0.026	3.50
10	33.96	2889	0.037	3.58
11	57.95	2831	0.056	3.65
12	427.3	2403	0.20	3.73
13	729.4	1674	0.44	3.81
14	387.9	1286	0.57	3.89
15	284.1	1002	0.67	3.96
16	262.9	738.9	0.75	4.04
17	240.6	498.3	0.83	4.12
18	215.7	282.6	0.91	4.20
19	186.9	95.73	0.97	4.27
20	95.73	0	1.0	4.35

Table 3-3. Total pulse charge for each pulse in the pulsed charging experiment. The corresponding cumulative discharged capacity, estimated SOC, and estimated OCV after the pulse are also listed.

3.2.2 Pulsed Experiments

The parameter extraction method for the distributed SOC model parameters involves performing pulsed discharge and charge experiments to the cell. By performing analysis of the resulting data according to the method described in Section 2.3.1, the model parameters are extracted. In this section, the pulsed experiments are described. The procedure is first discussed in Section 3.2.2.1. The results are presented in Section 3.2.2.2.

3.2.2.1 Procedure

The discharge pulse procedure is described in Table 3-4. Like the slow discharge procedure described in Section 3.2.1.1, the first phase consists of initializing the cell to a repeatable fully charged state (*i.e.* SOC = 1.0). The second phase consists of applying discharging pulses to the cell. The cell rested for 60 minutes between pulses to allow the cell to approach equilibrium. The experiment is terminated when the cell voltage falls below 2.50 V during any pulse. This lower limit voltage is the rated minimum voltage for the cell according to its datasheet.

Phase	Step	Description
I. Initialization	1	Discharge the cell at 0.20 C (0.60 A) until the cell voltage falls below 2.50 V
	2	Rest for 1.0 hour
	3	Charge at 0.20 C (0.60 A) until the cell voltage reaches 4.35 V
	4	Hold the cell at 4.35 V until the cell current falls below 0.010 C (0.030 A)
	5	Rest for 1 hour
II. Pulsed Discharge	6	Discharge at chosen rate until n^{th} pulse cumulative discharged capacity reached or cell voltage falls below 2.50 V
	7	Rest for 1.0 hour
	8	Repeat steps 6 and 7, unless cell voltage falls below 2.50 V in step 6

Table 3-4. Pulsed discharge procedure for the parameter extraction experiments.

The test procedure of the pulsed charging experiments are shown in Table 3-5. The initialization phase of the procedure involves first charging the cell to the same repeatable fully charged state (Steps 1 to 5). Steps 6 to 8 bring the cell to a high cumulative discharged capacity state ($\text{SOC} \approx 0.0$), and then the pulsed charging experiments are performed. Like in the discharge pulse experiments, the rest time between pulses is one hour to allow the cell to reach equilibrium. The experiment is terminated when the cell voltage rises above 4.35 V during any charging pulse. This upper limit voltage is the rated maximum voltage of the cell according to its datasheet.

Phase	Step	Description
I. Initialization	1	Discharge the cell at 0.20 C (0.60 A) until the cell voltage falls below 2.80 V
	2	Rest for 1.0 hour
	3	Charge at 0.20 C (0.60 A) until the cell voltage reaches 4.35 V
	4	Hold the cell at 4.35 V until the cell voltage falls below 0.010 C (0.030 A)
	5	Rest for 1 hour
	6	Discharge at 0.20 C (0.60 A) until the cell voltage falls below 2.80 V
	7	Hold the cell at 2.80 V for 4 hours
	8	Rest for 4 hours
II. Pulsed Charge	9	Charge at chosen rate until n^{th} pulse charge capacity reached or cell voltage rises above 4.35 V
	10	Rest for 1.0 hour
	11	Repeat steps 9 and 10, until the cell voltage rises above 4.35 V in step 9

Table 3-5. Pulsed charge procedure for the parameter extraction experiments.

In this chapter, the dependence of the estimated parameters on current magnitude is also investigated. The maximum discharge current that this cell can sustain is 6.0 A according to the cell datasheet. The tested pulsed current magnitudes, and the associated C-rate, are shown in Table 3-6. The pulsed current spans two orders of magnitude, which is larger than most works in the literature [2]–[4], [6], [7], [30]. The lowest current consists of 0.020 C discharge, which is a quite low discharge rate, as discharging a fully charged cell (SOC = 1.0) at 0.020 C would take 50 hours until the cell is fully discharged (SOC \approx 0.0). Compared to most everyday lithium-ion cell applications, such as in laptop computers and mobile phones, this is a long duration discharge. The highest current corresponds to charge or discharge in half an hour – the maximum

rate for this cell, as specified by the manufacturer. Therefore, this range of applied currents is considered to be a wide range.

Pulsed Current Magnitude (A)	Pulse C-Rate (-C)
6.00	2.00
2.79	0.928
0.600	0.200
0.129	0.0431
0.0600	0.0200

Table 3-6. Table of tested pulsed current magnitudes and their corresponding C-rates.

3.2.2.2 Results and Analysis

The objective of this section is to obtain the model parameters of the distributed SOC model, so that they can be used in the MATLAB® SIMULINK® model simulations and compared to the validation experiment results (discussed later in Section 3.3). As the full-capacity-equivalent capacitance C_{FCE} is determined in Section 3.2.1.2 for these cells to be 10,800 F, the remaining model parameters required are open-circuit voltage V_{OC} , diffusion resistance R_D , and series resistance R_S , as discussed in Section 2.1. The dependence of these parameters on cell SOC, current magnitude, and current direction (charge/discharge) are investigated.

The experimental results for 6.0 A pulsed discharge are shown in Figure 3-7. In the top plot of the figure, the applied current profile is shown. As the convention that negative current indicates discharging current is adopted in this thesis, the current during the pulse phase is negative. The duration of each current pulse is determined by its total pulse charge shown in Table 3-2. The

current pulse duration is greatest in pulses 7 to 9, as the diffusion capacitance C_D at the corresponding SOC is highest, illustrated by the slow drop in cell voltage there in Figure 3-6. The measured cell voltage response is shown in the bottom plot of Figure 3-7. Only 13 pulses are measured for the 6.0 A experiment because the cell voltage dropped below the lower cell operating limit of 2.50 V. This can be attributed to the large voltage drop observed during the pulse phase of the 6.0 A pulses.

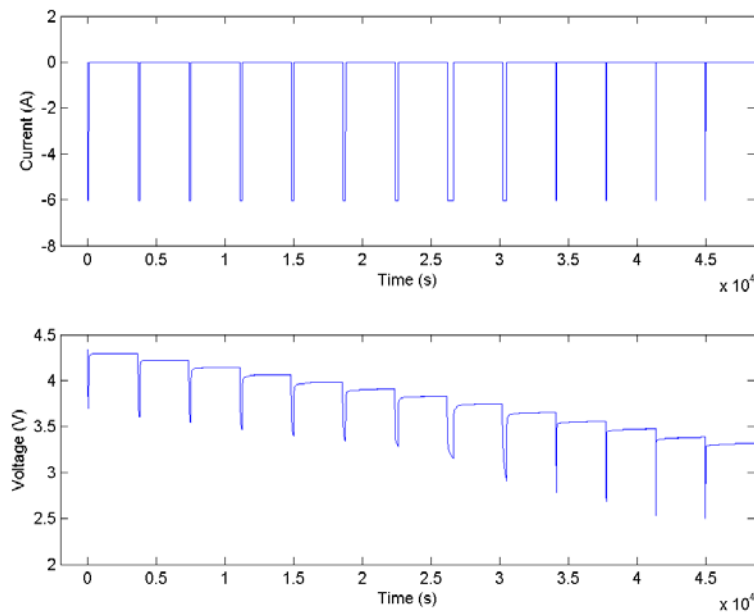


Figure 3-7. 6.0 A pulsed discharge experimental results for the 30U cell. The current pulse profiles are shown in the top plot, while the measured cell voltage is shown in the bottom.

The cell voltage response to the first current pulse is shown in Figure 3-8. As expected, the cell voltage drops instantaneously at the beginning of the pulse phase, and the rate of voltage drop slows down as time increases. First there is an instantaneous $I_P R_S$ drop in cell voltage due to the internal resistance R_S . I_P is the current magnitude during the pulse phase. This is followed by the initially steep change in voltage at the start of the diffusion profile, as described in Section

2.3.3. In this initial period of the current pulse, the cell voltage is expected to evolve in proportion to $t^{1/2}$, according to the diffusion limited situation described by equation [2-27]. When the pulse phase ends, the magnitude of the applied current returns to zero, and the cell voltage rises instantaneously due to $I_p R_s$. Then the cell voltage continues to rise due to re-equilibration, as the steep lithium ion diffusion gradients within the rapidly charged electrodes dissipate. The measured voltage responses to the other pulses in Figure 3-7 behaved similarly.

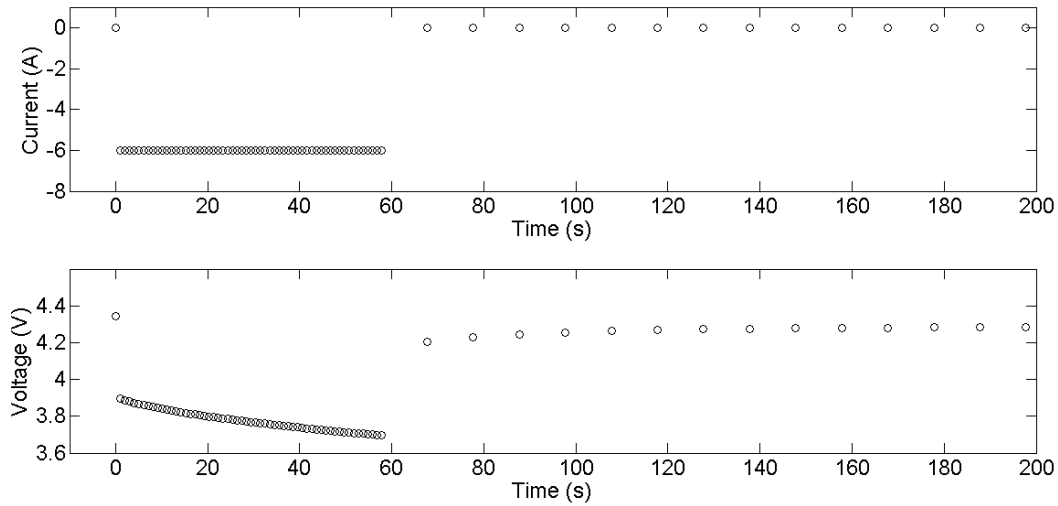


Figure 3-8. Cell response to the first 6.0 A discharge current pulse. The top plot shows the applied current, and the bottom plot shows the measured cell voltage response.

Figure 3-9 shows the experimental results for 60 mA discharge pulses (0.020 C). The top plot of Figure 3-9 shows the applied current profile. In this experiment, all 20 pulses are measured before the termination condition (cell voltage falling below 2.50 V) is reached. Only in the final 5 pulses, when the stored charge is nearly completely exhausted and the diffusion capacitance is small, is there significant relaxation. Compared to the current profile shown in Figure 3-7, the

current pulses are longer in duration, as total charge of the pulses are the same while the applied current is reduced. The experiment on this one cell lasted close to 3 days. Figure 3-10 shows the first discharge pulse response to the 60 mA pulsed discharge currents. Compared to the 6.0 A discharge results, the cell voltage drops during the pulse phase are much less significant. The small voltage relaxation during the relaxation phase for most of the experiment shows that at 60 mA pulsed discharge the cell is quite close to being at equilibrium.

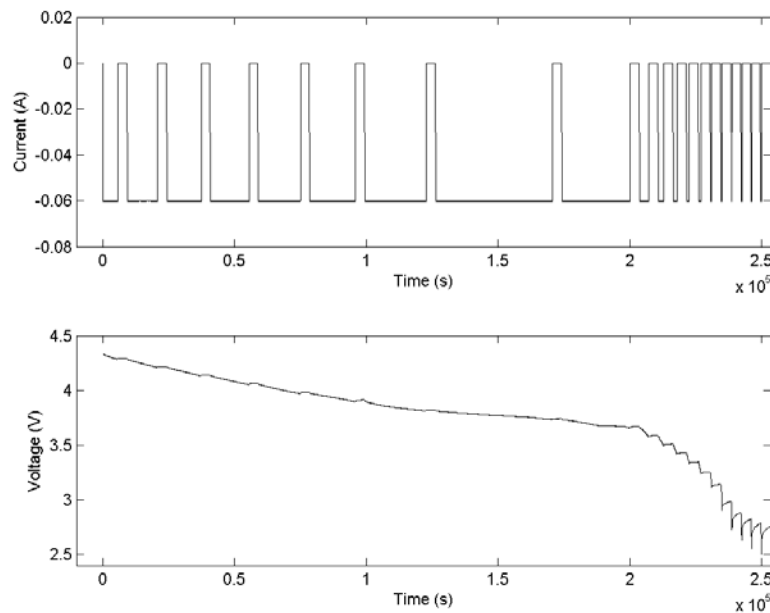


Figure 3-9. 60 mA pulsed discharge experimental results for the 30U cell. The top plot shows the long duration pulse phase of the current pulses, separated by relaxation phase of 60 minutes. The bottom plot shows the measured cell voltage.

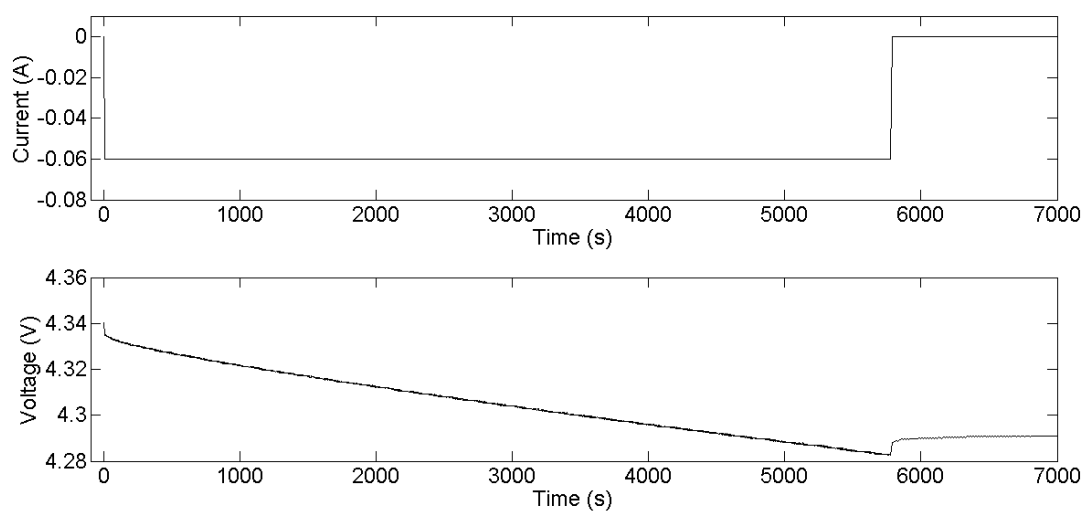


Figure 3-10. Cell response to the first 60 mA discharge current pulse. The top plot shows the applied current, and the bottom plot shows the measured cell voltage response.

Results for the 6.0 A charging pulses are shown in Figure 3-11. Like the 6.0 A discharging pulses, the cell voltage changes significantly during the pulse phase, only this time in the positive direction.

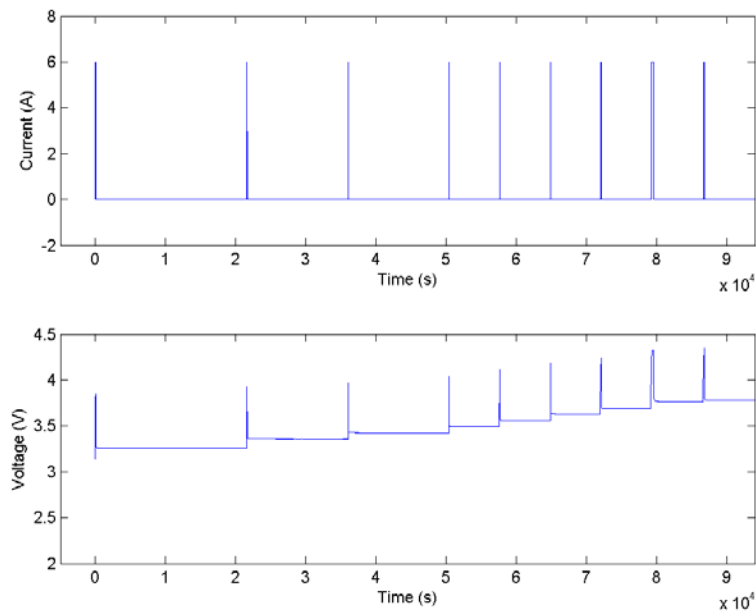


Figure 3-11. 6.0 A pulsed charging experimental results. The top plot shows the short pulse phase of the current pulses with high current, separated by the 60 minute relaxation phases. The bottom plot shows the measured cell voltage.

The 60 mA charging pulse results are shown in Figure 3-12. As in the 60 mA discharging pulse results, the cell voltage changes are much less pronounced than the 6.0 A experiments.

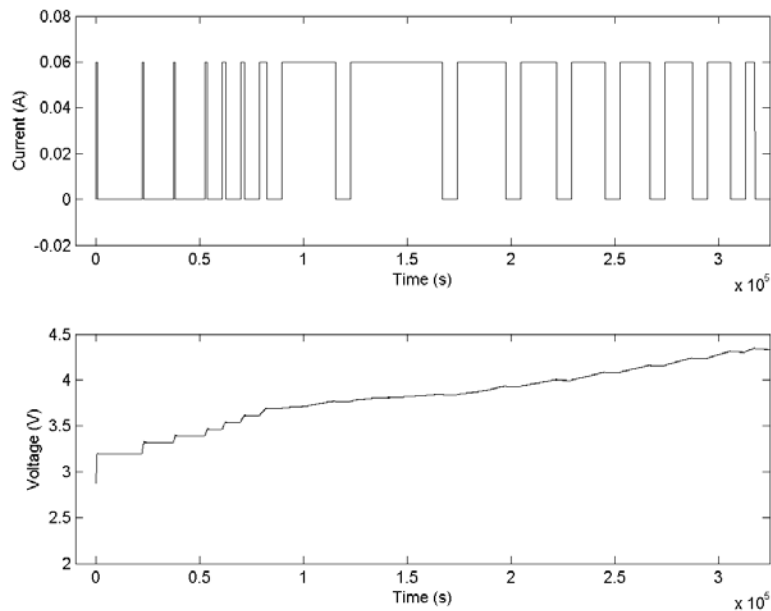


Figure 3-12. 60 mA pulsed charging experimental results. The top plot shows the mostly long duration pulse phases, separated by 60 minute relaxation phases. Initial pulses are short due to the small diffusion capacitance near full discharge. The bottom plot shows the measured cell voltage.

The results presented so far in this section are the applied current and measured cell voltage as a function of time. A useful visualization of these results can be obtained by plotting the measured cell voltage as a function of cumulative discharged capacity. This is shown in Figure 3-13 for the 6.0 A pulsed discharge experiment. Before the pulsed discharge experiment begins, the cell is fully charged (SOC = 1.0) and is represented at the top left of the plot. During the pulse phase of the first discharge pulse, the cell cumulative discharged capacity increases (proceed to the right) with the corresponding cell voltage drop (proceed downwards). Once the pulse phase of this first current pulse is completed, the total charge accumulated in this pulse phase brings the cell to a new SOC. Then, the cell voltage relaxes during the relaxation phase with no change in cumulative discharged capacity during this time. Therefore, the relaxation phase of this pulse

consists of an upward vertical line. At the end of the one hour relaxation period, the cell is considered to be completely relaxed, and cell voltage at this time is the estimated cell OCV. Therefore, cell voltage at the peak of this vertical line is the cell OCV at this new SOC. Then the next pulse is applied, and the above repeats.

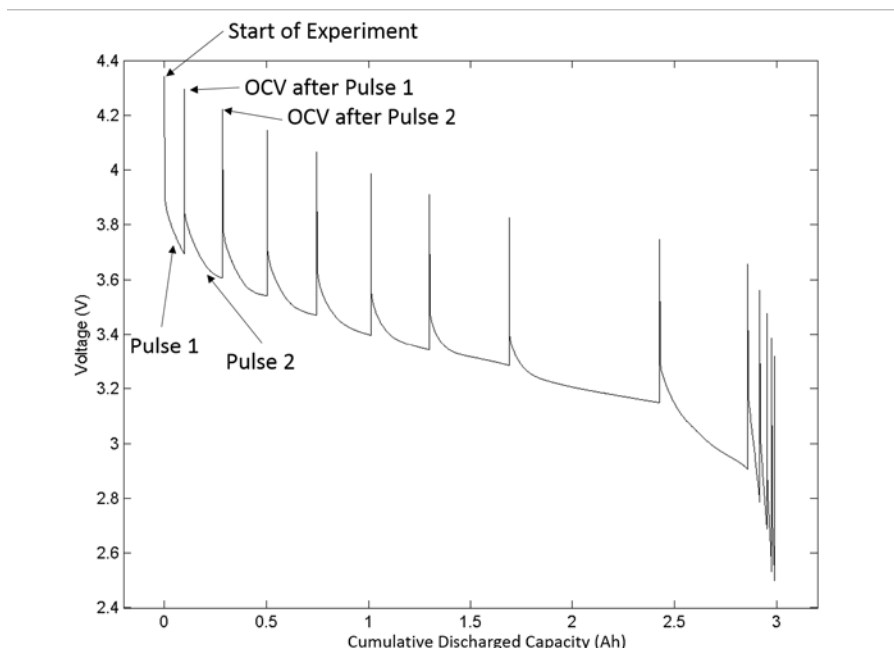


Figure 3-13. Cell voltage as a function of cumulative discharged capacity for 6.0 A pulsed discharge. Here the vertical lines show relaxation of cell voltage (upwards) over the course of the one hour relaxation phase, and the following rapid discharge.

The results for 60 mA discharge pulses are similarly plotted in Figure 3-14. The cell voltage changes during the pulse phase, and the subsequent relaxation phase, are much less pronounced due to the one hundred times smaller current magnitude. This illustrates that, at this low applied current during the pulse phase of the current pulses, the cell is not far from equilibrium.

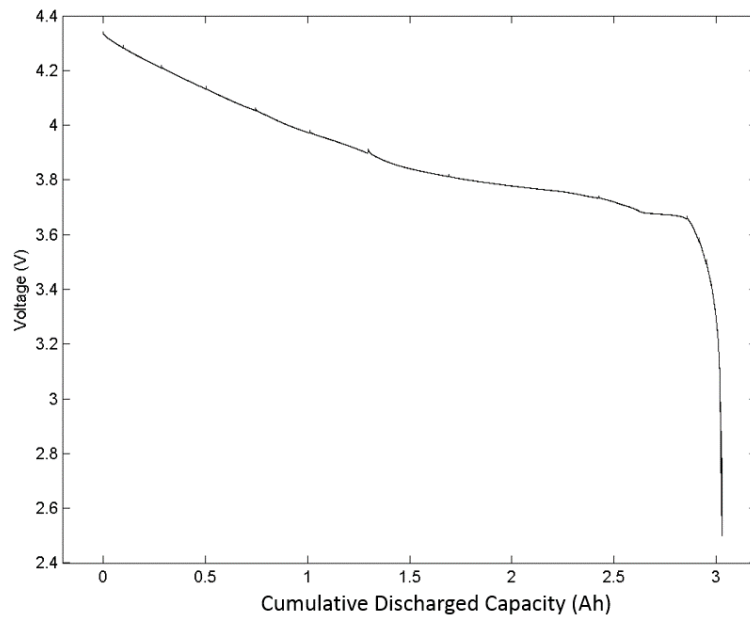


Figure 3-14. Cell voltage as a function of cumulative discharged capacity for 60 mA pulsed discharge. The small upward spikes represent relaxation at open circuit following the pulse phase.

The results for the five tested discharge currents (Table 3-6) are shown in Figure 3-15. The cumulative discharged capacity after each pulse is the same for all current magnitudes, so the rising vertical lines are aligned in cumulative discharged capacity. The voltage peaks at the end of the relaxation phase of the pulses give the cell OCV. Although not visible in this plot, it will be shown later in this section that the OCV from the five tested discharge currents matched well (later in Figure 3-18). During the pulse phase, the cell voltage drops the most for 6.0 A, while it drops the least for 60 mA. This behaviour is expected from examination of the distributed SOC model in Figure 2-5 (p. 61), since the higher current leads to a larger voltage drop across the series resistance R_s , and a larger concentration gradient, which produces a larger voltage difference.

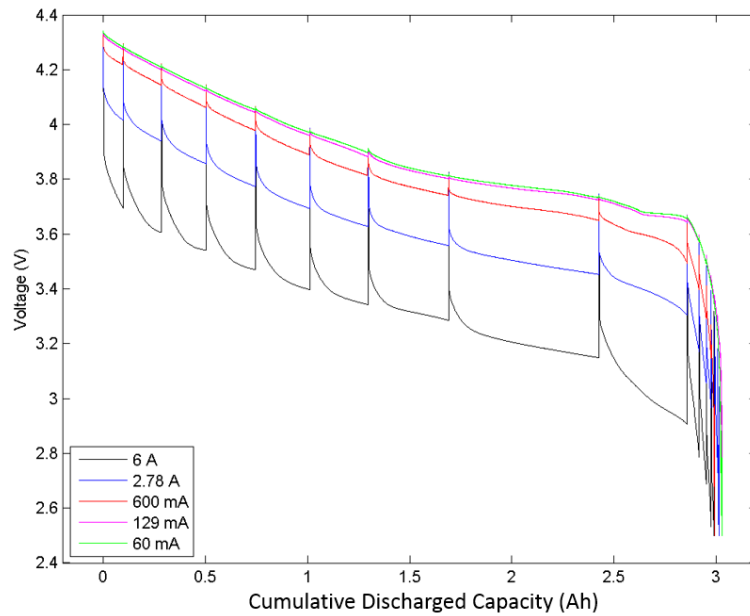


Figure 3-15. Cell voltage as a function of cumulative discharged capacity for all five tested pulsed discharge current magnitudes.

The results from the charging pulses can be visualized similarly. Figure 3-16 shows the cell voltage during the 6.0 A charging pulse experiment, plotted as a function of cumulative discharged capacity. For charging pulse experiments, the cell starts in the fully discharged state (*i.e.* at high cumulative discharged capacity, or low SOC) and the corresponding low cell voltage, which is represented at the bottom right of the plot. During the pulse phase, the cumulative discharged capacity is decreased (proceeds to the left) as the applied current charges the cell and the cell voltage increases (proceeds upwards). After the pulse phase, the cell has arrived at a new SOC. The cumulative discharged capacity stays constant in the relaxation phase, while the cell voltage decreases to its equilibrium voltage as the cell relaxes. In this plot, this relaxation phase is characterized by a decreasing vertical line. The cell voltage at the bottom

of this vertical portion gives the cell OCV at this cumulative discharged capacity (new SOC). This 6.0 A charging pulse experiment terminated after only nine pulses, as the cell voltage exceeded the 4.35 V upper limit before all 20 pulses were applied, due to the large voltage rise during the pulse phase.

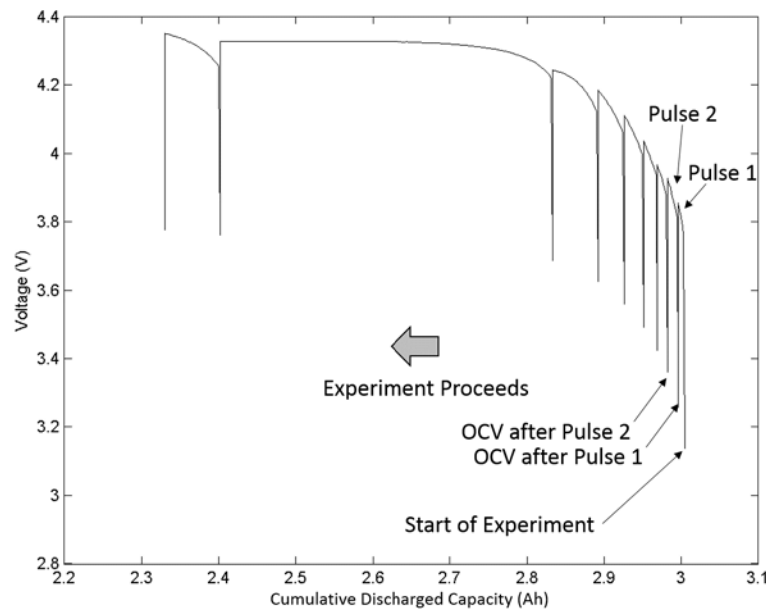


Figure 3-16. Experimental results for the 6.0 A charging pulse experiment.

Results for the charging pulse experiments at the five tested current magnitudes are shown in Figure 3-17. As in the case of the discharging pulses, the OCV obtained (bottom of the vertical line at the end of each relaxation phase) from the different tested current magnitudes matched well. This is not clearly visible in the figure, but will be shown later in this section (in Figure 3-18). During the pulse phase, the cell voltage rises the most for 6.0 A experiment, while it rises the least for the 60 mA one. This confirms expectation as the higher current leads to a larger

voltage drop across the series resistance R_s , which is seen as a rise in voltage at the instant the current is applied. Subsequently, a larger concentration gradient is produced during the pulse phase at higher current, which also produces a larger voltage difference.

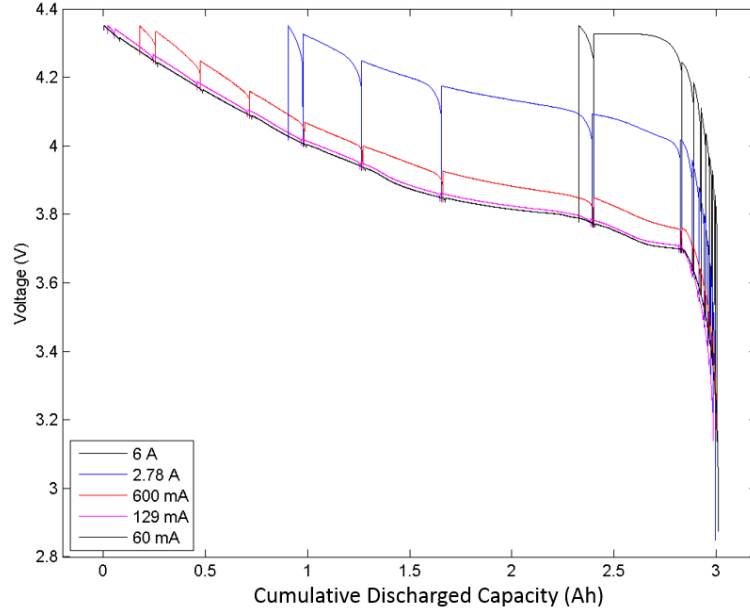


Figure 3-17. Cell voltage as a function of cumulative discharged capacity for the charging pulse experiments at different current magnitudes.

The SOC of the cell at any cumulative discharged capacity is given by

$$SOC = \frac{Full\ Cell\ Capacity - Cumulative\ Discharged\ Capacity}{Full\ Cell\ Capacity}, \quad [3-1]$$

where the full cell capacity is given by the cumulative discharged capacity at the lower cutoff voltage (*i.e.* 2.80 V) during slow discharge (see Figure 3-6), starting from a fully charged cell.

The estimated OCV as a function of SOC for the five discharge and charge currents is shown in Figure 3-18. This plot shows that the extracted OCV for the different currents and different

current directions (charge/discharge) match well. This means that the cell open circuit voltage depends strongly on the cell SOC, and weakly on the current magnitude that brought the cell to this SOC.

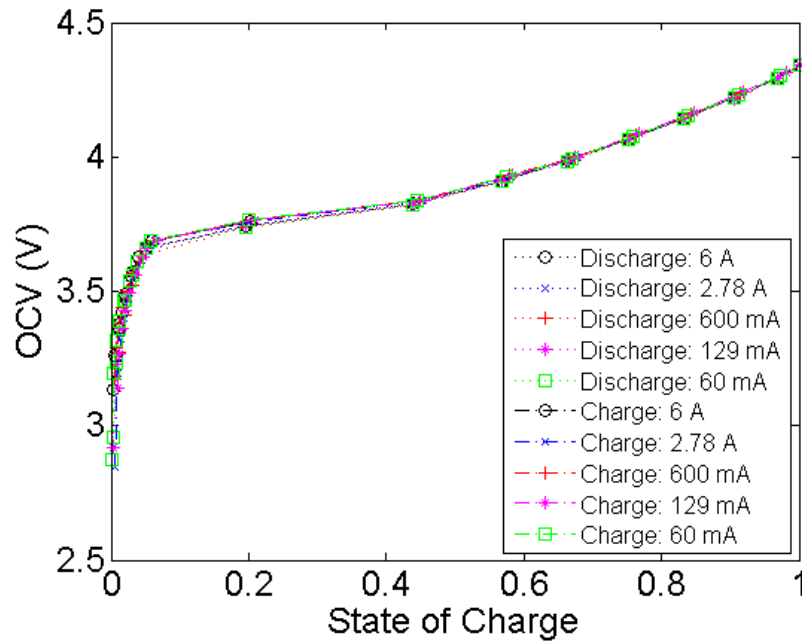


Figure 3-18. Extracted OCV from discharge and charge current pulses of different pulse magnitudes.

Figure 3-19 shows the magnified view of the “knee” of the graph (SOC at *ca.* 0.05) in Figure 3-18. A comparison of the OCV extracted from discharging pulse experiments (dotted lines) shows an appreciable spread of *ca.* 25 mV at SOC \approx 0.05. This can be attributed to a cycle-to-cycle difference in full cell capacity, and minor differences in the starting SOC established by the initialization procedure. At this “knee” of the OCV curve, where the OCV falls rapidly for decreasing SOC, this capacity difference leads to the observed OCV difference of up to 25 mV amongst the different discharge current magnitudes. The OCV extracted from charging pulse

experiments are shown as dashed-dotted lines, also in Figure 3-18. The obtained OCV also exhibits a spread of *ca.* 25 mV at SOC \approx 0.05.

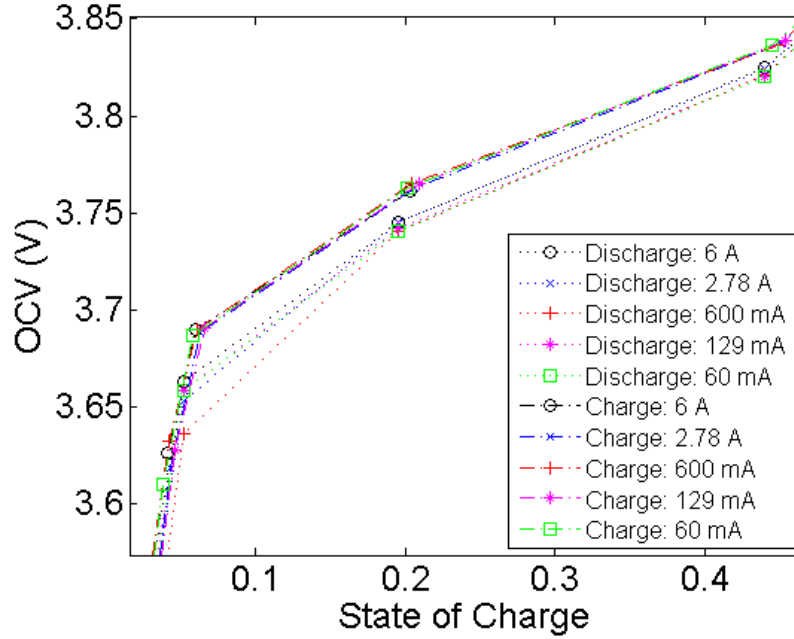


Figure 3-19. Magnified view of the extracted OCV as a function of SOC in the low SOC region.

Also shown in Figure 3-19 is that the OCV obtained from discharging pulses (shown as dotted lines) tend to be closer to each other in voltage, as is the case for the OCV obtained from charging pulses (shown as dashed-dotted lines). As is known in the literature [5], [45], [91], [92], there is typically an OCV difference observed from charging and discharging experiments. This OCV difference is known as the hysteresis voltage. From Figure 3-18, the hysteresis voltage appears most pronounced in SOC between *ca.* 0.05 and 0.4. This hysteresis voltage is shown in greater detail in Figure 3-19. The largest hysteresis voltage is observed to be *ca.* 50 mV, at the knee of the OCV curve (SOC \approx 0.05). One way to account for this hysteresis voltage

in the distributed SOC model, shown previously in Figure 2-5 (p. 61), is to use a different set of model parameters for each current direction. Alternatively, in this work, the open-circuit voltage V_{OC} parameter in the distributed SOC model uses the average between the OCV extracted from discharging and charging pulse experiments. In this way, the expected maximum error introduced from excluding the hysteresis effect is half of *ca.* 50 mV, which is *ca.* 25 mV. At cell SOC away from the knee of the OCV curve, the expected error would be less. This is a commonly adopted simplification [2]–[4], [6], [7], [18], [19], [30], [59], [67], and simplifies the model implementation.

The technique to extract the diffusion capacitance C_D , diffusion resistance R_D , and series resistance R_S for the distributed SOC model is discussed previously in Section 2.3. From Equation [2-19],

$$C_D = \frac{\Delta Q}{(V_{OC,f} - V_{OC,i})}. \quad [3-2]$$

C_D only depends on the OCV before ($V_{OC,i}$) and after ($V_{OC,f}$) each pulse, and the total amount of charge inserted or extracted during the pulse phase. Therefore, the dependence of C_D on SOC for the different pulse currents and current directions should match each other well, since the OCV dependence on SOC is shown to overlap significantly in Figure 3-18. The dependence of C_D on SOC for the discharging pulse experiments are shown in Figure 3-20, and the corresponding results for charging pulse experiments are shown in Figure 3-21. The diffusion capacitance C_D extracted from different currents and different current directions (charge/discharge) match well, except the noticeable deviation at SOC of *ca.* 0.05 and 0.2 from the discharging current pulse experiments. This is likely due to the cycle-to-cycle capacity

differences or minor differences in starting cell SOC established by the initialization procedure, which resulted in a difference in SOC at the beginning of the corresponding pulse phase. As the cell OCV decreases steeply at low SOC, this SOC difference at the beginning of the pulse leads to a significant OCV difference. In turn this causes the extracted diffusion capacitance C_D to be different between the different discharging pulse experiments at low SOC.

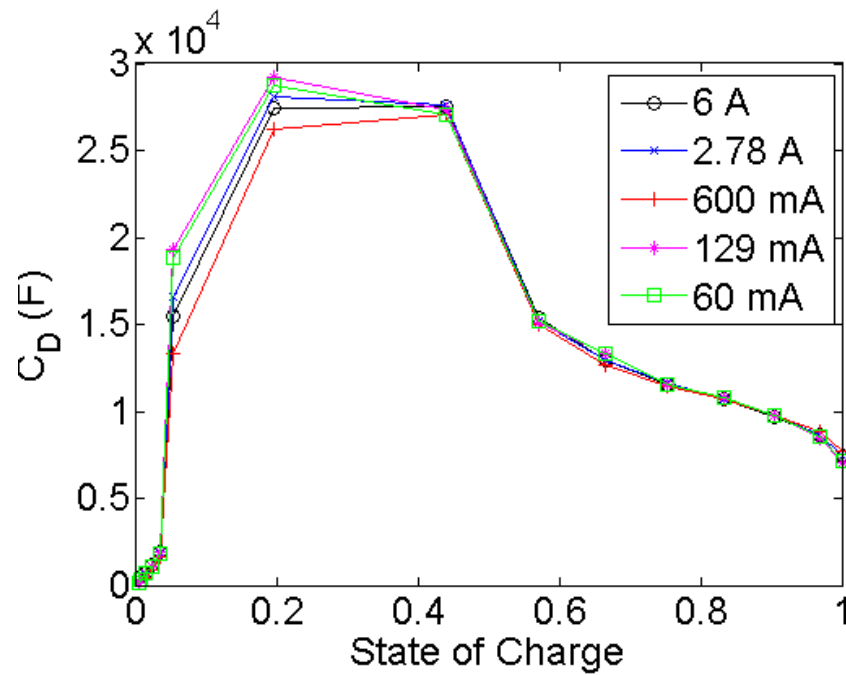


Figure 3-20. Diffusion capacitance as a function of SOC, extracted from discharging pulses.

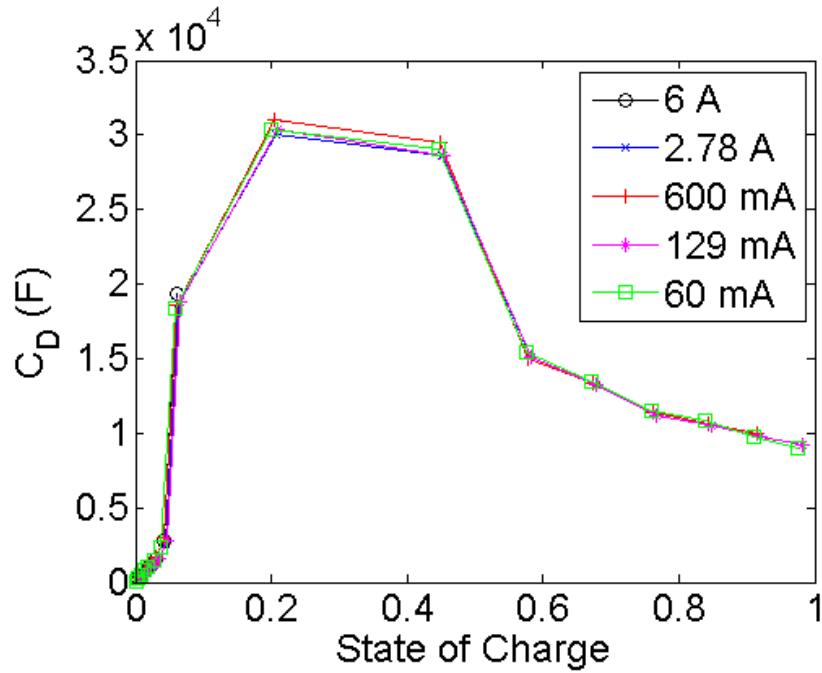


Figure 3-21. Diffusion capacitance as a function of SOC, extracted from charging pulses.

In Figure 3-20 and Figure 3-21, there appears to be a broad diffusion capacitance C_D peak between states of charge of *ca.* 0.2 to 0.45. This corresponds to the flattest section in the OCV plot in Figure 3-18. There is lower, but still appreciable, capacitance towards higher SOC. As in the case of the diffusion capacitance C_D of the Dow Kokam lithium-ion polymer cell discussed in Section 2.3.3, the capacitance peaks shown in this figure is related to the quasi-phase equilibria of the reactions [82]–[84] in the positive electrode material (transition metal ions) and negative electrode material (intercalation of lithium ions at different stages in the carbon) [85]–[87]. It is interesting to compare the diffusion capacitance C_D obtained for the Dow Kokam lithium-ion polymer cell in Section 2.3.3, shown in Figure 2-19, and the capacitance C_D obtained for the 30U cylindrical cell shown in Figure 3-20 and Figure 3-21. The diffusion capacitance of the Dow

Kokam lithium-ion polymer cell has more peaks, at states of charge of *ca.* 0.1, 0.25, and 0.45. This can be attributed to the existence of phase equilibria reactions of the transition metal ions $\text{Ni}^{2+}/\text{Ni}^{3+}$, $\text{Mn}^{2+}/\text{Mn}^{3+}$, and $\text{Co}^{2+}/\text{Co}^{3+}$ that occur at different states of charge in the Nickel-Manganese-Cobalt-Oxide positive electrode and intercalation of lithium ions at different stages of the carbon negative electrode. On the other hand, the precise chemistry of the 30U cylindrical cell tested in this chapter is not known. It is therefore likely that the chemical identity of the positive and/or negative electrodes in the 30U cell are different from the Dow Kokam lithium-ion polymer cell. Another possible reason for the difference in diffusion capacitance between the two cells is that the fewer applied pulses used to test the 30U cylindrical cell does not effectively yield the detailed shapes of the diffusion capacitance curve. However, as will be shown in Section 3.3, the number of pulses employed in the discharging and charging pulse experiments here is sufficient to yield model parameters that give good simulation accuracy for the validation tests. Finding the origin of the broad peak of the diffusion capacitance of the 30U cylindrical cell would require additional electrochemical experiments such as differential capacity analysis [82]–[84], [95].

As discussed in Section 2.3.1, the initial evolution of the cell voltage response to the current pulse is used to extract diffusion resistance R_D according to equation [2-29], which is

$$R_D = (M_0/2I)^2 \pi C_D. \quad [3-3]$$

The cell voltage at the instant the current pulse is applied is used to extract series resistance R_S , according to equation [2-31], which states that

$$R_S = \frac{M_1 - V_{OC,i}}{I_P}. \quad [3-4]$$

Using the fitted parameters C_D , R_D and R_S , the theoretical prediction of the cell response (given by equation [2-20]),

$$V(\alpha, t) = V_{OC,i} + 2I_p R_T (t/\tau)^{1/2} \sum_{n=0}^{\infty} \left\{ ierfc \left(\frac{(2n+1) - \alpha}{2(t/\tau)^{1/2}} \right) + ierfc \left(\frac{(2n+1) + \alpha}{2(t/\tau)^{1/2}} \right) \right\}, \quad [3-5]$$

can be compared to the measured response of the cell to quantify the suitability of the distributed SOC model. A good match validates the use of this model for the pulse, while a poor match means the model is unsuitable. The next step is to look at the effectiveness of the fit used to extract the model parameters.

In this work, the quality of fit between the measured and predicted cell voltage during the pulse phase of each pulse can be quantified using the measure Normalized-Root-Mean-Square-Error (NRMSE), defined as

$$NRMSE = 1 - \frac{\|V_{sim} - V_{exp}\|}{\|V_{sim} - \overline{V_{exp}}\|}, \quad [3-6]$$

where V_{sim} is the simulated cell voltage, V_{exp} is the measured cell voltage, and $\overline{V_{exp}}$ is the mean measured cell voltage. All three of these measures are applied to the pulse phase of the current pulse. The term in the far-right of Equation [3-6] is the ratio of the simulation error to the difference between the simulated and mean experimental voltage (all points). The NRMSE varies between 1 (best fit) and $-\text{Infinity}$ (bad fit). The NRMSE of the discharging pulse experiments at the five tested current magnitudes are shown in the left plot of Figure 3-22, while the corresponding results for the charging pulse experiments are shown in the left plot of Figure 3-23. In the right plot of the respective figures, the magnified view of the low SOC region is shown.

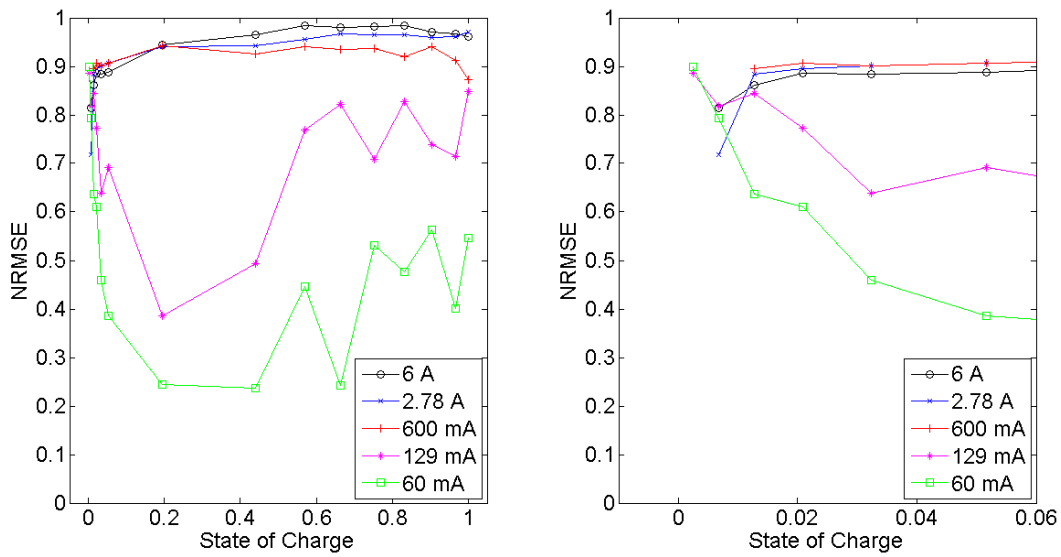


Figure 3-22. NRMSE for the discharging pulse experiments at different current magnitudes. The left plot shows the entire SOC range, while the right plot shows the magnified view of the low SOC region.

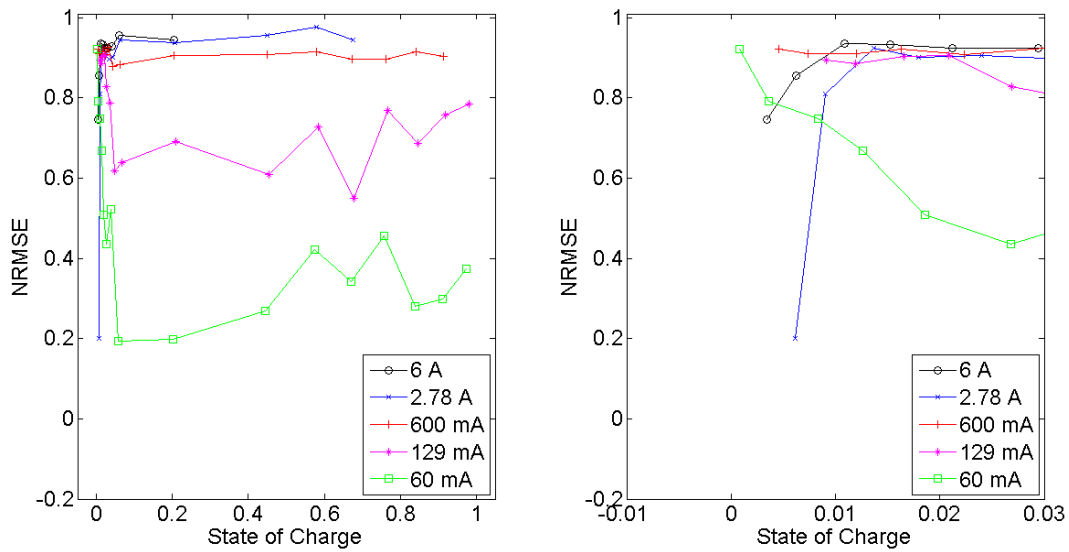


Figure 3-23. NRMSE for the charging pulse experiments at different current magnitudes. The left plot shows the entire SOC range, while the right plot shows the magnified view of the low SOC region.

Three observations can be made here. First, the higher current pulse experiments (6.0 A, 2.78 A, and 600 mA) have generally high NRMSE (>0.85). An example is the first pulse from the 6.0 A discharging pulse experiment, which is shown in Figure 3-24. The fit NRMSE is 0.96. As seen in this plot, the theoretical response (equation [3-5]) fits quite well to the experimental results.

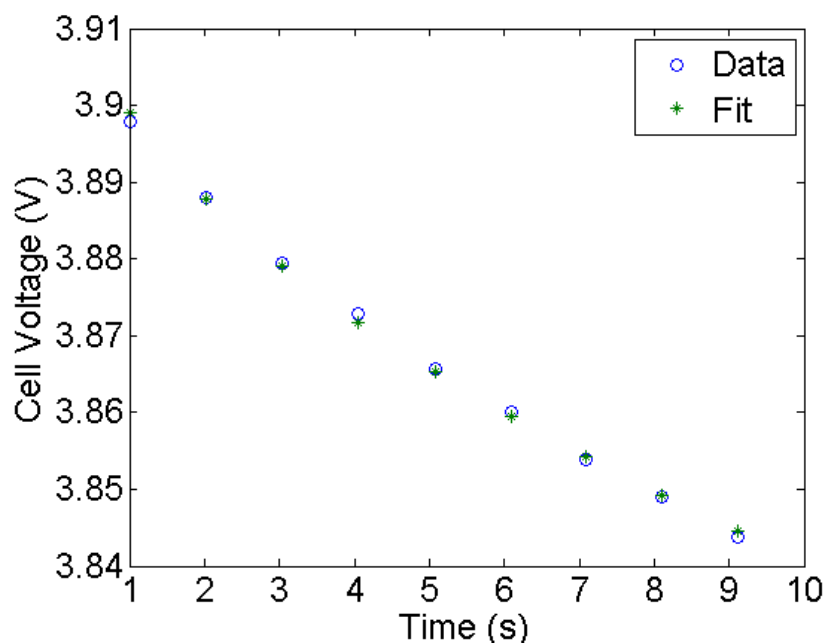


Figure 3-24. Comparison of the experimental data and calculated fit of the pulse phase cell voltage for the 1st pulse in the 6.0 A discharging pulse experiment. The NRMSE of the fit is 0.96.

Second, in both discharging and charging pulse experiments, the NRMSE is significantly lower for the 129 mA and 60 mA cases. An example of one of these fits between the measured and theoretical pulse phase cell voltage is shown in Figure 3-25. This is from the second pulse of the 129 mA discharging pulse experiment, which has a NRMSE of 0.71. The reason for the poor fit can be attributed to the readily visible quantization error. The quantization error is significant

because for the 129 mA and 60 mA current magnitudes (0.043 C and 0.020 C, respectively), the induced cell voltage change during the pulse phase is too small for accurate measurement from the battery tester used. This is an instrumentation issue. Nevertheless, the trend is similar.

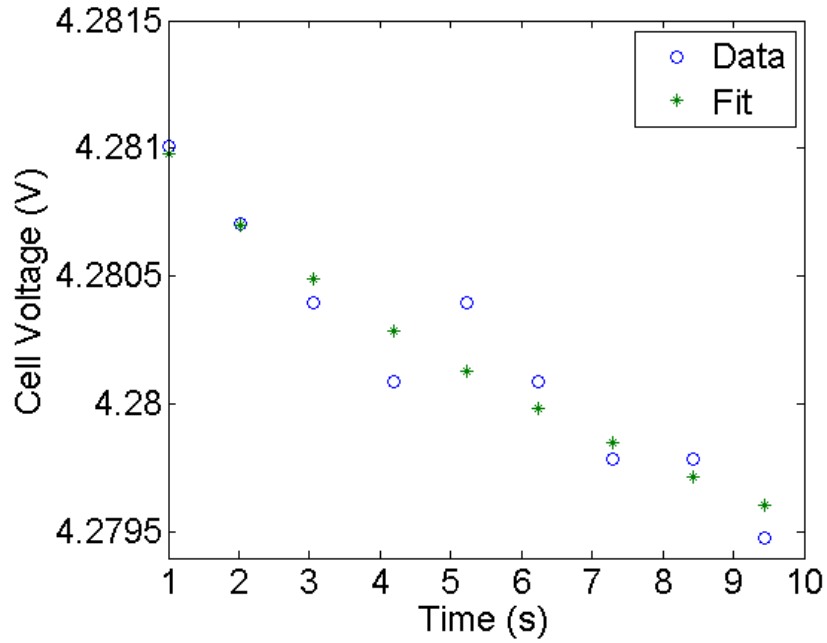


Figure 3-25. Comparison of the experimental data and calculated fit of the pulse phase cell voltage during the 2nd pulse in the 129 mA pulsed discharge experiment. The NRMSE of the fit is 0.71.

Third, while the experiments with higher current magnitudes (6.0 A, 2.78 A, and 600 mA) have generally high NRMSE (>0.85), there are some pulses at low SOC where the NRMSE is low.

This is visible in the right plots of Figure 3-22 and Figure 3-23. An example is the low NRMSE of 0.81 for the 13th pulse of the 6.0 A discharging pulse experiment, shown in Figure 3-26. The experimental data exhibits a nearly linear fall with a negative curvature, while the theoretical response proceeds according to the best $t^{1/2}$ fit. The shape of the measured cell response could be attributed to the rapidly changing diffusion capacitance C_D of the cell at low SOC, as shown in

Figure 3-20. As the capacitance C_D drops rapidly, the assumption that the distributed SOC model parameters are constant, which is used to derive equation [3-5] in Section 2.3.1, is violated. Similar but more pronounced behavior was observed in Section 2.3.3 for the pulsed discharge experiments on the Dow Kokam lithium ion polymer cell (see Figure 2-18). This was one possible reason for the poor match between the simulated and experimental results at low SOC of the validation experiments.

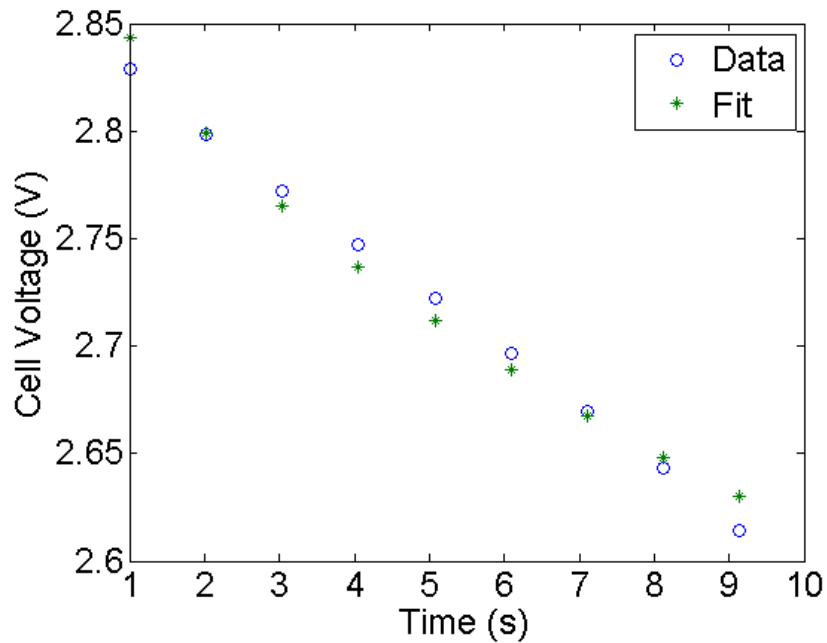


Figure 3-26. Comparison of the experimental data and calculated fit of the pulse phase cell voltage during the 13th pulse in the 6.0 A discharging pulse experiment. The NRMSE of the fit is 0.81.

From the above discussion, it is apparent that the value of NRMSE can be used as a quantitative measure of the goodness-of-fit to screen out poor fits between the experimental and theoretical (equation [3-5]) cell voltage during the pulse phase of the pulsed experiments. Good fit between the two means that the theory matches measured data well, and so the extracted model

parameters for the distributed SOC model should be accurate. Therefore, poor fit of the theoretical prediction to the measured cell voltage can be used to eliminate the corresponding extracted model parameters from being used in the model for simulations. It is decided that a cutoff value of 0.85 NRMSE can be used as a threshold to eliminate poorly fitted discharging and charging current pulses.

The dependence of the cell model parameter V_{OC} (open-circuit voltage), R_D (diffusion resistance), and R_s (series resistance), on cell SOC for the different charge and discharge current pulses is fit to empirical expressions in this work, so that simulations of different load conditions (later in Section 3.3) can be performed using a single empirical relationship for that model parameter. Model parameters extracted from pulses with fits between the measured and theoretical pulse phase voltage that have NRMSE greater than 0.85 will be shown here, together with the empirical fitting results.

The functional form of the fit for the OCV parameter V_{OC} as a function of SOC, based on the work of Chen and Rincon-Mora [2], is

$$V_{OC}(SOC) = A_1 \exp(-B_1 SOC) + C_1 + D_1 SOC + E_1 SOC^2 + F_1 SOC^3, \quad [3-7]$$

where parameters A_1 , B_1 , C_1 , D_1 , E_1 , and F_1 are parameters obtained from the fit. The fit is performed using MATLAB® and are shown in Table 3-7. Comparison of the fit to the extracted OCV is shown in Figure 3-27. This plot shows that the fit matches the extracted OCV results well, demonstrating the suitability of the chosen form of equation [3-7]. At SOC above 0.20, the maximum difference between the predicted and extracted V_{OC} is 13 mV. At SOC below 0.2, due

to the drastic drop in OCV for decreasing SOC, the max difference between the predicted and measured OCV is 80 mV.

Model Parameter V_{oc} (open-circuit voltage)	Fitted Value
A_1	-0.654 ± 0.050
B_1	37.5 ± 6.5
C_1	3.76 ± 0.06
D_1	-0.245 ± 0.420
E_1	0.986 ± 0.812
F_1	-0.167 ± 0.463

Table 3-7. Fitted parameters for the OCV dependence on SOC. The empirical relationship between the OCV and SOC has the form shown in equation [3-7].

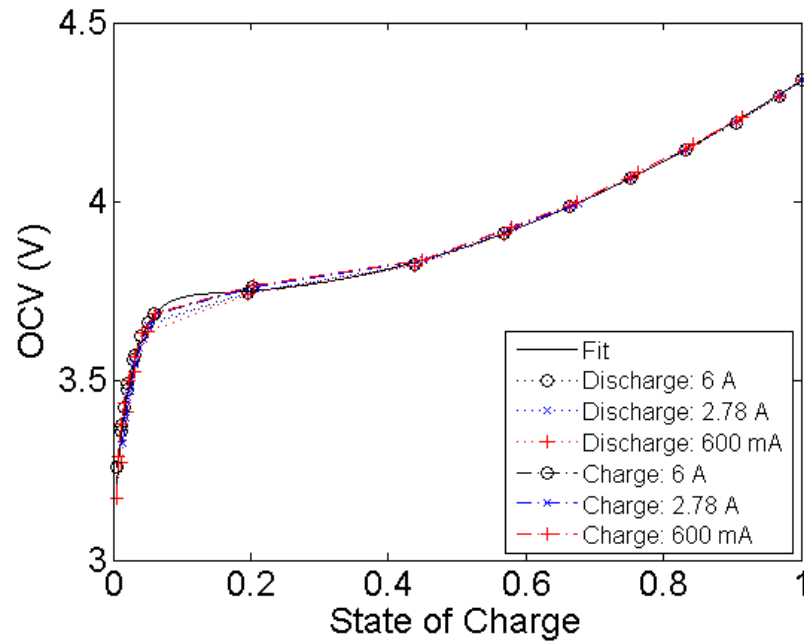


Figure 3-27. Plot of the OCV as a function of SOC obtained from the different pulsed current experiments, and the empirical fit.

The diffusion resistance R_D , which is given by Equation [3-3], is calculated from the diffusion capacitance C_D (shown in Figure 3-20 and Figure 3-21), and fitting the initial cell voltage response during the pulse phase of the pulsed experiments. The extracted diffusion resistance R_D is shown in Figure 3-28. As mentioned earlier in Section 2.3.3, R_D is interpreted physically as a diffusion resistance that determines the rate of transport of ions inside the cell's electrodes. The variation of the diffusion resistance as a function of SOC can be attributed to the differences in diffusion coefficients in the electrodes as they evolve amongst various charge states and phases during charge and discharge [85]–[87]. Like the open-circuit voltage parameter V_{OC} , the R_D dependence on SOC was fit to an empirical equation. In this case, R_D is fitted to a 6th-order polynomial

$$R_D(SOC) = A_2 + B_2SOC + C_2SOC^2 + D_2SOC^3 + E_2SOC^4 + F_2SOC^5 + G_2SOC^6, \quad [3-8]$$

where A_2 , B_2 , C_2 , D_2 , E_2 , F_2 , and G_2 , are parameters obtained from the fit. The fitting results are shown in Figure 3-28. The obtained fit parameters are shown in

Table 3-8. The largest deviation between the obtained fit and the extracted diffusion resistance R_D is for the 6.0 A discharging pulse at SOC close to *ca.* 0.05. This may be attributed to over-estimation of the diffusion capacitance C_D of the cell at low SOC. As the diffusion resistance R_D is proportional to diffusion capacitance C_D (equation [3-5]), over-estimation of the diffusion capacitance would lead to the corresponding over-estimation of the diffusion resistance. As it is rapidly decreasing at low SOC, the diffusion capacitance C_D , shown in Figure 3-20, is most prone to over-estimation there.

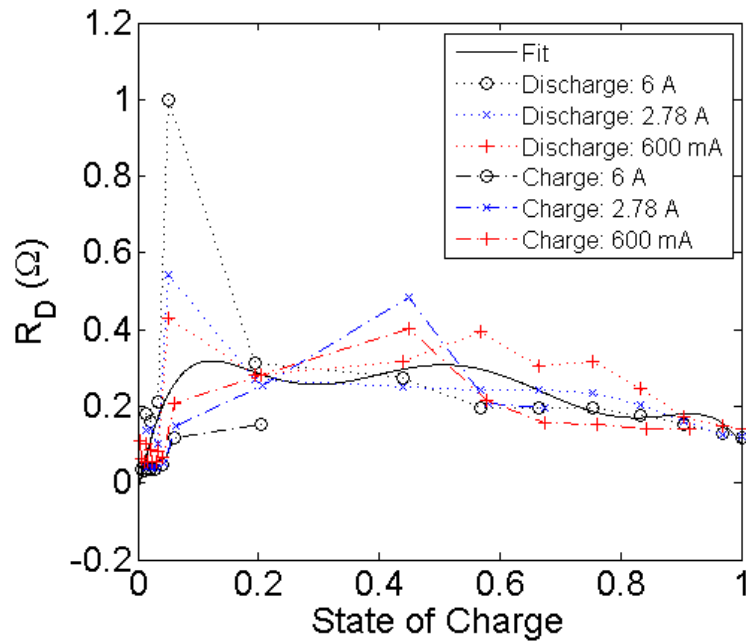


Figure 3-28. Plot of the extracted diffusion resistance R_D from pulsed current experiments at different current magnitudes, and the obtained empirical fit.

Model Parameter R_D (Diffusion Resistance)	Fitted Value
A_2	-0.0221 ± 0.108
B_2	7.55 ± 5.04
C_2	-59.6 ± 49.4
D_2	208 ± 191
E_2	-355 ± 362
F_2	289 ± 299
G_2	-90.4 ± 98.0

Table 3-8. Fitted parameters for the diffusion resistance dependence on SOC. The empirical relationship between the diffusion resistance and SOC has the form shown in Equation [3-8].

The series resistance R_S for the discharging and charging pulses is extracted using equation [3-4], which makes use of the projected transmission line voltage at the electrode/electrolyte interface ($\alpha=1$), at the instant the current is applied (*i.e.* $V(\alpha=1, t=0)$). This series resistance is the sum of the resistive drops along the path of charge transport. For example, the lithium ion transport in the electrolyte solution and electronic conduction in the current collectors are contributors to the series resistance. It also includes the charge transfer resistance that represent the insertion and extraction of lithium ions at the surface of the active material particles. The extracted series resistances are shown in Figure 3-29. Consistent with the series resistance obtained for the Dow Kokam lithium-ion polymer cell in Section 2.3.3, the series resistance R_S extracted here shows a slight downward trend towards high SOC. This downward trend is also seen in a number of works in the literature [2], [27], [48], [57], [60], [88], [89]. As discussed previously in Section 2.3.3, this can be attributed to enhancement of the contact amongst the active material particles in each electrode, and between the active materials and their respective current collectors at increasing SOC. One reason for this may be that the total volume of lithium ion electrodes have been shown to increase at increasing SOC by Wang *et. al.* [90]. Since the volume of the cylindrical cell is confined by the cell can, the contact between the components of each electrode can be enhanced at increasing SOC, thereby decreasing the measured series resistance R_S .

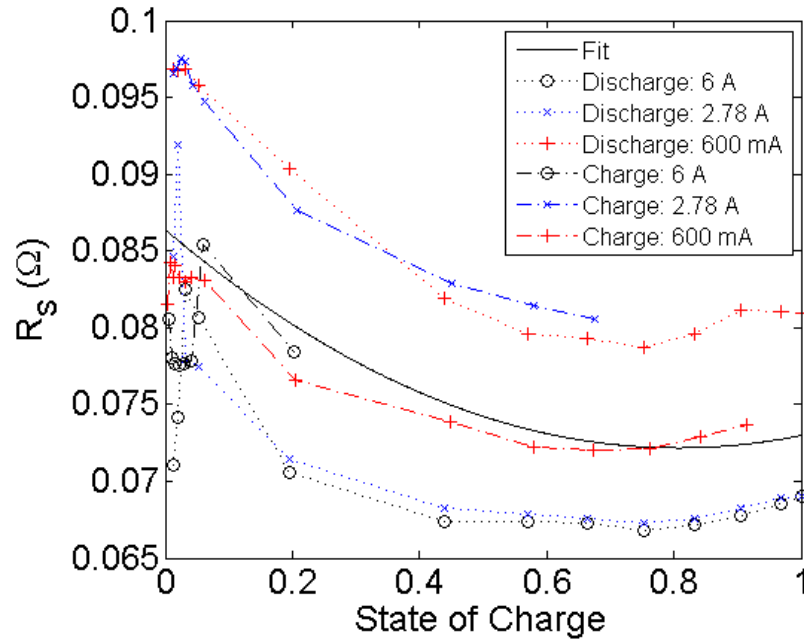


Figure 3-29. Plot of the extracted series resistance as a function of SOC, and the empirical fit of the dependence of the series resistance parameter R_s on the cell SOC.

Like the open-circuit voltage V_{OC} and diffusion resistance R_D , the dependence of series resistance R_s on SOC was fit to an empirical equation. The functional form of the fit chosen is a 2nd-order polynomial

$$R_s(SOC) = A_3 + B_3 SOC + C_3 SOC^2, \quad [3-9]$$

where A_3 , B_3 , and C_3 are parameters obtained by the fit. The fitted parameters are shown in Table 3-9. The fitting results are also shown in Figure 3-29. From this figure, it can be seen that the deviations between the fit and the extracted series resistances are generally within *ca.* 10 mΩ, or within 15%.

Model Parameter R_s (Series Resistance)	Fitted Value
A_3	0.0864 ± 0.0027
B_3	-0.0353 ± 0.0194
C_3	0.0218 ± 0.0211

Table 3-9. Fitted parameters for the series resistance dependence on SOC. The empirical relationship between the series resistance and SOC has the form shown in Equation [3-9].

From these results, it can be seen that the extracted parameters for the distributed SOC model are consistent amongst the different tested discharging and charging pulsed current magnitudes. These model parameters are fitted to empirical relationships of equations [3-7]-[3-9] (with fit parameters shown in Table 3-7 to Table 3-9), which will be used in the simulation of the validation tests in Section 3.3 to evaluate the performance of the distributed SOC model.

3.2.2.3 Comparison to Relaxation Pulse Analysis

In this section, the key innovations of the distributed SOC equivalent-circuit model developed in this thesis work are discussed. The key physical effect that has been included in this model is the use of a transmission line to account for the local SOC distribution through the depth of the cell's electrodes. This accounts for the effect of concentration variation inside the electrode particles in the electrochemical models discussed in Section 1.3.1. This distinguishes the present work from the models in the literature [2]–[7], [27], [28], [30], [53], [54], [56]–[60], [63] which use a single bulk SOC to represent the charge state in all regions of the cell. In the following

discussion, the characteristics for a popular literature model are presented first. Then the differences are discussed.

The distributed SOC model and the parameter extraction method developed in this work is most comparable to the popular model by Chen and Rincon-Mora [2], and the extraction method by relaxation phase analysis [3], [4], [6], [7], [64] commonly used with this model. As discussed in Section 1.3.2.3, Chen and Rincon-Mora's equivalent-circuit model consists of two pairs of parallel RC segments, in series with a resistance and a SOC-dependent voltage source. The model is shown in (p. **Error! Bookmark not defined.**). The resistive and capacitive elements in the main circuit on the right are dependent on a single bulk SOC in this model.

In order to extract the circuit parameters of Chen and Rincon-Mora's model for simulation, there are two main methods, depending on whether the parameter extraction is applied to measured cell voltage during the pulse phase [2], [30], [59] or the relaxation phase [3], [4], [6], [7], [64] of the applied current pulse. An illustration of the pulse and relaxation phases of a pulsed current experiment are shown in Figure 2-8 (p. 67). First, parameter extraction can be performed during the beginning seconds of the pulse phase of the pulsed current experiment [2], [30], [59]. The cell voltage at this initial time period is fitted to the main equivalent-circuit (right side circuit of Figure 1-24, p. 38) to obtain the parameters as follows. The voltage across the series resistor R_{Series} is

$$V_0 = I_{Batt} R_{Series}, \quad [3-10]$$

where I_{Batt} is the applied current during the pulse phase. The voltage across the parallel combination of $R_{Transient_S}$ and $C_{Transient_S}$ is given by

$$V_1 = I_{Batt} R_{Transient_S} \left(1 - \exp \left(- \frac{t}{R_{Transient_S} C_{Transient_S}} \right) \right), \quad [3-11]$$

while the voltage across the parallel combination of $R_{Transient_L}$ and $C_{Transient_L}$ is

$$V_2 = I_{Batt} R_{Transient_L} \left(1 - \exp \left(- \frac{t}{R_{Transient_L} C_{Transient_L}} \right) \right). \quad [3-12]$$

Therefore, the cell terminal voltage V_{Batt} is given by

$$\begin{aligned} \frac{V_{Batt} - V_{OC}}{I_{Batt}} = & R_{Series} + R_{Transient_S} \left(1 - \exp \left(- \frac{t}{R_{Transient_S} C_{Transient_S}} \right) \right) \\ & + R_{Transient_L} \left(1 - \exp \left(- \frac{t}{R_{Transient_L} C_{Transient_L}} \right) \right), \end{aligned} \quad [3-13]$$

where V_{OC} is the cell OCV prior to the applied pulse.

The model parameters (R_{Series} , $R_{Transient_S}$, $C_{Transient_S}$, $R_{Transient_L}$, and $C_{Transient_L}$) are obtained from fitting equation [3-13] to the measured results. Only the beginning seconds of the pulse phase cell voltage can be used, because the cell SOC would be appreciably altered by the applied current beyond this time. This means that this method of parameter extraction can only extract time constants ($\tau_1 = R_{Transient_S} C_{Transient_S}$ and $\tau_2 = R_{Transient_L} C_{Transient_L}$) on the order of seconds [2], [30], [59]. Long time constants cannot be obtained.

The second main parameter extraction method performs the data fitting in the relaxation phase of the pulsed current experiment [3], [4], [6], [7], [64]. For each tested current magnitude, the pulse phase of the current pulse shifts the cell to the targeted bulk SOC. The relaxation phase response is analyzed to obtain the model parameters at this SOC. Then, the next current pulse is applied and the process is repeated. Like the pulsed discharging and charging experiments described in

Section 3.2.2.1, the pulse phase durations would have to be adjusted for different currents to reach the same target SOC.

In the relaxation phase, as the current has been stopped, the SOC stays constant. The voltage across R_{Series} becomes zero, while the charges stored in the capacitors $C_{Transient_S}$ and $C_{Transient_L}$ in the pulse phase are discharged by resistors $R_{Transient_S}$ and $R_{Transient_L}$, respectively. The voltage across the parallel combination of $R_{Transient_S}$ and $C_{Transient_S}$ is given by

$$V_1 = I_{Batt} R_{Transient_S} \left(\exp \left(-\frac{t}{R_{Transient_S} C_{Transient_S}} \right) \right), \quad [3-14]$$

and the voltage across the parallel combination of $R_{Transient_L}$ and $C_{Transient_L}$ is

$$V_2 = I_{Batt} R_{Transient_L} \left(\exp \left(-\frac{t}{R_{Transient_L} C_{Transient_L}} \right) \right). \quad [3-15]$$

The cell terminal voltage V_{Batt} is given by

$$\begin{aligned} \frac{V_{Batt} - V_{OC}}{I_{Batt}} = & R_{Series} + R_{Transient_S} \left(\exp \left(-\frac{t}{R_{Transient_S} C_{Transient_S}} \right) \right) \\ & + R_{Transient_L} \left(\exp \left(-\frac{t}{R_{Transient_L} C_{Transient_L}} \right) \right), \end{aligned} \quad [3-16]$$

where V_{OC} is the cell OCV when the cell has relaxed at this SOC. Using the set of equations [3-14]-[3-16], with I_{Batt} set to the applied current during the pulse phase, the model parameters are extracted by fitting. It has been shown that the obtained circuit parameters not only depend on cell SOC, they also depend strongly on the current direction (charge vs. discharge) and the current magnitude [3], [4], [6]. This means that model parameter extraction using this method requires a large number of pulsed current experiments to obtain a model for an application. Prior to the parameter extraction, the range of discharge and charge currents for the intended

application needs to be known, and a sufficient number of pulsed current experiments over the designed current range would need to be performed. The obtained circuit parameters would be dependent on SOC, current direction (charge vs. discharge), and current magnitude.

The parameter extraction results can be compared between Chen and Rincon-Mora's model [2] using relaxation phase extraction as described above, and the distributed SOC model developed in this thesis work. The term on the left side of equation [3-13], $(V_{Batt} - V_{OC})/I_{Batt}$, which is used for fitting to obtain the circuit model parameters, is plotted in Figure 3-30 for the cell during the relaxation phase of the first pulse at the five tested discharge current magnitudes. As shown in this plot, the higher the pulse current magnitude, the faster the cell voltage decays during the subsequent relaxation phase. This results in shorter extracted time constants τ_1

($=R_{Transient_S}C_{Transient_S}$) and τ_2 ($=R_{Transient_L}C_{Transient_L}$), which confirms the need for different model parameters at different current magnitudes. At the two lower tested current magnitudes, the quantization error mentioned earlier is again visible, but the trend that higher pulse current magnitude results in faster cell voltage decay still holds.

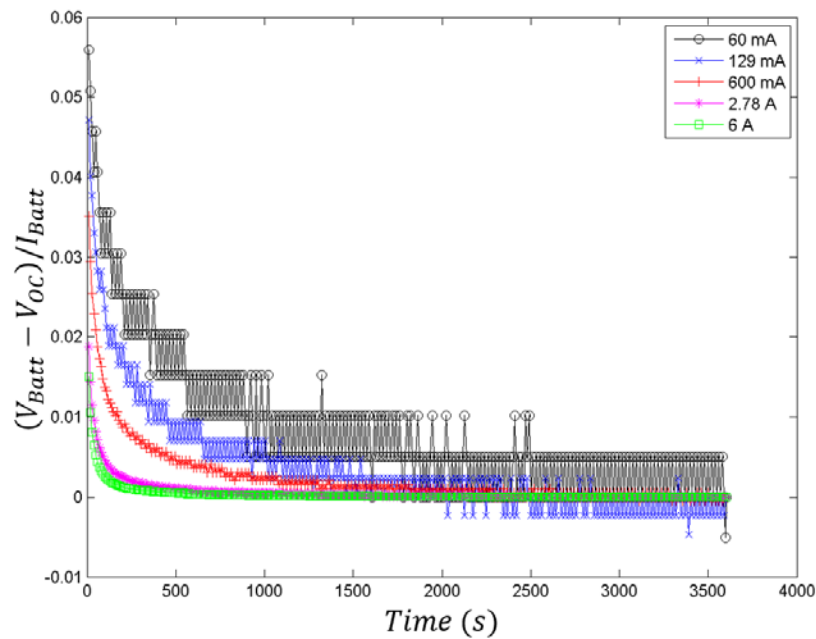


Figure 3-30. 30U cell voltage during the relaxation phase of the first pulse of the pulsed discharge experiment at the five tested discharge current magnitudes.

Physically, the relaxation cell voltage seen in Figure 3-30 are simply the result of re-equilibration of the injected charge redistributing itself. Since charge diffuses into the electrodes, it takes time to redistribute, as represented by the linear version of the distributed SOC model, shown in Figure 2-4 (p. 59). If diffusion can explain the response, then a model that includes diffusion behaviour will not need to re-measure the apparent time constant at multiple currents, saving time and effort, and making the model more accurate. If two RC time constants is used in place of such a diffusion model, then it is expected that the apparent equilibration time constant will be a function of current, as is now explained.

The argument used to justify that it is reasonable to assume that changing apparent relaxation time is explained by diffusion is based on the fact that larger currents are applied for shorter time, as the current pulses are of the same total charge. When currents are applied for shorter times, there is more build-up of charge close to the surface ($\alpha=1$) of the electrode (or in fact close to the surface of the particles that make up the electrode). This spatially more compact concentration gradient will initially dissipate faster, as expected by Fick's first law. Later it is shown that indeed parameters extracted from the pulse phase at one current magnitude are quite consistent with those extracted at other current magnitudes.

For simplicity, this analysis will consider that this model is linear, meaning that the local SOC in the transmission line does not deviate significantly from the equilibrium local SOC. During the pulse phase, the SOC distribution in the transmission line is governed by equations [2-16]-[2-18], which are reproduced here

$$\frac{\partial V}{\partial t} = \frac{1}{\tau} \frac{\partial^2 V}{\partial \alpha^2}, \quad [3-17]$$

$$\frac{\partial V}{\partial \alpha} = 0, \quad \text{at } \alpha = 0, \quad [3-18]$$

$$\frac{\partial V}{\partial \alpha} = I_P R_D, \quad \text{at } \alpha = 1. \quad [3-19]$$

At time t_P of the pulse phase, the voltage $V(\alpha, t_P)$ along the transmission line is given by the solution to this set of equations [3-17]-[3-19], which is shown to be given by equation [2-20] in Section 2.3.1, reproduced here

$$V(\alpha, t_P) = V_{OC,i} + 2I_P R_D (t_P/\tau)^{1/2} \sum_{n=0}^{\infty} \left\{ \operatorname{ierfc} \left(\frac{(2n+1) - \alpha}{2(t_P/\tau)^{1/2}} \right) + \operatorname{ierfc} \left(\frac{(2n+1) + \alpha}{2(t_P/\tau)^{1/2}} \right) \right\}. \quad [3-20]$$

The $ierfc(x)$ term decays quickly as x increases, allowing the approximation of the infinite sum in equation [3-20] as the first term ($n = 0$) at short time t . This in turns allows an approximate solution for R_D extraction according to equation [2-29].

As mentioned earlier in this section, for parameter extraction for the same target cell SOC, the pulse phase duration, T_P , differs depending on the current magnitude used during the pulsed parameter extraction experiment. The highest pulse discharge current has the shortest pulse phase duration T_P . The duration difference is inversely proportional to the current, *i.e.* one-hundred times higher current results in one-hundredth the pulse phase duration. The final voltage distribution in the transmission line at the end of the pulse phase (with duration T_P), $V_f(\alpha, T_P)$, can be shown to be given by an alternative solution to equations [3-17]-[3-19], from Carslaw and Jaeger [70], as

$$V_f(\alpha, T_P) = V_{OC,i} + I_P R_D T_P + I_P R_D \left\{ \frac{3\alpha^2 - 1}{6} - \frac{2}{\pi^2} \sum_{n=1}^{\infty} \frac{(-1)^n}{n^2} e^{-n^2 \pi^2 T_P / \tau} \cos(n\pi\alpha) \right\}. \quad [3-21]$$

As shown in this equation, the voltage distribution at the end of the pulse phase is given by the sum of constant terms and an infinite series of spatial cosines in dimensionless position α . The cosines decay at long times due to the exponentially decaying term $e^{-n^2 \pi^2 T_P / \tau}$. Therefore, for high current magnitude I_P (with small T_P), the voltage (and therefore SOC) distribution in the electrode at the end of the pulse phase has the highest contributions due to high frequency spatial cosines in dimensionless position α . At lower current magnitude I_P (with large T_P), the lower harmonics have been retained, but the higher harmonics have decayed due to exponential term $e^{-n^2 \pi^2 t_P / \tau}$, at the end of the pulse phase. This voltage distribution, $V_f(\alpha, T_P)$, is the beginning voltage distribution in the transmission line during the relaxation phase.

In the relaxation phase, the applied current has been stopped. At time t_R of the relaxation phase, the cell terminal voltage, $V_C(t_R)$, is equal to the voltage at the front (*i.e.* $\alpha=1$) of the transmission line, $V(I, t_R)$, because the resistive voltage drop from the series resistance ($I_P R_S$) is zero. The cell terminal voltage at time t_R of the relaxation phase, $V_C(t_R)$, is then given by the solution to the governing equations [3-17]-[3-19] with $I_P=0$, and initial voltage distribution along the transmission line given by $V_f(\alpha, T_P)$ of equation [3-21]. The cell terminal voltage $V_C(t_R)$ can be shown from Carslaw and Jaeger [70] to be

$$V_C(t_R) = \int_0^1 V_f(\alpha', T_P) d\alpha' + 2 \sum_{n=1}^{\infty} e^{-n^2 \pi^2 t_R / \tau} \cos(n\pi) \int_0^1 V_f(\alpha', T_P) \cos(n\pi \alpha') d\alpha'. \quad [3-22]$$

The integral in the second term on the right side of this equation is just the magnitude of the spatial cosine function, with frequency $n\pi$, of the initial voltage distribution, $V_f(\alpha, T_P)$, in the transmission line. This term is multiplied by an exponential ($e^{-n^2 \pi^2 t_R / \tau}$) that decays with time. This exponential contains $-n^2 \pi^2$, meaning that higher spatial frequencies (with higher n) in the voltage (or SOC) distribution decay much faster than lower ones. This explains the trend observed in Figure 3-30, which shows that higher discharge currents give relaxation phase cell voltages that have lower time constants. To reach the same target SOC for relaxation phase parameter extraction, the pulse phase that has a higher current magnitude I_P would use a shorter pulse phase duration T_P . This shorter pulse phase duration results in higher harmonics in the voltage distribution $V_f(\alpha, T_P)$ at the end of the pulse phase, according to equation [3-21]. This voltage distribution is the beginning distribution of the transmission line in the relaxation phase. During relaxation, the higher harmonics of the distribution $V_f(\alpha, T_P)$ decays more quickly according to equation [3-22]. This results in a cell terminal voltage $V_C(t_R)$ that decays more

quickly. For lower current magnitude in the pulse phase, the pulse phase duration is long (large T_P). The voltage distribution, $V_f(\alpha, T_P)$, at the end of the pulse phase is again given by equation [3-21], but the higher harmonics of $V_f(\alpha, T_P)$ have decayed, retaining the lower harmonics. This voltage distribution is the initial distribution in the transmission line in the relaxation phase. The lower harmonics of the distribution $V_f(\alpha, T_P)$ decays slowly during the relaxation phase, according to equation [3-22]. Therefore, the cell terminal voltage $V_C(t_R)$ decays at a slower rate than the case when higher current magnitude is used during the pulse phase. This is consistent with the behavior observed in figure 3-33.

It is the spatial frequency of the voltage (and therefore SOC) distribution that determines the decay of the cell voltage in the relaxation phase. At higher currents, the response is merely scaled proportionally. Therefore, a more accurate extraction process for the relaxation phase should be performed as a function of pulse phase durations, not currents.

In contrast with Chen and Rincon-Mora's model parameters that are extracted from relaxation phase analysis, the extracted parameters for the distributed SOC model are consistent over a large range of pulse phase current magnitudes both in charging and discharging pulse experiments. This is because parameter extraction for the distributed SOC model is performed using the cell voltage during the initial seconds (nine seconds in this thesis typically) of the pulse phase. Before the pulse phase begins, the electrode charges have equilibrated along the transmission line. A corresponding comparison of the term $(V_{Batt} - V_{OC,i})/i_{Batt}$ obtained for the pulse phase cell voltage with different current magnitudes is shown in Figure 3-31. It is shown that the cell voltage during these initial seconds of the pulse phase match very well

between 600 mA to 6 A current magnitudes. At lower pulse phase current magnitudes, the quantization error at these lower currents limit the accuracy of the measured responses at 60 mA and 129 mA current magnitudes. Nonetheless the cell voltage response is still shown to be similar in trend to the model. In conclusion, the transmission line model shows promise for avoiding the need for parameter extraction at multiple current ranges. The avoidance of the use of current dependent parameters in the distributed SOC model is likely the result of the use of a more physically accurate model.

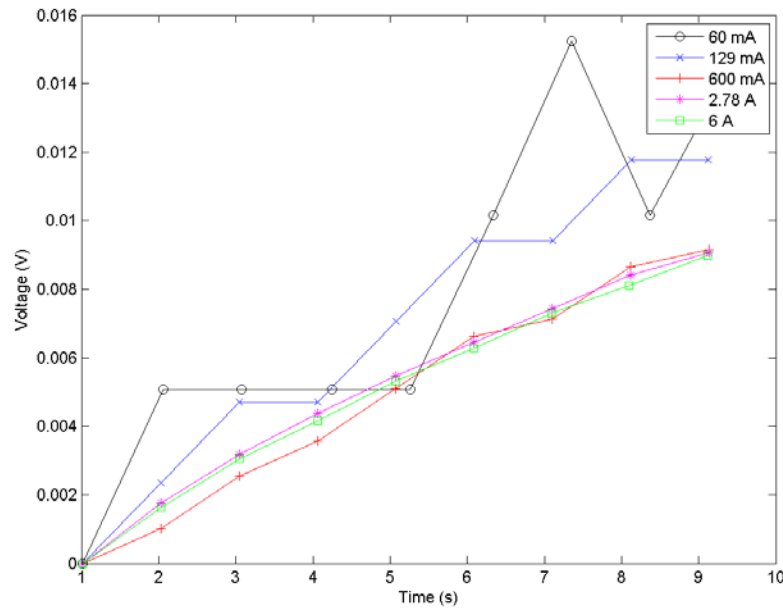


Figure 3-31. Plot of the term $(V_{Batt} - V_{OC,i})/i_{Batt}$ during the initial 9 seconds of the pulse phase at different current magnitudes.

As a result only two pulsed current parameter extraction experiments should be needed, which cuts down on the model construction significantly. One discharging pulse and one charging

pulse experiment are needed to find a good estimate of the cell open-circuit voltage V_{OC} due to the hysteresis effect discussed in Section 3.2.2.2. The further assumption used in the transmission line fit, which is that the SOC has not changed significantly in the data used in parameter extraction, appears reasonable as only the initial seconds are used even for the highest currents used. This holds as long as the diffusion coefficient is not depth dependent, or multiple diffusion coefficients come in to play at longer times.

While circuit parameters in the equivalent circuit models in the literature (such as Chen and Rincon-Mora's model [2]) depend on bulk cell SOC, the dependence of the distributed SOC model's circuit parameters on local SOC of the electrode provides a more intuitive understanding of the electrode's state during runtime. For example, the SOC distribution in the electrode during the initial eight seconds of the first 6.0 A discharge pulse is shown in Figure 3-32. Before the discharge current is applied ($t = 0$ s), the cell is fully charged and the electrode's SOC is uniformly at 1.0. After two seconds of discharge ($t = 2$ s), the SOC at the electrode's surface ($\alpha = 1$) is appreciably lower than the rest of the electrode because charges are extracted at the electrode's surface. This charge state difference leads to charges deeper in the electrode to diffuse towards the surface. As discharge proceeds, the SOC at the surface continues to decrease, while the SOC decay continues to move deeper (towards $\alpha = 0$) into the electrode. At the end of the eight seconds shown here, the SOC of the electrode at dimensionless position between 0 (electrode/current collector interface) and 0.6 are still unaffected.

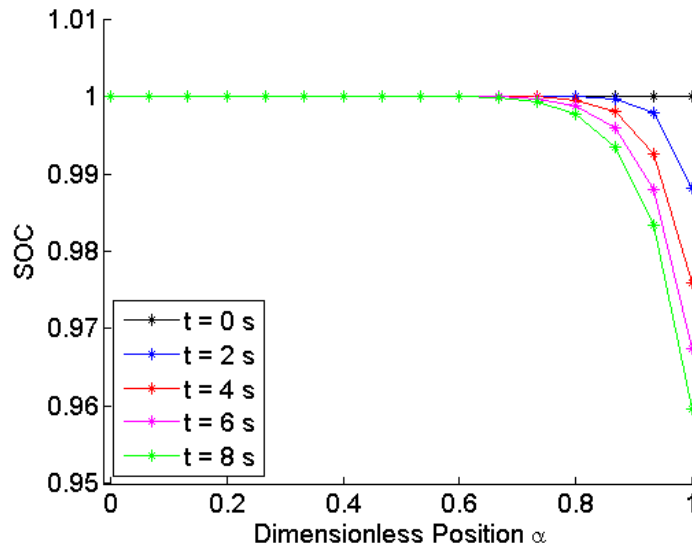


Figure 3-32. The SOC distribution in the electrode model during the initial eight seconds of the first 6.0 A discharge pulse.

Another example is the electrode's SOC distribution during the relaxation phase after the first 6.0 A discharge pulse is applied to the cell. This is shown in Figure 3-33. Due to the 6.0 A discharge current that is applied to the electrode for the duration of the pulse phase, the electrode's SOC difference between the surface ($\alpha = 1$) and the electrode/current collector interface ($\alpha = 0$) is most pronounced at the beginning of the relaxation phase ($t = 0$ s). Because the current is stopped during the relaxation phase, the SOC at the electrode's surface ($\alpha = 1$) no longer decreases during relaxation. In contrast to the pulse phase simulation shown in Figure 3-32, the SOC there increases as relaxation proceeds because the charges from deeper inside the electrode diffuse towards the surface because of the charge state difference. This leads to a corresponding decrease in the SOC deep in the electrode. After 800 seconds of relaxation, the electrode has reached equilibrium, with a uniform SOC throughout.

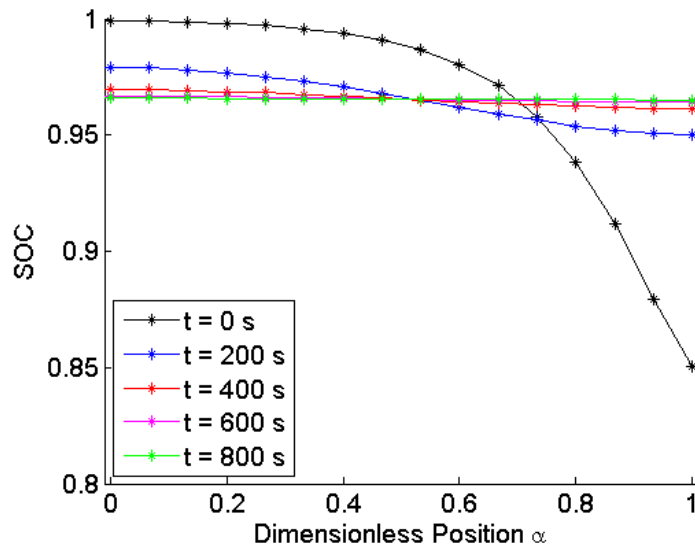


Figure 3-33. The SOC distribution in the electrode model during the relaxation phase of the first 6.0 A discharge pulse.

3.3 Validation

To test the predictive capabilities of the distributed SOC model, simulations are performed and compared to validation experiment results. The validation experiments performed are: 1. dynamic discharge tests, and 2. constant current discharge tests. The objective of the dynamic discharge test is to study the performance of the model in predicting the cell voltage behaviour under a dynamic load. Due to the proliferation of the use of lithium ion batteries in motive applications, such as electric vehicles and electric bicycles, the validation of the distributed SOC model using a dynamic load that has similar transient characteristics to those expected in these applications would be useful. The second validation profile chosen is the constant current discharge test. In this test, the cell is first fully charged, and then discharged at constant current until the cell voltage reaches its rated lower limit. This is a commonly used test that informs

how much energy can be extracted, and the remaining run-time, from a cell under different loads. This is applicable to more static load profiles, examples of which include lighting and heating applications.

This section is divided into two parts. Section 3.3.1 discusses validation of the proposed model using the dynamic discharge test, and Section 3.3.2 presents the model's validation using constant current discharge tests at four different currents. The distributed SOC model is shown to be effective at simulating dynamic stresses over a wide range of currents. On the other hand, it does not perform particularly well in describing constant current discharge at higher currents. A modification is described which enables the model to perform well in the latter case.

3.3.1 Validation Test #1

The validation of the proposed model using a dynamic discharge test is presented in this section. Section 3.3.1.1 describes the test procedure employed. The results and analysis are discussed in Section 3.3.1.2. A π -model is proposed as an alternative to the RC-structure in the transmission line model in Section 3.3.1.3. The resulting improvements in the modeling accuracy is also discussed.

3.3.1.1 Test Procedure

In this work, the key aspect of the dynamic discharge test is that its load profile captures the transient nature of application profiles of motive applications. The Dynamic Stress Test (DST),

which is shown in plot A of Figure 3-34, provides such an application profile. The DST is a test profile designed by the United States Advanced Battery Consortium (USABC) to characterize the effect of electric vehicle driving behavior on the performance and life of a battery. The definition of the DST profile can be found on the website of the United States Council for Automotive Research (USCAR) [96].

The DST is a 360 second sequence of steps with 7 discrete power levels. It is designed to be a simplified approximation of the auto-industry standard Federal Urban Driving Schedule (FUDS), which is a complex 1372 second time-velocity profile based on actual driving data. In this work, the dynamic testing is called the Dynamic Discharge Test (DDT), which will have a load profile that has the same shape as the DST's variable-power profile, but defined as current levels relative to a chosen maximum current. The variable-current load profile of the DDT is shown in plot B of Figure 3-34, which is used to validate the distributed SOC model here. The use of current levels simplifies testing and simulations, and the transient nature of loading is captured.

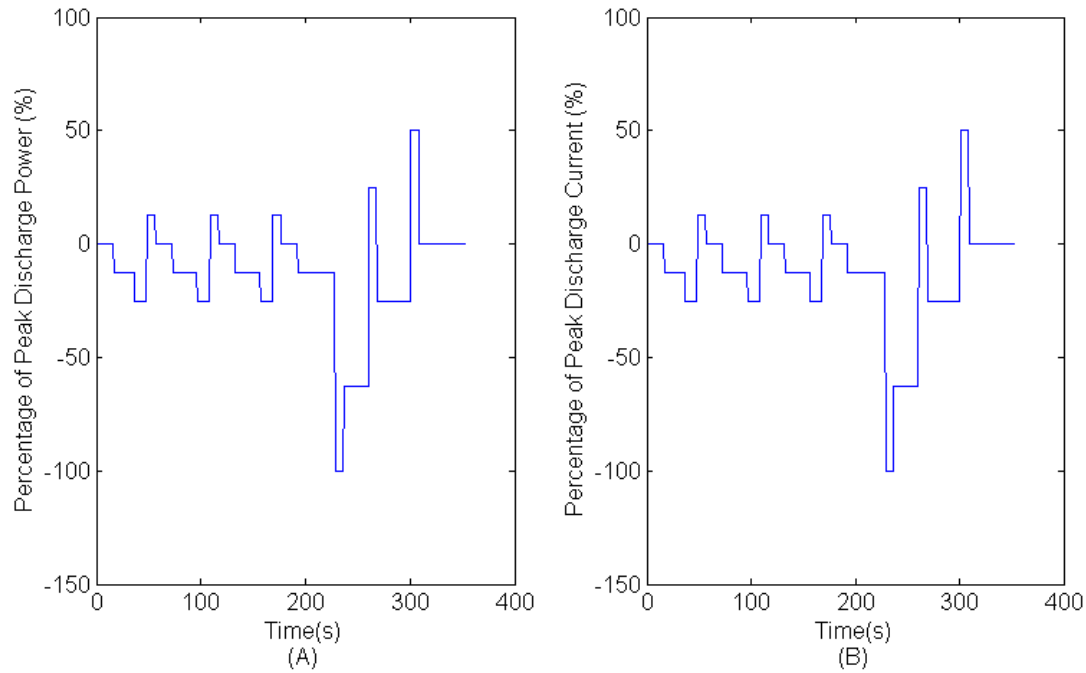


Figure 3-34. (A) The DST profile. It is a variable-power profile defined using percentages of the peak discharge power of the test. (B) The DDT profile defined in this work. This profile has the same shape as the DST, but is defined using percentages of the peak discharge current of the test. The DDT profile is simpler to simulate than the DST.

The full procedure of the DDT is shown in Table 3-10. Like the pulsed current discharge test described earlier (for example in Section 3.2.2.1), the cell is brought to a repeatable starting point through an initialization phase. The initialization is identical to the parameter extraction pulse procedure, with the addition of a step of 0.60 A (0.20 C) discharge for one hour to bring the cell to 0.80 SOC before the DDT cycling. This prevents the cell from exceeding the cell upper voltage limit of 4.35 V during the early DDT cycles, which involved charging (simulating regenerative braking for example), as well as discharge. Three DDTs are performed with different maximum currents: 6.0 A, 2.0 A, and 600 mA. For the rest of this work, the tests are

simply called the 6.0 A-, 2.0 A-, and 600 mA-DDTs, respectively. The duration of each cycle is 360 s, and the cycle procedure is repeated until the cell voltage falls below 2.50 V, which is the rated minimum voltage of the cell.

Phase	Step	Description	Step Current for 6.0 A DDT (mA)	Step Current for 2.0 A DDT (mA)	Step Current for 600 mA DDT (mA)
I. Initialization	1	Discharge the cell at 0.20 C (0.60 A) until the cell voltage falls below 2.50 V	-	-	-
	2	Rest for 1.0 hour	-	-	-
	3	Charge at 0.20 C (0.60 A) until the cell voltage reaches 4.35 V	-	-	-
	4	Hold the cell at 4.35 V until the cell voltage falls below 0.010 C (0.030 A)	-	-	-
	5	Rest for 1.0 hour	-	-	-
	6	Discharge the cell at 0.20 C (0.60 A) for 1.0 hour	-	-	-
	7	Rest for 1.0 hour	-	-	-
II. Dynamic Cycle	8	Discharge the cell at 12.5% of chosen max test current for 28 s	-750	-250	-75
	9	Discharge the cell at 25% of chosen max test current for 12 s	-1500	-500	-150
	10	Charge the cell at 12.5% of chosen max test current for 8 s	750	250	75
	11	Rest for 16 s	0	0	0
	12	Discharge the cell at 12.5% of chosen max test current for 24 s	-750	-250	-75
	13	Discharge the cell at 25% of chosen max test current for 12 s	-1500	-500	-150
	14	Charge the cell at 12.5% of chosen max test current for 8 s	750	250	75
	15	Rest for 16 s	0	0	0
	16	Discharge the cell at 12.5% of chosen max test current for 24 s	-750	-250	-75
	17	Discharge the cell at 25% of chosen max test current for 12 s	-1500	-500	-150
	18	Charge the cell at 12.5% of chosen max test current for 8 s	750	250	75
	19	Rest for 16 s	0	0	0
	20	Discharge the cell at 12.5% of chosen max test current for 36 s	-750	-250	-75
	21	Discharge the cell at 100% of chosen max test current for 8 s	-6000	-2000	-600
	22	Discharge the cell at 62.5% of chosen max test current for 24 s	-3750	-1250	-375
	23	Charge the cell at 25% of chosen max test current for 8 s	1500	500	150
	24	Discharge the cell at 25% of chosen max test current for 32 s	-1500	-500	-150
	25	Charge the cell at 50% of chosen max test current for 8 s	3000	1000	300
	26	Rest for 44 s	0	0	0
	27	Return to Step 8	-	-	-

Table 3-10. DDT procedure, and the associated step currents for the three chosen max test currents of a) 6.0 A, b) 2.0 A, and c) 600 mA.

Some characteristics of the three DDTs are shown in Table 3-11. For the 6.0 A DDT, the maximum discharging current is 6.0 A (2.0 C current) and the maximum charging current is 3.0 A (1.0 C current). The DDT profile has a net discharge effect in each cycle. The cumulative discharged capacity per cycle for the 6.0 A DDT is 75 mAh. This net discharge of 75 mAh per cycle equates to an average discharge current of 750 mA (or 0.25 C). The corresponding data for the 2.0A- and 600 mA-DDTs are also shown in Table 3-11. Therefore, a wide range of charge and discharge currents are tested using these three DDT profiles.

DDT	Maximum Discharging Current (A)	Maximum Charging Current (A)	Cumulative Discharged Capacity Per Cycle (mAh)	Average Discharging Current (mA)	Average Discharging Rate (C)
6.0 A	6.0	3.0	75	750	0.25
2.0 A	2.0	1.0	25	250	0.083
600 mA	0.60	0.30	7.5	75	0.025

Table 3-11. Characteristics of the three DDTs.

3.3.1.2 Results and Analysis

This section presents the obtained validation results from the DDTs and their analysis. As in Section 2.4.1, the distributed SOC equivalent-circuit model of Figure 2-23 (p. 90), is used for simulating the cell behavior. In Section 2.4, an 8-RC segment model is shown to give accurate simulation results for the Dow Kokam lithium-ion polymer cell characterized and validated at a single current (15 A, equivalent to 0.20 C). Simulations beyond 8-RC segments does not yield appreciable accuracy improvements. In this section, the 32 RC-segment model is used for the simulations, which should show near best-case capability of the distributed SOC model. Later in

the chapter the appropriate number of transmission line elements needed for reasonable accuracy is studied.

The lumped distributed SOC equivalent-circuit model is implemented in MATLAB® Simulink® using components in the SimPowerSystems package. By employing the full-capacity-equivalent capacitance C_{FCE} of 10,800 F (found in Section 3.2.1.2), and empirical fits for open-circuit voltage V_{OC} (equation [3-7] with parameters in Table 3-7), diffusion resistance R_D (equation [3-8] with parameters in

Table 3-8), and series resistance R_S (equation [3-9] with parameters in Table 3-9) from Section 3.2.1.2, the cell voltage responses to the validation experiment load profiles are simulated and compared to the experimental results. As the extracted values for each of the model parameters are largely independent of current magnitude in the pulsed current experiments, single empirical fits for model parameters V_{OC} , R_D , and R_S , are used to show that current-independent parameters can be used in the model to simulate the cell's response accurately. As discussed in Section 1.3.2.3, the error between the simulations and experimental cell voltages is quantified using the PVE (equation [1-9], p. 46), while the overall simulation accuracy over an entire validation test is quantified using the MAPVE (equation [1-10], p. 46) and RMSPVE (equation [1-11], p. 47). The model validation results for the three DDTs are discussed in turn below.

6.0 A DDT

As shown in Table 3-11, the maximum discharging and charging currents for the 6.0 A DDT are 6.0 A (or 2.0 C) and 3.0 A (or 1.0 C), respectively. Each cycle of the 6.0 A DDT accumulatively

discharges 75 mAh (decreases SOC by 0.025) from the cell. This corresponds to an average discharge current of 750 mA (or 0.25 C). The experimental and simulation results for the 6.0 A DDT are shown in Figure 3-35. The top plot shows the simulated and experimental cell voltage, which matches well at this magnification except towards the end of the test, which corresponds to very low cell SOC. The PVE, as defined in equation [1-9], is shown in the middle plot. The bottom plot shows the 6.0 A DDT current profile.

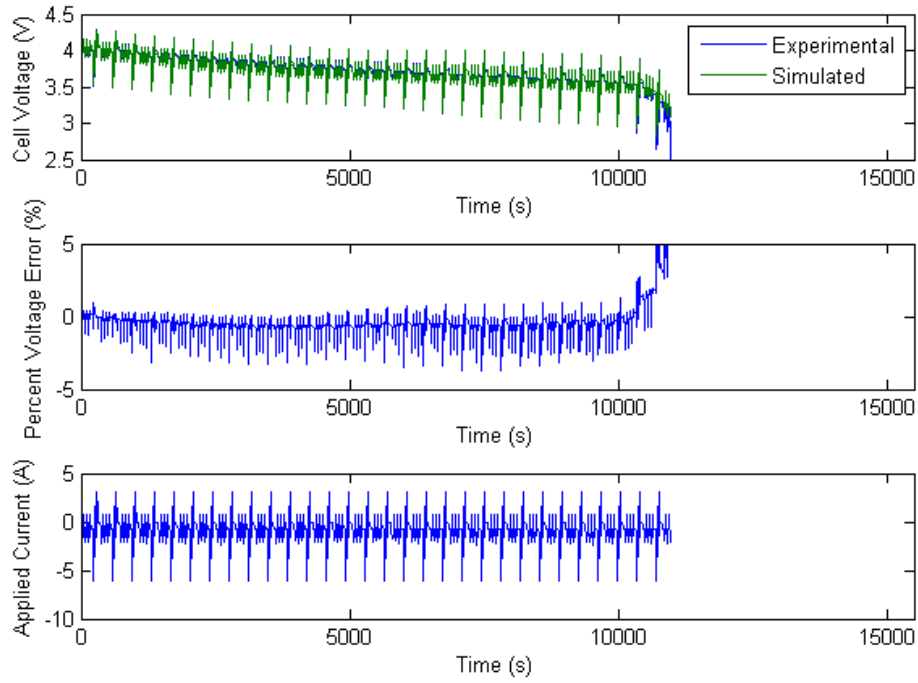


Figure 3-35. Plot of results from the 6.0 A DDT. The top plot shows the experimental and simulated results. The middle plot is the PVE of the simulated cell voltage compared to the experimental voltage. The bottom plot shows the measured current profile. As per the convention adopted in this work, negative and positive current corresponds to discharging and charging currents, respectively.

The PVE is much larger towards the end of the experiment where the SOC is lowest (as much as 20% at the end of the experiment, which is not shown). This is a commonly seen effect [3], [4], [6], [7], which is often attributed to the rapid drop of the OCV at low SOC, as shown in Figure 3-27. This means that small shifts in the initial SOC of the cell obtained from the initialization phase of the test, and minor cycle-to-cycle cell full capacity differences can affect the simulation accuracy severely.

As mentioned in Section 1.2.1, lithium ion cells can be damaged easily by over-discharge. Therefore, electronic protection circuits are typically used in conjunction with lithium ion batteries to protect the cell from over-discharge, and other abusive conditions. Due to the rapid drop in cell voltage at low SOC, there is a high risk of over-discharge while the cell is operated at low SOC. Therefore, in most applications, the cell is not operated, and the model accuracy does not demand high accuracy, in the low SOC region. For example, Lam *et. al.* [4] excluded the low SOC data in their analysis of the simulation accuracy of their equivalent-circuit model. Their reasoning was that electric vehicles batteries very rarely fall below 10% SOC. In a similar fashion, quantification of the simulation accuracy in this work will focus on the first 95% duration of the validation test results. This allows the analysis to focus on the commonly useful range of SOC (from 1.0 down to *ca.* 0.05), and removes the distortion introduced due to simulation errors observed at low SOC.

For the first 95% duration of the 6.0 A DDT (*ca.* 1.04×10^4 s), the MAPVE and root-mean-square-percent-voltage error are tabulated in Table 3-12. For this test, the MAPVE is 3.7% (or 120 mV). This is the maximum percentage deviation between the simulated and experimental results over the first 95% duration of the test. From the middle plot of Figure 3-35, it can be seen that the largest magnitude of percentage deviation occurs towards the end of the test. The RMSPVE is 0.84% (or 30 mV). As mentioned in Section 1.3.2.3, the expected MAPVE for equivalent-circuit models is on the high side of the 1-5% range suggested by Chen and Rincon-Mora [2], while the RMSPVE is expected to be on the low side of this range. Therefore, these results are within the desired range, and so the distributed SOC model is considered to work well for the 6.0 A DDT.

DDT	MAPVE (%)	MAPVE (mV)	RMSPVE (%)	RMSPVE (mV)
6.0 A	3.7	120	0.84	30
2.0 A	2.2	81	0.30	11
600 mA	1.5	53	0.46	17

Table 3-12. Tabulated results of the MAPVE (in terms of both percentage and voltage), and RMSPVE (also in terms of percentage and voltage) for the beginning 95% duration of the three DDTs. The results shown are the average over the three tested cells.

2.0 A DDT

As shown in Table 3-11, the maximum discharging and charging currents for the 2.0 A DDT are 2.0 A (or 0.67 C) and 1.0 A (or 0.33 C), respectively. Each cycle of the 2.0 A DDT accumulatively discharges 25 mAh (decreases SOC by 8.3×10^{-3}) from the cell. This corresponds to an average discharge current of 250 mA (or 0.083 C). The simulated and experimental results for the 2.0 A DDT are shown in Figure 3-36. The top plot shows the simulated and experimental cell voltage, which matches well at this magnification.

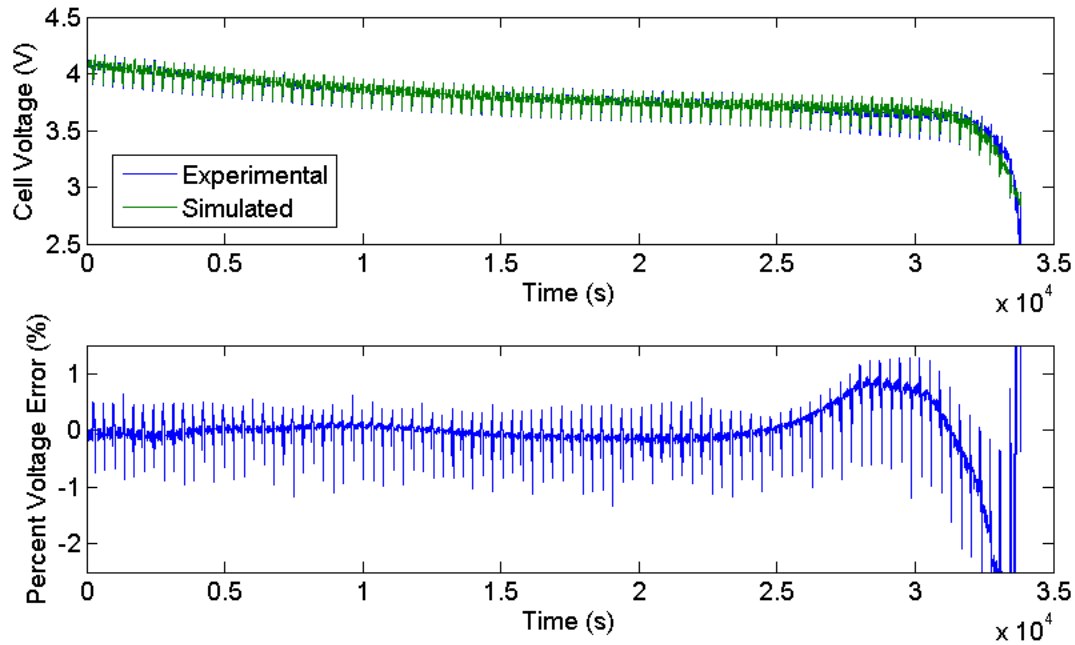


Figure 3-36. Plot of results from the 2.0 A DDT. The top plot shows the measured and simulated cell voltages. The bottom plot shows the PVE.

For the first 95% duration of the test results (*ca.* 3.21×10^4 s), the MAPVE and root-mean-square-percent-voltage error are tabulated in Table 3-12. The MAPVE is 2.2% (or 81 mV). Over this same time range, the RMS PVE is 0.30% (or 11 mV). These results are improvements compared to the 6.0 A DDT results discussed earlier. This can be attributed to the lower applied currents of this test. A lower current causes lower deviation of the cell voltage from equilibrium, and any mis-estimated resistances in the distributed SOC model would have lower resistive drops. The rapid fall and rise of the PVE towards the very end of the test (after 3.2×10^4 s) is beyond the initial 95% duration of the test, and so is not considered further. This observed behavior is likely a result of small shifts in the initial SOC of the cell, and minor cycle-to-cycle cell full capacity differences as discussed earlier in the section.

The bottom plot of Figure 3-36 shows the PVE over the duration of the 2.0 A DDT. The PVE has a pronounced rise that starts at *ca.* 2.5×10^4 s, and it begins to fall at *ca.* 3.0×10^4 s. This observed behavior can be explained as follows. To obtain the parameters used in the distributed SOC model, the experiments consist of current pulses that has pulse phases that begins at the targeted SOC listed in Table 3-2 for discharging pulses and Table 3-3 for charging pulses. As mentioned in Section 3.2.1.2, the charges of the pulses, and the corresponding sampled SOC, are designed such that the change in cell OCV after each pulse is approximately one-twentieth of the total voltage range (1.55 V) between the maximum (4.35 V) and minimum (2.80 V) rated voltages of the cell. From the results, the model parameters at these sampled SOC are extracted according to the procedure described in Section 2.3.1, and the model parameters between the sampled SOC are obtained by fitting of empirical functions of equations [3-7] to [3-9], to the obtained parameters at the sampled SOC, which is discussed in Section 3.2.2.2. Based on the number of DDT cycles (360 s each) that have been performed up to these times (*ca.* 2.5×10^4 s and 3.0×10^4 s) in the 2.0 A DDT profile, the approximate bulk SOC of the cell is estimated to be *ca.* 0.2 and 0.07 for the experiment times of 2.5×10^4 s and 3.0×10^4 s, respectively. From Table 3-2, the distributed SOC model parameters are extracted at SOC of *ca.* 0.20 (pulse 8), and the next lower SOC of *ca.* 0.056 (pulse 9). Therefore, the model parameters are susceptible to not have captured the detailed cell parameters in the region between SOC of 0.2 and 0.07.

This can be confirmed by examination of the pulsed discharge experimental results at 60 mA pulse current magnitude shown in Figure 3-14 (p. 127). Due to the low current magnitude during the pulse phase, the cell voltage in this plot is approximately equal to the cell OCV at the

respective cumulative discharged capacity. The SOC of 0.2 and 0.056 correspond to cumulative discharged capacities of 2.4 Ah and 2.8 Ah, respectively. As seen in this plot, the cell voltage has a plateau between cumulative discharged capacities of *ca.* 2.6 and 2.8. The empirical fit of the cell open-circuit voltage V_{OC} , shown in Figure 3-27, has over-estimated the cell OCV in this region, leading to the observed model accuracy degradation. In the future, the simulation accuracy in this region can be improved by modifying the pulsed experiments to obtain distributed SOC model parameters at SOC between 0.2 and 0.056.

600 mA DDT

As shown in Table 3-11, the maximum discharging and charging currents for the 600 mA DDT are 600 mA (or 0.20 C) and 300 mA (or 0.10 C), respectively. Each cycle of the 600 mA DDT accumulatively discharges 7.5 mAh (decreases SOC by 2.5×10^{-3}) from the cell. This corresponds to an average discharge current of 75 mA (or 0.025 C). The experimental and simulation results for the 600 mA DDT is shown in Figure 3-37. The top plot shows the simulated and measured cell voltages, which match well at this magnification, except again at low SOC.

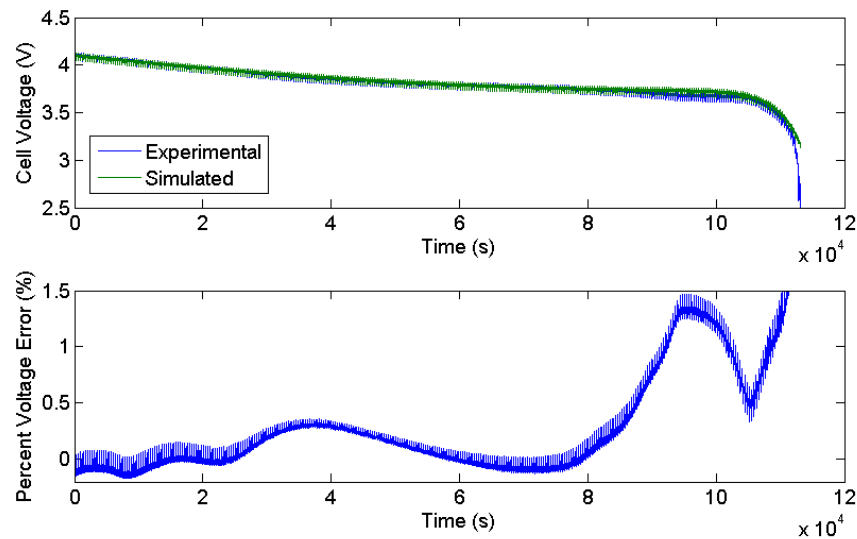


Figure 3-37. Plot of results from the 600 mA DDT. The top plot shows the measured and simulated cell voltages. The bottom plot is the PVE.

For the first 95% duration of the test results (*ca.* 1.07×10^5 s), the MAPVE and root-mean-square-percent-voltage error are tabulated in Table 3-12. The MAPVE is 1.5% (or 53 mV). Over this same time range, the RMSPVE is 0.46% (or 17 mV). The MAPVE and RMSPVE results for the three DDTs are tabulated in Table 3-12 for comparison. The MAPVE decreases for smaller test currents. This might be expected due to the lower deviation of the cell voltage from equilibrium, and any mis-estimations of the model resistances lead to lower voltage drops.

However, RMSPVE is higher for the 600 mA DDT than for the 2.0 A one. This can be examined using the bottom plot of Figure 3-37, which shows that the PVE also exhibits a rise (at *ca.* 8×10^4 s) and subsequent fall (at *ca.* 10×10^4 s), which occurs in a similar SOC region as that observed in Figure 3-36. The peak of PVE in this region for the 600 mA DDT is larger than that in the 2.0 A one. This could be due to a larger deviation between the empirical fit of the

extracted open-circuit voltage V_{OC} parameter (equation [3-7] with parameters in Table 3-7) and the real OCV at smaller currents. This can be examined using the measured cell voltage for the pulsed current experiment at different current magnitudes, which was initially shown in Figure 3-15 (p. 128). In this plot, the cell voltage during each pulse is plotted as a function of cumulative discharged capacity. In the region between SOC of 0.2 (cumulative discharged capacity of 2.40 Ah) and 0.056 (cumulative discharged capacity of 2.83 Ah), the cell voltage evolution for lower pulse current magnitudes is shown to exhibit a more pronounced plateau. This can be explained by the fact that the lower the current during the pulse phase, the closer the cell is to equilibrium. As mentioned earlier, the model open-circuit voltage parameter V_{OC} overestimates the cell OCV in this plateau region. Therefore, the more pronounced plateau at lower applied currents leads to a larger error. This may explain the observation that the RMSPVE in the 600 mA DDT is higher than that in the 2.0 A one. To improve the simulation accuracy in this region (SOC between *ca.* 0.2 and 0.056) in the future, the distributed SOC model parameters need to be extracted for more SOC's within this region.

The simulation results presented in this section use 32-RC segments in the nonlinear transmission line of the model shown in Figure 2-23 (p. 90). Here are four of the key results from this section. First, the simulation performance of the distributed SOC model is generally good. This is illustrated by the low values of the MAPVE and RMSPVE in Table 3-12. As mentioned in Section 1.3.2.3, the expected MAPVE for equivalent-circuit models is on the high side of the 1-5% range suggested by Chen and Rincon-Mora [2], while the RMSPVE is expected to be on the low side of this range. Therefore, the results tabulated in Table 3-12 are quite promising. Second, the percent-voltage error increases towards the very end of the DDTs. This

corresponds to the cell being in a very low SOC (*i.e.* high cumulative discharged capacity). This error can be attributed to minor differences in the initial cell SOC obtained from the initialization phase of the test, and cycle-to-cycle capacity differences. However, since lithium ion cells are usually not operated at such low SOC due to possibility of unexpected cutoff from the protection electronics, this reduced simulation performance of the model is not a big concern. Third, the performance of the model improves when the test currents are lowered, as illustrated by the better accuracy of the model when the maximum current of the DDT profile is reduced (see Table 3-12). This can be explained by fact that a lower current causes lower deviation of the cell voltage from equilibrium, and any mis-estimated resistances in the distributed SOC model would have lower resistive drops. Fourth, there is an SOC range between *ca.* 0.07 to 0.2 where the PVE is elevated compared to higher cell SOC. This can be attributed to a pronounced plateau in the cell open-circuit-voltage that is not well captured by the empirical fit of the open-circuit-voltage parameter V_{OC} in the model. This can be improved in the future by increasing the number of pulses to better extract the model parameters in this SOC range.

In the next section, the effect of the number of RC segments used on the accuracy is studied. Also, an alternate transmission line structure is proposed and shown to perform better using a similar number of resistive and capacitive elements. These modifications enable a simpler implementation of the distributed SOC model to be used.

3.3.1.3 The π -Model and Comparisons between Different Number of Segments

The distributed SOC model used so far in this work has the form shown in Figure 2-5 (p. 61). As discussed in Section 2.1, this model is derived from non-linearizing the equivalent-circuit model shown in Figure 2-4 (p. 59). In power and communication systems modeling, the π -form is a commonly used configuration for the RC-segment [97]. The use of π -form RC-segments will be studied as an alternative transmission line structure in this section.

The π -form RC-segment consists of the capacitance broken into two halves, and a resistance connected in between. Using such π -form segments, a one segment distributed SOC model would have the form shown in Figure 3-38. The single resistance in the π -form segment is broken into two halves as well, so the resistance of each is made dependent on the local SOC of the closest-neighboring SOC-tracking circuit. One or more segments can be added to this model. A two segment model is shown in Figure 3-39. At short times in this approach the response is dominated by the open-circuit voltage element $V_{OC}(V_{SOC1})$, which is the dependent voltage source closest to the series resistance R_S in the circuit, rather than the full resistance $R_D(V_{SOC1})/n$. The resistive and effective capacitive (from the combination of the dependent-voltage source and SOC-tracking circuit) impedances are also spread out more uniformly, which should smooth out the lumped nature of the circuit. In the limit of a large number of elements, both models converge to the continuum behaviour.

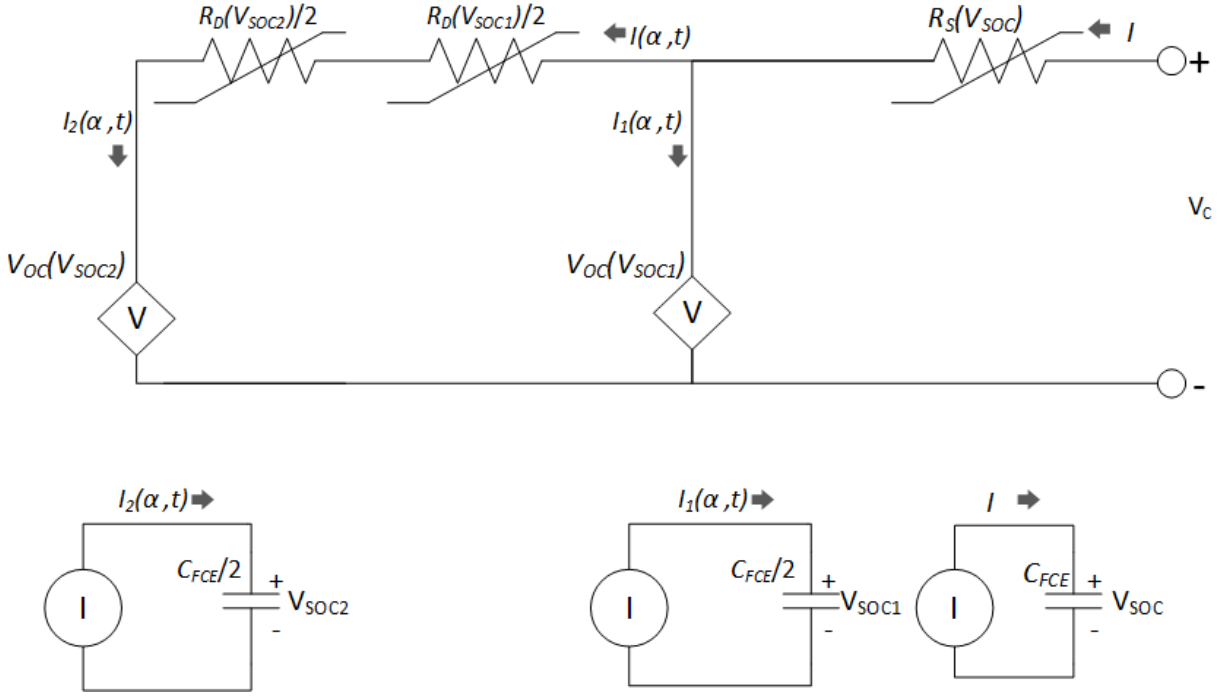


Figure 3-38. Schematic diagram of the one segment transmission line model using π -form segments.

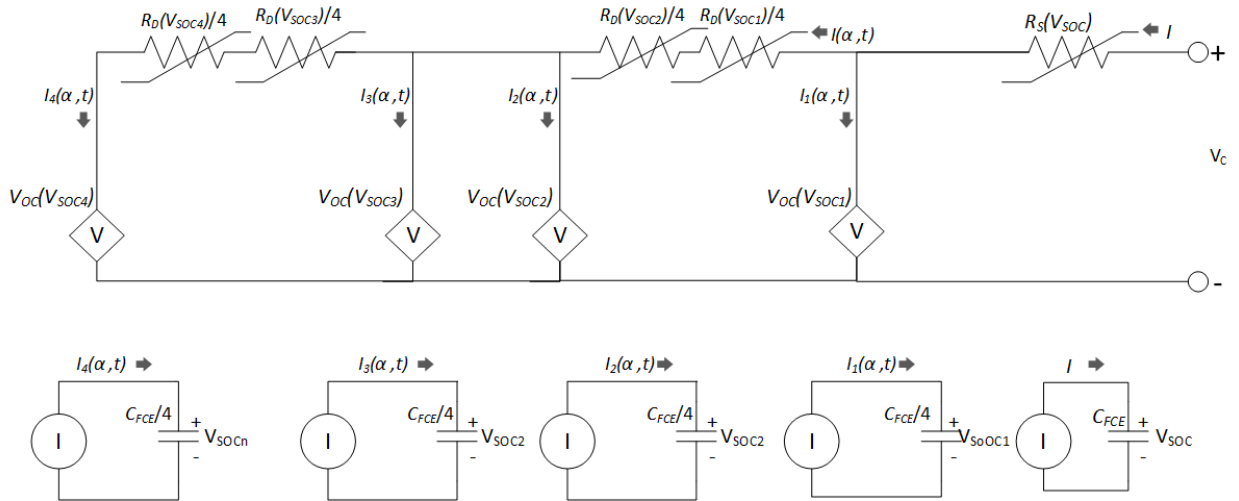


Figure 3-39. Schematic diagram of the two segment model using π -form segments.

In applying the model, the aim is to reduce the number of segments to simplify the model implementation. In the literature, it is common to employ two RC pairs [2]–[4], [16], [30], [31],

[57]–[59], [63], [64]. The 32-RC segments used in Section 3.3.1.2 is quite high in comparison, and as we will see, more than necessary. As seen in the validation of Dow Kokam lithium-ion polymer cells in Section 2.4, the number of RC segments needed to give close to the best case results is 8-RC segments. Adding more elements does not appear to improve the simulation accuracy appreciably. In this chapter, the number of RC-segments of the original form of the distributed SOC model (shown in Figure 2-5, p. 61), and the alternate π -form is studied to evaluate the effect of the number of RC-segments on the accuracy of the model. The dependence of the RMSPVE, as defined in equation [1-11], is used to compare the simulation accuracy between models with different form and number of RC-segments. To compare between the original form and the π -form of the model, the number of segments of the π -form is chosen to obtain the closest number of circuit elements (total numbers of resistors and dependent-voltage sources) to the original form. Six versions of the models with varying number of segments are studied. The number of segments in the two models and the corresponding number of RC-elements for each model are shown in Table 3-13.

Original Form	Model Configuration	2-segments	4-segments	8-segments	16-segments	32-segments
	Number of Resistive and Dependent-Voltage Source Elements in Transmission Line	4	8	16	32	64
π -form	Model Configuration	1-segments	2-segments	5-segments	10-segments	21-segments
	Number of Resistive and Dependent-Voltage Source Element in Transmission Line	4	7	16	31	64

Table 3-13. The model configuration and number of equivalent circuit elements that are tested in order to compare simulation accuracy.

As will be shown in the following discussion, the difference in RMSPVE between the models with differing form and number of RC-segments can be on the order of 0.1%. It is therefore important to have an estimate of the uncertainty of the model. First, according to the specifications of the battery tester, the voltage measurement accuracy is 1 mV, which is equivalent to approximately 0.03 % uncertainty for a test that spans the full SOC range of the cell. Second, there is model uncertainty that results from the timing uncertainty of the applied pulse. Recall from Section 3.2.2.1 that the series resistance in the model is extracted as follows. Using the measured cell voltage at the initial seconds of the pulse phase, a $t^{1/2}$ fit is performed to extrapolate the transmission line voltage, and therefore the $I_P R_S$ voltage drop, at the instant the current step is applied (beginning of pulse phase). However, the sampling rate of the cell voltage is one second per sample, and the timing resolution of the battery tester can be estimated to be approximately 1 ms according to its specifications. From this, the uncertainty in the extracted series resistance can be approximated to be 0.1%. Since the series resistance results in a proportional vertical shift of the simulated cell voltage, this can roughly equate to a model uncertainty of 0.1% also. Therefore, the model uncertainty can be estimated as 0.1-0.2%.

The RMSPVEs for simulating the 6.0 A DDT using the original- and π -form RC-segments are shown in Figure 3-40. The number of RC-segments used in the simulation is shown on the x-axis, where the number outside (inside) the parentheses is the number of RC-segments in the original- (π -) form. As shown in the figure, the simulation performance increases monotonically using the original-form of the RC-segment. The improvement from 16- to 32-RC segments is marginal. The improvement in simulation accuracy for increasing the number of RC-segments

can be attributed to the increasing resemblance of the lumped model to a true transmission line with infinitesimal elements.

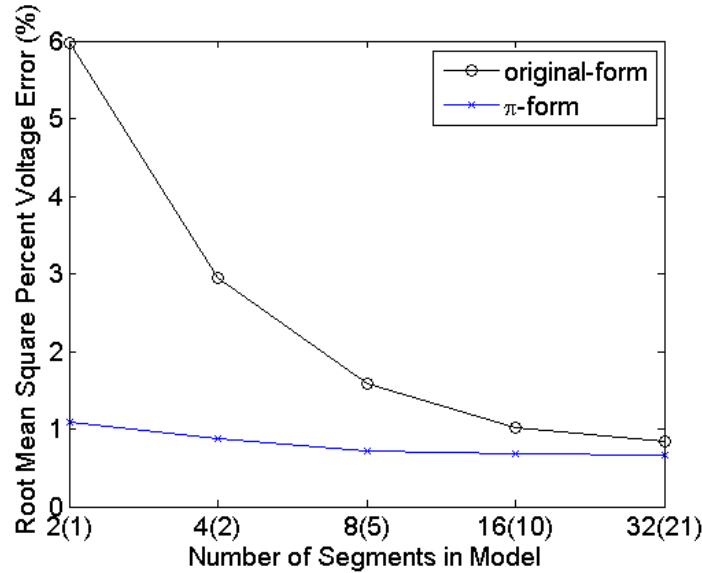


Figure 3-40. Plot of the RMSPVE for the simulated response of 6.0 A DDT for different structure of the proposed model. The x-axis shows the number of segments in the transmission line for the original-form (outside parentheses) and π -form (inside parentheses).

On the other hand, the π -form models of differing element number perform similarly well. According to Table 3-13, the number of π -form segments chosen for comparison to the original-form is based on the closest number of resistive and dependent-voltage source elements in the model. In this way, the performance of the simulation at each x-value in the plot can be compared as they use similar total number of elements in the transmission line. From this figure, the performance of the π -form model performs as well or better than the original-form for all simulations performed for the 6.0 A DDT. This may be attributed to two causes. First, the original-form model contains a R_D/N resistance (N is the number of RC-segments in the model)

at the beginning of the transmission line. This contributes to a constant IR_D/N voltage shift at all times, in the same manner as the series resistance R_S . For small number of RC-segments, the effect of this constant voltage shift is more pronounced, as N is small, and leads to an appreciable simulation error. Second, as mentioned at the beginning of this section, the π -form model spreads out the resistive and effective capacitive (from the combination of the dependent-voltage source and SOC-tracking circuit) elements more evenly. Therefore, for the same number of elements, the π -form model more closely resembles a true RC transmission line than the original-form model.

The RMSPVE for simulating the 2.0 A DDT using the original- and π -form RC-segments is shown in Figure 3-41. The original-form simulation accuracy improves for increasing number of segments, except the 16-segment model performs marginally better than the 32-segment one, but this difference is within the uncertainty of the model discussed earlier. From this figure, the original-form model with four or less segments performs worse than the corresponding π -form model. The relatively poorer performance of the original-form model may again be attributed to the R_D/N resistance at the beginning of the transmission line, which shifts the simulated voltage by a constant IR_D/N at all times. Therefore, the simulation errors are larger for small N . For larger number of segments, the performance of the two models fall within the uncertainty of the model.

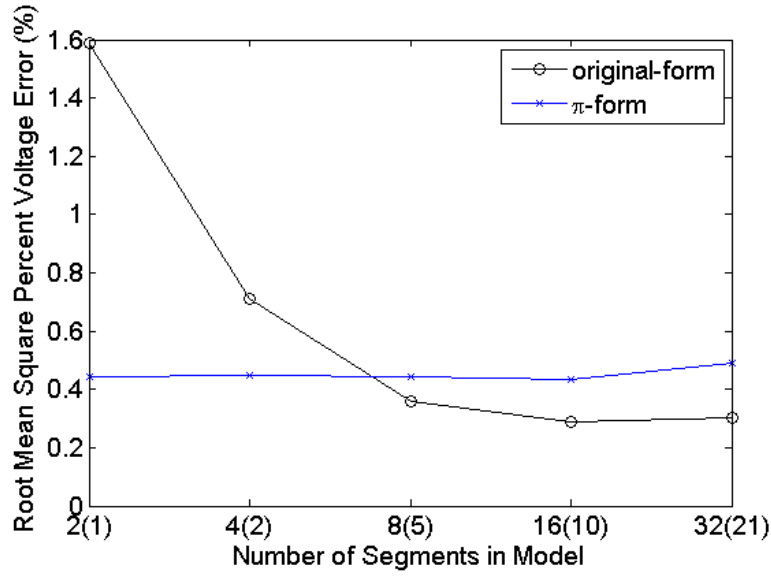


Figure 3-41. Plot of the RMSPVE for the simulated response of 2.0 A DDT for different structure of the proposed model. The x-axis shows the number of segments in the transmission line for the original-form (outside parentheses) and π -form (inside parentheses).

Compared to the 6.0 A DDT results, the simulation accuracy is better for the 2.0 A case. As discussed in Section 3.3.1.2, this can be attributed to the lower applied currents of this test. This causes both lower deviation of the cell voltage from equilibrium, and mis-estimated resistances (including R_D/N resistance at the beginning of the transmission line) in the model have lower resistive drops.

The RMSPVE for simulating the 600 mA DDT using the original- and π -form RC-segments is shown in Figure 3-42. All the simulation results fall within the uncertainty of the model. This can be attributed to the low currents involved in the 600 mA DDT. This means that the excited concentration gradients in the electrodes of the cell is small, resulting in the good performance of

the model for low number of RC-segments. Compared to the 2.0 A DDT, the original-form model simulation accuracy is worse. As mentioned during the comparisons of the RMSPVE between the 2.0 A and 600 mA DDTs in Section 3.3.1.2, this can be attributed to the more pronounced plateau voltage in the SOC range at *ca.* 0.2 to 0.07 at smaller applied currents. As this plateau is not well captured by the open-circuit voltage parameter V_{OC} of the model, this may be the cause of the increased average error at the lower applied currents of the 600 mA DDT. In the future, this can be improved by performing more pulses to extract the model parameters more frequently in this SOC region.

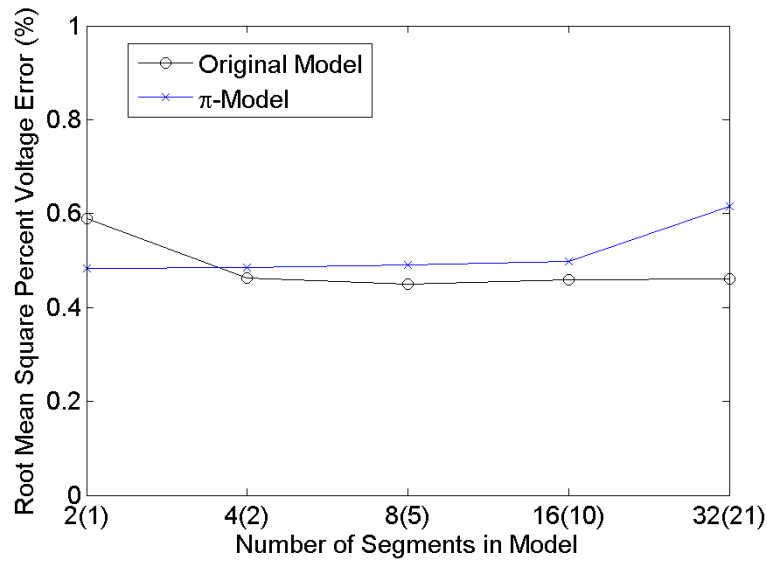


Figure 3-42. Plot of the RMSPVE for the simulated response of 600 mA DDT for different structure of the proposed model. The x-axis shows the number of segments in the transmission line model for the original-form (outside parentheses) and π -form (inside parentheses).

From these results, it can be seen that the original-form of the proposed model improves with increasing number of segments, but the improvement from 16- to 32-RC segments falls within

the uncertainty of the model. Compared to the π -form model, the original form generally performs worse in cases where simultaneously the number of RC-segments is small ($N \leq 4$) and the applied currents are large (6.0 A DDT). This may be attributed to the R_D/N resistance at the beginning of the transmission line, which shifts the simulated cell voltage by the constant amount IR_D/N at all times. The error introduced by this resistance is more pronounced for smaller number of RC-segments, and larger currents. The two forms of models perform similarly for large number of segments ($N \geq 16$) or when the applied current is small. One reason may be that the voltage shift from the R_D/N resistance is much reduced. The choice of the number of segments then depends on the acceptable implementation complexity, and accuracy, which depends on the application of the model [16], [22].

In this section the simulation performance of the distributed SOC model is demonstrated using three DDTs. The model is shown to provide good simulation accuracy as tabulated in Table 3-12. In the next section, the model is validated using constant current discharge tests, which consist of discharging a fully charged cell at different constant currents.

3.3.2 Validation Test #2

In this section, the validation of the distributed SOC model using constant current discharge tests is discussed. This is a standard test that provides information on the maximum amount of energy that can be stored and extracted from the cell, and the cell's remaining operating time, when it is placed under various constant current loads. This data can often be found in the product specifications. Four constant current discharge tests, at currents of 600 mA (0.20 C), 1.5 A (0.50

C), 3.0 A (1.0 C), and 6.0 A (2.0 C) are performed and the experimental results are compared to the simulated results to evaluate the performance of the model. As in Section 3.3.1.2, quantification of the simulation accuracy is evaluated using the PVE, MAPVE, and RMSPVE, defined in equations [1-9]-[1-11], respectively. The performance of the distributed SOC model to predict the cell voltage during this validation test, together with that for the DDTs described in Section 3.3.1, serves to illustrate the range of applicability of the distributed SOC model.

In Section 3.3.2.1, the procedures for the constant current tests are described. The results and analysis are discussed in Section 3.3.2.2. It is found that the structure of the model used thus far in this thesis performs poorly for the larger constant current discharges, despite performing well in response to intermittent currents of the DDTs shown in the previous section. An alternate model structure, based on a spherical electrode, is found to perform significantly better for this test.

3.3.2.1 Test Procedure

For constant current discharge experiments, the cells are first initialized in the same way as the pulsed experiments in 3.2.2.1. At this reproducible fully charged state (SOC=1.0), the cells are discharged at 0.60 A (0.20 C), 1.5 A (0.50 C), 3.0 A (1.0 C), and 6.0 A (2.0 C). The experimental procedure is included in Table 3-14.

Phase	Step	Description
I. Initialization	1	Discharge the cell at 0.20 C (0.60 A) until the cell voltage falls below 2.80 V
	2	Rest for 1.0 hour
	3	Charge at 0.20 C (0.60 A) until the cell voltage reaches 4.35 V
	4	Hold the cell at 4.35 V until the cell current falls below 0.010 C (0.030 A)
	5	Rest for 1.0 hour
II. Constant Current Discharge	6	Discharge at chosen current until cell voltage falls below 2.80 V

Table 3-14. Test procedure for constant current discharge tests for validation of the distributed SOC model.

3.3.2.2 Results and Analysis

For simulating the behavior of the cell to the four constant current discharge tests, the 32-RC segment model, with the original-form RC segments, is used. The structure of the model is shown in Figure 2-23 (p. 90). The measured cell voltage for the four constant current discharge tests are shown as solid lines in Figure 3-43. From this figure, it can be seen that the cell voltage is lower at increasing discharge current. This is consistent with the proposed model, as the larger current induces larger IR_S drop in the series resistor R_S , and $IR_D\Delta\alpha$ drop in the non-linear transmission line.

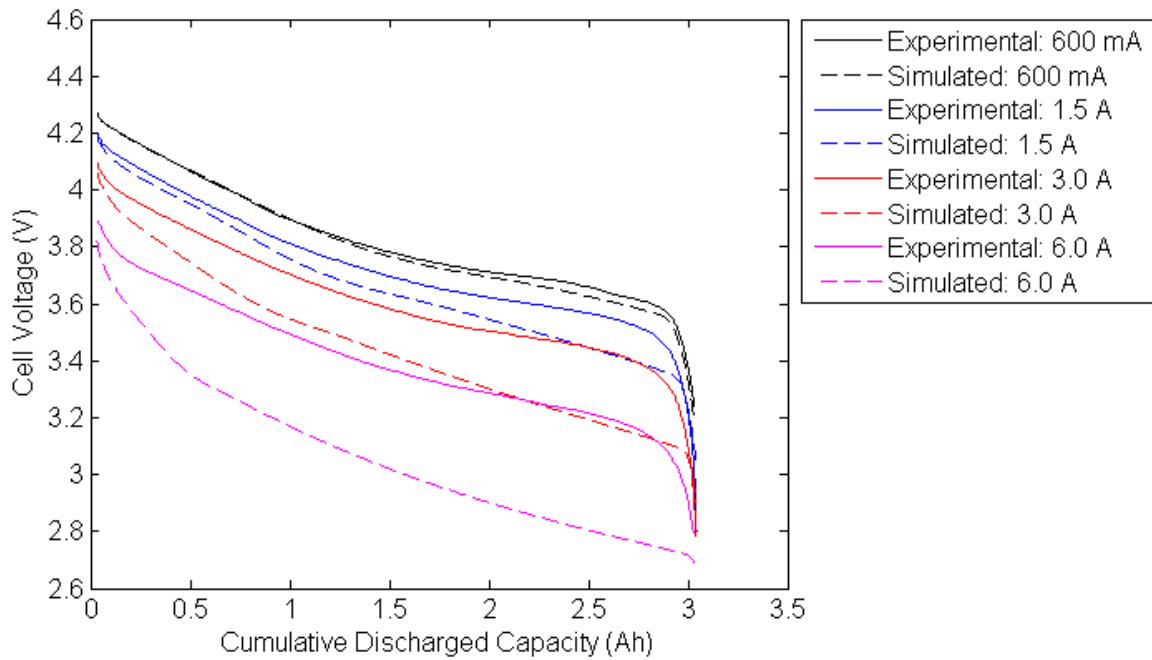


Figure 3-43. Experimental and simulated results for four constant current discharge tests.

Simulated results from the distributed SOC model for the constant current discharge tests are shown as dashed lines in Figure 3-43. At 600 mA, the simulated results matched the experimental ones well. However, the prediction accuracy of the model is much worse for the other currents, and the errors increase for increasing currents.

For the first 95% duration of the four constant current discharge tests, the MAPVE is shown in Table 3-15. The MAPVE is the largest percent deviation between the simulated and experimental results in the test. As the discharge current is increased, the MAPVE progressively increases. The MAPVE is as high as 13% (or 410 mV), which is obtained from the 6.0 A constant current discharge test. The RMSPVE is also shown in Table 3-15. As seen here, the RMSPVE increases for increasing current, up to 10% (or 370 mV) for the 6.0 A constant current

discharge test. This poor performance of the model for constant current discharge is in sharp contrast to the DDT validation results discussed in Section 3.3.1, where the simulation accuracy is generally good, with MAPVE and RMSPVE being 3.7% (or 120 mV), and 0.84% (or 30 mV), respectively, for the 6.0 A DDT. The results for the 2.0 A and 600 mA DDTs are even better, as was shown in Table 3-12.

Constant Current Discharge Test	MAPVE (%)	MAPVE (mV)	RMSPVE (%)	RMSPVE (mV)
6.0 A	13	410	10	370
3.0 A	7.6	260	5.0	180
1.5 A	3.6	130	2.1	74
600 mA	0.96	35	0.49	18

Table 3-15. Tabulated results of the MAPVE (in terms of both percentage and voltage), and RMSPVE (also in terms of percentage and voltage) for the beginning 95% duration of the four constant current discharge tests. The results shown are the average over the three tested cells.

The corresponding PVEs comparing the measured and simulated cell voltages during the constant current discharge tests are shown in Figure 3-44. As the predicted voltage is consistently lower than the measured cell voltage, the percent-voltage error is generally negative in this plot. The percent voltage error tends to increase at very low SOC, at cumulative discharge capacity greater than *ca.* 2.8 Ah. The poor accuracy at low SOC is true across all four constant current discharge tests. This can again be attributed to the drastic drop in cell open circuit voltage in that low SOC region, where small shifts in the initial cell SOC obtained from the initialization procedure and minor cycle-to-cycle capacity differences can lead to this poor simulation accuracy. As mentioned in Section 3.3.1.2, most applications do not operate the cell,

or do not require high model accuracy, in this low SOC region as a result. In a similar fashion to the results analysis performed in that section, the simulation accuracy here will be focused on the first 95% duration of the test results. This allows the analysis to focus on the useable range of SOC, and removes the distortion introduced due to the errors observed at low SOC.

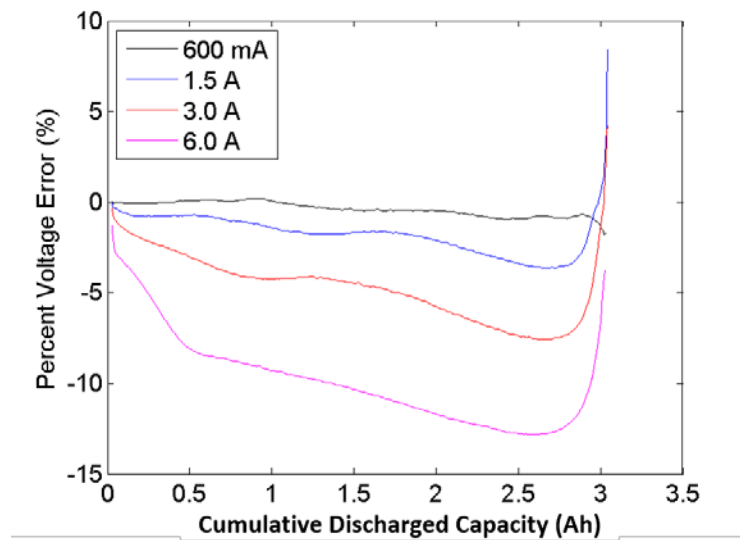


Figure 3-44. Plot of PVE during cell discharge at different constant discharge currents.

For the 600 mA constant current discharge test, the simulation accuracy is generally within 1.2%. For the 1.5 A constant current discharge test, the simulation accuracy is within 1% up to cumulative discharged capacity of *ca.* 0.50 Ah, but gets worse for higher cumulative discharged capacity. The simulation accuracy for the two highest constant current discharge tests (3.0 A and 6.0 A) degrades even further, with the 6.0 A test reaching *ca.* 13% PVE at *ca.* 2.7 Ah cumulative discharged capacity.

As mentioned in Section 1.3.2.3, the expected MAPVE for equivalent-circuit models is on the high side of the 1-5% range suggested by Chen and Rincon-Mora [2], while the RMSPVE is expected to be on the low side of this range. The key results observed above for the simulation performance of the distributed SOC model for the constant current discharge tests can be summarized as follows. First, the simulation of the lowest current test (600 mA constant current, or 0.20 C) performed well. This is illustrated by the maximum-absolute-percent-voltage error and RMSPVE of 0.96% (or 35 mV) and 0.49% (or 18 mV), respectively. Second, for the higher constant current discharge tests (1.5 A, 3.0 A, and 6.0 A), the model performance is generally poor, and performance degrades as the discharge current increases. For the 1.5 A (0.50 C) constant current discharge test, the maximum-absolute-percent-voltage error and RMSPVE of 3.6% (or 130 mV) and 2.1% (or 74 mV), respectively. For the 6.0 A constant current test, the maximum-absolute-percent-voltage error increases to 13% (or 410 mV). While the distributed SOC model may still be moderately useful at 1.5 A constant current discharge, it is clearly unfit for simulations of higher discharge currents. Third, the PVE becomes increasingly negative as the discharge proceeds (increasing cumulative discharged capacity), and higher discharge current results in increasingly negative PVE.

The last observations listed above suggests that the depletion of charge from the electrode surface (close to the electrode/electrolyte interface) is more significant in the model than that observed from the experimental results. To understand the potential causes of this poor simulation accuracy for the constant current discharge validation tests, it is useful to compare to the electrochemical models, which are more complete models that include more detailed physical phenomena. As described in Section 1.3.1, two popular electrochemical models are the P2D

model and the SPM. The geometries of these two models are shown in diagrams A and B of Figure 1-8 (p. 22). The SPM can be obtained from the P2D model by neglecting the thicknesses of the positive and negative electrodes, effectively modeling each electrode as a single layer of spherical active material particles. Also, in the SPM, the variation of the potential and ionic concentration in the electrolyte are neglected. In comparison to the electrochemical models, the distributed SOC model treated in this thesis, which is shown in diagram C of Figure 1-8 (p. 22), has three key factors that may cause the discrepancies between the simulated and experimental results. The first is the use of a transmission line which models planar rather than spherical diffusion. The second is the modeling of only one diffusion time constant. A third aspect that is not included in the distributed SOC model is the transport through the thickness of the porous electrode. These factors are now discussed and an argument is made that the spherical diffusion be included in a revised model.

First, the distributed SOC model proposed in this thesis work consists of a transmission line that is derived from a planar electrode model. The transmission line has diffusion resistance R_D and dependent-voltage source V_{OC} as model parameters. These represent the effective resistance and capacitance (as discussed earlier in Section 2.1) present at each incremental depth into the particles that make up the electrodes. On the other hand, both the P2D model and the SPM use spherical particles, with lithium ion transport inside the particle governed by the diffusion equation. Intuitively, the response of a spherical particle is different from a planar electrode. In a one-dimensional RC transmission line, each segment in depth has the same resistance and capacitance values. On the other hand, in a spherical electrode, each segment of an equivalent transmission line would model a shell of the sphere. The equivalent resistance and capacitance

of each shell would be expected to be a function of radial position r . As r increases, the capacitance in the local spherical shell increases due to the increase in shell volume, whereas the resistance decreases due to the increase in area. Therefore, a spherical model has a different response than the planar RC transmission line proposed in this thesis. As a result it is proposed that a spherical model be used to describe the transport. The model is derived in the next section.

Second, in both the P2D model and the SPM, the bottleneck in diffusion is primarily attributed to the transport of ions inside the particles. However, in those models, there are two sets of solid-phase lithium ion diffusion, one for the positive electrode, and the other for the negative electrode. During application of the current pulse, both electrodes undergo the pulsed response. The measured response is a result of the two $t^{1/2}$ responses in series. However, as mentioned in Section 1.3.2.2, the impedance of lithium ion cells have been successfully modeled as a single Randles circuit [28], [29], [48], [49]. Therefore, the existence of the two electrodes in series is not expected to lead to the significant errors that are observed in the simulations of the constant current discharge discussed above.

Third, there is another resistive contribution in the P2D model that is not accounted for in the planar distributed SOC model. It is the resistance in the thickness direction of the porous electrode. In the P2D model, the electrodes consist of spherical particles that are distributed throughout the thickness of the porous electrode. The solution phase and solid phase potentials in the electrode varies as a function of depth in this thickness direction due to electrolyte and Ohmic resistances. This leads to the front of the electrode (interface between the electrode and separator) being charged first, before the back (interface between the electrode and current

collector), leading to another time constant. Therefore, the spherical particles at different depth of the electrode behaves differently. This thickness dimension of the porous electrode is neglected in both the SPM and the distributed SOC model. As mentioned in Section 1.3.1, the diffusion coefficient is a few orders of magnitude lower in the particle (on the order of 10^{-9} cm^2/s), as compared to the diffusion coefficient in solution (on the order of 10^{-6} cm^2/s) [67]. Therefore, the solid phase diffusion should be the dominant transport mechanism governing the behavior of the electrode, and the effect of the thickness of the porous electrode is not expected to be able to explain such a large deviation between simulated and experimental results observed in the above results (Table 3-15).

Of the three reasons suggested above that may explain the discrepancy between the simulated and experimental results in the constant current discharge tests, the spherical nature of diffusion is deemed the most significant missing aspect that could help improve simulation performance. This is due to the more concentrated distribution of the storage capacity of the spherical electrode towards its surface, improving its ability to supply charge at sustained discharge at higher currents. This may explain the errors observed between the simulations using the distributed SOC model (derived using the planar electrode model), and the measured results for constant current discharge at 1.5 A and above. Therefore, another distributed SOC model that is based on the use of a spherical electrode will be derived in the remainder of this chapter to investigate whether this would show performance improvements. For the remainder of this work, the distributed SOC model that is derived from the planar electrode will be called the planar distributed SOC model. The distributed SOC model derived using the spherical electrode will be called the spherical distributed SOC model.

The performance of the planar distributed SOC model can be summarized as follows. For simulating the behavior of the four constant current discharge tests, the model performed well at 600 mA, with MAPVE of 0.96% (or 35 mV), and RMSPVE of 0.49% (or 18 mV). However, for the three remaining constant current discharge tests, the model performance is much worse. As mentioned in Section 1.3.2.3, the expected MAPVE for equivalent-circuit models is on the high side of the 1-5% range suggested by Chen and Rincon-Mora [2], while the RMSPVE is expected to be on the low side of this range. Therefore, considering these results for the constant current discharge tests, together with its good performance in simulating the behavior of the three DDTs (see Table 3-12), it can be concluded that the planar distributed SOC model is sufficiently accurate for use in applications that have low average discharging current (up to 750 mA, or 0.25 C, as shown in Table 3-11), with discharging and charging current pulses up to 6.0 A (2.0 C) and 3.0 A (1.0 C), respectively.

In the next section, the distributed SOC model is also derived using a spherical electrode and evaluated. The simulation results are compared to the experimental results to demonstrate the model capabilities.

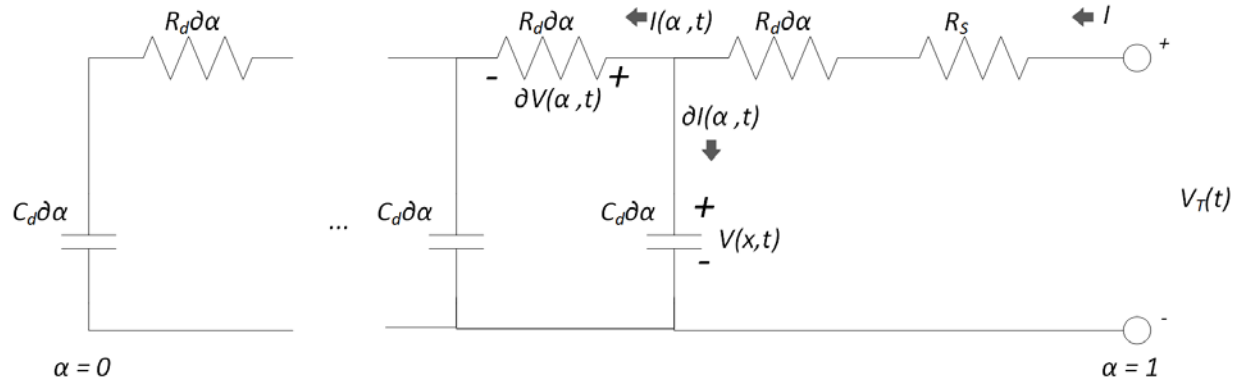
3.3.2.3 Spherical Model

The diffusion element employed so far in this work uses a planar geometry because of simplicity. This model is shown to work well for the Dow Kokam lithium-ion polymer cell described in Chapter 2 at relatively low pulse discharge currents (0.20 C) and for the 30U cylindrical lithium

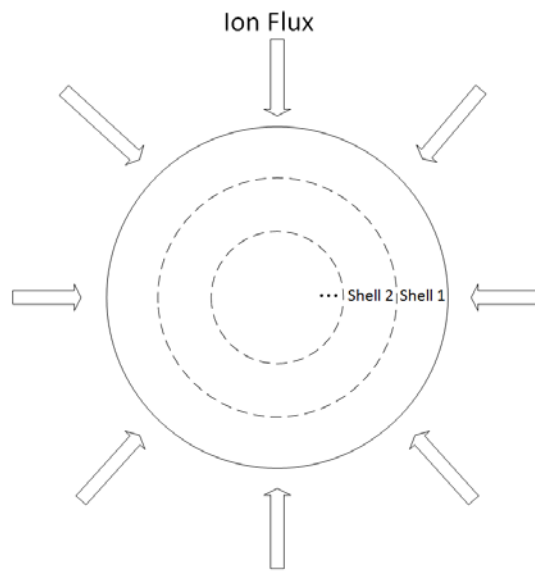
ion cells in Chapter 3 for the DDTs (variable-currents up to current magnitude of 2.0 C, but average discharge rates of only as high as 0.25 C) and slow constant current discharge tests (0.20 C). However it is shown in the last section that the simulation performance for moderate to high current (0.50 C to 2.0 C) continuous discharge becomes increasingly worse as current increases. The effect does not appear to be due to the omission of non-linearities associated with electron transfer reactions since for the responses to high current pulses, and the initial responses to a step in current seen in Figure 3-43, the simulation works well. The issue is that as discharge progresses the cell voltage is increasingly underestimated, especially at high currents.

A potential cause of this cell voltage under-estimation is that the planar electrode model used to derive the distributed SOC model has its capacitance distributed uniformly throughout the thickness of the electrode, as shown in diagram A of Figure 3-45. Inside real lithium ion cells, the electrodes typically consist of active material particles that are closer in shape to spheres. If a spherical electrode is used instead, there would be a larger capacitance close to the electrode surface ($\alpha=1$) than that at the core ($\alpha=0$). As the total capacitance of the electrode should stay the same, the spherical electrode has a larger capacitance at the electrode surface ($\alpha=1$) than the planar model (also at $\alpha=1$). This results in an improved ability to supply charge to the load for the spherical electrode, as a higher proportion of the stored charge is located close to the electrode surface. This effect of charge availability is more pronounced at higher sustained currents, so the simulation accuracy of the planar distributed SOC model performs increasingly worse for higher constant current discharge tests. To correct for this longer time effect a spherical diffusion equivalent circuit is proposed, as is now described and tested for continuous current discharge. Then, by non-linearizing the transmission line as was done in Section 2.1 to

obtain the circuit model shown in Figure 2-5, the non-linear model based on spherical diffusion will be obtained.



A) Planar Model



B) Spherical Model

Figure 3-45. Depiction of A) the equivalent-circuit derived from the planar model and B) the spherical model geometry.

A RC-network model for a spherical electrode can be built by assuming that it consists of a homogeneous material with capacitance per unit volume β , and effective resistivity κ . In Section 2.1, the planar transmission line non-dimensionalized so that it has a dimensionless length of 1. Similarly, the sphere radius can be made non-dimensional, with a dimensionless radius of 1. The ions enter the spherical electrode from its surface. A model of the spherical electrode can be built by breaking the sphere into a number of shells. This is shown in diagram B of Figure 3-45. The differential capacitance C_r , per-unit-radius, is given by

$$C_r = 4\beta\pi r^2. \quad [3-23]$$

The differential resistance R_r , per-unit-radius, is given by

$$R_r = \frac{\kappa}{4\pi r^2}. \quad [3-24]$$

Therefore, large radius shells have higher capacitance than smaller radius ones. On the other hand, shells with larger radius have lower resistance. The differential capacitance and resistance are plotted in Figure 3-46. The RC time constant of the shell τ_r of shell thickness ∂r is a constant at all radii, given by

$$\tau_r = \beta\kappa(\partial r)^2. \quad [3-25]$$

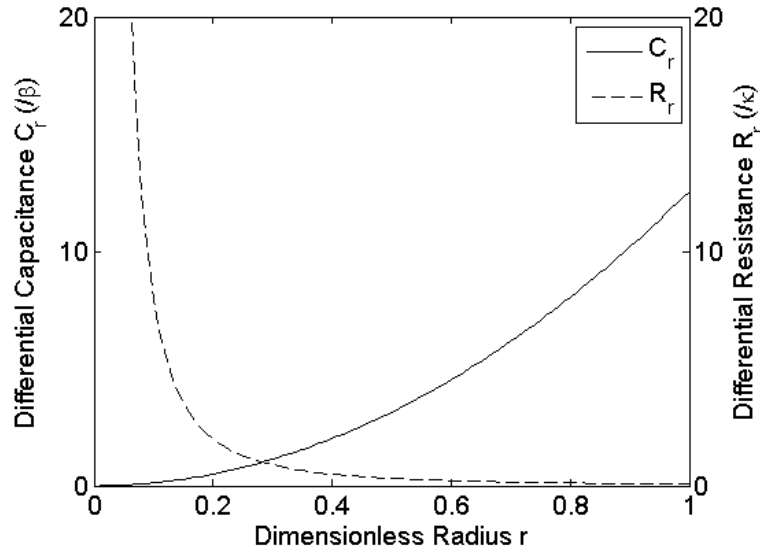


Figure 3-46. Plot of the differential capacitance C_r , and differential resistance R_r , according to equations [3-23] and [3-24]. The plotted differential capacitance C_r is normalized to material capacitance per unit volume β , while the plotted differential resistance R_r is normalized to material resistivity κ .

For a spherical model with the same diffusion capacitance, C_D , as that of a planar RC transmission line, the response to a pulse current is expected to be different, as will be shown here. In the planar RC transmission line (Figure 2-4) treated in Section 2.1, each RC-segment has the same resistance $R_D \partial \alpha$ and capacitance $C_D \partial \alpha$, so the capacitance is evenly distributed throughout dimensionless position α between 0 and 1. The RC time constant τ at any position α is given by

$$\tau = R_D C_D (\partial \alpha)^2. \quad [3-26]$$

In the spherical electrode case, the flux of ions can be inserted into the particle along the entire spherical surface. The capacitance distribution is shifted towards the surface of the sphere ($r = 1$), as shown in Figure 3-46. In the discharging case, for example, there is a larger reservoir of lithium ions closer to the surface ready to be supplied to the surface to be extracted. On the other

hand, in the planar RC transmission line, the capacitance is evenly distributed, which means that there is comparatively less capacitance close to the surface ($\alpha = 1$). This means that the surface concentration of lithium ions drops more in the planar case compared to the spherical model. This is consistent with the error voltage ($V_{sim}-V_{exp}$) observed in the results in Section 3.3.2.2, where the planar RC transmission line simulated cell voltages are lower than the measured voltage during constant current discharge. In the following, an RC-network representation of the spherical model is derived, and used to simulate the four constant current discharge tests described in Section 3.3.2.2.

A lumped equivalent-circuit representation of the spherical model can be derived as follows. The sphere is divided into N lumped shells, with an equivalent diffusion resistance and diffusion capacitance for each shell. The equivalent-circuit of each shell is connected in series to give the circuit model of the spherical particle.

For a shell with outer-radius r_o and inner radius r_i , and capacitance per unit volume β , the capacitance of the shell, C_{shell} , is given by

$$C_{shell} = \beta \int_{r_o}^{r_i} 4\pi r^2 dr = \frac{4\pi\beta}{3} (r_o^3 - r_i^3). \quad [3-27]$$

For the shell resistance, each shell is sub-divided into an outer-shell and an inner-shell, shown in Figure 3-47. The outer-shell has outer-radius r_o and inner radius r_m , where r_m is the midpoint between r_o and r_i . The inner-shell has outer-radius r_m and inner radius r_i . Then, the equivalent resistance of the outer-shell, R_{out} , is

$$R_{out} = \int_{r_m}^{r_o} \frac{\kappa}{4\pi r^2} \partial r = \frac{\kappa}{4\pi} (r_m^{-1} - r_o^{-1}), \quad [3-28]$$

and the inner-shell resistance, R_{in} , is given by

$$R_{in} = \int_{r_i}^{r_m} \frac{\kappa}{4\pi r^2} \partial r = \frac{\kappa}{4\pi} (r_i^{-1} - r_m^{-1}), \quad [3-29]$$

where κ is the material resistivity. Then, the RC representation of the shell consist of a T-shaped section, shown in Figure 3-47.

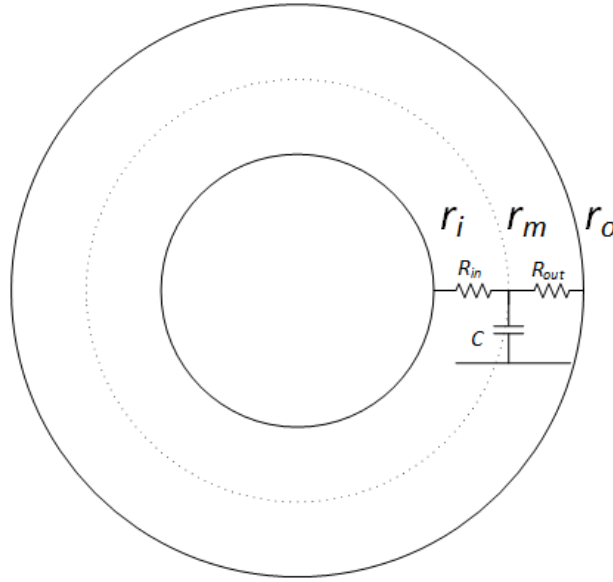


Figure 3-47. RC-network representation of a shell of inner-radius r_i , and outer-radius r_o .

Notice that equation [3-29] contains the reciprocal of radius r_i , so r_i cannot be zero. Therefore, in the spherical model, the innermost core of the sphere is modeled only as a lumped capacitive element. The core sphere of radius r_o is modeled only as a core capacitance, C_{core} , given by equation [3-27] to be

$$C_{core} = \frac{4\pi\beta}{3} r_o^3 \quad [3-30]$$

Then, using $N=4$ as an example, the sphere is modeled as four lumped capacitances, with lumped resistances interconnecting them. The four capacitances represent the capacitance of the three shells, each of thickness $1/N$, and a core of radius $1/N$. This is shown in Figure 3-48.

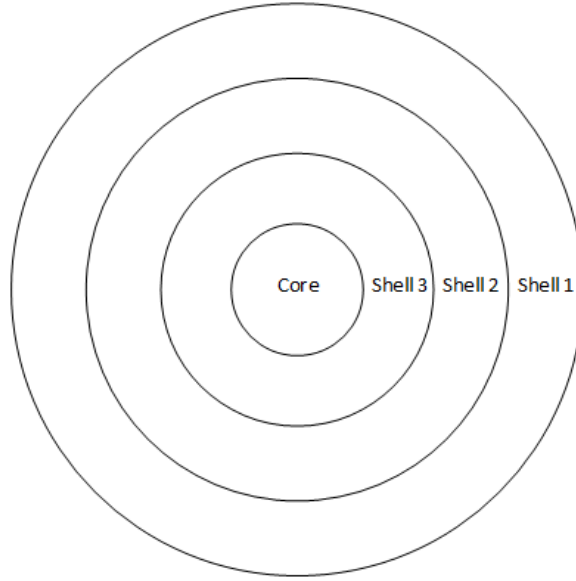


Figure 3-48. Breakdown of spherical electrode into 4 sections, consisting of 3 shells and a spherical core.

Adding the series resistance R_S to the RC-network described above gives the complete spherical model, which is shown in Figure 3-49. An additional index is introduced in the resistive and capacitive components of the equivalent circuit, as the values of the resistive and capacitive components changes depending on the radial position of the particular shell (or core). $R_{i,in}$ and $R_{i,out}$ are the inner- and out-shell resistances of the i -th shell of the sphere. $C_{i,shell}$ is the shell capacitance of the i -th shell. The index i can take on any integer value from 1 to $N-1$. As the

core of the sphere is represented only by a lumped capacitance, $C_{N,core}$ in the figure is the core capacitance of the sphere.

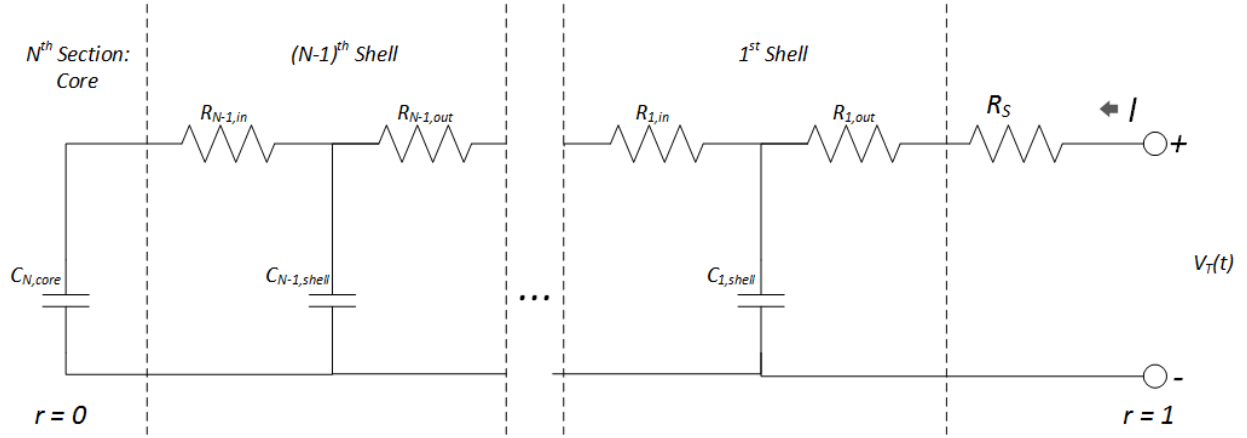


Figure 3-49. Completed linear version of the distributed SOC equivalent-circuit model for a spherical electrode.

The model parameters that are needed to complete the spherical model are the capacitance per unit volume β , and material resistivity κ . These can be related to the extracted parameters from the planar RC transmission line, discussed in Section 2.3. The total transmission line capacitance in both models is the same, so the material capacitance per unit volume β is given by

$$\beta \frac{4}{3} \pi r^3 \Big|_{r=1} = C_D, \text{ or} \quad [3-31]$$

$$\beta = \frac{3C_D}{4\pi}. \quad [3-32]$$

In the planar RC transmission line discussed in Section 2.3, the diffusion resistance R_D is given by equation [2-29], which states that

$$R_D = (M_0/2I)^2 \pi C_D. \quad [3-33]$$

This diffusion resistance is obtained from fitting to the cell voltage during the initial seconds of the pulse phase. At short times, the spherical particle can also be approximated as exhibiting planar diffusion as the curvature effect of the spherical particle is small. The effective capacitance at the surface of the planar and spherical models can be made equal to estimate capacitance per unit volume for the spherical model. Therefore,

$$C_D \Delta \alpha|_{\alpha=1} = \beta 4\pi r^2 \Delta r|_{r=1}. \quad [3-34]$$

Inserting equation [3-32] into equation [3-34] gives

$$C_D \Delta \alpha|_{\alpha=1} = \frac{3C_D}{4\pi} 4\pi r^2 \Delta r \Big|_{r=1}, \quad [3-35]$$

so

$$\Delta \alpha = 3\Delta r. \quad [3-36]$$

Likewise, the material resistivity κ in the spherical model can be related to the diffusion resistance R_D of the planar model because at short times, the two models behave the same.

Therefore,

$$R_D \Delta \alpha|_{\alpha=1} = R_r \Delta r|_{r=1}, \quad [3-37]$$

Inserting equation [3-24] into equation [3-37] gives

$$R_D \Delta \alpha|_{\alpha=1} = \frac{\kappa}{4\pi r^2} \Delta r \Big|_{r=1} \quad [3-38]$$

Making use of equation [3-36], then

$$R_D 3\Delta r = \frac{\kappa}{4\pi} \Delta r \quad [3-39]$$

so

$$\kappa = 12\pi R_D. \quad [3-40]$$

As discussed in Section 2.1, the model parameters of the distributed SOC model depend on SOC. By utilizing the relationships found above that relates the capacitance per unit volume β , and material resistivity κ , of the spherical model to the planar model parameters, the dependence of these parameters on SOC is found. Like in the case of non-linearization of the RC equivalent circuit model of the planar electrode (Figure 2-4) to obtain the finalized distributed SOC model shown in 2-6, the linear RC equivalent circuit model of the spherical electrode (Figure 3-49) can be non-linearized in the same way. First, the series resistor R_S is introduced, which depends on the overall cell SOC, through cell SOC-tracking circuit at the bottom right. Second, the capacitance of each section of the transmission line is replaced by dependent-voltage source V_{OC} and SOC-tracking circuits. Third, the outer-shell resistance R_{out} , and inner-shell resistance R_{in} , are made dependent on the local SOC through V_{SOC} of the local SOC-tracking circuit.

In this model, the full-capacity-equivalent capacitance C_{FCE} and dependence of series resistance R_S on SOC stays the same as the planar model. As illustrated by the better simulation accuracy of the π -form model compared to the original-form RC model for the same number of segments in section 3.3.1.3, more evenly distributed capacitance and resistance of the equivalent-circuit model leads to better model accuracy. Therefore, in the implementation of the spherical model here, the full-capacity of each section (shell or core) is set to be the same, *i.e.* the full-capacity of each section is C_{FCE}/N , where N is the number of sections chosen. This means that the volume of each shell V_{shell} (or core V_{core}) are the same, so

$$V_{shell} = \frac{4\pi r^3}{3} \Big|_{r=r_o} - \frac{4\pi r^3}{3} \Big|_{r=r_i} . \quad [3-41]$$

Also, the ratio of the volume of each shell (or core) to the volume of the full sphere V_{sphere} is $1/N$.

$$\frac{V_{shell}}{V_{sphere}} = \frac{\frac{4\pi r^3}{3}\Big|_{r=r_o} - \frac{4\pi r^3}{3}\Big|_{r=r_i}}{\frac{4\pi r^3}{3}\Big|_{r=1}} = \frac{1}{N}, \quad [3-42]$$

which simplifies to

$$r_i = \left(r_o^3 - \frac{1}{N}\right)^{1/3}. \quad [3-43]$$

Knowing that the outermost shell of the sphere has dimensionless radius of 1, the outer-radius r_o and inner-radius r_i of all the shells and the core of the model can be found recursively. Finally, the dependence of the open-circuit voltage V_{OC} on local SOC stays the same as in the planar model. The non-linearization of the distributed SOC model for the spherical electrode is complete. The final spherical distributed SOC equivalent-circuit model is shown in Figure 3-50. This will be used in the remainder of this section to simulate the constant current discharge and DDTs to characterize the performance of this model.

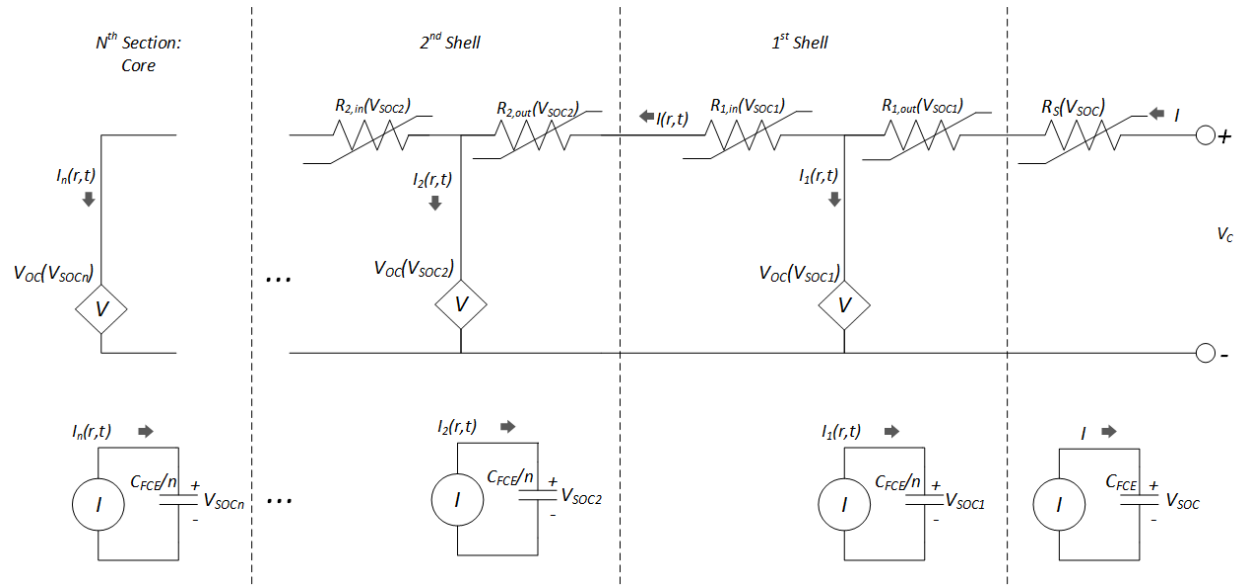


Figure 3-50. Final (non-linear) spherical distributed SOC equivalent-circuit model, based on the spherical electrode model.

The geometries of the electrochemical models (P2D model and SPM) and the two distributed SOC models (planar and spherical) are shown in Figure 3-51 for comparison. The spherical distributed SOC model, shown in diagram D of the figure, can be thought of as a layer of spherical particles at the surface of the current collector. It is a modification of its planar counterpart (diagram C) by changing its diffusion mechanism to spherical geometry. As illustrated in this section, this has the effect of re-distributing the capacitance towards the spherical electrode's surface. The geometry of the spherical distributed SOC model bares some strong similarities to the SPM, which is shown in diagram B of the figure. Both models represent the electrode as a spherical particle at the surface of the current collector. Diffusion is the model's governing mechanism for charge transport. On the other hand, there are also important differences between these two models. First, the spherical distributed SOC model is an equivalent-circuit model, as shown in Figure 3-50. The SPM requires the mathematical

solution of the diffusion equation to model the ion diffusion in the electrodes. Second, the SPM requires 15 material and structural parameters in order to perform the simulation. Knowledge of lithium ion cell physics, the internal structural properties of the cell, and the performance of specialized experiments are needed to obtain these parameters for model construction. On the other hand, the parameters of the spherical distributed SOC model can be extracted using the method presented in this section using only simple charge and discharge experiments and analysis. Third, the spherical distributed SOC model represents the cell as a single electrode, whereas both the positive and negative electrodes are separately modeled in the SPM. The P2D model is shown in diagram A of Figure 3-51. One key effect that is included in this model, but not in the other models in this figure, is the thickness of the porous electrodes.

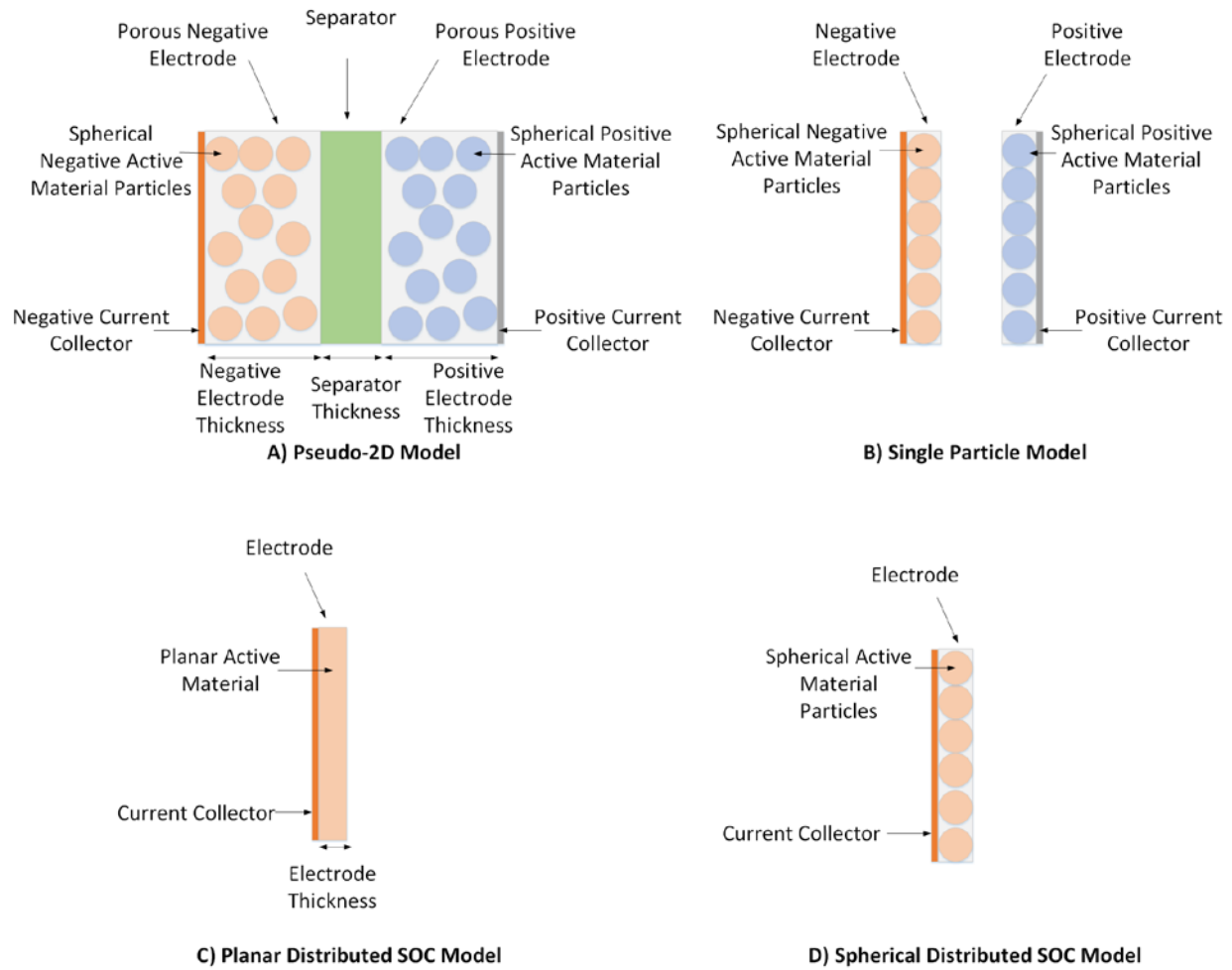


Figure 3-51. Depiction of the geometries of the four lithium ion cell models. A) P2D model, B) SPM, C) planar distributed SOC model, and D) spherical distributed SOC model.

Constant Current Discharge Tests

The four constant current discharge tests are simulated using a 32-RC segment spherical model, and the simulated and experimental results are shown in Figure 3-52. For the three lower discharge currents (600 mA, 1.5 A, and 3.0 A), the simulation predicted cell voltages that match well with the measured results. For the 6.0 A constant current discharge test, the simulated cell

voltage falls more rapidly than the measured one as the cumulative discharged capacity is increased above *ca.* 2.0 Ah.

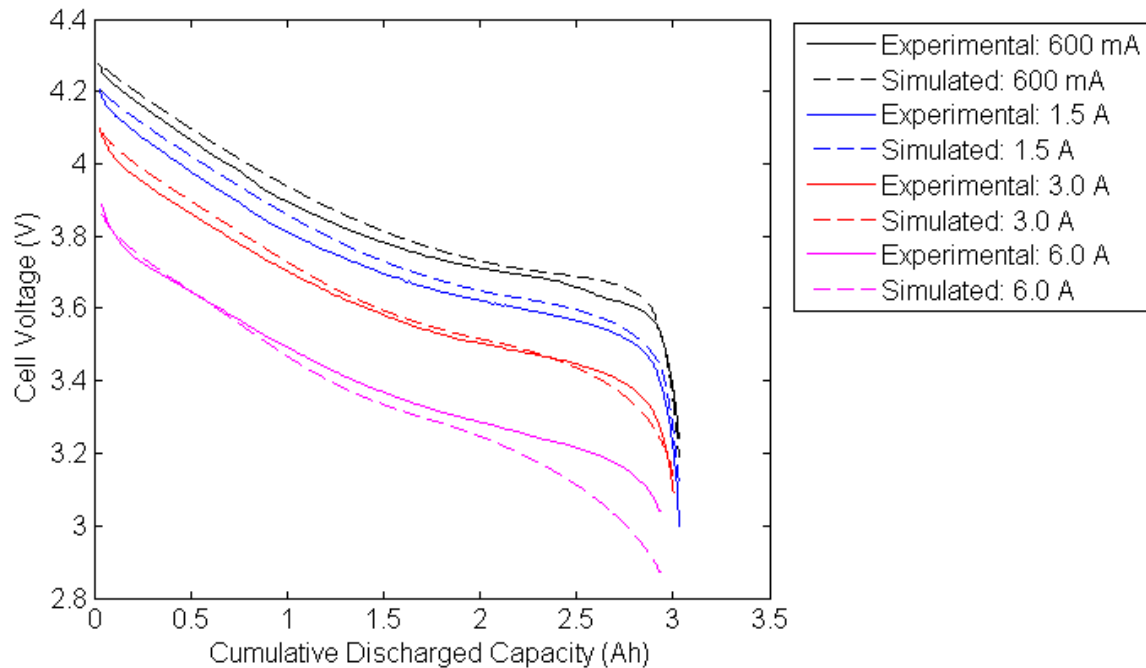


Figure 3-52. Simulated results from the spherical model is shown together with the experimental ones for the four constant current discharge tests.

The MAPVE and root-mean-square-percent-voltage error (RMSPVE) for the first 95% duration of the discharge tests are shown in Table 3-16. The results for the three lower currents are similar in terms of these two measures. The 6.0 A constant current discharge test results are noticeably worse. For the 6.0 A test, the MAPVE is 5.2% (or 160 mV), while the RMSPVE is 1.8% (or 64 mV). As mentioned in Section 1.3.2.3, the expected MAPVE for equivalent-circuit models is on the high side of the 1-5% range suggested by Chen and Rincon-Mora [2], while the RMSPVE is expected to be on the low side of this range. Therefore, from the results tabulated in

Table 3-16, it can be seen that the spherical distributed SOC model performs well for the 600 mA, 1.5 A, and 3.0 A constant current discharge tests, while its performance is borderline acceptable for simulation of the 6.0 A test.

Electrode	Constant Current Discharge Test	MAPVE (%)	MAPVE (mV)	RMSPVE (%)	RMSPVE (mV)
Spherical	6.0 A	5.1	160	1.8	64
	3.0 A	1.3	43	0.65	23
	1.5 A	1.3	52	0.95	34
	600 mA	1.3	47	0.83	30
Planar	6.0 A	13	410	10	370
	3.0 A	7.6	260	5.0	180
	1.5 A	3.6	130	2.1	74
	600 mA	0.96	35	0.49	18

Table 3-16. Tabulated results of the MAPVE (in terms of both percentage and voltage), and RMSPVE (also in terms of percentage and voltage) for the beginning 95% duration of the four constant current discharge tests. Results for both planar and spherical electrodes are shown. The results shown are the average over the three tested cells.

The PVE over the duration of the four constant current discharge tests using the spherical electrode model are shown in Figure 3-53. As in the earlier results in Sections 3.3.1.2 and 3.3.2.2, the simulation accuracy is significantly worse at low cell SOC (equivalent to high cumulative discharged capacity). As mentioned in Section 3.3.1.2, and earlier in this section, most applications do not operate the cell at such low SOC, or do not require high simulation accuracy there, because the OCV drops rapidly at low SOC. This means small shifts in the initial cell SOC obtained from the initialization procedure of the discharge test, and minor cycle-

to-cycle capacity differences, result in large simulation errors at low SOC. Like in the earlier discussion, the focus is on the beginning 95% duration of the test as a result.

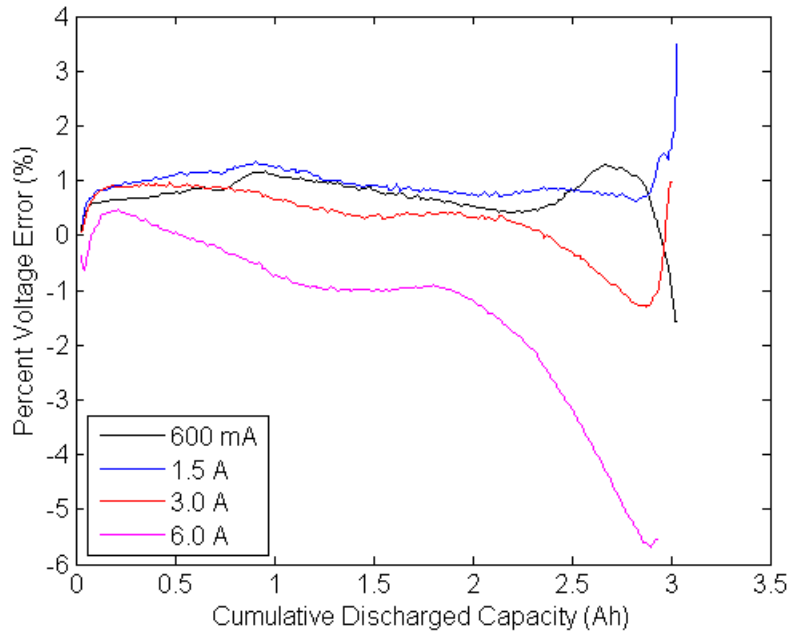


Figure 3-53. The PVE for the simulated cell voltage using the spherical distributed SOC model.

As shown in Figure 3-53, the PVE for the simulated results of the three lower current tests (600 mA, 1.5 A, and 3.0 A) are, for the vast majority of the test duration within *ca.* +/- 1.2%. For the 6.0 A constant current discharge test, the simulated and measured cell voltages are close (PVE within +/- 1 %) for cumulative discharged capacity below *ca.* 1.8 Ah, but the PVE becomes increasingly negative (i.e. simulated cell voltage is increasingly lower than measured) as cumulative discharged capacity increases. One possible reason is the mis-estimation of the resistances in the distributed SOC model at lower SOC. As mentioned earlier in the discussion of the parameter extraction results (Section 3.2.2.2), the extracted diffusion capacitance C_D is

prone to over-estimation due to the rapid decrease of the capacitance at low SOC. As the diffusion resistance R_D is proportionally related to the diffusion capacitance (equation [2-29]), the diffusion resistance R_D of the model is also possibly over-estimated at low SOC. This leads to a more rapid decay of cell voltage that is especially pronounced at higher constant discharge currents.

The MAPVE and RMSPVE obtained for the four constant current discharge tests using the spherical electrode model can be compared to those results obtained from the planar electrode model, which is also shown in Table 3-16. At the lowest tested discharge current (600 mA, or 0.20 C), the planar electrode model performs better, but both models perform well within the 1-5% accuracy range expected of equivalent-circuit models [2]. More importantly, the results obtained using the spherical electrode is significantly better than the planar electrode for the three higher discharge currents (6.0 A, 3.0 A, and 1.5 A). Therefore, this confirms that the higher concentration of charge storage capacity at the surface of the spherical electrode model improves the simulation performance of the distributed SOC model for sustained high current discharge. In the remainder of this section, the performance of the spherical distributed SOC model in simulating the DDTs is discussed.

DDTs

The three DDTs (6.0 A, 2.0 A, and 600 mA) are simulated using a 32-RC segment spherical distributed SOC model. The simulated and experimental results for the 6.0 A DDT are shown in

Figure 3-54. The MAPVE and RMSPVE results for the 6.0 A DDT are shown in Table 3-17.

The MAPVE is large (7.7%, or 240 mV), but the RMSPVE is good (1.5%, or 54 mV).

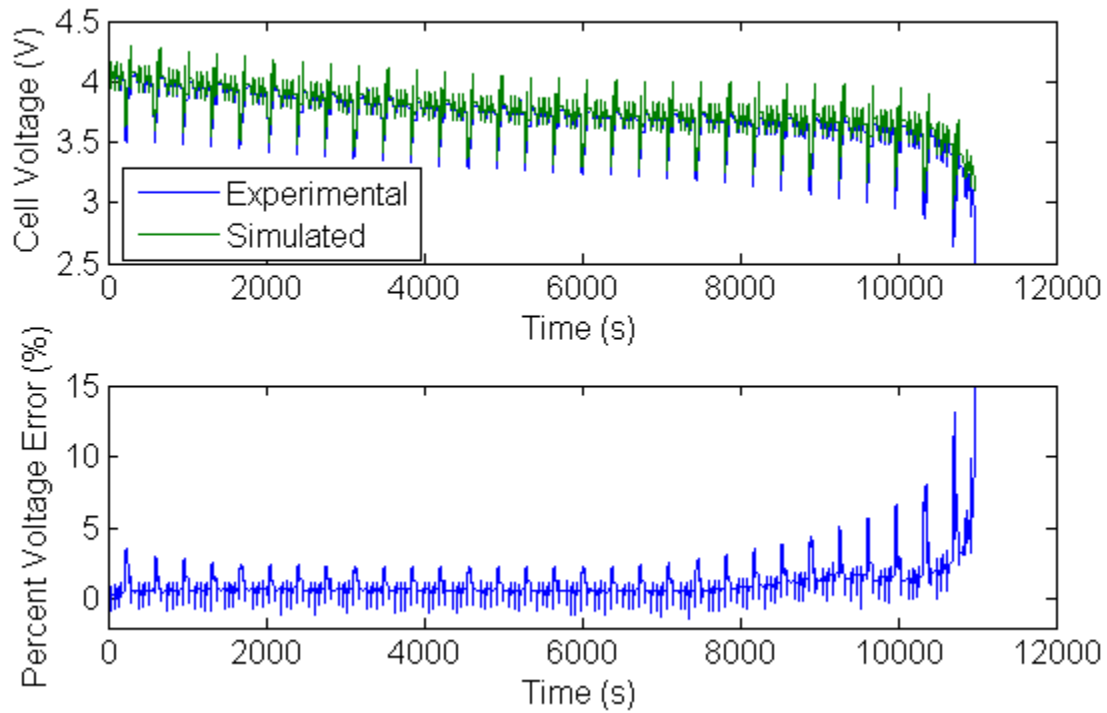


Figure 3-54. Plot of results from the 6.0 A DDT. The top plot shows the measured and simulated cell voltages.

The simulations were performed using the spherical electrode model. The bottom plot is the PVE.

Model	DDT	MAPVE (%)	MAPVE (mV)	RMSPVE (%)	RMSPVE (mV)
Spherical	6.0 A	7.7	240	1.5	54
	2.0 A	3.3	110	0.85	31
	600 mA	1.9	69	0.59	21
Planar	6.0 A	3.7	120	0.84	30
	2.0 A	2.2	81	0.30	11
	600 mA	1.5	53	0.46	17

Table 3-17. Tabulated results of the MAPVE (in terms of both percentage and voltage), and RMSPVE (also in terms of percentage and voltage) for the beginning 95% duration of the three DDTs. Results are shown for both planar and spherical models. The results shown are the average over the three tested cells.

From the bottom plot in Figure 3-54, which shows the PVE over the course of the test, it can be seen that the large value of MAPVE comes from the parts of the load profile when the discharge current is 6.0 A. This error is positive, meaning that the simulated cell voltage is higher than the experimental results. The cause of this may be attributed to the spherical electrode model as follows. In the spherical electrode, the distribution of capacitance is more heavily distributed towards the surface. However, inside a real lithium ion cell, there is a finite thickness in the porous electrode, as shown in diagram A of Figure 3-51. Therefore, the spherical particles that are located at different depths in the electrode behave differently. In contrast, in the spherical distributed SOC model proposed in this thesis work, the electrode is modeled as a single spherical particle. Therefore, the ionic and electronic transport losses are neglected in the spherical distributed SOC model. If the solution-phase and electronic phase resistances are included to model the thickness dimension of the porous electrode, it will lead to a drop in voltage during discharge, so it may account for the over-estimation of cell voltage by the

spherical distributed SOC model. This porous electrode thickness effect is also suggested as a contributing factor in the observed impedance response of the electrode in the work by Troltzsch *et al.*[29].

The simulated and experimental results for the 2.0 A and 600 mA DDTs are shown in Figure 3-55 and Figure 3-56, respectively. The MAPVE and RMSPVE for these two tests are also tabulated in Table 3-17. Two observations can be made from these results. First, when the test currents are lowered (for example, 2.0 A DDT vs. 6.0 A DDT), the simulation accuracy of the spherical distributed SOC model increases. This is consistent with the results obtained for the planar distributed SOC model discussed earlier. As discussed previously in this section, this accuracy improvement at lower current can be attributed to lower resistive drops in the circuit and lower effects of mis-estimation of the circuit resistances, leading to lower PVEs. Second, there is a SOC range towards the end of discharge where the PVE is higher compared to SOC outside this range. This was also observed for the planar distributed SOC model earlier in this section (shown in Figure 3-36 and Figure 3-37). During the analysis of the planar model results, it is found that this SOC range is between *ca.* 0.07 to 0.2, and can be explained by the pronounced plateau in the cell open-circuit-voltage that is not sufficiently well captured by the open-circuit-voltage V_{OC} parameter, which is an empirical fit, used in the model. This can be resolved by including more parameter extraction pulses in this SOC region to get a more accurate representation of the OCV there.

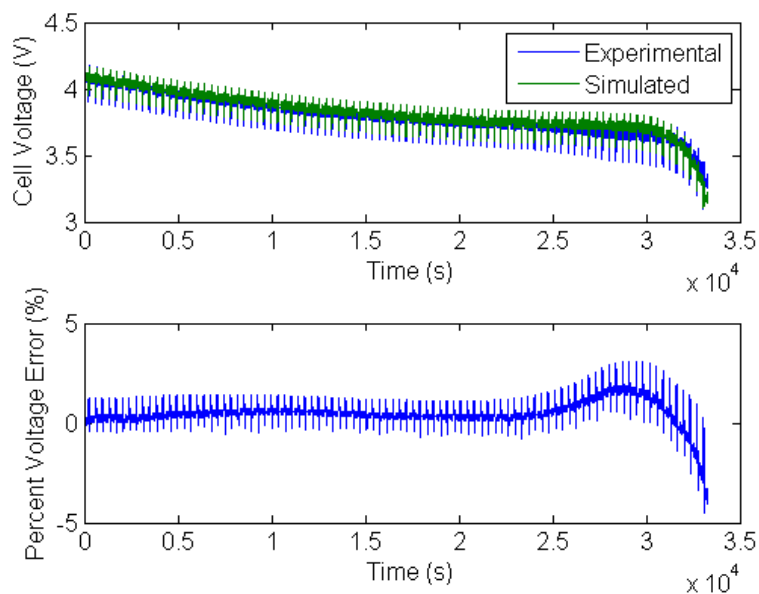


Figure 3-55. Plot of results from the 2.0 A DDT. The top plot shows the measured and simulated cell voltages. The simulations were performed using the spherical electrode model. The bottom plot is the PVE.

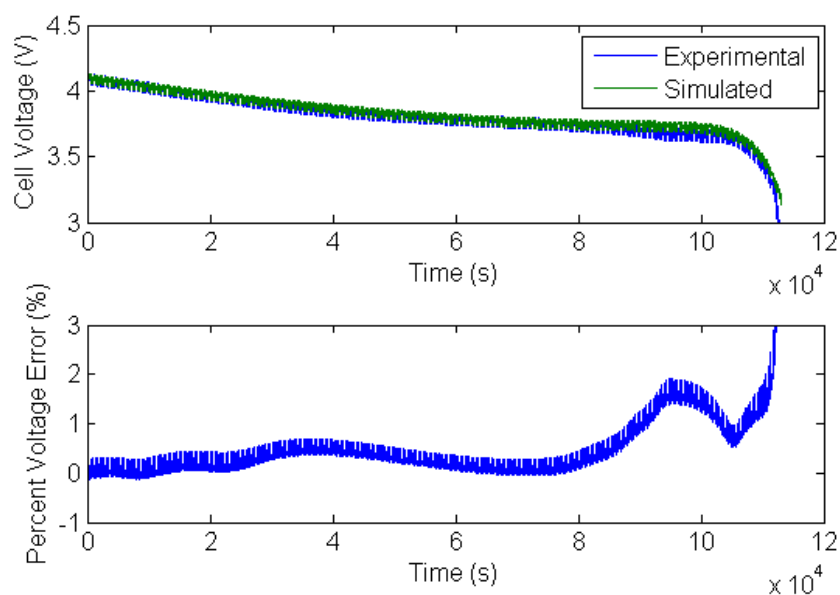


Figure 3-56. Plot of results from the 600 mA DDT. The top plot shows the measured and simulated cell voltages. The simulations were performed using the spherical electrode model. The bottom plot is the PVE.

As mentioned in Section 1.3.2.3, the expected MAPVE for equivalent-circuit models is on the high side of the 1-5% range suggested by Chen and Rincon-Mora [2], while the RMSPVE is expected to be on the low side of this range. The performance of the spherical distributed SOC model can be summarized as follows. From the results of the DDTs (see Table 3-17), it can be seen that for the two lower current tests, 2.0 A and 600 mA, the performance is satisfactory. The MAPVE are between 1.9-3.3% (or 69-110 mV), and the RMSPVEs are between 0.59-0.85% (or 21-31 mV). However, for the 6.0 A DDT, the MAPVE rose to 7.7% (or 240 mV), which makes the spherical model unsuitable for this test. This is due to the large 6.0 A pulses within its profile. As explained in this section, this large error during the 6.0 A discharge pulses may be caused by an over-estimation of available capacitance by the spherical electrode model. On the other hand, for simulating the behavior of the four constant current discharge tests, the model performed well at 3.0 A (1.0 C) or below. For the three discharge tests with constant currents between 600 mA and 3.0 A, the MAPVE are *ca.* 1.3% (or 43-52 mV), and RMSPVE ranged between 0.65-0.95% (or 23-30 mV). However, for the 6.0 A constant current discharge test, the performance was much worse. The MAPVE is 5.1% (or 160 mV), while the RMSPVE is 1.8% (or 64 mV). Considering the simulation performance of both these validation tests together, it can be concluded that the spherical distributed SOC model is sufficiently accurate for use in applications that have average discharging current up to 3.0 A (or 1.0 C), or have discharging and charging currents bounded by the limits of 2.0 A (0.66 C) and 1.0 A (0.33 C), respectively.

The planar distributed SOC model is shown to perform well for dynamic discharge, but poorly for constant current discharge at 1.5 A (0.50 C) or above. This restricts the utility of the planar model to low average discharge currents (0.60 A, or 0.20 C), with discharging and charging

pulses of up to 6.0 A (2.0 C) and 3.0 A (1.0 C), respectively. On the other hand, the spherical distributed SOC model is sufficiently accurate for use in applications that have average discharging current up to 3.0 A (or 1.0 C), or discharging and charging pulsed currents bounded by limits of 2.0 A (0.67 C) and 1.0 A (0.33 C), respectively. Therefore, it can be seen that there is a tradeoff between the constant and dynamic discharge performance of the distributed SOC models. As discussed in this section, this difference in performance of the models can be attributed to the distribution of charge storage capacitance in the electrode. The spherical model has a higher proportion of its capacitance located towards the electrode surface than the planar model. This contributes to the better simulation performance for the high current constant current discharge than the planar model. However, because of the simplified nature of the single spherical electrode, it neglects the thickness of the porous electrodes in real cells. Therefore, the spherical electrode over-estimates the available capacitance, and contributes to the over-estimate of the cell voltage during high current pulses in the DDTs. Therefore, there is merit to both electrode models.

As one reason for the inaccuracy of the models, in the case of over-estimation of cell voltage, is the lack of accounting for the thickness of the porous electrodes (shown in diagram A of Figure 3-51), this is one possible avenue for future work. By resolving this issue, the extent of application of the distributed SOC model would be increased. It is useful to once again compare to the P2D model, as discussed in Section 1.3.1. In that model, the spherical particles throughout the thickness of the porous electrode are modeled. To include the effect of the porous electrode thickness, an equivalent-circuit model of the form shown in Figure 3-57 can be used. The solution-phase resistance, illustrated as R_{sp} , connects the spherical electrode particles at different

porous electrode depth. The electronic phase resistance is excluded because it is usually much smaller than the solution phase one. When applying this model, the solution-phase resistance can be found by fitting the constant current discharge results to simulations. This two dimensional transmission line is an interesting avenue for future work. A disadvantage of the approach however is the increased number of parameters, some of which are not directly measurable without a destructive test. For example the ionic resistance through the thickness of the composite is not readily determined independently. The simplicity of the planar and spherical distributed SOC models, in which there are only three physical properties needed for each SOC (open-circuit voltage V_{OC} , diffusion resistance R_D , and series resistance R_S), makes these approaches attractive.

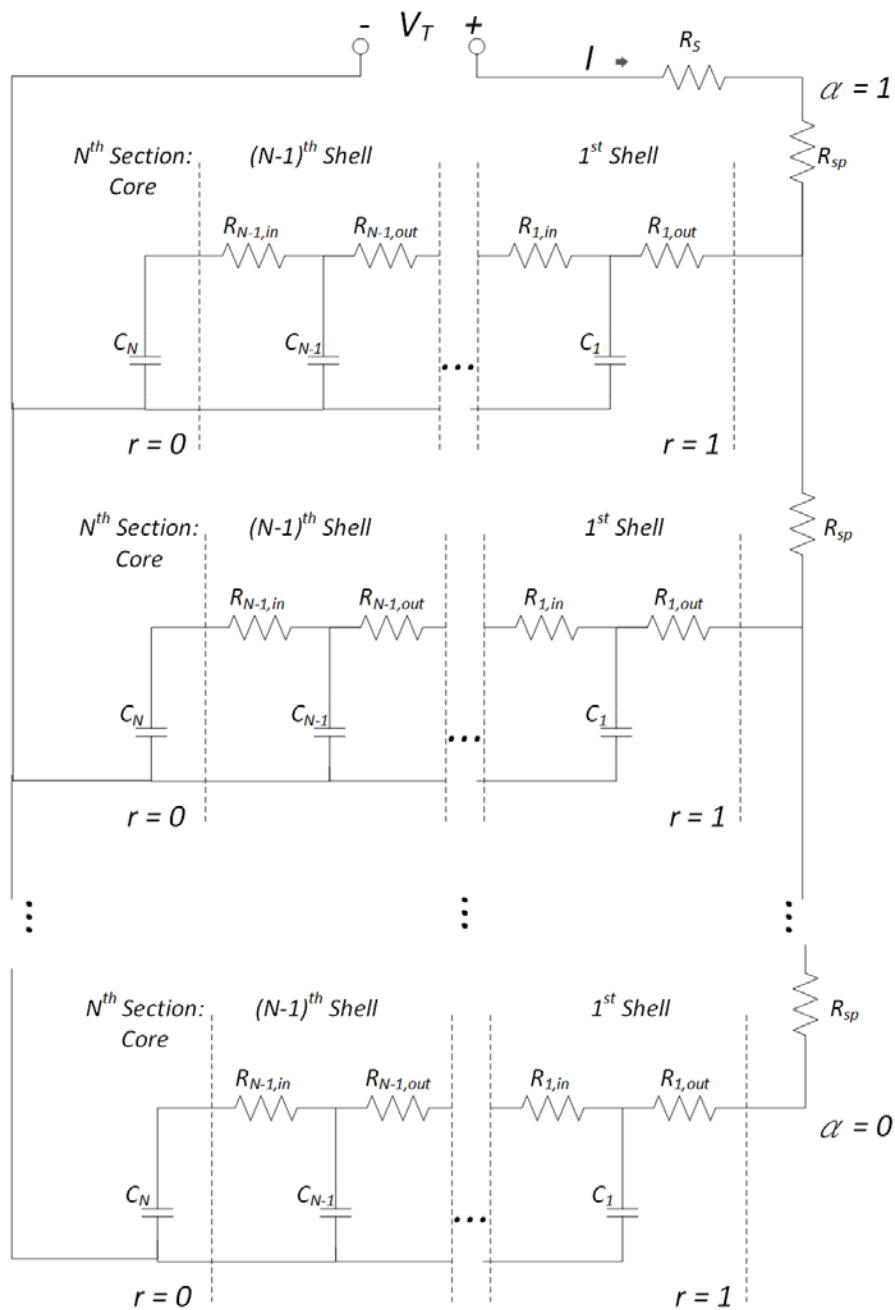


Figure 3-57. Equivalent-circuit model that adds solution-phase resistance effects to the spherical electrode to model the thickness of the porous electrode. This is an avenue for extending the range of applicability of the distributed SOC model.

In this section, the validation of the distributed SOC model is performed using dynamic and constant current discharge tests. While the planar distributed SOC model performed well for simulating the DDTs at 6.0 A, 2.0 A, and 600 mA, it performed poorly for higher current constant current discharge tests (1.5 A, 3.0 A and 6.0 A). This can be attributed to the planar electrodes charge storage capacitance distribution being uniform through the electrode thickness. This contrasts with the spherical particles that are commonly found within the electrodes in real lithium ion cells. A spherical distributed SOC model is derived and its performance is validated using the same discharge tests. It is found that the spherical model performs better than the planar model for higher current constant discharge tests, but not as well for DDTs. Therefore, there appears to be a tradeoff between simulation accuracy for constant current discharge and DDTs. This can be attributed to the thickness of the porous electrodes within real lithium ion cells. In this way, both spherical (due to particle shape) and planar (due to porous electrode thickness) effects govern the cell performance. An avenue for model improvement would be to account for both effects in the equivalent-circuit model, as shown in the two-dimensional model (Figure 3-57). Nevertheless, the performance of the spherical model has been shown to be good for constant current discharge tests performed up to 3.0 A, and the two lower current DDTs (600 mA and 2.0 A). The planar model performed well for all the DDTs (up to 6.0 A), and for the 600 mA constant current discharge. Therefore, for specific applications that fit these load profiles, the proposed circuit models are still sufficiently accurate, when considering the expected accuracy range for equivalent-circuit models is 1-5% according to Chen and Rincon-Mora [2]. The key advantage of the proposed (planar and spherical) distributed SOC models are their simplicity, and ease of model parameter extraction, so there is still significant utility of these models for use by engineers in simulating cell responses.

3.4 Chapter Conclusions

In this chapter, the pulsed current method for extracting parameters of the distributed SOC model discussed in Chapter 2 is applied to three commercial cylindrical GP18650-30U lithium ion cells. Discharging and charging current pulses of different magnitudes (as high as 6.0 A, or 2.0 C) are used. The circuit parameters are extracted and used to create fits of open-circuit voltage V_{OC} , diffusion resistance R_D , and series resistance R_S as functions of cell SOC. It was shown that the extracted parameters are largely independent on magnitude and direction of current used for parameter extraction. Therefore, relative to similar equivalent-circuit models in the literature, the distributed SOC model's advantage is the relative reduction in experimental time and effort required for parameter extraction and model construction.

The cells were further characterized according to two types of validation testing. The simulation performance of the distributed SOC models were based on the MAPVE and RMSPVE obtained, which were averaged for the three tested 30U cells. As mentioned in Section 1.3.2.3, the expected MAPVE for equivalent-circuit models is on the high side of the 1-5% range suggested by Chen and Rincon-Mora [2], while the RMSPVE is expected to be on the low side of this range. The first type of validation is a DDT that is based on the transient features of automotive testing. Three separate DDTs with different maximum discharge currents (6.0 A, 2.0 A, and 600 mA) are performed. The experimental results obtained from this validation test was compared to simulated results obtained from the planar distributed SOC model. It was found that the MAPVE ranged between 1.5-3.7% (or 53-120 mV), while the RMSPVE ranged between 0.30-

0.84% (or 11-30 mV). Therefore, by both these measures, they are well within the 1-5% value expected of equivalent-circuit models. The results showed that the simulation performance improved with lower test currents. This can be attributed to the lower IR effects from the circuit resistances, and differences between the estimated and true resistances. Also a SOC range has been identified (between *ca.* 0.07 and 0.2) that has reduced simulation accuracy. This may be due to the empirical fit that is used for the open-circuit voltage V_{OC} model parameter not capturing the plateau behavior of the cell OCV very well. In the future, this can be improved by performing more parameter extraction pulses in this SOC region. Further, a π -model is introduced, which is shown to perform better than the original model in Chapter 2 in cases where simultaneously the number of RC-segments is small and the applied current is large. This may be attributed to the resistance R_D/N (where N is the number of segments in the model) at the beginning of the transmission line in the original-form model. This resistance shifts the simulated voltage by a constant IR_D/N . Therefore, when the model has a small number of segments and larger currents are applied, the error introduced by this resistance leads to an appreciable error. For large number of RC-segments or low applied currents, the two models perform similarly.

The second type of validation test is a constant current discharge test at currents ranging from 0.60 A (0.20 C) to 6.0 A (2.0 C). Comparisons of the experimental results and the simulated results, obtained using the planar distributed SOC model, show that the model performs well at low current (0.60 A). The MAPVE was 0.96% (or 35 mV), while the root-mean-square-percent-voltage error was 0.49% (or 18 mV). However at higher currents (between 1.5 A to 6.0 A), the performance was poor. It was found that the MAPVE ranged between 3.6-13% (or 130-410

mV), while the RMSPVE ranged between 2.1-10% (or 74-370 mV). This points to the model under-estimating the capability of the electrode to supply charge. It can be concluded that the planar distributed SOC model is sufficiently accurate for use in applications that have low average discharging current (up to 750 mA, or 0.25 C, as shown in Table 3-11), with discharging and charging current pulses up to 6.0 A (2.0 C) and 3.0 A (1.0 C), respectively.

This issue was investigated further by the derivation and use of the distributed SOC model based on spherical electrodes. It was found that simulation performance for the three lower tested constant discharge currents (600 mA, 1.5 A, and 3.0 A) was good. The MAPVE was consistently at 1.3% (or 43-52 mV), while the RMSPVE ranged between 0.65-0.95% (or 23-30 mV). The performance of the spherical model for the highest constant discharge current tested (6.0 A) was worse, with a MAPVE of 5.1% (or 160 mV) and RMSPVE of 1.8% (or 64 mV). This performance drop-off can be attributed to over-estimation of the diffusion capacitance from the parameter extraction process, as the diffusion capacitance falls off rapidly at low SOC. This results in over-estimation of diffusion resistance as well, since the diffusion resistance and capacitance are proportionally related. This in turn limits the circuit model's ability to deliver charge at high constant current discharge.

The spherical distributed SOC model was also validated using the three DDTs. From comparing the measured results to the simulated results, it was found that for the two lower current tests, 2.0 A and 600 mA, the performance is satisfactory, as both are within the 1-5% accuracy expected of equivalent-circuit models [2]. The MAPVEs are between 1.9-3.3% (or 69-110 mV), and the RMSPVEs are between 0.59-0.85% (or 21-31 mV). However, for the 6.0 A DDT, the MAPVE

rose to 7.7% (or 240 mV), which makes the spherical model unsuitable for this loading profile. The large maximum error occurs during the large 6.0 A discharge pulses within the DDT profile. The observed over-estimation of the cell voltage may be attributed to the spherical electrode over-estimating the available capacitance, as the porous electrodes' thicknesses in a typical lithium ion cell serve to distribute the available capacitance throughout the thickness of the electrodes. Considering the simulation performance of both these validation tests together, it can be concluded that the spherical distributed SOC model is sufficiently accurate for use in applications that have average discharging current up to 3.0 A (or 1.0 C), or load profiles with discharging and charging currents bounded by 2.0 A (0.66 C) and 1.0 A (0.33 C), respectively.

Therefore, it can be seen that there is a tradeoff between the constant and dynamic discharge performance of the distributed SOC model. As discussed in this section, this difference in performance of the models can be attributed to the distribution of charge storage capacitance in the electrode. The spherical model has more capacitance distributed towards the electrode surface than the planar model. This contributes to the better simulation performance for the high current constant discharge than the planar model. However, because of the simplified nature of the single spherical electrode, it neglects the thickness dimension in the porous electrodes in real cells. Therefore, the spherical electrode over-estimates the available capacitance, and contributes to the over-estimate of the cell voltage during high current pulses in the DDTs. Therefore, there is merit to both electrode models.

Depending on the expected load profile of the application, the planar or spherical distributed SOC model may be chosen. For applications with low sustained discharge rates (0.60 A, or 0.20

C), and high charging or discharging pulses, the planar model performs well. On the other hand, if the average discharge rate is higher (up to 3.0 A, or 1.0 C) or if the load is bounded by discharge and charge currents of 2.0 A (or 0.67 C) and 1.0 A (or 0.33 C), the spherical model performs better. For load profile that exceeds the bounds discussed here, additional validation experiments would be needed. It may be the case that a more detailed electrochemical model that accounts for the underlying physical phenomena more accurately is necessary to give accurate simulation results in these cases.

Compared to these more sophisticated electrochemical models, the benefits of the suggested distributed SOC models lie in their simplicity, the extraction method, and their suitability for engineers to use, without the need for de-constructing cells and understanding the underlying physics of the cell to use. Also, the use of a smaller number of parameter extraction experiments is a key advantage of the distributed SOC models compared to similar equivalent-circuit models in the literature. A two-dimensional model is suggested as a further avenue to improve the equivalent-circuit performance to cover both sustained and pulsed discharge.

The contributions made in this work that have been presented thus far is summarized here.

a. The planar distributed SOC equivalent-circuit model is developed (Section 2.1). This model is derived based on a planar electrode. This model consists of a non-linear transmission line with parameters that are dependent on the cell- and local-SOC. This is the key difference of this model when compared to equivalent-circuit models in the literature. The other published models can contain non-linear RC networks, but they serve to provide the desired impedance, which is

placed in series to a voltage source. This makes the arrangement similar to a Thévenin equivalent-circuit. In these models, the RC networks do not represent energy storage inside the cell. In the distributed SOC model, there are SOC-tracking circuits associated with each depth of the electrode, and the circuit parameter values are dependent on this local-SOC.

b. A method to extract the circuit parameters, and their dependence on SOC, is presented (Section 2.3.1). This method consists of pulsed current experiments. The four model parameters obtained are the full-capacity-equivalent capacitance C_{FCE} , the open-circuit voltage V_{OC} , the diffusion resistance R_D , and series resistance R_S . Analysis of the measured cell voltage during the pulsed current experiment is used to extract these four model parameters. While this extraction method is similar to the Galvanostatic Intermittent Titration Technique (GITT), it is important to note that the GITT method is aimed at obtaining the solid-phase diffusion coefficient D of solutes in an electrode material. The method requires as inputs the physical dimensions and stoichiometries of the material to obtain this diffusion coefficient. In the distributed SOC model, the physical details of the materials inside the cell are abstracted away by using a non-dimensionalized electrode model. In this way, the engineer can construct the distributed SOC equivalent-circuit model without detailed understanding of the internal structure of the cell, which is beneficial to the engineers who only require an equivalent-circuit model for simulations to support application design and verification. In fact, this is one of the key advantages of equivalent-circuit models when compared to electrochemical models that, although the latter include more physical mechanisms and details, they are far more complex to construct and understand.

c. The parameters of the distributed-SOC equivalent-circuit model is shown to be largely independent on applied current (current magnitude and direction), as shown in Section 2.3.3. Other equivalent-circuit models published in the literature are shown to have strong dependence on the current magnitude and direction [3], [4], [6]. The reason that these models show such dependence is that the different applied currents used in these tests excite different charge distributions inside the cell electrodes. This is discussed in Section 3.2.2.3. The re-equilibration of the charge distribution in the electrodes during the relaxation phase of the pulse tests used to determined equivalent circuit parameters causes a different cell voltage response. This leads to a strong dependence of the parameters in these equivalent-circuit models on applied current (current magnitude and direction). In the distributed SOC equivalent-circuit model proposed here, the use of a non-linear transmission line to model ion diffusion in the electrode provides a more accurate picture of the physics occurring inside the cell. This is the reason the parameters of the distributed SOC equivalent-circuit model are largely independent on current magnitude or direction. This means that parameter extraction experiments for constructing the distributed SOC model will require far fewer (as few as one or two) experiments. This reduces the model construction efforts.

d. The simulation of commercial lithium ion cells using the planar distributed SOC model is shown to match well to the measured cell response during DDTs. The DDT is a variable-current load profile that captures the transient nature of loading in electric vehicles. This profile is used to illustrate the performance of the planar distributed SOC model to simulate cell behavior in similar loading conditions. It was found that the MAPVE ranged between 1.5-3.7% (or 53-120 mV), while the RMSPVE ranged between 0.30-0.84% (or 11-30 mV). As mentioned in Section

1.3.2.3, the expected MAPVE for equivalent-circuit models is on the high side of the 1-5% range suggested by Chen and Rincon-Mora [2], while the RMSPVE is expected to be on the low side of this range. Therefore, by both these measures, the performance of the planar distributed SOC model in simulating the dynamic discharge loading profile is good.

e. The use of π -form RC segments in the non-linear transmission line of the planar distributed SOC model is shown to perform better than the original-form RC segments (Section 3.3.1.3) in cases where simultaneously the number of RC-segments is small ($N \leq 8$, where N is the number of segments in the model) and the applied currents are large (6.0 A DDT). This may be attributed to the resistance R_D/N at the beginning of the transmission line in the original-form model. This resistance shifts the simulated voltage by a constant IR_D/N . When the model has a small number of segments and larger currents are applied, the error introduced by this resistance leads to an appreciable error. In cases where the model contains a large number of RC-segments ($N \geq 16$) or the applied currents are low (600 mA DDT), the two models perform similarly.

f. The performance of the planar distributed SOC model in simulating the same commercial lithium ion cells in constant current discharge tests is also studied. It is shown that the model performs well at low constant current discharge (0.60 A, or 0.20 C). The MAPVE was 0.96% (or 35 mV), while the root-mean-square-percent-voltage error was 0.49% (or 18 mV). However at higher currents (between 1.5 A to 6.0 A), the performance was poor. It was found that the MAPVE ranged between 3.6-13% (or 130-410 mV), while the RMSPVE ranged between 2.1-10% (or 74-370 mV). Therefore, the planar model used initially to derive the distributed SOC equivalent-circuit model works well at low constant currents, and for pulsed currents of larger

magnitudes (tested at 6.0 A, or 2.0 C, which is the rated maximum for the tested cells). The errors at larger constant currents may be attributed to the spherical nature of the active material particles in the real lithium ion cell electrodes.

g. An alternative structure of the distributed SOC equivalent-circuit model is suggested that is based on a spherical electrode (Section 3.3.2.3). This is called the spherical distributed SOC model. The advantage of the model is its larger charge storage capacitances located towards the surface of the electrode. It is shown that the simulation performance of this model for higher constant current discharge is much improved, when compared to the planar circuit model. It was found that for the three lower tested currents (600 mA, 1.5 A, and 3.0 A), the MAPVE was consistently at 1.3% (or 43-52 mV), while the RMSPVE ranged between 0.65 and 0.95% (or 23-30 mV). The performance of the spherical model for the highest constant current discharge current tested (6.0 A) was worse, with a MAPVE of 5.1% (or 160 mV) and RMSPVE of 1.8% (or 64 mV). It was still significantly better than the corresponding results from the planar model.

h. The spherical distributed SOC model was also used to simulate the DDTs. The simulation performance of the spherical model for the 600 mA and 2.0 A DDTs was acceptable, with maximum-absolute-percent-voltage error between 1.9-3.3% (or 69-110 mV) and RMSPVE of 0.59-0.85% (or 21-31 mV). However, for the 6.0 A DDT, the maximum-absolute-percent-voltage error is 7.7% (or 240 mV), while the RMSPVE is 1.5% (or 54 mV). This high MAPVE for the 6.0 A test may be due to too much capacitance available at the surface of the electrode, leading to an over-estimation of cell voltage during large current pulses (6.0 A) of the DDT.

This is due to the spherical distributed SOC model neglecting the thickness of the porous electrodes that are in real lithium ion cells. This thickness is captured in the P2D model.

i. There is tradeoff between the two versions (planar and spherical) of the distributed SOC model. The expected load profile of the specific application determines which of the two models should be chosen. For applications with low average discharge rates (0.60 A, or 0.20 C), and high discharging (up to 6.0 A, or 2.0 C) and charging (up to 3.0 A, or 1.0 C) pulses, the planar model performs well. If the average discharge rate is higher (up to 3.0 A, or 1.0 C), or if the discharging and charging currents are bounded, respectively, by 2.0 A (or 0.67 C) and 1.0 A (or 0.33 C), the spherical model performs better. Outside of these two ranges of applied loads, both distributed SOC models may perform poorly, with errors much larger than 5%. In this case, the use of the P2D model discussed in Section 1.3.1 may be necessary. Alternatively, the two-dimensional distributed SOC model (shown in Figure 3-57) suggested at the end of this chapter may also be a promising approach.

In the next chapter, extraction of the distributed SOC model parameters for a tin thin film electrode is shown. This tin electrode belongs to a class of lithium-alloying electrodes that shows strong phase transformation characteristics during the charge and discharge process. The next chapter is a preliminary study on the use of this equivalent-circuit model to model the tin electrode by analyzing the extracted parameters.

Chapter 4: Characterization of Tin Electrodes¹

This chapter is a preliminary study of the suitability of the planar distributed SOC equivalent-circuit to model the behavior of a tin thin film electrode. Tin is of interest because it is one of a class of alloying electrodes that is promising as a high capacity anode material. Tin has much higher capacity than the graphitic electrodes currently used in lithium ion cells (ca. 1000 mAh/g vs. 372 mAh/g) [98].

In the previous two chapters, the distributed SOC equivalent-circuit model is proposed and its performance is validated using two commercial lithium-ion cells. The model consists of a non-linearized RC network, which is derived based on diffusion of lithium ions inside the active material particles in the electrodes. It is found that this model can be used to successfully simulate the behavior of these tested cells under certain loads. However, tin, and other alloying elemental electrodes, are known to exhibit pronounced phase change characteristics over several wide SOC ranges. Therefore, aspects of the tin electrode's behavior are expected to be poorly explained using the diffusion model. The aim of this chapter is to investigate the shortcomings of the proposed distributed SOC equivalent-circuit model if it was to be used in modeling of tin and other alloying elemental electrodes.

¹ A version of this chapter has been published in a peer-reviewed conference transactions (Reused with permission from “Eddie C.W. Fok and John D. Madden. (2013) Measurement of the Diffusion Coefficient of Lithium in Tin Thin Films Including Phase Transformation Effects. ECS Trans. 53:131-142.”, Copyright 2013).

To isolate the response of the tin electrode, an electrochemical configuration called a half-cell is used. A pulsed current method, like that used in the last two chapters to extract the equivalent-circuit model parameters, is used to characterize the tin electrode. In electrochemistry, this is a well-known technique called GITT [69], [99], [100]. It is commonly applied to measure the solid-phase lithium ion diffusion coefficient inside various materials. This chapter also explores the validity of using a diffusion model alone to characterize transport within electrodes with prominent phase changes, such as tin.

In this chapter it is found that a diffusion model suggests orders of magnitude drop in diffusion coefficient at states of charge where phase changes occur. A better description of these transitions may be provided by a two phase model.

Section 4.1 discusses the background for this chapter's work. The experimental setup is described in Section 4.2. The results are discussed in Section 4.3, while the chapter conclusions are presented in Section 4.4.

4.1 Background

Lithium alloys are promising materials for use as the negative electrode active material in lithium-ion batteries due to their high lithium storage capacities. Alloys such as lithium-silicon and lithium-tin have capacities of 4200 mAh/g and 990 mAh/g, respectively [98]. Figure 4-1 shows the gravimetric capacities (left y-axis), and volumetric capacities (right y-axis) of various alloying electrodes of lithium. Some of these candidates have significantly higher specific

capacities than the 372 mAh/g of graphitic materials that are commonplace in today's lithium ion batteries.

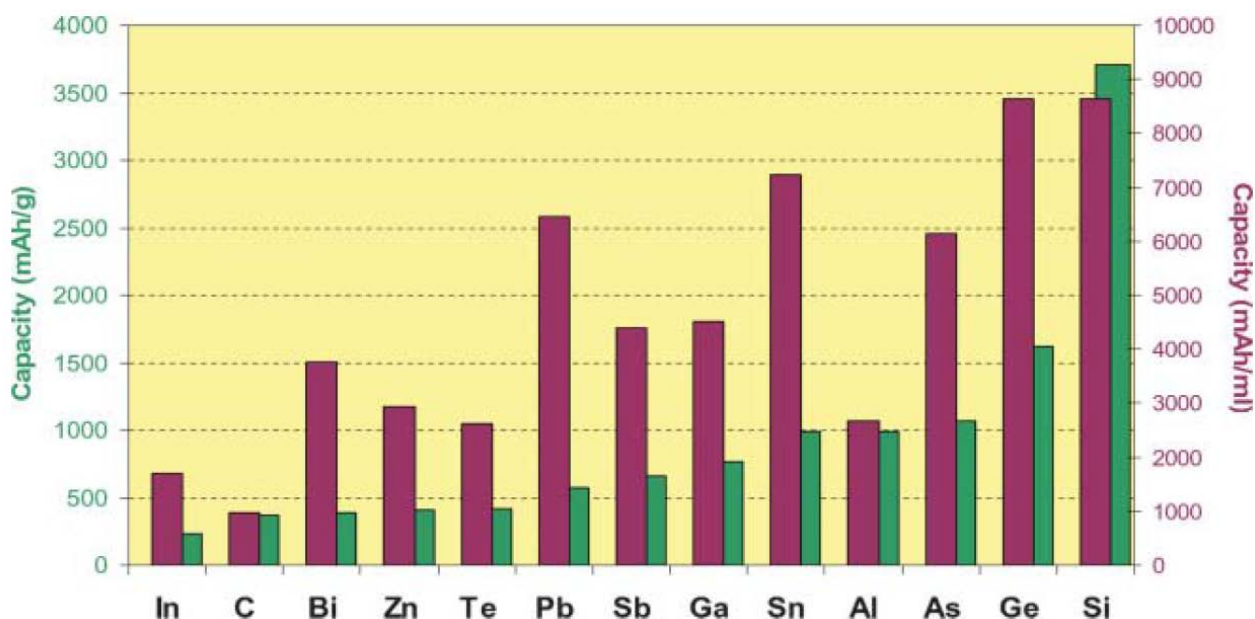


Figure 4-1. Comparisons of capacities (gravimetric (green) and volumetric (purple)) between different elemental electrodes. Reproduced from [101] with permission of The Royal Society of Chemistry.

It is well known that charging and discharging of alloying elements involve transitions amongst multiple phases. There is a marked difference in the governing physics when phase changes are present. This is akin to the solidification of water to form ice, where a requisite amount of heat energy is required to be removed to convert the water at the ice-water interface into ice. In the case of a phase change of a lithium electrode during charging, conversion of mobile lithium ions to form part of the new crystal structure of the new phase occurs [85]. This requires a significant quantity of lithium ions and explains the high capacities of these alloying electrodes [69], [85]. Silicon and tin electrodes are two alloying materials that feature phase changes, and have

recently been of great interest due to their exceptional capacities. These electrodes however also exhibit cycle life challenges due to decrepitation [85], which is the crumbling of the electrodes due to the large volume changes of the electrode as it is repeatedly charged and discharged. In this chapter, the response of a tin thin film electrode is investigated to identify shortcomings of modeling this electrode using the planar distributed SOC equivalent-circuit model and the use of a diffusion model in general.

The GITT was first proposed and used to measure the lithium-ion diffusion coefficient in solid state materials by Weppner and Huggins [69]. It assumes the mobile species transport is governed by diffusion. The diffusion coefficient is of interest fundamentally to enable the description of transport – in this case of lithium. It is related to the reciprocal of the diffusion resistance R_D in the distributed SOC equivalent-circuit model. This can be shown by comparing the diffusion equation governing lithium ion transport in the planar electrode (equation [2-1]), to the differential equation governing charge transport in the RC transmission line (equation [2-16]). In the model, a large diffusion resistance R_D (small diffusion coefficient) results in a large impedance to ion transport in the electrode. It is also influenced by the reciprocal of the diffusion capacitance C_D . Increased diffusion capacitance slows the propagation of charge just as increased heat capacity slows the spread of heat. Diffusion limits performance of a battery. For example during discharge, charges stored deep inside the electrode (small α in planar model, or small r in spherical model) cannot be transported to the surface quickly enough to be extracted before the surface voltage drops below the rated lower voltage limit of the electrode, leading to the termination of the cell discharge by the user or the battery management system to prevent cell over-discharge. In general a small diffusion coefficient limits the rate of discharge and charge.

Knowledge of diffusion rates can help cell designers tradeoff between particle size and the desired charge/discharge rate. Also, the diffusion coefficient of lithium in the positive and negative electrode active materials are needed in the electrochemical models for simulating the behavior of the cell electrodes.

The modeling of phase changes is first discussed by Stefan [102]. Additional discussions on phase change problems with different boundary conditions can be found in the work by Carslaw and Jaeger [70]. As opposed to diffusive transport, where closed-form analytical solutions for various sets of boundary conditions can be derived [70], there is no closed form solution to the phase change problem with flux condition at the boundary. Use of numerical solution techniques such as finite-difference- or finite-element-methods are required to obtain a solution. The governing equations for the modeling of diffusive transport are contrasted to those of diffusive transport including phase transformation effects below.

The extraction of the diffusion coefficients of a mobile species inside a solid using current pulses was first proposed by Weppner and Huggins [69]. The example of a planar model is given here as it will be used to model the transport through a thin film of tin. The charge and discharge process of a planar electrode are modeled as a one-dimensional system, with thickness L . This is illustrated in Figure 4-2. The extraction of the lithium ion diffusion coefficient is done by fitting an infinite diffusion model to the voltage curve resulting from the step current. The method assumes both that the charging pulse is brief relative to the diffusion time constant. It also assumes that there are no phase changes in the material.

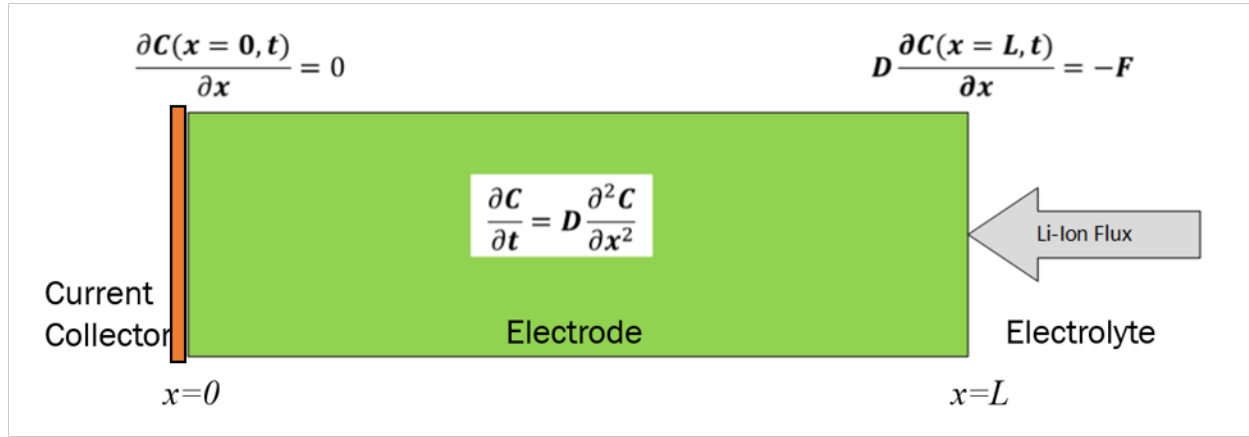


Figure 4-2. Planar diffusion element for modeling lithium ion diffusion into the tin thin film.

In the case of a single phase material, the concentration of lithium ions is a function of time and position, $C(x,t)$, and the lithium ion distribution is governed by the diffusion equation

$$\frac{\partial C}{\partial t} = D \frac{\partial^2 C}{\partial x^2}, \quad [4-1]$$

where D is the lithium ion diffusion coefficient, and x is the position in the thickness direction of the electrode. The boundary conditions specified at the solution/electrode surface ($x=L$) and current collector/electrode interface ($x=0$) are determined using Fick's First Law. At the solution/electrode interface the concentration gradient is determined by the applied current density, j ,

$$\frac{\partial C(x=L, t)}{\partial x} = -\frac{j}{nFD}, \quad [4-2]$$

where n is the charge number of electroactive species (for a Li-ion electrode, $n = 1$), and F is the Faraday constant (number of Coulombs per mole of electrons). At the current collector/electrode interface, there is no ionic current, so

$$\frac{\partial C(x = 0, t)}{\partial x} = 0. \quad [4-3]$$

As mentioned earlier, the GITT is a standard technique to obtain the lithium ion diffusion coefficient using pulsed current. The procedure to obtain the lithium ion diffusion coefficient is analogous to the extraction procedure of diffusion resistance R_D in Section 2.3.1, and the results shown in Sections 2.3.3 and 3.2.2.2. Similar to the extraction of diffusion resistance R_D , the initial response of the electrode voltage to the pulse phase of the current is fitted to $t^{1/2}$. From Weppner and Huggins [69], the lithium diffusion coefficient D can be approximated by

$$D = \frac{4}{\pi} \left(\frac{V_M J}{nF} \right)^2 \left[\left(\frac{\partial E}{\partial \delta} \right) / \left(\frac{\partial E}{\partial \sqrt{t}} \right) \right]^2, \quad [4-4]$$

where E is the electrode potential (vs. Li/Li^+), V_M is the electrode's molar volume, δ is the stoichiometry of the electrode, F is Faraday's constant, n is the number of electrons transferred in the reaction, and $dE/d\delta$ is the change in electrode potential due to the stoichiometry change as a result of the current pulse phase. As mentioned earlier, the diffusion coefficient D is related to the reciprocal of the diffusion resistance R_D , as well as the diffusion capacitance, C_D . In this case the physical properties of the material are used in equation [4-4] to obtain a material-specific parameter. The extraction procedure of the diffusion resistance R_D and diffusion capacitance C_D for the cells in Chapter 2 and 3 uses a dimensionless electrode thickness of 1, so the specific material properties of the electrode are abstracted away. This is useful for the engineer of application systems, as there is no need to take apart lithium ion cells to measure detailed physical properties of the lithium ion cell. The abstracted model provides a useful means of obtaining a simulation tool for the engineer to perform the required design and verification work.

Transport involving a phase change has been described by a combination of diffusion in each phase, and the addition of a phase boundary across which mass – in this case in the form of lithium – is exchanged. In the phase-change model, equations [4-1]-[4-3] are modified to include the presence of these two phases, and a phase boundary between them. The moving boundary model that will be used in this work was first proposed by Wagner [103]. The phase boundary location ξ splits the electrode thickness into regions I ($\xi \leq x \leq L$) and II ($0 \leq x \leq \xi$).

The diffusion equation applies individually to both phases, so

$$\frac{\partial C}{\partial t} = D_I \frac{\partial^2 C}{\partial x^2} \quad (\xi \leq x \leq L), \quad [4-5]$$

$$\frac{\partial C}{\partial t} = D_{II} \frac{\partial^2 C}{\partial x^2} \quad (0 \leq x \leq \xi), \quad [4-6]$$

where D_I and D_{II} are the lithium ion diffusion coefficients in phases *I* and *II*, respectively. The phase boundary movement satisfies the conservation of lithium ions at the interface, which can be written as

$$C_d \frac{\partial \xi}{\partial t} = D_I \left(\frac{\partial C(x = \xi^+, t)}{\partial x} \right) - D_{II} \left(\frac{\partial C(x = \xi^-, t)}{\partial x} \right), \quad [4-7]$$

where C_d is the quantity of lithium ions consumed per unit movement of the phase boundary location ξ required by the reaction that converts the underlying phase structure of phase *I* to the that of phase *II*. Fick's First Law determines the net influx of lithium at the phase boundary, which in turn drives a movement of the boundary as concentrations raised or lowered sufficiently to drive a phase change.

As before, the boundary conditions are

$$\frac{\partial C(x=L, t)}{\partial x} = -\frac{j}{nFD'}, \quad [4-8]$$

and

$$\frac{\partial C(x=0, t)}{\partial x} = 0. \quad [4-9]$$

The initial conditions have become

$$C(x, \tau = 0) = C_0 \quad (\xi \leq x \leq L), \quad [4-10]$$

and

$$C(x, \tau = 0) = C_d \quad (0 \leq x \leq \xi). \quad [4-11]$$

Equations [4-5]-[4-11] can be made dimensionless by introducing equations

$$\alpha = \frac{x}{L} \quad [4-12]$$

$$\tau = \frac{D_I t}{L^2} \quad [4-13]$$

$$C' = \frac{C - C_0}{C_0} \quad [4-14]$$

$$J = \frac{jL}{nFD C_0} \quad [4-15]$$

$$\varepsilon = \frac{\xi}{L}, \quad [4-16]$$

$$\lambda = \frac{D_{II}}{D_I}, \quad [4-17]$$

$$\gamma = \frac{C_d}{C_0}, \quad [4-18]$$

where α is the dimensionless position, τ is the dimensionless time, C' is the dimensionless concentration, J is the dimensionless current density, ε is the dimensionless phase boundary

position, λ is the ratio of lithium ion diffusion coefficient in phase *II* to that in phase *I*, and γ is the dimensionless form of C_d . Then equations [4-5]-[4-11] become

$$\frac{\partial C'}{\partial \tau} = \frac{\partial^2 C'}{\partial \alpha^2} \quad (\xi \leq x \leq L), \quad [4-19]$$

$$\frac{\partial C'}{\partial \tau} = \lambda \frac{\partial^2 C'}{\partial \alpha^2} \quad (0 \leq \alpha \leq \varepsilon), \quad [4-20]$$

$$\frac{\partial C'(\alpha = L, \tau)}{\partial \tau} = -J, \quad [4-21]$$

$$\frac{\partial C'(\alpha = 0, \tau)}{\partial \tau} = 0, \quad [4-22]$$

$$\gamma \frac{\partial \varepsilon}{\partial \tau} = \left(\frac{\partial C'(\alpha = \varepsilon^+, \tau)}{\partial \alpha} \right) - \lambda \left(\frac{\partial C'(\alpha = \varepsilon^-, \tau)}{\partial \alpha} \right), \quad [4-23]$$

$$C'(\alpha, \tau = 0) = 0 \quad (\varepsilon \leq \alpha \leq 1), \quad [4-24]$$

and

$$C'(\alpha, \tau = 0) = \gamma \quad (0 \leq \alpha \leq \varepsilon). \quad [4-25]$$

Unlike the set of equations [4-1]-[4-3], there is no closed-form solution for equations [4-19]-[4-25]. In this work, the finite-element solver COMSOL Multiphysics® is used to numerically calculate a solution to this set of equations.

The simulation of a lithium ion electrode with the inclusion of phase change physics was first shown by Pollard and Newman [104]. This model assumes the electrode is always in pseudo-steady-state, meaning that it cannot be applied to higher rate charge or discharge. A more complete model without this restriction was first proposed by Srinivasan and Newman [40]. The model consists of spherical particles with a core of one phase, covered by a shell of the second phase. The flux of lithium ions at the particle surface changes the ion concentration in the shell

via diffusive transport, which in turn affects the concentration at the phase boundary to drive its movement. This model has been applied to the lithium iron-phosphate electrode that has become popular in recent years.

There are no equivalent-circuit models found in the literature that explicitly treat the presence of phase changes. In this chapter, the shortcomings of the planar distributed SOC equivalent-circuit model in modeling phase-change electrodes is examined in an exploratory study to better understand the limitations.

4.2 Experimental Method

Electrodeposition is chosen as the production method for a tin thin film that can be used for the electrochemical study of tin charge and discharge. Since tin would be used as the negative electrode in a lithium ion cell, the convention used in this chapter is that charging current has negative polarity, whereas discharging current has positive polarity. This is because charging of a negative electrode in a lithium ion cell refers to the insertion of lithium ions into the electrode from the electrolyte solution (and the associated injection of electrons into the electrode at the current collector), so the current is negative, with the resulting decrease in electrode potential. During discharge, lithium ions are removed from the electrode, and into the electrolyte solution (with the associated removal of electrons from the electrode at the current collector), so the current is positive, and results in the increase in electrode potential. This is in reverse to the convention adopted in Chapters 2 and 3, because the full cell is treated there.

Copper foil (lithium-ion battery grade, MTIXTL) was degreased by sonication for 15 minutes in acetone. Oxide on the foil was removed by placing the foil in 10% (volume/volume percent) H_2SO_4 for 5 minutes. The foil was sealed onto a PVC plate with electroplating tape (3M) so that tin is coated on one side. The tin deposition bath consists of 137 g/L potassium pyrophosphate, 36 g/L tin pyrophosphate, and 0.3 g/L gelatin. The electrodeposition was performed at a constant current density of 2.5 mA/cm^2 for 5 minutes at room temperature with stirring. This deposition procedure was taken from Yang *et al.* [105] because the authors found that this method produced tin films that performed relatively well in terms of cycling performance compared to other deposition methods.

The tin electrode was a disc of 1 cm diameter cut from the tin-coated copper foil. A custom designed setup was built to hold the electrodes inside a stainless steel coin cell case (MTIXTL). The reference and counter electrodes were lithium foils (99.9%, Sigma-Aldrich). Glass microfiber filters were used as separators between the working and reference electrodes, as well as between the reference and counter electrodes. The electrolyte solution was 1 M LiClO_4 in propylene carbonate (BASF). Approximately 200 μL of electrolyte solution was used to wet the separators.

Pulsed current charging and discharging tests are used to characterize the tin electrode. Before the pulsed current test, the electrode was cycled between the potential limits of 0.80 V and 0.050 V vs. Li/Li^+ for 5 cycles at $40 \mu\text{A/cm}^2$ to stabilize the behaviour of the electrode. Charging and discharging pulse experiment profiles are depicted in the left and right diagrams, respectively, in Figure 4-3. As mentioned earlier in this section, negative applied current corresponds to

electrode charging, while positive applied current corresponds to electrode discharging. As in the case in Chapters 2 and 3, the pulses current experiment consists of repeating periods when the current is applied (pulse phase), and when the current is zero (relaxation phase). The pulsed current test procedure consist of pulse magnitude of $40 \mu\text{A}/\text{cm}^2$ for 6 minutes duration during the pulse phase, followed by a relaxation phase of 40 minutes. These pulse parameters are similar to that used by Xie *et. al.* [100], and is chosen because it is found to result in between 25 to 35 pulses in each direction of the experiment, which is a sufficient number of pulses to enable extraction of model parameters. The pulsed current charging test (decreasing potential) was performed until the electrode potential reached below 0.010 V. The pulsed current discharging test (increasing potential) was performed until the electrode potential went above 1.2 V. The 0.010 V and 1.2 V limits are chosen because previous experiments showed that there is negligible capacity outside of this potential range. Electrochemical tests were performed using an Autolab PGSTAT101 (Metrohm AG), controlled using NOVA software (Metrohm AG). Cell assembly and testing were performed in an argon-filled glovebox.

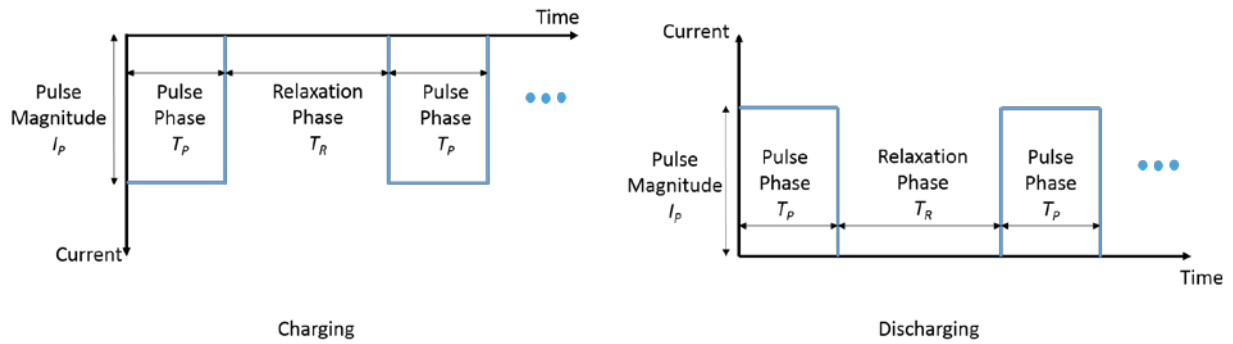


Figure 4-3. Depiction of the pulsed charging experiment profile is shown in the left diagram. As the tin electrode would be used as the negative electrode active material, charging of the electrode consists of a negative current, and leads to a decreasing electrode potential. The corresponding depiction of the pulsed discharging experiment profile is shown in the right diagram. Discharging of the electrode consists of a positive current, and leads to an increasing electrode potential.

Scanning electron microscopy and Auger microscopy were performed using a Thermo VG Microlab scanning Auger microscope to observe the morphology and chemical purity of the tin thin film.

4.3 Results and Analysis

This section discusses the results to the pulsed current charge and discharge experiments on the tin thin film electrode, and their implications for applying the planar distributed SOC equivalent-circuit model, discussed in chapters 2 and 3, to simulations of lithium ion cells that contain similar alloying electrodes. First, the measured physical properties of the deposited tin thin film is presented. Then, the diffusion capacitance C_D and diffusion resistance R_D of the planar

distributed SOC equivalent-circuit model are extracted. It is demonstrated that the extracted diffusion capacitance C_D has peak values at the ranges of states of charge that correspond to the phase change reactions. Another result is that the extracted diffusion resistance R_D also contains peaks at these states of charge. This corresponds to a dramatic drop in diffusion coefficient D near these phase change points, which is explained using the phase change model.

The mass of the deposited tin film is measured by weighing the copper foil before and after the electrodeposition. The thickness of the film is estimated to be *ca.* 1 μm . A scanning electron microscope image of the tin surface is shown in Figure 4-4. The tin film appears to completely cover the copper foil, with small grains on the order of 0.5 microns in diameter. The morphology observed from this image has the same granular features as those found by Yang *et al.* [105]. Scanning Auger microscopy before and after a series of Ar^+ sputtering did not show presence of impurities inside the bulk of the sample, within the resolution limit of the instrument (0.1 to 1 % atomic resolution depending on the element).

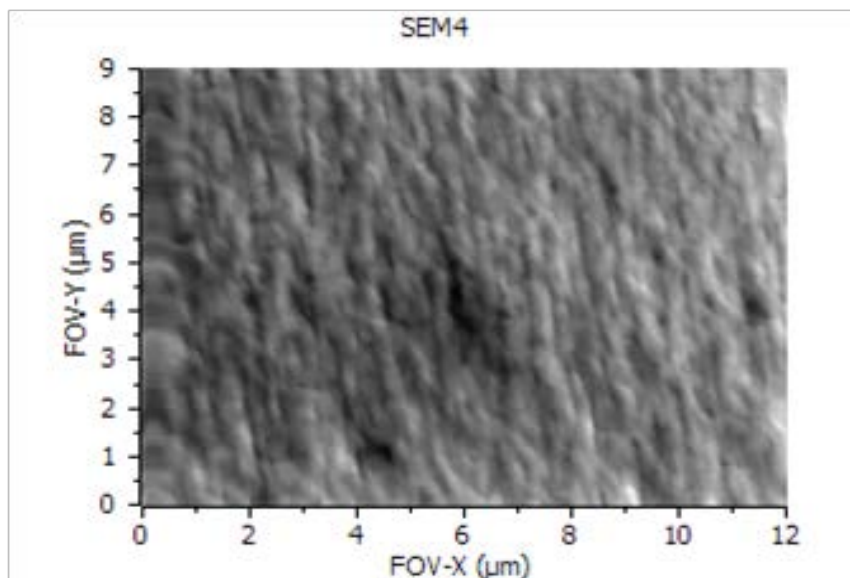


Figure 4-4. Scanning electron microscope image of the tin surface.

The potential of the tin film electrode during constant current charge (decreasing potential) and discharge (increasing potential) at $60 \mu\text{A}/\text{cm}^2$ is shown in Figure 4-5. The constant current charge was terminated when the electrode potential fell below 0.050 V (vs. Li/Li^+), while the constant current discharge was terminated when the electrode potential reached above 1.2 V (vs. Li/Li^+). During charging (up to *ca.* $8,500 \text{ s}$ in the plot), three potential plateaus are observed at *ca.* 0.70 V , 0.51 V , and 0.43 V . During discharging (from $8,500 \text{ s}$ to the end of the plot), three potential plateaus are also observed, at potentials of *ca.* 0.77 V , 0.71 V , and 0.58 V . As a potential plateau indicates occurrence of a phase transformation in an electrode in this system [85], these observed plateaus indicate ranges of states of charge when phase transformations are occurring in the tin electrode. Specific phase transformations can be associated to these potential plateaus, but the potential at, or close to, equilibrium is required, which is discussed later in this section.

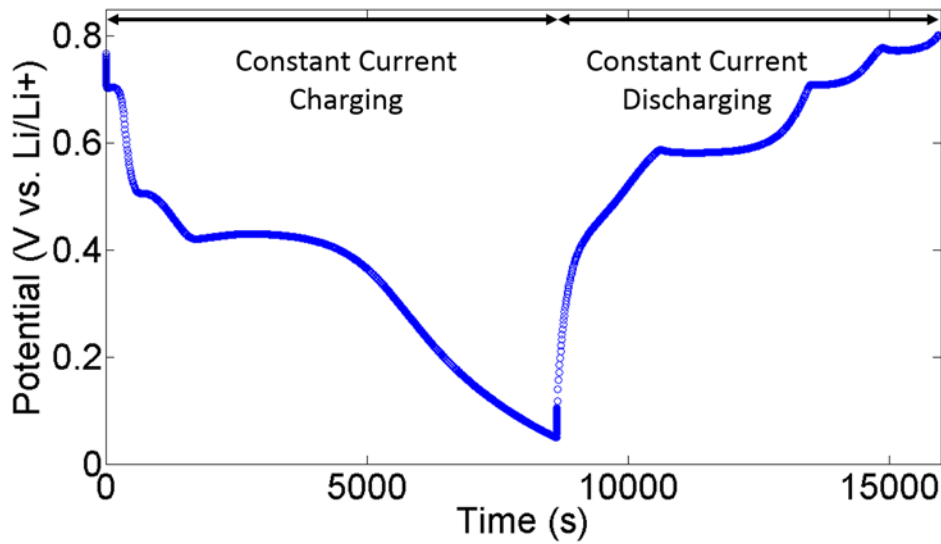


Figure 4-5. Potential of the tin electrode during constant current charge and discharge at $60 \mu\text{A}/\text{cm}^2$.

The model parameters of the planar distributed SOC model are extracted here for the tin thin film electrode to demonstrate some of the observed differences exhibited by the alloying elemental electrode. Like in Chapters 2 and 3, a series of current pulses are applied to the electrode and the results analyzed to extract these model parameters. First, the dependence of the open-circuit voltage V_{OC} is treated. Then the diffusion capacitance C_D and diffusion resistance R_D for this electrode are extracted and discussed.

The results from the pulsed charging experiments are shown in Figure 4-6. The applied current profile is shown in the top plot, while the measured electrode potential is shown in the bottom one. As discussed previously in Chapters 2 and 3, negative current pulses, which in this case represents charging, lead to sharp downward potential peaks in the plot. The subsequent potential reversal is due to relaxation of the concentration gradients when the current is switched off during the relaxation phase. To obtain the open-circuit potential, the electrode needs to rest

until equilibrated, like in Section 3.2.2.2. However, the electrode potential exhibited a continuing upward shift even after several hours. This may be the results of a leakage current, the cause of which may be the exposure of fresh electrode surface, as will be discussed shortly. In this case, the 40 minutes relaxation time is chosen to give a reasonable estimate of the open-circuit potential. Three plateaus in the open circuit potential can be identified at *ca.* 0.74 V, 0.66 V, and 0.50 V.

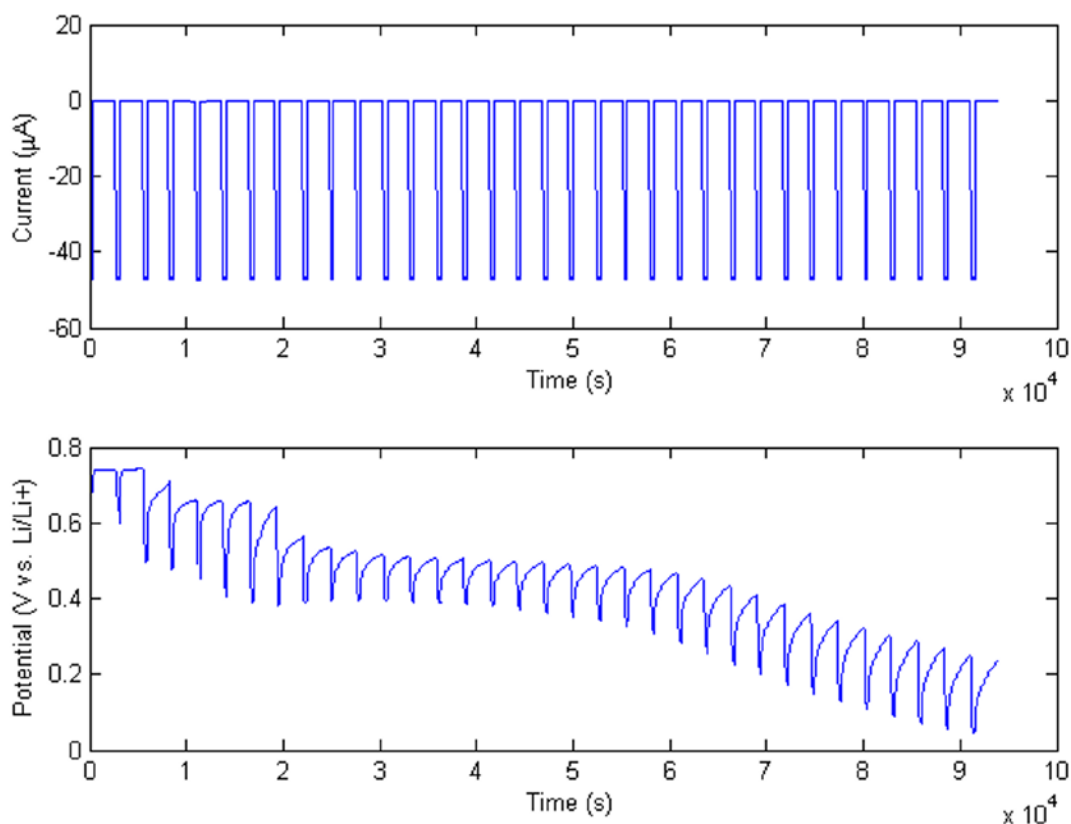
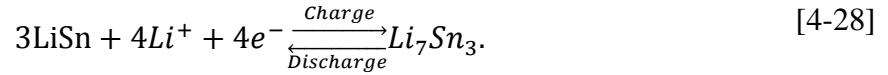
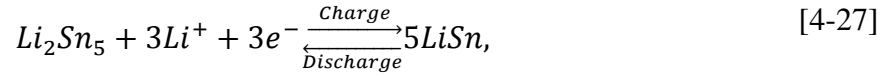
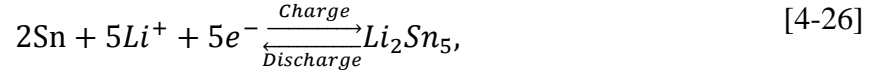


Figure 4-6. The top plot shows the applied current profile during the pulsed charging experiment for the tin thin film electrode. The bottom plot shows the corresponding measured electrode potential.

By comparing the potentials of these three plateaus to those in the work by Winter and Besenhard [106], the specific phase transformations that can be assigned to the 0.74 V, 0.66 V, and 0.50 V plateaus are, respectively,



Below *ca.* 0.40 V, the extended slope is due to the closely spaced transformations subsequently to phases Li_7Sn_3 , Li_5Sn_2 , $\text{Li}_{13}\text{Sn}_5$, Li_7Sn_2 , and $\text{Li}_{22}\text{Sn}_5$ [106]. The potentials are assigned to these phase transitions based on the coulometric titration results by Wang *et. al.* [107]. The formation of these Li-Sn phases and the interphase-transitions during electrode charge and discharge has been confirmed by Courtney and Dahn [108] using in-situ x-ray diffraction on various tin oxide compounds at different lithiation states.

Figure 4-7 shows the measured electrode potential during the pulsed discharge experiment. The pulsed discharging current profile is shown in the top plot, while the measured tin electrode potential is shown in the bottom plot. In this case, the positive current during the pulse phase leads to the sharp rises in electrode potential, followed by falling potential during the relaxation phase. As in the charging case, examination of the potential at the end of each relaxation period shows three plateaus that are associated with phase change reactions. The three potential plateaus are at *ca.* 0.57 V, 0.68 V, and 0.74 V. The reversed order of transformations from Li_7Sn_3 to Sn (according to the left-proceeding reactions [4-26]-[4-28]) can be assigned to these

plateaus. At the end of these relaxation periods, the rates of potential change are approximately $10 \mu\text{V/s}$. This suggests that the 40 minutes relaxation period allows the electrode to sufficiently relax before the subsequent discharge pulse, and that the open-circuit potentials can be estimated accurately in the discharging case. Although the same relaxation time of 40 minutes is used between the discharging pulses, the leakage current does not affect the electrode potential during relaxation phase to the same extent as for the charging pulses. Therefore, a lower leakage current is observed during discharge. One reason may be because tin undergoes large volume increase during charging, which creates new surfaces. The specific volume of the fully lithiated tin phase, $\text{Li}_{4.4}\text{Sn}$, is 283% of pure tin [85]. This in turns leads to the consumption of lithium ions from the electrode to form the solid-electrolyte interface at the surface of the electrode [109]. This might explain the large leakage current during charging of the thin film tin electrode, but not observed during discharging.

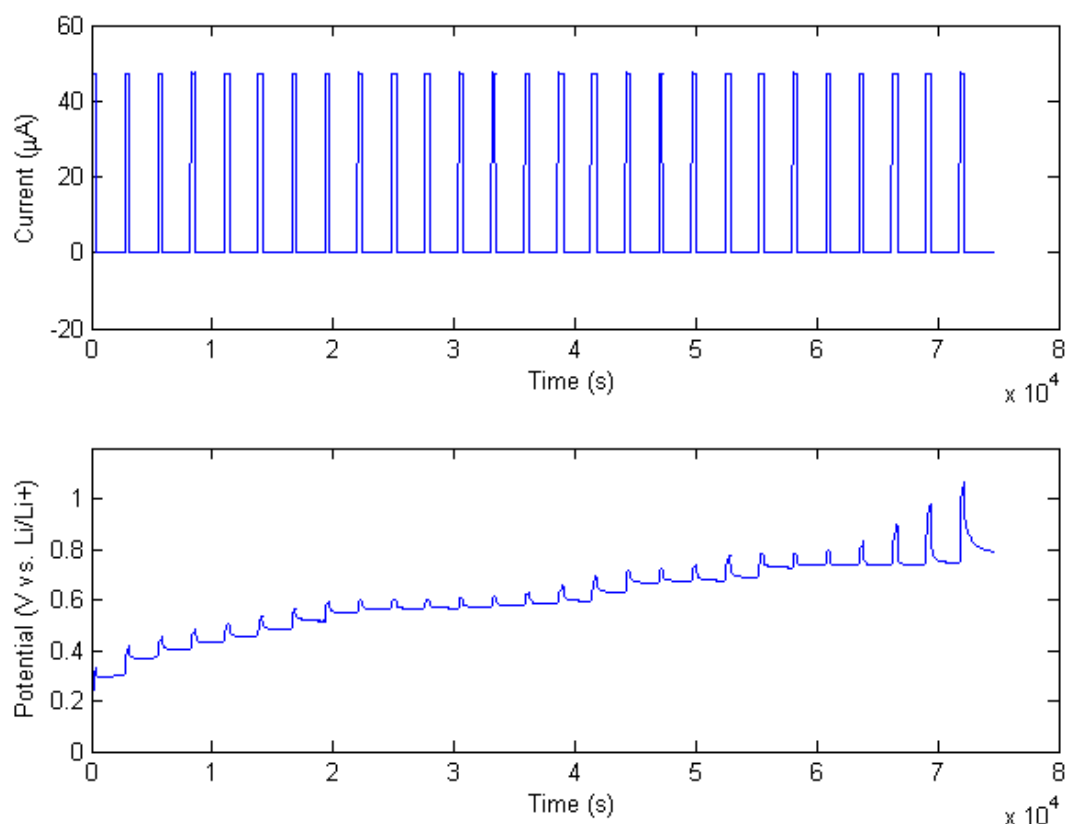


Figure 4-7. The top plot shows the applied current profile during the pulsed discharging experiment for the tin thin film electrode. The bottom plot shows the corresponding measured electrode potential.

The extracted dependence of the open-circuit potential on electrode SOC for the charging and discharging directions are shown in Figure 4-8. The potentials of the three plateaus in the pulsed charging and discharging experiments can be seen in the figure. As mentioned earlier, the three plateaus in the charging direction, from highest to lowest potential, can be assigned to (right-proceeding) reactions [4-26]-[4-28]. The three plateaus in the discharging direction, can also be assigned to these same reactions, but in the left-proceeding direction. There is clear hysteresis in the two lower potential plateaus, but not for the highest one. However, since estimation of the

open-circuit potential in the charging direction is affected by the presence of leakage current, the hysteresis voltage may not be accurate.

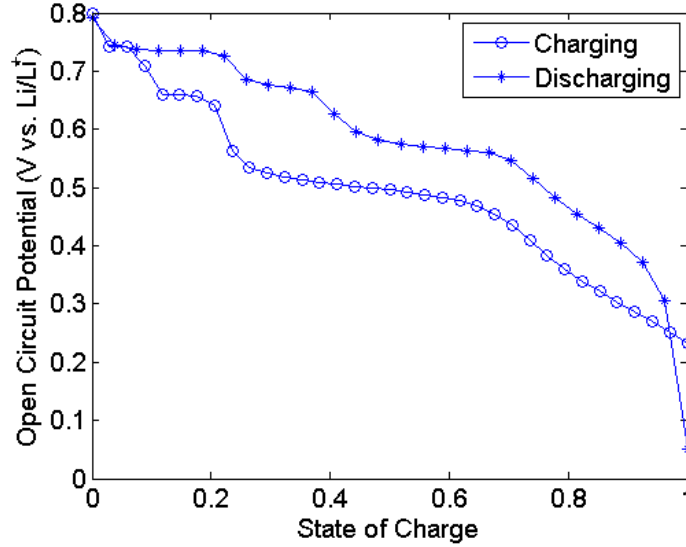


Figure 4-8. Open-circuit potential of the tin thin film during charge and discharge.

The diffusion capacitance C_D is extracted from the pulsed discharging data using equation [2-19], which is reproduced here as

$$C_D = \frac{\Delta Q}{(V_{OC,f} - V_{OC,i})}, \quad [4-29]$$

and the results are shown in Figure 4-9. This plot shows three capacitance peaks, at the same state of charge ranges as the plateaus in the open-circuit potential plot (Figure 4-8). This is consistent with expectations, as the plateau in the open-circuit potential means that the extraction of charge results in a very small change in open-circuit potential. Therefore, according to equation [4-29], the diffusion capacitance is high at the plateaus of electrode potential. This is also consistent with the phase change model discussed in Section 4.1. The charge that is

extracted is originating from the phase change reaction that has moved the interface of the two phases. This leads to a small open-circuit potential change, and results in a large effective diffusion capacitance at the ranges of SOC where the phase change effect is significant.

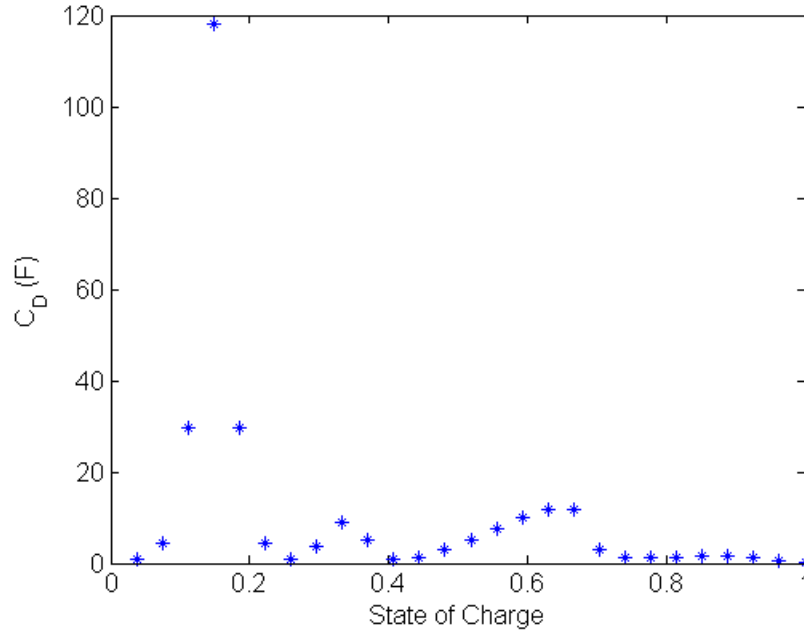


Figure 4-9. Diffusion capacitance C_D of the tin thin film, extracted from the pulsed discharging data.

The differential resistance is extracted using equation [2-29], which is reproduced here as

$$R_D = (M_0/2I)^2 \pi C_D, \quad [4-30]$$

and the results are shown in Figure 4-10. Like the diffusion capacitance C_D , the differential resistance R_D is also far larger at the same ranges of states of charge as the open-circuit potential plateaus. The resistance R_D is orders of magnitude larger at these ranges of SOC. This contrasts heavily with the case of the commercial lithium ion cells in Sections 2.3.3 and 3.2.2.2, which show a far narrower range of R_D values for each cell. As mentioned in Section 4.1, the diffusion

resistance R_D and diffusion capacitance C_D are both proportional to the reciprocal of the lithium ion diffusion coefficient D in the material. To confirm that this large range of diffusion resistance is also obtained by other authors in the literature, the diffusion coefficient of lithium ion in the tin thin film is calculated and compared to those by other authors, as is now discussed.

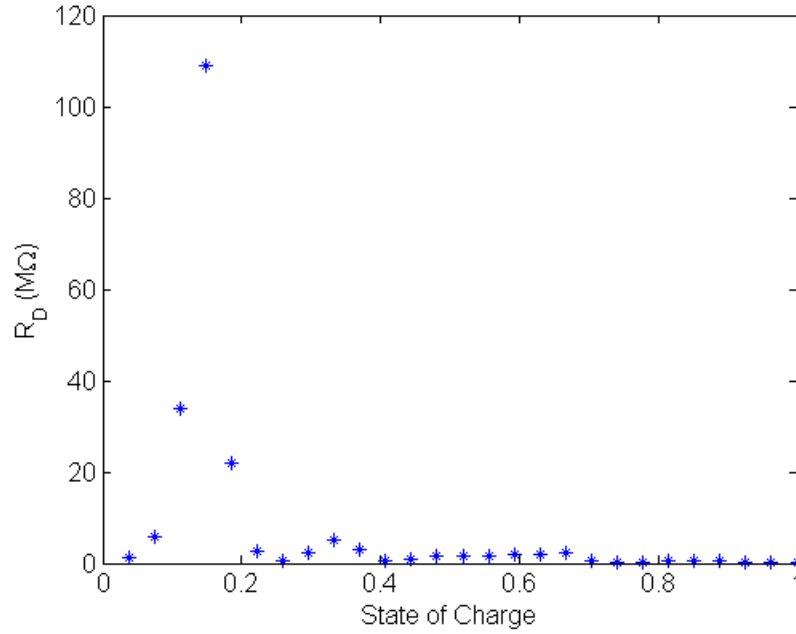


Figure 4-10. Diffusion resistance R_D of the tin thin film, extracted from the pulsed discharging data.

Using the single phase approximation, the lithium ion diffusion coefficient D in the electrode can be calculated from equation [4-4]. The electrode potential at the initial times of the applied pulse is fitted to $t^{1/2}$, similar to the extraction of diffusion resistance R_D in Chapters 2 and 3. The extracted diffusion coefficients for the pulsed discharging experiment are shown in Figure 4-11. The range of diffusion coefficients found here is consistent with those reported by Xie *et. al.*

[100] for tin. Large dips of three orders of magnitude in the diffusion coefficients can be seen at potentials close to the phase change potentials.

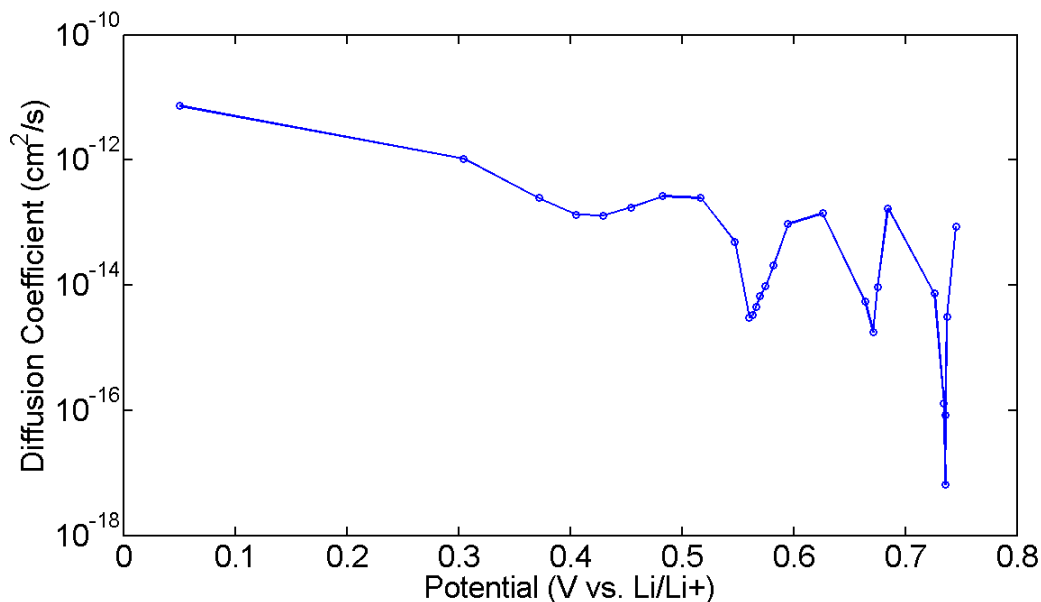


Figure 4-11. Lithium ion diffusion coefficient in the tin film, extracted from the pulsed discharging experiment.

The origin of these large dips in the diffusion coefficient D , and the corresponding peaks in R_D and C_D , is further examined here. The left plot of Figure 4-12 shows the potential transients during four consecutive discharging current pulses at the 0.54 V plateau. The tin electrode potential in both the pulse phase and the subsequent relaxation phase are shown. The potential transient at the end of the relaxation phase is quite close to zero, meaning that the electrode potential before and after the pulse are close, illustrating the plateau effect. As mentioned earlier, this small open-circuit potential change after the pulse relaxation phase means the estimated diffusion capacitance C_D is large for these pulses. A large diffusion capacitance slows transport, and leads to a low diffusion coefficient. The diffusion resistance R_D that is estimated

is also large, but this is more difficult to interpret as the shape of the response that is purely one dimensional diffusion is not the same as that seen or expected from a two phase limited response. The high values of both R_D and C_D nonetheless combine to produce very low estimated diffusion coefficients.

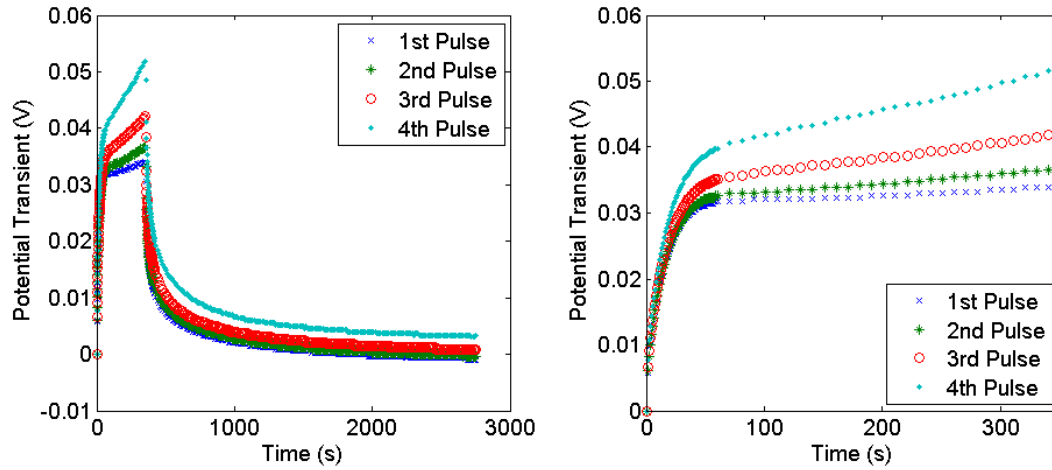


Figure 4-12. Potential transients during four consecutive discharging pulses of the experiment (1st: cross, 2nd: star, 3rd: circle, 4th: dot) near the 0.54 V open-circuit potential plateau.

The right plot shows the magnified view of the pulse phase (part of pulse when current is applied) of the four pulses. The plot shows that during the pulse phase, a rapid increase in electrode potential occurs at the beginning, before the potential begins to flatten. Each subsequent pulse produces a higher potential than the last. These voltage responses can be contrasted with the response of the single phase diffusion model, given by equations [4-1]-[4-3], to a constant current pulse. From the work by Carslaw and Jaeger [70], the solution can be shown to be given by

$$V(\alpha = L, t) = 2J \sqrt{\frac{t}{\tau D}} \sum_{n=0}^{\infty} \left[ierfc\left(\frac{n}{\sqrt{t/\tau}}\right) + ierfc\left(\frac{n+1}{\sqrt{t/\tau}}\right) \right], \quad [4-31]$$

where $ierfc(x)$ is given earlier by equation [2-21], and reproduced here as

$$ierfc(x) = \frac{1}{\sqrt{\pi}} \exp(-x^2) - x[1 - erf(x)]. \quad [4-32]$$

Equation [4-31] is evaluated and plotted in Figure 4-13. The observed response in the right plot in Figure 4-12 cannot be fit by a single phase diffusion model with constant parameters, as can be seen by comparing the shape of the response to that in Figure 4-13. The effect observed in Figure 4-12 can be hypothesized to be caused by a moving phase boundary. The phase transformation model is used to reproduce these qualitative features in the pulsed current response below.

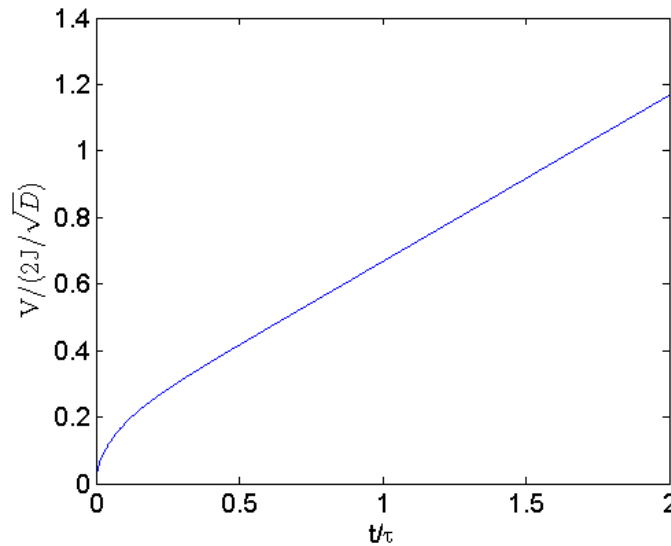


Figure 4-13. Calculated transient cell voltage during the pulse phase (when current is applied) of a pulsed experiment using the single phase model. The scale is much larger here than in the previous figure as the single phase model leads to a continued rise in overpotential, while the existence of a phase boundary acts as a charge sink which can be close to the surface.

The phase transformation model system of equations [4-19]-[4-25] was solved using COMSOL Multiphysics®. The arbitrary Lagrange Eulerian method was used to calculate and monitor the position of the phase boundary. The parameters used in the calculations are all assigned a value of 1, with the exception of those shown in Table 4-1. This is because a qualitative prediction is sought that is consistent with the observed electrode behavior shown in Figure 4-12. An illustration of the model is shown in Figure 4-14. For simulation of the discharging current pulses, the phase *I* region (closer to electrode/electrolyte interface) is the alloy phase that has lower lithium concentration. The phase *II* region (closer to electrode/current collector interface) is the alloy phase that has higher lithium concentration. The two regions are divided by a phase boundary at dimensionless location ξ . During electrode discharge, a flux of lithium ions are discharged from the electrode at the electrode/electrolyte interface ($\alpha = 1$). As the discharge proceeds, this depletion of lithium ions from the phase *I* region reaches the phase boundary and causes the transformation of the phase *II* alloy to that of phase *I*, which shifts the phase boundary to the left (reduces ξ). Therefore, in the simulations, a smaller starting phase boundary location, ξ_0 , means the phase boundary that is located further away from the electrode/electrolyte interface, and represents simulation of a later pulse.

Model Parameter	Single Phase Model	Phase Transformation Model
J	0.1	0.1
ξ_0	-	0.2, 0.4, 0.6, 0.8

Table 4-1. Values of Model Parameters Used in the Calculations

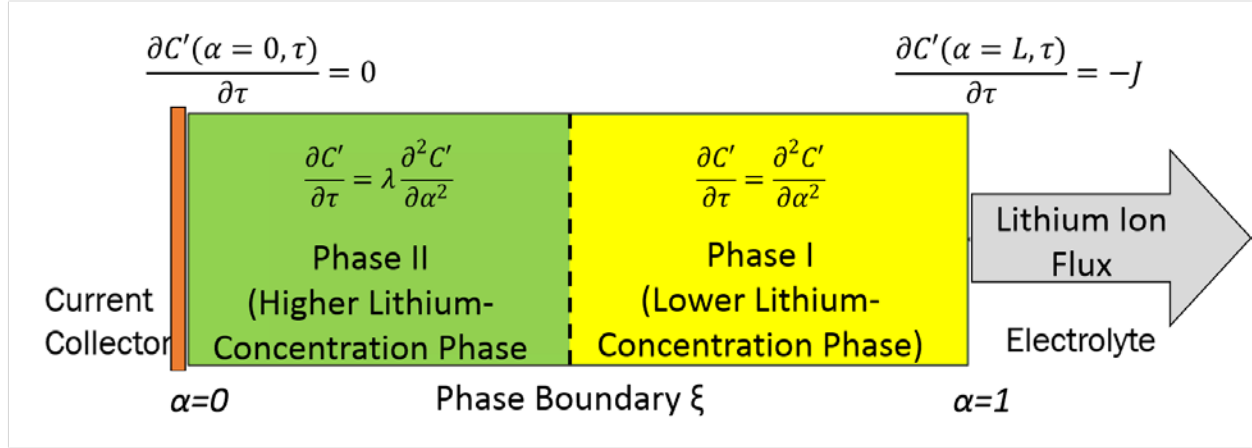


Figure 4-14. Illustration of the phase transformation model that consist of two regions of different phases.

The computed electrode potential during the pulse phase using the phase change model are shown in Figure 4-15. For all four initial phase boundary positions, there is a rapid increase in electrode potential, followed by flattening of the potential. Also, subsequent current pulses (decreasing ξ_0) result in increasing overpotentials. These features are consistent with the observations made in the experimental results in Figure 4-12. This can be explained by the effects of the phase boundary position on the early potential transient. The further the boundary is away (smaller ξ_0) from the electrode/electrolyte interface, the later the effect of the phase boundary and phase changes are reflected in the surface lithium ion concentration. This is because there is initially diffusion of the ions until they reach the phase boundary. Therefore, subsequent pulses of a moving boundary reach a higher potential before flattening.

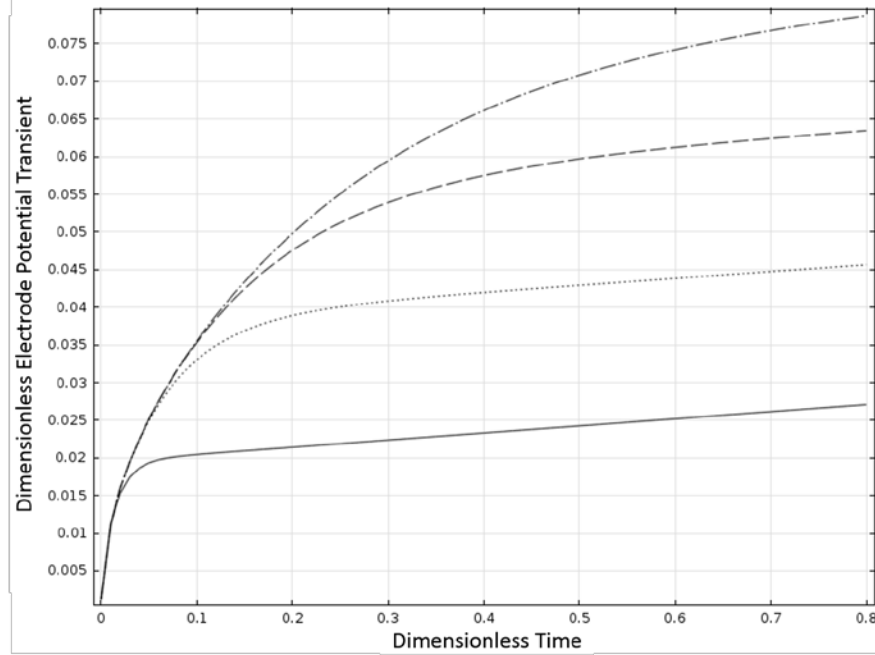


Figure 4-15. Calculated concentration transient during the pulse phase of the pulsed discharging experiment using the phase transformation model. The four curves correspond to different starting phase boundary locations ξ_0 : 0.2 (dash dot), 0.4 (dash), 0.6 (dot), and 0.8 (solid).

On the other hand, from the single phase model results shown in Figure 4-13, a small overpotential is seen at the beginning, followed by a sloping potential transient at later times. Therefore, the phase change model predicts the general shape of the current pulse response more accurately than the single phase model.

The phase transformation model for the electrode can be used to explain the observed peaks in diffusion capacitance C_D , and diffusion resistance R_D (and therefore the dips in diffusion coefficient D) at states of charge where the open-circuit potential is at a plateau. At the beginning of the pulse phase, the electrode responds according to the diffusive transport properties of the phase closest to the electrode-electrolyte interface (phase I in the model). The

diffusion capacitance C_D and diffusion resistance R_D of phase I determines the rise of the electrode potential during this time. As time proceeds, the charges (or depletion) reach the phase boundary, and is consumed (released) by the phase transformation. As a large quantity of charge is required by the phase transformation, this causes the lithium concentration at the electrode surface, and therefore also the electrode potential, to flatten. When the applied current is switched off during the relaxation phase, the lithium concentration in phase I returns to a value close to that before the pulse is applied, leading to the observed potential plateau at the end of the relaxation phase.

The above description illustrates that, for elemental alloy electrodes that exhibit phase transformation behavior, three characteristics of the extracted model parameters for the distributed SOC model are expected. First, the open-circuit potential will exhibit plateaus that is caused by the phase transformation reaction. Second, there are peaks in the extracted diffusion capacitance C_D . These peaks correspond to the effect of the phase transformation, as injection or extraction of lithium ions result in very small changes in electrode potential. Third, there are corresponding peaks in the extracted diffusion resistance R_D . Due to the large estimated diffusion capacitance C_D and diffusion resistance R_D , the diffusion coefficient D extracted for the electrode is also significantly lower at these states of charge where there are phase transformations. These observed characteristics of the extracted diffusion coefficient D are due to the use of a diffusive transport model to extract model parameters from a phase changing electrode.

The provided explanation shows the critical role played by the phase transformation in the potential response of the tin electrode to a current pulse. This should be true also for other lithium-alloying electrodes such as silicon. Since the distributed SOC equivalent-circuit model is derived from a model of the electrode governed by diffusive transport, its lack of consideration of the phase change effect is expected to result in poor simulation accuracy in simulating cells containing tin or other lithium-alloying electrodes.

In order for the phase transformation effect to be captured, an equivalent-circuit model that can account for the diffusive transport of two phases, and the movement of the phase boundary is needed. Also, a method to extract the diffusion capacitance C_D and the diffusion resistance R_D would be needed. The development and validation of such a model is an avenue for future work to build upon the work presented in this thesis.

4.4 Chapter Conclusions

In this chapter, the model parameters for the planar distributed SOC equivalent-circuit model is obtained for a tin thin film electrode by analyzing the results from pulsed current experiments. The open-circuit potential is shown to exhibit plateaus at certain ranges of states of charge. This is indicative of the presence of phase transformations at these states of charge. The extracted diffusion capacitance C_D and diffusion resistance R_D are shown to have large peaks that can be explained by the phase change.

The lithium ion diffusion coefficient D was first extracted from the resulting data under the single phase assumptions. Large drops in diffusion coefficients were observed at potentials close to the phase transformation potentials of tin. This can be explained by the phase change that occurs at these potentials. A moving boundary model was numerically computed to explain the shape of the potential transients during the constant current pulses.

The initial conclusion is that the distributed SOC equivalent-circuit model does not contain the correct charge transport mechanism to model the phase change effect in tin, and other lithium-alloying electrodes. However, it is possible that two phases could coexist along the length of the transmission line, with differing values of C_D and R_D , and with a large narrow peak in capacitance at the transition between them to account for the large amount of charge needed to change phase. However, the extraction technique used at present does not account for a phase boundary, with movement governed by the phase change physics described in this chapter. This is an avenue for future work to build upon the results presented in this thesis. At present it is

predicted that electrodes with numerous large phase changes, such as tin and silicon, may not be well represented by the combination of the extraction process and transmission line model.

Chapter 5: Conclusion

This work has made the following contributions to the field of equivalent-circuit modeling of lithium-ion cells:

a. Two new equivalent-circuit models are developed. The planar distributed SOC model is based on planar diffusion (Section 2.1), while the spherical distributed SOC model is based on spherical diffusion (Section 3.3.2.3). Both distributed SOC models incorporate a non-linear RC network for runtime simulation. Like sophisticated circuit models, the distributed SOC models' parameters depend on SOC. The RC network accounts for the energy storage and lithium ion diffusion effects inside the lithium-ion cell. The distributed SOC models account for the local variation of SOC inside the cell, and the local equivalent-circuit parameters are dependent on the local SOC. Although other resistive-capacitive network models have been presented previously, they were Thévenin-like in that they consist of a voltage source in series with the resistive-capacitive network impedance. In these models, the capacitors do not account for local state of charge inside the energy storage material. The newly demonstrated distributed SOC models are designed for predicting responses to dynamic and constant loads by accounting for a variation in charge state within a cell.

b. A pulsed current method to extract the parameters of the planar distributed SOC model is developed (Section 2.3.1). Equations that relate the model parameters of the planar distributed SOC model to the spherical counterpart are shown in Section 3.3.2.3. While the pulsed current method is similar to GITT, which is well known for characterizing an electrode to extract the

solid-phase diffusion coefficient of the solute inside the electrode, it is a new way of extracting parameters for an equivalent-circuit model. In the GITT method, the objective is to use as inputs the physical dimensions and stoichiometries of the material to obtain the diffusion coefficient. The methods developed in this thesis work abstract away the physical details of the materials inside the cell by using non-dimensionalized equivalent-circuits. The engineer using these models can construct the distributed SOC equivalent-circuits for cell simulations without detailed understanding of the internal structure of the cell or the underlying physical mechanisms. This benefits engineers who only intend to use the equivalent-circuit model to support application design and verification. This is one of the key advantages of equivalent-circuit models when compared to more sophisticated electrochemical models that, although include more physical mechanisms and details, are far more complex to construct and understand. This method is used to extract the circuit parameters from commercial cells (Chapters 2 and 3) and also used to analyze a single electrode in Chapter 4 (tin).

c. Another key advantage of the distributed SOC models shown in this work is that the models' parameters are largely independent on applied current (current magnitude and direction). This is shown in Section 3.2.2.3. This is unlike conventional circuit models, where the parameters have been shown to strongly depend on both current magnitude and direction [3], [4], [6]. The reason that these models show such dependence on the different applied currents used is that these tests excite different charge distributions inside the cell electrodes. The re-equilibration of the charge distribution in the electrodes during the relaxation phase of the pulse test causes a different cell voltage response. This leads to a strong dependence of the parameters in these equivalent-circuit models on applied current (current magnitude and direction). In contrast, in the distributed SOC

equivalent-circuit models, the use of a non-linear RC network to model ion diffusion in the electrode provides a more accurate picture of the diffusion physics occurring inside the cell. This is the reason the parameters of the distributed SOC equivalent-circuit models are largely independent on current magnitude or direction. This means a much-reduced amount of parameter extraction experiments in order to construct a full model.

d. The model capabilities are shown by comparing the simulated to the experimental results of the commercial cells from validation tests. In Chapter 2 this is performed for a lithium-ion polymer cell at a single current value, while in Chapter 3 extractions and simulations are performed for a cylindrical lithium ion cell at widely varying currents. The planar distributed SOC model is validated using two tests: 1. DDTs, and 2. constant current discharge tests. The RMSPVE and MAPVE are two measures that were used to quantify the simulation errors in the validation tests. As discussed in Section 1.3.2.3, the expected RMSPVE from equivalent-circuit models is on the low side of the 1-5% suggested by Chen and Rincon-Mora [2], while the MAPVE is expected to be on the high side of this range. Therefore, 1% and 5% are used as benchmarking values for the RMSPVE and MAPVE, respectively. For the DDTs, it was found that simulations using the planar distributed SOC model yielded MAPVE ranging between 1.5-3.7% (or 53-120 mV), while the RMSPVE ranged between 0.30-0.84% (or 11-30 mV). The performance of the planar distributed SOC model in simulating the behavior of the cells to constant current discharge tests is also studied. It is shown that the model performs well at low constant current discharge (0.60 A, or 0.20 C). The MAPVE was 0.96% (or 35 mV), while the root-mean-square-percent-voltage error was 0.49% (or 18 mV). However at higher currents (between 1.5 A to 6.0 A), the performance was poor. It was found that the MAPVE ranged

between 3.6-13% (or 130-410 mV), while the RMSPVE ranged between 2.1-10% (or 74-370 mV). Therefore, the planar model used initially to derive the distributed SOC equivalent-circuit model works well at low constant discharge currents up to 0.60 A (or 0.20 C), and pulsed currents of larger magnitudes (tested up to 6.0 A, or 2.0 C, which is the rated maximum for the tested cells). The errors at larger constant currents may be attributed to the spherical nature of the active material particles in tested cell's electrodes.

e. The spherical distributed SOC equivalent-circuit model, which is adapted to simulate spherical diffusion (Section 3.3.2.3), is intended to better represent the transport into particles that make up the electrodes. This is done by scaling lumped capacitances down linearly as they approach the end of the transmission line, and resistances up in proportion to the inverse of the remaining length. The effective diffusion coefficient remains the same, but the diffusion is now meant to approximate the dependence on radius seen in spherical particles. The spherical distributed SOC model was also validated using the dynamic discharge and constant current discharge tests. It is shown that the simulation performance of this model for higher current constant current discharge is much improved, when compared to the planar model circuit. It was found that for the three lower tested currents (600 mA, 1.5 A, and 3.0 A), the MAPVE was consistently at 1.3% (or 43-52 mV), while the RMSPVE ranged between 0.65-0.95% (or 23-30 mV). The performance of the spherical model for the highest constant current discharge current tested (6.0 A) was worse, with a MAPVE of 5.1% (or 160 mV) and RMSPVE of 1.8% (or 64 mV). It was still significantly better than the corresponding results from the planar model. In simulating the DDTs, the simulation performance of the spherical model for the 600 mA and 2.0 A DDTs is acceptable, with maximum-absolute-percent-voltage error between 1.9-3.3% (or 69-110 mV) and

RMSPVE of 0.59-0.85% (or 21-31 mV). However, for the 6.0 A DDT, the maximum-absolute-percent-voltage error is 7.7% (or 240 mV), while the RMSPVE is 1.5% (or 54 mV). This high MAPVE for the 6.0 A test may be attributed to too much capacitance available at the surface of the electrode, as the spherical electrode model does not account for the thickness of porous electrodes in real lithium ion cells. This leads to an over-estimation of cell voltage during large current pulses (6.0 A) of the DDT. Therefore, it is seen that the spherical electrode model is suitable for continuous discharge simulation of the cell at up to 3.0 A (or 1.0 C), or dynamic discharge profiles bounded by discharging current and charging currents of 2.0 A (0.67 C) and 1.0 A (0.33 C), respectively.

f. From the application of the two distributed SOC models (planar and spherical) to the two types of validation tests (DDTs and constant current discharge tests), it is clear that there is tradeoff between them. For applications with low average discharge rates (0.60 A, or 0.20 C), and high charging or discharging pulses, the planar model performs well. If the average discharge rate is higher (up to 3.0 A, or 1.0 C), or if the cell loading consists of pulsed currents bounded by lower currents (up to 2.0 A discharge and 1.0 A charge in this case), the spherical model performs better. The simplicity of the model, together with the reduced number of experiments necessary for model parameter extraction, are key advantages of these models compared to more sophisticated electrochemical models.

g. Finally, pulsed current techniques are applied to study lithium diffusion in tin electrodes (Chapter 4). The diffusion capacitance C_D and diffusion resistance R_D of the planar distributed SOC equivalent-circuit model are extracted. It is demonstrated that the extracted diffusion

capacitance C_D and diffusion resistance R_D have peak values at the ranges of states of charge that correspond to the phase change reactions. This corresponds to a dramatic drop in diffusion coefficient D near these phase change points, which is explained using the phase change model.

Previous work has also shown orders of magnitude dips in diffusion coefficient. These dips are shown to be consistent with the potentials and stoichiometries at which phase transitions occur in the lithium-tin alloy. A two-phase transport model is used to show that the pulsed current responses observed are consistent with the existence of phase transitions. These transitions pin the voltage in a manner analogous the temperature stabilization achieved in a mixed ice and water bath. The method helps understand the mechanisms of transport in tin – a high capacity and highly conductive lithium electrode material. Extraction of parameters for such electrodes may prove challenging however as the single phase diffusion model that is used to extract effective diffusion coefficient and transmission line resistance does not apply in regions where two phases co-exist, and when multiple phase changes are closely spaced – as in tin – it is difficult to distinguish the diffusion coefficients associated with each phase.

The potential applicability of the distributed SOC equivalent-circuit model work stems from the ease with which this model can be used in industry for system design and optimization. This work has introduced two new equivalent-circuit models (planar and spherical versions of the distributed SOC model) that can readily be implemented in simulation software, such as the popular MATLAB® Simulink®. The parameter extraction tests can be performed with basic electrical testing equipment, and the circuit parameters can be extracted simply from the pulsed current characterization test data.

This work represents an initial validation of the model. Testing on a larger number of cells, cell sizes and variations in cell chemistries will help determine the extent of its applicability. The model relies on there being one dominant diffusion mechanism, with the diffusion coefficient being only a function of SOC. In some cells the rate of diffusion may also depend on the depth of penetration of charge – due for example to structural or morphological variations. Multiple diffusion mechanisms may come into play as a result of the two electrodes, transport through the porous electrode depth, transport into particles, and the existence of a range of particle sizes. Other future work that can follow from this thesis is to study the effects of temperature on the circuit parameters. The tests performed in this work have been performed at room temperature. In some applications, such as in electric vehicles and e-bikes, the environmental temperature can vary over a wide range and will affect the cell's properties. Also, at high applied currents, the cell's heat generation and absorption should be accounted for. Applying methods to account for state of health are also of great benefit, as it would allow the model to be readily adapted for use with battery management systems. It is hoped that the non-linear RC network models developed here will evolve and prove useful as a component for use by system designers to simulate the system response to different application conditions, assist in illustrating the different design tradeoffs, and manage battery operation in real time.

Bibliography

- [1] “Corvus Energy Storage System ESS.” [Online]. Available: <http://corvus-energy.com/>. [Accessed: 17-Dec-2015].
- [2] M. Chen and G. A. Rincon-Mora, “Accurate electrical battery model capable of predicting runtime and I-V performance,” *IEEE Trans. Energy Convers.*, vol. 21, no. 2, pp. 504–511, Jun. 2006.
- [3] Y.-C. Hsieh, T.-D. Lin, R.-J. Chen, and H.-Y. Lin, “Electric circuit modelling for lithium-ion batteries by intermittent discharging,” *IET Power Electron.*, vol. 7, no. 10, pp. 2672–2677, 2014.
- [4] L. Lam, P. Bauer, and E. Kelder, “A Practical Circuit-based Model for Li-ion Battery Cells in Electric Vehicle Applications,” *2011 IEEE 33rd Int. Telecommun. Energy Conf. Intelec*, 2011.
- [5] D. Doerffel and S. Abu Sharkh, “A critical review of using the Peukert equation for determining the remaining capacity of lead-acid and lithium-ion batteries,” *J. Power Sources*, vol. 155, no. 2, pp. 395–400, Apr. 2006.
- [6] A. Hentunen, T. Lehmuspelto, and J. Suomela, “Time-Domain Parameter Extraction Method for Thevenin-Equivalent Circuit Battery Models,” *IEEE Trans. Energy Convers.*, vol. 29, no. 3, pp. 558–566, Sep. 2014.
- [7] D. Gandolfo, A. Brandão, D. Patiño, and M. Molina, “Dynamic model of lithium polymer battery – Load resistor method for electric parameters identification,” *J. Energy Inst.*, vol. 88, no. 4, pp. 470–479, Nov. 2015.
- [8] J. M. Tarascon and M. Armand, “Issues and challenges facing rechargeable lithium batteries,” *Nature*, vol. 414, no. 6861, pp. 359–367, Nov. 2001.
- [9] “Ford Investing \$4.5 Billion in Electrified Vehicle Solutions, Reimagining How to Create Future Vehicle User Experiences | Ford Media Center.” [Online]. Available: <https://media.ford.com/content/fordmedia/fna/us/en/news/2015/12/10/ford-investing-4-5-billion-in-electrified-vehicle-solutions.html>. [Accessed: 25-Jan-2016].
- [10] B. Dunn, H. Kamath, and J.-M. Tarascon, “Electrical Energy Storage for the Grid: A Battery of Choices,” *Science*, vol. 334, no. 6058, pp. 928–935, Nov. 2011.
- [11] C. Hendricks, N. Williard, S. Mathew, and M. Pecht, “A failure modes, mechanisms, and effects analysis (FMMEA) of lithium-ion batteries,” *J. Power Sources*, vol. 297, pp. 113–120, Nov. 2015.
- [12] M. Yoshio, R. J. Brodd, and A. Kozawa, *Lithium-ion batteries science and technologies*. New York, NY: Springer, 2009.
- [13] C. Glaize and S. Genies, *Lithium batteries and other electrochemical storage systems*. Hoboken; London: Wiley ; ISTE, 2013.
- [14] N. A. Chaturvedi, R. Klein, J. Christensen, J. Ahmed, and A. Kojic, “Algorithms for Advanced Battery-Management Systems,” *IEEE Control Syst.*, vol. 30, no. 3, pp. 49–68, Jun. 2010.
- [15] P. Arora, R. E. White, and M. Doyle, “Capacity Fade Mechanisms and Side Reactions in Lithium-Ion Batteries,” *J. Electrochem. Soc.*, vol. 145, no. 10, pp. 3647–3667, Oct. 1998.
- [16] A. Seaman, T.-S. Dao, and J. McPhee, “A survey of mathematics-based equivalent-circuit and electrochemical battery models for hybrid and electric vehicle simulation,” *J. Power Sources*, vol. 256, pp. 410–423, Jun. 2014.

- [17] J. Newman and W. Tiedemann, "Porous-Electrode Theory with Battery Applications," *Aiche J.*, vol. 21, no. 1, pp. 25–41, 1975.
- [18] M. Doyle, T. F. Fuller, and J. Newman, "Modeling of Galvanostatic Charge and Discharge of the Lithium/Polymer/Insertion Cell," *J. Electrochem. Soc.*, vol. 140, no. 6, pp. 1526–1533, Jun. 1993.
- [19] M. Doyle, J. Newman, A. S. Gozdz, C. N. Schmutz, and J. M. Tarascon, "Comparison of modeling predictions with experimental data from plastic lithium ion cells," *J. Electrochem. Soc.*, vol. 143, no. 6, pp. 1890–1903, Jun. 1996.
- [20] C. M. Doyle, "Design and simulation of lithium rechargeable batteries," Ph.D., University of California, Berkeley, United States -- California, 1995.
- [21] T. Fuller, M. Doyle, and J. Newman, "Simulation and Optimization of the Dual Lithium Ion Insertion Cell," *J. Electrochem. Soc.*, vol. 141, no. 1, pp. 1–10, Jan. 1994.
- [22] V. Ramadesigan, P. W. C. Northrop, S. De, S. Santhanagopalan, R. D. Braatz, and V. R. Subramanian, "Modeling and Simulation of Lithium-Ion Batteries from a Systems Engineering Perspective," *J. Electrochem. Soc.*, vol. 159, no. 3, pp. R31–R45, Jan. 2012.
- [23] S. Santhanagopalan, Q. Guo, P. Ramadass, and R. E. White, "Review of models for predicting the cycling performance of lithium ion batteries," *J. Power Sources*, vol. 156, no. 2, pp. 620–628, Jun. 2006.
- [24] S. K. Rahimian, S. Rayman, and R. E. White, "Comparison of single particle and equivalent circuit analog models for a lithium-ion cell," *J. Power Sources*, vol. 196, no. 20, pp. 8450–8462, Oct. 2011.
- [25] J. S. Newman and K. E. Thomas-Alyea, *Electrochemical systems*. Hoboken, N.J.: J. Wiley, 2004.
- [26] A. J. Bard, L. R. Faulkner, and John Wiley & Sons, *Electrochemical methods: fundamentals and applications*. Hoboken: John Wiley & Sons, 2007.
- [27] P. L. Moss, G. Au, E. J. Plichta, and J. P. Zheng, "An Electrical Circuit for Modeling the Dynamic Response of Li-Ion Polymer Batteries," *J. Electrochem. Soc.*, vol. 155, no. 12, pp. A986–A994, Dec. 2008.
- [28] S. Buller, M. Thele, R. W. A. A. De Doncker, and E. Karden, "Impedance-based simulation models of supercapacitors and Li-ion batteries for power electronic applications," *IEEE Trans. Ind. Appl.*, vol. 41, no. 3, pp. 742–747, May 2005.
- [29] U. Troltzsch, O. Kanoun, and H. R. Trankler, "Characterizing aging effects of lithium ion batteries by impedance spectroscopy," *Electrochimica Acta*, vol. 51, no. 8–9, pp. 1664–1672, Jan. 2006.
- [30] B. Schweighofer, K. M. Raab, and G. Brasseur, "Modeling of high power automotive batteries by the use of an automated test system," *IEEE Trans. Instrum. Meas.*, vol. 52, no. 4, pp. 1087–1091, Aug. 2003.
- [31] F. Baronti, G. Fantechi, E. Leonardi, R. Roncella, and R. Saletti, "Enhanced model for Lithium-Polymer cells including temperature effects," *IECON 2010 - 36th Annu. Conf. IEEE Ind. Electron.*, pp. 2329–33, 2010.
- [32] T. Kim and W. Qiao, "A Hybrid Battery Model Capable of Capturing Dynamic Circuit Characteristics and Nonlinear Capacity Effects," *IEEE Trans. Energy Convers.*, vol. 26, no. 4, pp. 1172–1180, Dec. 2011.

- [33] T. Hu, B. Zanchi, and J. Zhao, "Simple Analytical Method for Determining Parameters of Discharging Batteries," *IEEE Trans. Energy Convers.*, vol. 26, no. 3, pp. 787–798, Sep. 2011.
- [34] Y. Hu, S. Yurkovich, Y. Guezennec, and B. J. Yurkovich, "A technique for dynamic battery model identification in automotive applications using linear parameter varying structures," *Control Eng. Pract.*, vol. 17, no. 10, pp. 1190–1201, Oct. 2009.
- [35] X. Hu, S. Li, and H. Peng, "A comparative study of equivalent circuit models for Li-ion batteries," *J. Power Sources*, vol. 198, pp. 359–367, Jan. 2012.
- [36] J. Brand, Z. Zhang, and R. K. Agarwal, "Extraction of battery parameters of the equivalent circuit model using a multi-objective genetic algorithm," *J. Power Sources*, vol. 247, pp. 729–737, Feb. 2014.
- [37] Y. Hu, S. Yurkovich, Y. Guezennec, and B. J. Yurkovich, "Electro-thermal battery model identification for automotive applications," *J. Power Sources*, vol. 196, no. 1, pp. 449–457, Jan. 2011.
- [38] M. Doyle and J. Newman, "Analysis of capacity–rate data for lithium batteries using simplified models of the discharge process," *J. Appl. Electrochem.*, vol. 27, no. 7, pp. 846–856, Jul. 1997.
- [39] M. Doyle, T. F. Fuller, and J. Newman, "The importance of the lithium ion transference number in lithium/polymer cells," *Electrochimica Acta*, vol. 39, no. 13, pp. 2073–2081, Sep. 1994.
- [40] V. Srinivasan and J. Newman, "Discharge Model for the Lithium Iron-Phosphate Electrode," *J. Electrochem. Soc.*, vol. 151, no. 10, pp. A1517–A1529, Oct. 2004.
- [41] M. Guo, G. Sikha, and R. E. White, "Single-Particle Model for a Lithium-Ion Cell: Thermal Behavior," *J. Electrochem. Soc.*, vol. 158, no. 2, pp. A122–A132, Feb. 2011.
- [42] S. Santhanagopalan, Q. Zhang, K. Kumaresan, and R. E. White, "Parameter Estimation and Life Modeling of Lithium-Ion Cells," *J. Electrochem. Soc.*, vol. 155, no. 4, pp. A345–A353, Apr. 2008.
- [43] S. Santhanagopalan, P. Ramadass, and J. (Zhengming) Zhang, "Analysis of internal short-circuit in a lithium ion cell," *J. Power Sources*, vol. 194, no. 1, pp. 550–557, Oct. 2009.
- [44] S. Li and B. Ke, "Study of battery modeling using mathematical and circuit oriented approaches," in *2011 IEEE Power and Energy Society General Meeting*, 2011, pp. 1–8.
- [45] H. Zhang and M.-Y. Chow, "Comprehensive dynamic battery modeling for PHEV applications," in *2010 IEEE Power and Energy Society General Meeting*, 2010, pp. 1–6.
- [46] Z. Salameh, M. Casacca, and W. Lynch, "A Mathematical-Model for Lead-Acid-Batteries," *Ieee Trans. Energy Convers.*, vol. 7, no. 1, pp. 93–97, Mar. 1992.
- [47] V. F. Lvovich, *Impedance spectroscopy: applications to electrochemical and dielectric phenomena*. Hoboken, N.J.: Wiley, 2012.
- [48] T. K. Dong, A. Kirchev, F. Mattera, and Y. Bultel, "Modeling of Lithium Iron Phosphate Batteries by an Equivalent Electrical Circuit: Method of Model Parameterization and Simulation," *ECS Trans.*, vol. 25, no. 35, pp. 131–138, Apr. 2010.
- [49] A. Barai, G. H. Chouchelamane, Y. Guo, A. McGordon, and P. Jennings, "A study on the impact of lithium-ion cell relaxation on electrochemical impedance spectroscopy," *J. Power Sources*, vol. 280, pp. 74–80, Apr. 2015.

- [50] W. Waag, S. Käbitz, and D. U. Sauer, "Application-specific parameterization of reduced order equivalent circuit battery models for improved accuracy at dynamic load," *Measurement*, vol. 46, no. 10, pp. 4085–4093, Dec. 2013.
- [51] T. Tanaka, S. Ito, M. Muramatsu, T. Yamada, H. Kamiko, N. Kakimoto, and Y. Inui, "Accurate and versatile simulation of transient voltage profile of lithium-ion secondary battery employing internal equivalent electric circuit," *Appl. Energy*, vol. 143, pp. 200–210, Apr. 2015.
- [52] E. Kuhn, C. Forgez, P. Lagonotte, and G. Friedrich, "Modelling Ni-mH battery using Cauer and Foster structures," *J. Power Sources*, vol. 158, no. 2, pp. 1490–1497, Aug. 2006.
- [53] M. Urbain, S. Rael, and B. Davat, "Energetical Modeling of Lithium-Ion Batteries," in *Conference Record of the 2007 IEEE Industry Applications Conference, 2007. 42nd IAS Annual Meeting, 2007*, pp. 714–721.
- [54] M. Urbain, M. Hinaje, S. Raël, B. Davat, and P. Desprez, "Energetical Modeling of Lithium-Ion Batteries Including Electro Porosity Effects," *IEEE Trans. Energy Convers.*, vol. 25, no. 3, pp. 862–872, Sep. 2010.
- [55] L. H. Saw, Y. Ye, and A. A. O. Tay, "Electro-thermal characterization of Lithium Iron Phosphate cell with equivalent circuit modeling," *Energy Convers. Manag.*, vol. 87, pp. 367–377, Nov. 2014.
- [56] L. Gao, S. Liu, and R. A. Dougal, "Dynamic lithium-ion battery model for system simulation," *IEEE Trans. Compon. Packag. Technol.*, vol. 25, no. 3, pp. 495–505, Sep. 2002.
- [57] R. C. Kroeze and P. T. Krein, "Electrical battery model for use in dynamic electric vehicle simulations," in *IEEE Power Electronics Specialists Conference, 2008. PESC 2008, 2008*, pp. 1336–1342.
- [58] J. Zhang, S. Ci, H. Sharif, and M. Alahmad, "Modeling Discharge Behavior of Multicell Battery," *IEEE Trans. Energy Convers.*, vol. 25, no. 4, pp. 1133–1141, Dec. 2010.
- [59] N. Watrin, R. Roche, H. Ostermann, B. Blunier, and A. Miraoui, "Multiphysical Lithium-Based Battery Model for Use in State-of-Charge Determination," *IEEE Trans. Veh. Technol.*, vol. 61, no. 8, pp. 3420–3429, Oct. 2012.
- [60] M. Einhorn, F. V. Conte, C. Kral, and J. Fleig, "Comparison, Selection, and Parameterization of Electrical Battery Models for Automotive Applications," *IEEE Trans. Power Electron.*, vol. 28, no. 3, pp. 1429–1437, Mar. 2013.
- [61] K. S. Hariharan and V. Senthil Kumar, "A nonlinear equivalent circuit model for lithium ion cells," *J. Power Sources*, vol. 222, pp. 210–217, Jan. 2013.
- [62] Á. G. Miranda and C. W. Hong, "Integrated modeling for the cyclic behavior of high power Li-ion batteries under extended operating conditions," *Appl. Energy*, vol. 111, pp. 681–689, Nov. 2013.
- [63] J. Zhang, S. Ci, H. Sharif, and M. Alahmad, "An Enhanced Circuit-Based Model for Single-Cell Battery," *2010 Twenty-Fifth Annu. IEEE Appl. Power Electron. Conf. Expo. Apec*, pp. 672–675, 2010.
- [64] S. Abu-Sharkh and D. Doerffel, "Rapid test and non-linear model characterisation of solid-state lithium-ion batteries," *J. Power Sources*, vol. 130, no. 1–2, pp. 266–274, May 2004.
- [65] "UN Vehicle Regulations - 1958 Agreement, Addendum 100: Regulation No. 101, Revision 3." [Online]. Available:

- <http://www.unece.org/fileadmin/DAM/trans/main/wp29/wp29regs/updates/R101r3e.pdf>. [Accessed: 19-May-2016].
- [66] “Urban Dynamometer Driving Schedule.” [Online]. Available: <https://www.epa.gov/sites/production/files/2015-10/uddscol.txt>. [Accessed: 19-May-2016].
- [67] T. F. Fuller, M. Doyle, and J. Newman, “Simulation and Optimization of the Dual Lithium Ion Insertion Cell,” *J. Electrochem. Soc.*, vol. 141, no. 1, pp. 1–10, Jan. 1994.
- [68] “NI PCI-6251 - National Instruments.” [Online]. Available: <http://sine.ni.com/nips/cds/view/p/lang/en/nid/14124>. [Accessed: 17-Dec-2015].
- [69] W. Weppner and R. Huggins, “Determination of Kinetic-Parameters of Mixed-Conducting Electrodes and Application to System Li_3Sb ,” *J. Electrochem. Soc.*, vol. 124, no. 10, pp. 1569–1578, 1977.
- [70] H. S. Carslaw and J. C. Jaeger, *Conduction of heat in solids*. Oxford: Clarendon Press, 1967.
- [71] X. Wang, Y. Sone, and S. Kuwajima, “Effect of operation conditions on simulated low-earth orbit cycle-life testing of commercial lithium-ion polymer cells,” *J. Power Sources*, vol. 142, no. 1–2, pp. 313–322, Mar. 2005.
- [72] M. Broussely, S. Herreyre, P. Biensan, P. Kasztejna, K. Nechev, and R. J. Staniewicz, “Aging mechanism in Li ion cells and calendar life predictions,” *J. Power Sources*, vol. 97–98, pp. 13–21, Jul. 2001.
- [73] S. S. Choi and H. S. Lim, “Factors that affect cycle-life and possible degradation mechanisms of a Li-ion cell based on LiCoO_2 ,” *J. Power Sources*, vol. 111, no. 1, pp. 130–136, Sep. 2002.
- [74] L. Su, J. Zhang, C. Wang, Y. Zhang, Z. Li, Y. Song, T. Jin, and Z. Ma, “Identifying main factors of capacity fading in lithium ion cells using orthogonal design of experiments,” *Appl. Energy*, vol. 163, pp. 201–210, Feb. 2016.
- [75] S. Zhang, M. S. Ding, K. Xu, J. Allen, and T. R. Jow, “Understanding Solid Electrolyte Interface Film Formation on Graphite Electrodes,” *Electrochem. Solid-State Lett.*, vol. 4, no. 12, pp. A206–A208, Dec. 2001.
- [76] J. Christensen and J. Newman, “Cyclable Lithium and Capacity Loss in Li-Ion Cells,” *J. Electrochem. Soc.*, vol. 152, no. 4, pp. A818–A829, Apr. 2005.
- [77] M. Safari and C. Delacourt, “Aging of a Commercial Graphite/ LiFePO_4 Cell,” *J. Electrochem. Soc.*, vol. 158, no. 10, pp. A1123–A1135, Oct. 2011.
- [78] M. Safari and C. Delacourt, “Simulation-Based Analysis of Aging Phenomena in a Commercial Graphite/ LiFePO_4 Cell,” *J. Electrochem. Soc.*, vol. 158, no. 12, pp. A1436–A1447, Jan. 2011.
- [79] M. Dubarry and B. Y. Liaw, “Identify capacity fading mechanism in a commercial LiFePO_4 cell,” *J. Power Sources*, vol. 194, no. 1, pp. 541–549, Oct. 2009.
- [80] M. Dubarry, C. Truchot, and B. Y. Liaw, “Synthesize battery degradation modes via a diagnostic and prognostic model,” *J. Power Sources*, vol. 219, pp. 204–216, Dec. 2012.
- [81] T. Wang, L. Pei, T. Wang, R. Lu, and C. Zhu, “Capacity-loss diagnostic and life-time prediction in lithium-ion batteries: Part 1. Development of a capacity-loss diagnostic method based on open-circuit voltage analysis,” *J. Power Sources*, vol. 301, pp. 187–193, Jan. 2016.
- [82] I. Bloom, A. N. Jansen, D. P. Abraham, J. Knuth, S. A. Jones, V. S. Battaglia, and G. L. Henriksen, “Differential voltage analyses of high-power, lithium-ion cells: 1. Technique and application,” *J. Power Sources*, vol. 139, no. 1–2, pp. 295–303, Jan. 2005.

- [83] I. Bloom, J. Christophersen, and K. Gering, "Differential voltage analyses of high-power lithium-ion cells: 2. Applications," *J. Power Sources*, vol. 139, no. 1–2, pp. 304–313, Jan. 2005.
- [84] A. J. Smith, J. C. Burns, and J. R. Dahn, "High-Precision Differential Capacity Analysis of LiMn₂O₄/graphite Cells," *Electrochem. Solid-State Lett.*, vol. 14, no. 4, pp. A39–A41, Apr. 2011.
- [85] R. A. Huggins, *Advanced batteries: materials science aspects*. New York; [London]: Springer, 2009.
- [86] C. M. Julien, A. Mauger, K. Zaghib, and H. Groult, "Comparative Issues of Cathode Materials for Li-Ion Batteries," *Inorganics*, vol. 2, no. 1, pp. 132–154, Mar. 2014.
- [87] W. A. van Schalkwijk and B. Scrosati, *Advances in lithium-ion batteries*. New York, NY: Kluwer Academic/Plenum Publishers, 2002.
- [88] B. Yann Liaw, G. Nagasubramanian, R. G. Jungst, and D. H. Doughty, "Modeling of lithium ion cells—A simple equivalent-circuit model approach," *Solid State Ion.*, vol. 175, no. 1–4, pp. 835–839, Nov. 2004.
- [89] F. Huet, "A review of impedance measurements for determination of the state-of-charge or state-of-health of secondary batteries," *J. Power Sources*, vol. 70, no. 1, pp. 59–69, Jan. 1998.
- [90] X. Wang, Y. Sone, G. Segami, H. Naito, C. Yamada, and K. Kibe, "Understanding Volume Change in Lithium-Ion Cells during Charging and Discharging Using In Situ Measurements," *J. Electrochem. Soc.*, vol. 154, no. 1, pp. A14–A21, Jan. 2007.
- [91] G. L. Plett, "Extended Kalman filtering for battery management systems of LiPB-based HEV battery packs - Part 2. Modeling and identification," *J. Power Sources*, vol. 134, no. 2, pp. 262–276, Aug. 2004.
- [92] M. A. Roscher and D. U. Sauer, "Dynamic electric behavior and open-circuit-voltage modeling of LiFePO₄-based lithium ion secondary batteries," *J. Power Sources*, vol. 196, no. 1, pp. 331–336, Jan. 2011.
- [93] "GP18650-30U | 3.78V - 3000mAh." [Online]. Available: <http://www.gpbmindustry.com/en/products/lithiumrechargeable/gp18650-30u>. [Accessed: 17-Dec-2015].
- [94] "Arbin BT2000 - Battery Test Equipment | Arbin Instruments." [Online]. Available: <http://www.arbin.com/index.php/products/battery>. [Accessed: 17-Dec-2015].
- [95] M. Dubarry, V. Svoboda, R. Hwu, and B. Y. Liaw, "Incremental Capacity Analysis and Close-to-Equilibrium OCV Measurements to Quantify Capacity Fade in Commercial Rechargeable Lithium Batteries," *Electrochem. Solid-State Lett.*, vol. 9, no. 10, pp. A454–A457, Oct. 2006.
- [96] "ELECTRIC VEHICLE BATTERY TEST PROCEDURES MANUAL." [Online]. Available: http://www.uscar.org/guest/article_view.php?articles_id=86. [Accessed: 29-Jan-2016].
- [97] S. Ramo, J. R. Whinnery, and T. Van Duzer, *Fields and waves in communication electronics*. New York: J. Wiley, 1965.
- [98] A. Mukhopadhyay and B. W. Sheldon, "Deformation and stress in electrode materials for Li-ion batteries," *Prog. Mater. Sci.*, vol. 63, pp. 58–116, Jun. 2014.
- [99] K. I. Pridatko, "Electrochemical insertion of lithium in thin tin films," *Russ. J. Electrochem.*, vol. 42, no. 1, pp. 63–70, Jan. 2006.

- [100] J. Xie, N. Imanishi, A. Hirano, Y. Takeda, O. Yamamoto, X. B. Zhao, and G. S. Cao, "Li-ion diffusion behavior in Sn, SnO and SnO₂ thin films studied by galvanostatic intermittent titration technique," *Solid State Ion.*, vol. 181, no. 35–36, pp. 1611–1615, Nov. 2010.
- [101] D. Larcher, S. Beattie, M. Morcrette, K. Edström, J.-C. Jumas, and J.-M. Tarascon, "Recent findings and prospects in the field of pure metals as negative electrodes for Li-ion batteries," *J. Mater. Chem.*, vol. 17, no. 36, pp. 3759–3772, Sep. 2007.
- [102] J. Stefan, "Ueber die Theorie der Eisbildung, insbesondere über die Eisbildung im Polarmeere," *Ann. Phys.*, vol. 278, no. 2, pp. 269–286, Jan. 1891.
- [103] W. Jost, *Diffusion in solids, liquids, gases*. New York: Academic Press, 1960.
- [104] R. Pollard and J. Newman, "Mathematical Modeling of the Lithium-Aluminum, Iron Sulfide Battery I. Galvanostatic Discharge Behavior," *J. Electrochem. Soc.*, vol. 128, no. 3, pp. 491–502, Mar. 1981.
- [105] J. Yang, M. Winter, and J. O. Besenhard, "Small particle size multiphase Li-alloy anodes for lithium-ion-batteries," *Solid State Ion.*, vol. 90, no. 1–4, pp. 281–287, Sep. 1996.
- [106] M. Winter and J. O. Besenhard, "Electrochemical lithiation of tin and tin-based intermetallics and composites," *Electrochimica Acta*, vol. 45, no. 1–2, pp. 31–50, 1999.
- [107] J. Wang, I. D. Raistrick, and R. A. Huggins, "Behavior of Some Binary Lithium Alloys as Negative Electrodes in Organic Solvent-Based Electrolytes," *J. Electrochem. Soc.*, vol. 133, no. 3, pp. 457–460, Mar. 1986.
- [108] I. A. Courtney and J. R. Dahn, "Electrochemical and In Situ X-Ray Diffraction Studies of the Reaction of Lithium with Tin Oxide Composites," *J. Electrochem. Soc.*, vol. 144, no. 6, pp. 2045–2052, Jun. 1997.
- [109] P. B. Balbuena and Y. Wang, *Lithium-ion batteries: solid-electrolyte interphase*. London: Imperial College Press, 2004.